

University of Windsor

Scholarship at UWindor

Electronic Theses and Dissertations

Theses, Dissertations, and Major Papers

2012

A structural investigation to develop guidelines for the finite element analysis of the Mini-Baja vehicle

Babak Shahabi
University of Windsor

Follow this and additional works at: <https://scholar.uwindsor.ca/etd>

Recommended Citation

Shahabi, Babak, "A structural investigation to develop guidelines for the finite element analysis of the Mini-Baja vehicle" (2012). *Electronic Theses and Dissertations*. 5342.
<https://scholar.uwindsor.ca/etd/5342>

This online database contains the full-text of PhD dissertations and Masters' theses of University of Windsor students from 1954 forward. These documents are made available for personal study and research purposes only, in accordance with the Canadian Copyright Act and the Creative Commons license—CC BY-NC-ND (Attribution, Non-Commercial, No Derivative Works). Under this license, works must always be attributed to the copyright holder (original author), cannot be used for any commercial purposes, and may not be altered. Any other use would require the permission of the copyright holder. Students may inquire about withdrawing their dissertation and/or thesis from this database. For additional inquiries, please contact the repository administrator via email (scholarship@uwindsor.ca) or by telephone at 519-253-3000ext. 3208.

**A STRUCTURAL INVESTIGATION TO DEVELOP GUIDELINES
FOR THE FINITE ELEMENT ANALYSIS OF THE MINI-BAJA
VEHICLE**

By

Babak Shahabi

A Thesis
Submitted to the Faculty of Graduate Studies
through the Department of Mechanical, Automotive and Materials Engineering
in Partial Fulfillment of the Requirements for
the Degree of Master of Applied Science at the
University of Windsor

Windsor, Ontario, Canada

2011

© 2011 Babak Shahabi

A structural investigation to develop guidelines for the finite element analysis of the
Mini-Baja vehicle

by

Babak Shahabi

APPROVED BY:

Dr. S. Das (Outside Program Reader)
Department of Civil & Environmental Engineering

Dr. R. Barron (Program Reader)
Department of Mechanical, Automotive and Materials Engineering

Dr. N. Zamani (Advisor)
Department of Mechanical, Automotive and Materials Engineering

Dr. S. Erfani (Co-advisor)
Department of Electrical & Computer Engineering

Dr. B. Zhou (Chair of Defence)
Department of Mechanical, Automotive and Materials Engineering

December 16, 2011

AUTHOR'S DECLARATION OF ORIGINALITY

I hereby certify that I am the sole author of this thesis and that no part of this thesis has been published or submitted for publication.

I certify that, to the best of my knowledge, my thesis does not infringe upon anyone's copyright nor violate any proprietary rights and that any ideas, techniques, quotations, or any other material from the work of other people included in my thesis, published or otherwise, are fully acknowledged in accordance with the standard referencing practices. Furthermore, to the extent that I have included copyrighted material that surpasses the bounds of fair dealing within the meaning of the Canada Copyright Act, I certify that I have obtained a written permission from the copyright owner(s) to include such material(s) in my thesis and have included copies of such copyright clearances to my appendix.

I declare that this is a true copy of my thesis, including any final revisions, as approved by my thesis committee and the Graduate Studies office, and that this thesis has not been submitted for a higher degree to any other University or Institution.

ABSTRACT

Mini-Baja is a special type of vehicle used for recreational and exploration purposes. In many aspects it is similar to an All-Terrain Vehicle (ATV) except that it is much smaller in size. An international competition is organized by the Society of Automotive Engineers (SAE) for universities throughout the world to design and fabricate their vehicles and then compete against each other.

The objective of the present research was to carry out finite element analysis and crash simulations for a Mini-Baja chassis structure. The aim of this task was to write a comprehensive finite element guide for a Mini-Baja SAE vehicle that had already been built by students at the University of Windsor for the year 2010 Baja competition in Rochester New York.

Initially, an example of a Z-frame is explained and evaluated by simple hand calculations. Subsequently, the preliminary design of the Mini-Baja roll cage was generated using CAD data. To study the effects of stress and deformation on the frame members, linear static analysis followed by transient modal superposition analysis was carried out as the first steps toward this project. The static analysis in this thesis was used to arrive at an acceptable mesh size for the Mini-Baja roll cage dynamic analysis.

Additionally, the more realistic frontal impact analysis was performed on the Mini-Baja vehicle at a cruise velocity of 48 km/h (30 mph). Different FEA commercial packages were used throughout the project and results obtained from Abaqus/CAE and LS-DYNA were compared with one another.

Furthermore, crash test simulations for side impact and vehicle-to-vehicle crash scenarios were also performed for the Mini-Baja frame to evaluate the structural rigidity and vehicle behaviour due to crash.

DEDICATION

*Dedicated to my parents and my brother,
for their endless support, love and encouragement*

ACKNOWLEDGEMENTS

I would like to express my most sincere gratitude and profound appreciation to Dr. Nader Zamani for his supervision, guidance and support. His knowledge and expertise has been of immeasurable assistance throughout my graduate studies and research. This work could not have been achieved without his help and support.

I owe my deepest gratitude to Dr. William Altenhof for his guidance and encouragement. I appreciate all his contributions to make my experience productive and stimulating at the University of Windsor. The joy and enthusiasm he has for his research was contagious and motivational for me throughout my graduate degree.

I would like to take this opportunity to also thank my co-advisor Dr. S. Erfani, and my committee members Dr. S. Das and Dr. R. Barron for helping me throughout this thesis.

Lastly, I offer my regards and blessings to my friends, colleagues, and all of those who supported me in any respect during the completion of this thesis.

Babak Shahabi

TABLE OF CONTENTS

AUTHOR’S DECLARATION OF ORIGINALITY	III
ABSTRACT	IV
DEDICATION	V
ACKNOWLEDGEMENTS	VI
LIST OF TABLES	XI
LIST OF FIGURES	XII
LIST OF APPENDICES	XXI
NOMENCLATURE	XXII
CHAPTER I	1
<i>INTRODUCTION</i>	<i>1</i>
1.1 Scope and objective of the project.....	1
1.2 About the SAE Mini-Baja.....	2
1.3 The CAD model of the Mini-Baja frame and chassis	3
1.4 The role of non-linearities in the analysis of Mini-Baja.....	7
1.5 Literature review.....	12
1.5.1 Literature review of “SAE Mini-Baja” capstone reports.....	12
1.5.2 Literature review of “Vehicle Crash Impact Analysis” papers	23
CHAPTER II	37
<i>FINITE ELEMENT THEORY WITH NUMERICAL EXAMPLE</i>	<i>37</i>
2.1 Objectives and overview of Chapter II	37
2.2 A brief history of finite element method	37

2.3	Finite element analysis fundamentals-----	38
2.4	Finite element form of the assumed solution-----	39
2.5	Finite element library -----	42
2.6	Z-frame example-----	43
2.6.1	Computer implementation (Matlab) for the Z-frame -----	47
2.6.2	Computer simulation (Catia) for the Z-frame -----	52
2.6.3	Z-frame modified -----	54
 CHAPTER III-----		61
<i>APPLICATION OF BEAM, SHELL, AND SOLID ELEMENTS FOR THE MINI-BAJA</i>		
<i>FRAME (LINEAR STATIC AND DYNAMIC ANALYSIS)-----</i>		<i>61</i>
3.1	Objectives and overview of Chapter III -----	61
3.2	Mini-Baja modeling methodology -----	61
3.2.1	Material properties-----	65
3.2.2	Section property-----	68
3.2.3	Loading condition-----	68
3.2.4	Connections -----	70
3.3	Static results -----	71
3.4	Transient dynamic analysis -----	76
3.4.1	Damping effect -----	78
3.4.2	Dynamic force -----	79
3.4.3	Transient dynamic simulation -----	80
3.5	Mesh convergence study -----	87
 CHAPTER IV -----		92
<i>NON-LINEAR DYNAMIC ANALYSIS OF THE MINI-BAJA FRAME IN FRONTAL</i>		
<i>CRASH (LS-DYNA)-----</i>		<i>92</i>
4.1	Objectives and overview of Chapter IV -----	92
4.2	Key parameters of a non-linear explicit vehicle simulation -----	93
4.2.1	Implicit vs. explicit time integration methodologies -----	93
4.2.2	Viscoplastic material model -----	95
4.2.3	Shell elements and B-L-T element -----	98

4.2.4	Hourglass energy modes-----	101
4.2.5	Time step and mass scaling -----	102
4.2.6	Contact and friction modeling-----	103
4.3	Simulation of the front portion of the frame (LS-DYNA)-----	107
4.4	Frontal impact simulation of the Mini-Baja frame structure (LS-DYNA) -----	112
4.4.1	Energy balance -----	118
CHAPTER V -----		121
<i>EVALUATION OF THE FRONTAL CRASH OF THE MINI-BAJA VEHICLE BY</i>		
<i>(ABAQUS/CAE)-----</i>		<i>121</i>
5.1	Objectives and overview of Chapter V -----	121
5.2	Simulation of the front portion of the frame (Abaqus/CAE)-----	122
5.3	Frontal impact simulation of the Mini-Baja frame chassis (Abaqus/CAE)-----	130
5.4	Further comparison of LS-DYNA and Abaqus/CAE results-----	134
CHAPTER VI -----		139
<i>A MORE COMPLETE MODEL OF THE MINI-BAJA VEHICLE FOR CRASH ANALYSIS</i>		
<i>(LS-DYNA)-----</i>		<i>139</i>
6.1	Objectives and overview of Chapter VI-----	139
6.2	Modeling of the tires -----	139
6.3	Simulation of the complete Mini-Baja vehicle-----	143
6.3.1	The frontal crash of the Mini-Baja vehicle -----	147
6.3.2	The side crash of the Mini-Baja vehicle-----	153
6.3.3	Head-on collision of two Mini-Baja vehicles at 30 degree impact angle -----	157
CHAPTER VII -----		161
<i>CONCLUSIONS AND RECOMMENDATIONS FOR FUTURE WORK -----</i>		<i>161</i>
7.1	Conclusions -----	161
7.2	Recommendations for future work -----	163
REFERENCES-----		166

APPENDICES -----	171
APPENDIX A -----	172
<i>A. SEAM WELD CONNECTION</i> -----	<i>172</i>
APPENDIX B -----	173
<i>B. WIREFRAME LINE CONNECTION ISSUE</i> -----	<i>173</i>
APPENDIX C -----	174
<i>C. TRANSIENT DYNAMIC ANALYSIS</i> -----	<i>174</i>
VITA AUCTORIS -----	175

LIST OF TABLES

Table 2.1 Nodal displacement of the Z-frame -----	54
Table 2.2 Nodal rotations of the Z-frame-----	54
Table 2.3 Frequency analysis of the Z-frame (Rout = 0.15 m , Rin = 0.10 m) -----	57
Table 2.4 von Mises stress for Z-frame (Rout = 0.15 m , Rin = 0.10 m) -----	60
Table 3.1 Alloy composition of 4130 chromoly (by weight) [35] -----	66
Table 3.2 Mechanical properties of 4130 steel [35] -----	66
Table 3.3 Structural property of 4130 chromoly used in static simulation -----	67
Table 3.4 Number of modes and corresponding natural frequencies -----	82
Table 3.5 Variation of maximum displacement and stress due to change in shell element size --	87
Table 3.6 Displacement and stress at selected points in the frame-----	90
Table 4.1 Effect of different hourglass control techniques on accuracy and computational time -----	108
Table 4.2 Effect of adaptive method on zero energy modes -----	109
Table 6.1 Aluminum 6061 material properties -----	144

LIST OF FIGURES

Figure 1.1 University of Windsor Mini-Baja vehicle, 2010-----	2
Figure 1.2 University of Windsor Mini-Baja vehicle, 2010-----	3
Figure 1.3 Preliminary design of the chassis from SAE rule guide [1] -----	5
Figure 1.4 Preliminary design of the chassis from SAE rule guide [1] -----	5
Figure 1.5 CAD model of the Mini-Baja vehicle-----	6
Figure 1.6 CAD model of the Mini-Baja chassis-----	6
Figure 1.7 Behaviour of transverse beam sections in (a) slender beams and (b) thick beams [8] --	9
Figure 1.8 Large deflection of a cantilever beam [8]-----	9
Figure 1.9 Non-linear load-displacement curve [8]-----	10
Figure 1.10 Front impact – loading point of application [14]-----	13
Figure 1.11 Full meshed model in Ansys [15]-----	14
Figure 1.12 Front impact scenario in Visual Nastran [16]-----	18
Figure 1.13 Rollover impact scenario in Visual Nastran [16] -----	19
Figure 1.14 Left: finite element mesh with masses and rigid-walls; Right: optimized design of the chassis [17] -----	21
Figure 1.15 Deformation of the chassis at 0.030 sec [17] -----	22
Figure 1.16 Energy plot for frontal impact [17] -----	22
Figure 1.17 The chassis frame [18] -----	23
Figure 1.18 Idealization with 58 and 22 nodes [18] -----	24
Figure 1.19 Digitization arm being used on underside of hood [20] -----	26

Figure 1.20 Flow chart of the project with digitization [20] -----	27
Figure 1.21 Consumer information label for a vehicle with at least one NCAP star rating [22]--	28
Figure 1.22 Crush depth location and comparison [21]-----	29
Figure 1.23 Crash output results at different stages of the simulation [21] -----	30
Figure 1.24 FE model of the 2006 Ford F250 [23] -----	31
Figure 1.25 Left: comparison of the global deformation for NCAP test and simulation; Right: simulation data for energy balance [23]-----	32
Figure 1.26 Simulation and impact test comparison [25]-----	33
Figure 1.27 Finite element model of the C2500 pickup truck [26] -----	34
Figure 1.28 Comparison of pendulum test 02025 and simulation [26] -----	35
Figure 1.29 Comparison of pendulum test 02027 and simulation [26] -----	35
Figure 2.1 Element generation -----	40
Figure 2.2 Beam element with uniform cross-section-----	41
Figure 2.3 Element library of LS-DYNA [30]-----	42
Figure 2.4 Z-frame setup-----	44
Figure 2.5 An arbitrary oriented frame element -----	45
Figure 2.6 Three-element model for the Z-frame -----	46
Figure 2.7 FE model of the Z-frame -----	52
Figure 2.8 Nodal displacement of the Z-frame -----	53
Figure 2.9 FE model of the Z-frame with beam, shell and solid elements -----	56
Figure 2.10 Displacement vector; beam, shell and solid-----	57

Figure 2.11 Vertical vibration behaviour of beam, shell and solid models -----	58
Figure 2.12 Horizontal vibration behaviour of beam, shell and solid models -----	59
Figure 2.13 Out of plane mode of vibration of beam, shell and solid models -----	59
Figure 2.14 von-Mises stress contour; shell and solid-----	60
Figure 3.1 Linear tetrahedron solid element [34] -----	62
Figure 3.2 Solid idealization of the Mini-Baja structure-----	63
Figure 3.3 Linear triangular shell element [34]-----	64
Figure 3.4 Shell idealization of the Mini-Baja structure-----	64
Figure 3.5 Beam idealization of the Mini-Baja structure -----	65
Figure 3.6 Stress-strain curves of different grades of steel [35]-----	67
Figure 3.7 Sectional property of beam and shell models -----	68
Figure 3.8 Linear impulse and momentum applied on Mini-Baja frontal collision -----	69
Figure 3.9 Seam welded connection CATIA V5 -----	70
Figure 3.10 Weld-connection for the beam model CATIA V5-----	71
Figure 3.11 Deformation shape for the beam model-----	72
Figure 3.12 Deformation shape for the shell model -----	73
Figure 3.13 Deformation shape for the solid model -----	74
Figure 3.14 von Mises stress distribution for the shell model -----	75
Figure 3.15 von Mises stress distribution for the solid model -----	75
Figure 3.16 Left: static response for a slowly varying load; Right: dynamic response for a fast varying load [31]-----	76

Figure 3.17 Structure response for different types of damping [37]-----	78
Figure 3.18 Schematic diagram of a vehicle model over a bump -----	79
Figure 3.19 Constraint condition for dynamic analysis -----	80
Figure 3.20 Constraint condition for dynamic analysis -----	81
Figure 3.21 Deformation shape in static analysis -----	81
Figure 3.22 Stress contours in static analysis -----	82
Figure 3.23 Time modulation of the dynamic applied load -----	83
Figure 3.24 Maximum displacement of the frame at 0.0135 sec in dynamic analysis -----	84
Figure 3.25 Node for displacement graphs -----	84
Figure 3.26 Three components of the displacement response of the selected point for the time duration of 0.9 sec -----	85
Figure 3.27 Three components of the velocity response of the selected point for the time duration of 0.9 sec -----	85
Figure 3.28 Distribution of von Mises stress through the cage in time -----	86
Figure 3.29 Mesh convergence study for maximum displacement -----	88
Figure 3.30 Mesh convergence study for maximum stress-----	88
Figure 3.31 Selection of points for the mesh convergence study -----	89
Figure 3.32 Mesh convergence study for displacement at selected points -----	90
Figure 3.33 Mesh convergence study for stress at selected points -----	91
Figure 4.1 Cost versus model size in explicit and implicit methodologies [8] -----	94
Figure 4.2 Determination of effective plastic strain -----	95
Figure 4.3 4130 chromoly plastic behaviour -----	96

Figure 4.4 Stress-strain response of a viscoplastic material at different strain rates [39] -----	97
Figure 4.5 Yield stress vs. effective plastic strain at different strain rates [30] -----	98
Figure 4.6 A representation of membrane forces on a membrane element and bending moments on a plate element [40] -----	99
Figure 4.7 LS-DYNA shell elements, node numbering for normal direction [30]-----	99
Figure 4.8 Representation of warped shell elements [42] -----	100
Figure 4.9 a) A fully integrated element to the left and a under integrated element to the right; b) Two hourglass modes for the under integrated element [41] -----	101
Figure 4.10 Penalty contact algorithm in LS-DYNA [37]-----	104
Figure 4.11 Tied contact between tubes-----	105
Figure 4.12 Front portion of the vehicle -----	107
Figure 4.13 von Mises stress at different speeds for the front portion of the vehicle -----	107
Figure 4.14 Adaptive method applied on the frame -----	108
Figure 4.15 Hourglass energy vs. hourglass control models -----	109
Figure 4.16 Deformation shape of models with different adaptive refinements (in terms of the threshold angle)-----	110
Figure 4.17 Deformation vector of 4 different models -----	111
Figure 4.18 Energy balance for front portion at 150 km/h (model 1) -----	111
Figure 4.19 Mini-Baja frame structure -----	112
Figure 4.20 von Mises stress at 0.013 sec -----	113
Figure 4.21 Maximum von Mises stress at 0.015 sec -----	113
Figure 4.22 Maximum plastic strain at 0.045 sec -----	114

Figure 4.23 Strain rate of 0.08/s at 0.006 sec -----	114
Figure 4.24 Strain rate of 80/s at 0.0109 sec -----	115
Figure 4.25 Highest Strain rate of 132/s at 0.014 sec-----	115
Figure 4.26 Strain rate of 5/s at 0.038 sec -----	115
Figure 4.27 Velocity contour in y-direction at 0.0109 sec-----	116
Figure 4.28 Selected joints for contact force -----	116
Figure 4.29 Highest contact forces at the joints -----	117
Figure 4.30 Rigid wall normal force -----	117
Figure 4.31 Percentage of mass increase-----	118
Figure 4.32 Energy balance for the complete mock-up at 48 km/h-----	120
Figure 4.33 Energy ratio of the simulation at 48 km/h-----	120
Figure 5.1 Front portion of the frame in frontal impact setup (Abaqus/CAE)-----	122
Figure 5.2 Tie contact (Abaqus/CAE)-----	123
Figure 5.3 Energy balance for front portion at 60 km/h (Abaqus/CAE)-----	124
Figure 5.4 Energy balance for front portion at 60 km/h modified (Abaqus/CAE)-----	125
Figure 5.5 Energy balance for front portion at 60 km/h (LS-DYNA)-----	125
Figure 5.6 The ratio of artificial strain energy over elastic strain energy-----	126
Figure 5.7 von Mises stress distribution of the front portion at 60 km/h (LS-DYNA) -----	127
Figure 5.8 von Mises stress distribution of the front portion at 60 km/h (Abaqus/CAE) -----	127
Figure 5.9 von Mises stress distribution of the front portion at 150 km/h (Abaqus/CAE)-----	128
Figure 5.10 von Mises stress distribution of the front portion at 150 km/h (LS-DYNA) -----	128

Figure 5.11 Comparison of energy balance of the front portion at 150 km/h-----	129
Figure 5.12 Frontal impact scenario of the Mini-Baja vehicle (Abaqus/CAE)-----	130
Figure 5.13 Example of a wrong material direction -----	131
Figure 5.14 Energy balance of the frontal impact at 48 km/h (Abaqus/CAE)-----	132
Figure 5.15 von Mises stress distribution at 0.013 sec (Abaqus/CAE) -----	132
Figure 5.16 Maximum von Mises stress at 0.016 sec (Abaqus/CAE)-----	133
Figure 5.17 Maximum plastic strain at the end of the simulation 0.045 sec (Abaqus/CAE) ----	133
Figure 5.18 Maximum plastic strain at the end of the simulation 0.045 sec -----	134
Figure 5.19 Energy balance of the full Mini-Baja mock-up at 48 km/h -----	135
Figure 5.20 Selected point for side displacement -----	135
Figure 5.21 Side displacement of point (P)-----	136
Figure 5.22 Selected roof point (Q)-----	136
Figure 5.23 Vertical displacement of the roof point (Q)-----	137
Figure 5.24 Wall reaction force-----	138
Figure 5.25 Reaction wall force versus resultant displacement (stiffness)-----	138
Figure 6.1 Actual tires and suspension assembly -----	140
Figure 6.2 CAD model of the tire -----	140
Figure 6.3 FE model of the tire assembly displaying the sectional thicknesses -----	141
Figure 6.4 Deformation of the tires at 90mm displacement of the wall-----	142
Figure 6.5 Deformation of the tires at 0.04 sec for the rear tires and at 0.032 sec for front tires -----	142

Figure 6.6 FE model of the completed Mini-Baja vehicle-----	143
Figure 6.7 Body panels and nodal rigid body constrained-----	144
Figure 6.8 Body panels, rear suspension, and shocks -----	145
Figure 6.9 Behaviour of the low density foam [30]-----	145
Figure 6.10 Stress-strain curve for the low density foam cushion -----	146
Figure 6.11 Revolute joint and angular velocity of the tires -----	146
Figure 6.12 Test setup for equilibrium check -----	148
Figure 6.13 Reaction force of the rigid ground-----	148
Figure 6.14 Isometric view of the detailed model simulation of the Mini-Baja vehicle into the rigid wall at 48 km/h-----	149
Figure 6.15 Left: the maximum von Mises stress at 0.011 sec; Right: effective plastic strain at the end of the simulation-----	149
Figure 6.16 Side, top and front views of the deformation at t = 0.014 sec -----	150
Figure 6.17 Side, top and front views of the deformation at t = 0.025 sec -----	150
Figure 6.18 Side, top and front views of the deformation at t = 0.036 sec -----	150
Figure 6.19 Traced nodes on the rear tire at t = 0.04 sec -----	151
Figure 6.20 Energy balance for frontal crash at 48 km/h -----	151
Figure 6.21 Energy balance for frontal crash at 48 km/h (low density tire)-----	152
Figure 6.22 Kinetic energy based on density of tires at 48 km/h-----	152
Figure 6.23 Side impact setup-----	153
Figure 6.24 Sequential views of the side impact scenario 1 at initial position -----	154
Figure 6.25 Sequential views of the side impact scenario 1 at t = 0.033 sec-----	154

Figure 6.26 Sequential views of the side impact scenario 1 at the end of the simulation -----	154
Figure 6.27 Energy balance of the side crash scenario 1 at 48 km/h -----	155
Figure 6.28 Sequential views of the side impact scenario 2 at initial position -----	155
Figure 6.29 Sequential views of the side impact scenario 2 at t = 0.016 sec-----	156
Figure 6.30 Sequential views of the side impact scenario 2 at t = 0.025 sec-----	156
Figure 6.31 Sequential views of the side impact scenario 2 at the end of the simulation -----	156
Figure 6.32 Energy balance of the side crash scenario 2 at 48 km/h -----	157
Figure 6.33 Configuration of the vehicle-to-vehicle crash at 30 degree impact angle -----	158
Figure 6.34 Sequential views of the vehicle-to-vehicle crash at initial position -----	158
Figure 6.35 Sequential views of the vehicle-to-vehicle crash at t = 0.017 sec -----	159
Figure 6.36 Sequential views of the vehicle-to-vehicle crash at t = 0.036 sec -----	159
Figure 6.37 Sequential views of the vehicle-to-vehicle crash at t = 0.07 sec -----	159
Figure 6.38 Energy balance of the vehicle-to-vehicle crash at 48 km/h -----	160
Figure 6.39 Maximum von Mises stress for vehicle-to-vehicle crash at t = 0.02 sec -----	160
Figure 7.1 Hybrid III occupant dummy -----	164
Figure 7.2 Two Mini-Baja's impact scenario at 30 degree impact angle-----	165
Figure A.1 Seam weld connection tutorial -----	172
Figure B.1 Line connection issue tutorial-----	173
Figure C.1 Transient dynamic analysis tutorial-----	174

LIST OF APPENDICES

APPENDICES -----	171
APPENDIX A -----	172
A. SEAM WELD CONNECTION -----	172
APPENDIX B -----	173
B. WIREFRAME LINE CONNECTION ISSUE -----	173
APPENDIX C -----	174
C. TRANSIENT DYNAMIC ANALYSIS -----	174

NOMENCLATURE

γ	Transverse shear strains
$[\bar{k}]$	Linear stiffness matrix
$[n]$	Incremental matrix
$[\bar{\sigma}_0]$	Initial stress matrix
$\{u\}$	Degree of freedom
$[K]$	Stiffness matrix
$[m]$	Mass matrix
$[c]$	Damping matrix
ω	Natural frequency of harmonic motion
$f_i(x)$	Shape function
r_q	Distributed loads
$R_{(\text{point loads and moments})}$	Point loads and moments
e^p	Plastic strain
e^e	Elastic strain
$\dot{\epsilon}$	Strain rate
SIGY	Initial yield stress
σ_y^s	Static stress
N_i	Membrane forces
L_c	Characteristic length
c	Sound speed
k	Bulk modulus
δ	Penetration distance

CHAPTER I

INTRODUCTION

1.1 Scope and objective of the project

In this thesis, considerable effort has been dedicated to the use of different commercial finite element analysis packages available at the University of Windsor. The intended objective of this thesis is to present some of the findings and challenges with regard of the finite element modeling of a Mini-Baja vehicle. It is anticipated that this research will assist undergraduate and graduate students or other readers who have limited experience in computational methods in using FEA tools for design purposes.

An introduction to the Mini-Baja vehicle, basic fundamentals of simulation, and the assumptions made for the non-linear dynamic analysis of the vehicle are discussed in Chapter 1. The finite element method and its application for a simple Z-frame is discussed in Chapter 2. There, the numerical results of a linear finite element analysis are compared with theoretical solution using a Matlab program.

In Chapter 3, the application of shell, beam and solid elements for a Mini-Baja frame are discussed for a linear static analysis. Later in this chapter, dynamic loads transmitted to the frame are simulated for a case where the vehicle goes over a bump. Chapter 4 provides an explicit non-linear dynamic simulation for a frontal crash of the frame into a rigid wall at 48 km/h (30mph). The results from this simulation are validated by another FEA package in Chapter 5.

In Chapter 6, the model is refined by including body panels and other components such as suspension arms, wheels and steering wheel for a more realistic vehicle analysis. Validation by experimental crash test on this vehicle is beyond the scope of the project.

1.2 About the SAE Mini-Baja

The Society of Automotive Engineers (SAE) organizes an inter-collegiate competition in which various universities from all around the world build a Mini-Baja vehicle to compete against one another. The automotive society has laid down a set of guidelines and rules [1] that every vehicle should follow. These guidelines are based on recommendations and tests conducted by design professionals and engineers.

Being a competition, every university has to develop its own design without any professional assistance or knowledge sharing. Baja SAE consists of three regional competitions that simulate real-world engineering design projects and their related challenges. Engineering students are tasked to design and build an off-road vehicle that will survive the severity of rough terrain and sometimes even water.



Figure 1.1 University of Windsor Mini-Baja vehicle, 2010

All vehicles are powered by a ten-horsepower Intek Model 20 engine donated by Briggs & Stratton Corporation. Figures 1.1 and 1.2 show snapshots of the University of Windsor's 2010 vehicle and gives the reader an idea of the terrain during the competition.

The mechanical engineering capstone project is an attempt to design a Mini-Baja from scratch, based on the guidelines provided by SAE. Certain practices by the industry in off-road vehicles and the concepts of mechanical engineering are employed to develop and design a chassis which is safe, ergonomic and has the minimum possible weight. Competitiveness of the vehicle in terms of sustainability and manoeuvrability should also be kept as a design goal.



Figure 1.2 University of Windsor Mini-Baja vehicle, 2010

The rules [1] are set in order to comprise a number of limitations on the vehicle's configuration, vehicle maximum size, all terrain capability of the vehicle as well as vehicle ergonomic capacity. As far as safety issues are concerned, there are several regulations concerning the electrical systems, battery location and orientation, kill switches and brake specifications.

1.3 The CAD model of the Mini-Baja frame and chassis

The Mini-Baja vehicle is designed and fabricated as a capstone project at the University of Windsor every year. Although the capstone team is divided into different sections, it is understood that the design and fabrication of the chassis is one of the main

challenges of the project. Each year students attempt to deliver a better design by analyzing the frame with the aid of computer modeling and simulation. The Mini-Baja vehicle for the academic year 2010 was available at the university and therefore, it was selected for the finite element analysis and discussion in this thesis. The reader should keep in mind that the impetus of this thesis is to analyze a pre-existing design to identify its important aspects and deficiencies.

The Society of Automotive Engineers has laid down a set of required specifications for the design and manufacturing of the roll cage. The cage must be designed to prevent any structural failure. It must be a space frame made up entirely of tubular steel components. Several members are mandatory in the design of the cage, which are shown in figures 1.3 and 1.4, the dimensions of these members; member's length, thicknesses and orientations are given in detail in the SAE guideline.

Some preliminary design data was available from previous reports and files on the 2010 Mini-Baja vehicle; nevertheless the CAD modeling of the frame and other components for this thesis were done again through reverse engineering of the vehicle leading to new CAD data, figures 1.5 and 1.6.

Several assumptions were made on the finite element modeling of the vehicle. Suspension arms, slender members such as A-arms and the frame's back axle were modeled with simple beam elements. The engine has been replaced by the equivalent of structural distributed mass over appropriate members. The spring and dampers were modeled with acceptable discrete elements to incorporate their effects on the vehicle's kinematics, whereas the models of the shocks themselves were excluded.

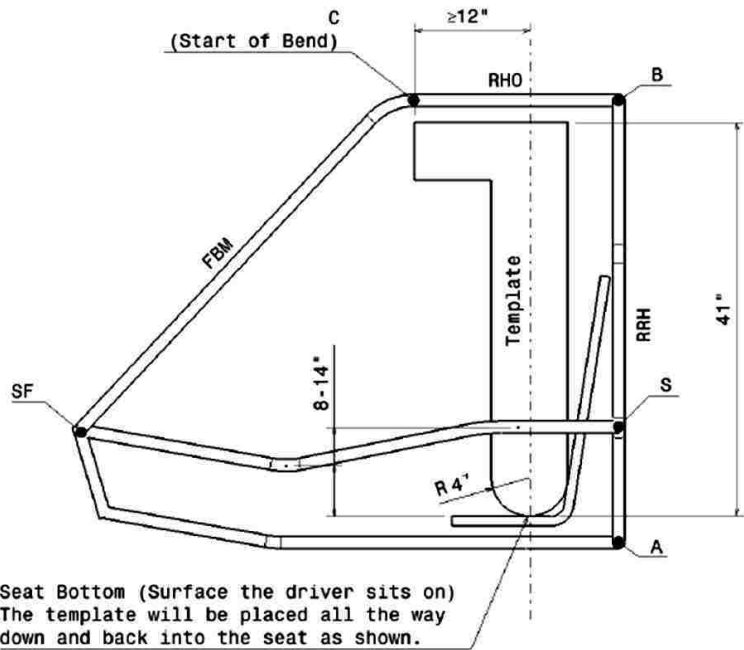


Figure 1.3 Preliminary design of the chassis from SAE rule guide [1]

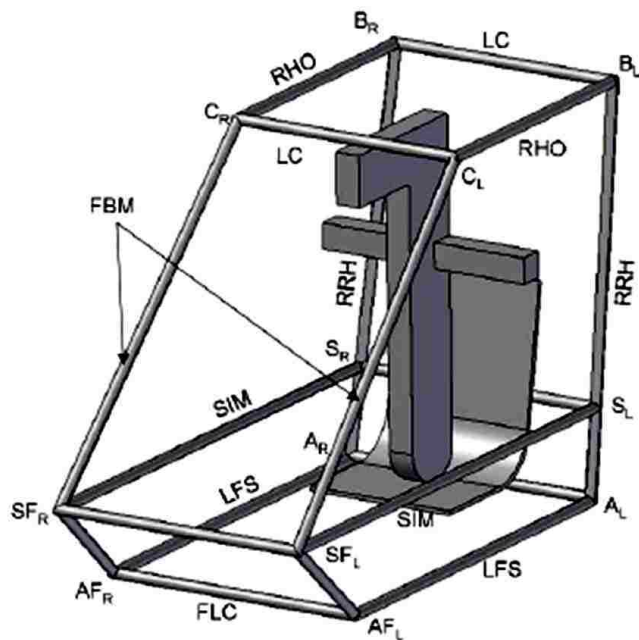


Figure 1.4 Preliminary design of the chassis from SAE rule guide [1]

In vehicle's structural analysis, four common crash scenarios are considered. These are; Front crash, Rear crash, Side crash and Rollover crash. It is understood that, among these crash scenarios, frontal impact crash is at the highest of importance. According to vehicle safety standards [2], for both fatally and seriously injured occupants, frontal impacts are the most important crash type followed by side impacts. Therefore, this thesis focuses mainly on frontal crash analysis.



Figure 1.5 CAD model of the Mini-Baja vehicle

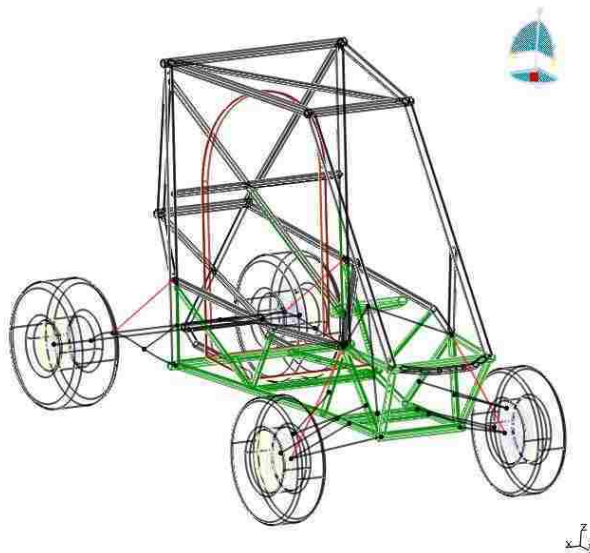


Figure 1.6 CAD model of the Mini-Baja chassis

1.4 The role of non-linearities in the analysis of Mini-Baja

The preponderance of finite element analyses in engineering design today is still linear FEM. In stress analysis, linear FEM is applicable only if the material behaviour is linear elastic, strains are infinitesimal and no contact is present. These assumptions are discussed in more detail later in the thesis. For most operational loads, linear analysis is adequate as it is usually undesirable to have excessive loads that can lead to non-linear material behaviour or large strains [3]. This however is not the case where large deformations exist such as impact engineering or vehicle crash problems.

There are three sources of non-linearities in the analysis of solid continua [4]:

- Material non-linearity, in which material properties are functions of the state of stress or strain. Examples include non-linear elasticity, plasticity and creep.
- Contact non-linearity, in which a gap between adjacent parts may open or close, the contact area between parts changes as the contact force changes, or there is sliding contact with frictional forces.
- Geometrical non-linearity, in which deformation is large enough that equilibrium equations must be written with respect to the deformed structural geometry. Also, loads may change direction as they increase. A typical example is the excessive bending of a fishing rod.

Material non-linearity occurs when the stress-strain behaviour given by the constitutive relation is non-linear (e.g. viscoplasticity), whereas geometric non-linearity is important when changes in geometry have a significant effect on the load-deformation behaviour. Material non-linearity can be considered to encompass contact friction, whereas geometric non-linearity includes deformation-dependent boundary conditions and loading [5].

Non-linear finite element analysis is an essential component of computer-aided design. Testing of prototypes is increasingly being replaced by simulation using non-linear finite elements. This provides a more rapid and economical way of evaluating design concepts and design details. For example, in the field of automotive design,

simulation of crash is replacing full scale tests, both for the evaluation of early design concepts and details of the final design. In many fields of manufacturing, simulation is speeding the design process by allowing simulation of processes such as sheet-metal forming, extrusion of parts and casting. For both users and developers of non-linear finite element programs, an understanding of the fundamental concepts of non-linear finite element analysis is essential. Without an understanding of the fundamentals, a user must treat the finite element program as a black box that is not desirable [6].

Yang and Lianis [7] developed one of the very first finite element displacement formulations and solution procedures for the analysis of large displacement problems of viscoelastic beams and frames. Because of the complexity involved in the non-linear integral-differential equation for viscoelastic beams, solution was only obtained by numerical approximations.

The term “large strain” problem is used repeatedly in this thesis and it is highly recommended that FEA users have some basic understanding of the non-linear finite element theory of solid mechanics to better interpret computer simulation results.

In the context of beam analysis, geometric non-linearity arises when deformations are large enough to alter the distribution or orientation of applied loads, or the orientation of internal resisting forces and moments [4]. In small deflection theory, the slope of the beam is assumed to be small and therefore its contribution is neglected in the curvature equation. The classical Euler-Bernoulli’s beam theory no longer holds when the beam is under large strains.

If the beam’s cross-sectional plane does not remain normal to the beam’s axis and undistorted under deformations, beam theory is not adequate to model the deformation; in general this is the limit of the applicability of the Euler-Bernoulli’s beam theory, (figure 1.7). Problems with geometrical non-linearity cannot be analysed with classical Euler-Bernoulli beam elements, since the shear deformation will govern the distribution of the internal forces and stresses rather than pure bending as assumed in classical beams. In such a case, beam elements (Timoshenko beams) are formulated such that their cross-

sectional area can change as a function of the axial deformation, an effect that is considered only in geometrically non-linear simulations [8].

Figure 1.7 illustrates the transverse shear behaviour of beams: in (a), beam's axis that is initially normal to the beam surface remain straight and normal to the deflected mid-surface throughout the deformation. Hence, transverse shear strains are neglected ($\gamma = 0$). On the other hand in (b): beam axis that is initially normal to the beam mid-surface does not necessarily remain normal to the surface throughout the deformation, thus transverse shear flexibility has a nonzero value, ($\gamma \neq 0$).

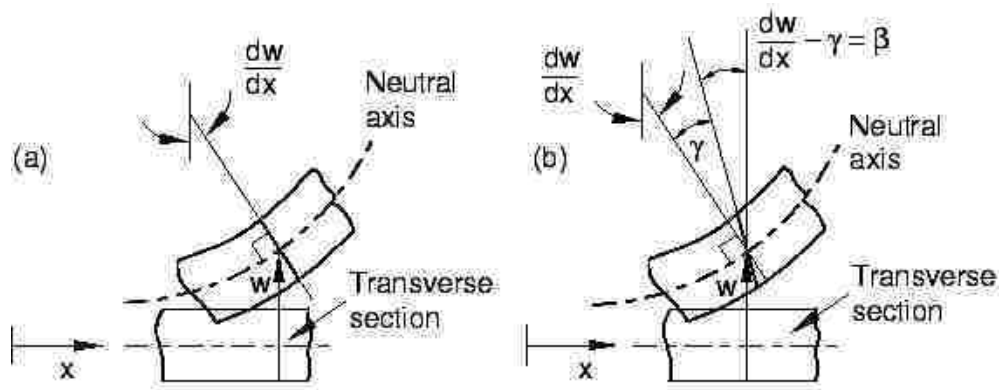


Figure 1.7 Behaviour of transverse beam sections in (a) slender beams and (b) thick beams [8]

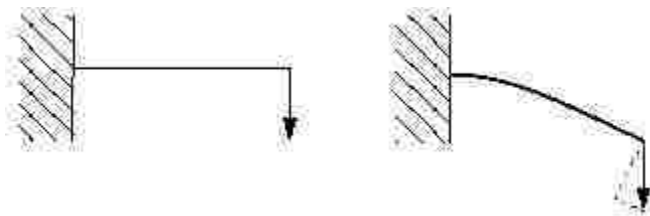


Figure 1.8 Large deflection of a cantilever beam [8]

For example, consider a cantilever beam loaded vertically at the tip, as shown in figure 1.8. If the tip deflection is small, the analysis can be considered as being approximately linear. However, if the tip deflection is large, the shape of the structure

and hence its stiffness changes and the load-deflection curve is non-linear as in figure 1.9. In other words, as the tip load increases, beam's stiffness changes non-linearly [8].

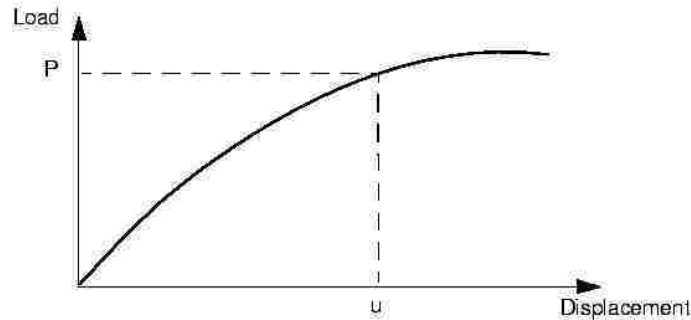


Figure 1.9 Non-linear load-displacement curve [8]

One would expect large strains to have a significant effect on the way that structures carry loads. However, strains do not necessarily have to be large for geometric non-linearity to be important [8], other situations such as large displacement of viscoelastic materials may happen when large strain theory is needed as well. Elongation of a fishing rod is a more tangible example of such a case.

It appears that a very simple yet highly effective way to treat the large deflection problem using finite elements is that developed by Yang [9]. The solution procedure includes the conventional stiffness formulation for small deflection where the effect of axial force is then taken into account by adding an incremental stiffness matrix or initial stress matrix to the original stiffness equation [10]:

$$\{p\} = \left[[\bar{k}] + [n] \right] \{u\} \quad (1-1)$$

where $\{p\}$ is the axial force, $[\bar{k}]$ is the linear stiffness matrix and $[n]$ is the incremental matrix associated with the effect of axial force on bending deflection. Because $[n]$ contains the load P , it is often referred to as the initial stress matrix $[\bar{\sigma}_0]$. This is a non-linear equation (i.e. figure 1.9) and a simple way to solve this equation is to use step-by-step linear incremental procedure. The prediction of this load-displacement path by linearized midpoint tangent incremental procedure together with coordinate transformation at every step can be found in [10] and the modified and modern technique

used in today's software can be found in [8]. Further studies in the vibration of frames and axial-flexural coupling effect in frame vibration can be found in [11] and [12].

Problems that display geometric non-linearity may simultaneously display contact non-linearity and plasticity, as for example in vehicle crash analysis. The linear theory assumes small strains. This approach may lead to inaccurate results or convergence difficulties in cases where these assumptions are not valid. The large displacement solution is needed when the acquired deformation alters the stiffness (ability of the structure to resist loads) significantly [13]. The large strain solution assumes that the stiffness changes during loading, so it applies the load in steps and updates the stiffness for each solution step as shown in eq. (1-1).

1.5 Literature review

As mentioned before, knowledge sharing is not allowed for SAE Mini-Baja participating teams. Therefore, it was difficult to collect detailed and specific information on this topic. Nonetheless, some capstone project reports and theses from other universities were secured from variety of sources and these are reviewed in section 1.5.1.

In addition, section 1.5.2 contains relevant literature published on the topics of dynamic analysis of space frame structures, frontal crash impacts, crashworthiness assessment and validation of automobiles finite element models which are equally applicable to a Mini-Baja vehicle.

The reader is advised that in some instances the writing of the original authors' best expresses the issue and for that reason, the paragraphs were incorporated with major editing for narrowing down the contribution of the literature on our subject of interest, so there might be some repetition or minor jump between each part.

1.5.1 Literature review of “SAE Mini-Baja” capstone reports

Although the Mini-Baja project has been developed by many universities worldwide, the detailed designs are not in the public domain. These projects were to design and manufacture a Mini-Baja vehicle that participated in the global Mini-Baja competition organised by SAE annually meeting their specifications.

To design the chassis of the vehicle, most of the universities develop a preliminary design based on specifications given in the SAE guideline, then the vehicle is tested using PVC pipes for driver space followed by checking the design using different finite element packages such as Solidworks, Ideas, Algor, Abaqus/CAE, Ansys, Catia, Nastran and LS-DYNA. Based on the literature collected on this subject, it is understood that selecting the appropriate impact forces to apply on the frame is one of the major challenges during the finite element analysis of the cage. Therefore, an effort has been made to present a short review on this issue.

In [14], an initial design of the roll cage was done using the Solidworks modeling package, followed by the analysis of the frame with the Algor finite element package. In

this report, it is mentioned that the human body will lose consciousness at loads greater than 9 times the force of gravity, or 9g. Therefore, the value of 10g was selected for the worst case collision of the frame. Based on other assumptions used by the automotive industry, an impact force of 5g and 2.5g were chosen for the side impact and rollover impact respectively.

In the case of frontal collision, an equivalent of 10g (7500 lbf) was applied on a front most point of the frame as shown in figure 1.10 with a red arrow.

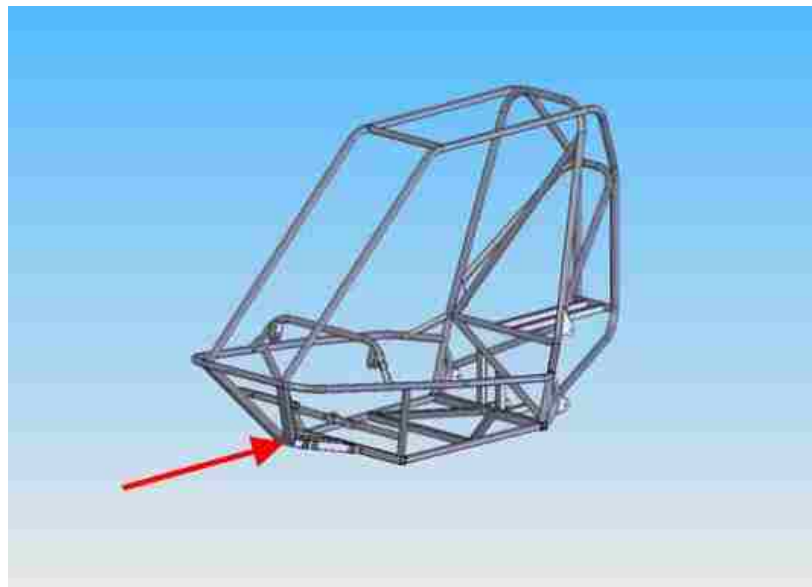


Figure 1.10 Front impact – loading point of application [14]

This procedure was also repeated for the analysis of side and rollover impact scenarios. Analyzing the outcome resulted in the addition of new structural member's braces to the frame as well as changes in dimensions and thicknesses of critical components. One of the major deficiencies in this report was that it does not replicate realistic crash of the vehicle into a rigid wall. Rather, it involves a rough estimation of impact forces applied at different locations on the frame which cannot be reliably used for a vehicle collision. Besides, vehicle crash is a dynamic process in which strain sensitive members are under significant deformation and therefore a linear finite element

analysis based on constraining or clamping a specific location of the cage and applying point loads is not appropriate.

In [15], the work plan was divided into 5 stages; initially, a preliminary design based on SAE specifications was prepared. This was then tested for driver space by building a plastic mock-up model using PVC pipes. It was next followed by modeling the chassis in Pro/E. The design was then checked using finite element analysis in Ansys for further optimization in terms of weight and safety. A rollover analysis was carried out to ensure safer rollover capabilities.

Material properties were assumed to be linear elastic and the model was meshed using just “Beam” elements as shown in figure 1.11. These elements are based on the Euler-Bernoulli beam theory and have 6 degrees of freedom at each node. In the context of vehicle crash, beam elements are considered as acceptable for specific members in a vehicle. A full beam model that was developed for a Mini-Baja is not capable of simulating a real vehicle crash scenario.

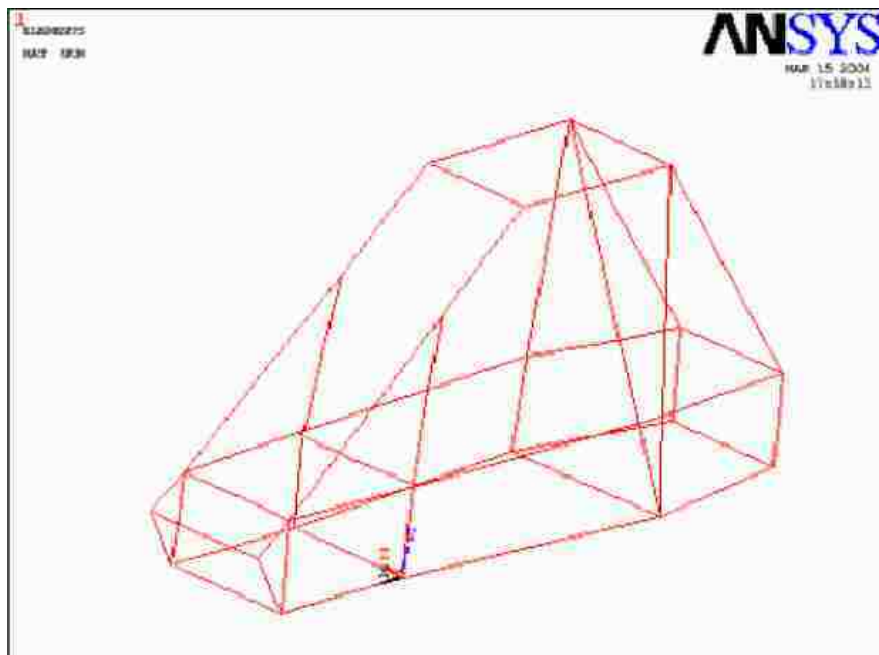


Figure 1.11 Full meshed model in Ansys [15]

In the project reported in [15], force estimations were based on perfectly inelastic collisions which are as follows:

- Estimation of front impact force.

$$DE \text{ (energy transferred)} = \frac{1}{2} M_1 M_2 / (M_1 + M_2) (u_2 - u_1)^2 \quad (1-2)$$

where M_1 and M_2 are the two colliding masses with velocities u_1 and u_2 respectively. The masses M_1 and M_2 were assumed to be equal, ($M_1 = M_2 = M$) and the vehicle M_2 is assumed at rest ($u_2 = 0$). The term in eq. (1-2) was derived from the impulse momentum equation. Using the above assumptions, one gets;

$$DE = \frac{1}{4} M_1 u_1^2 \quad (1-3)$$

$$F = DE/t \quad (1-4)$$

where 't' is the impact time. Therefore

$$F = \frac{1}{4} \times M_1 u_1^2 \times \frac{1}{t} \quad (1-5)$$

The mass of the vehicle was assumed to be 200 kg, whereas the driver's mass was taken to be 75 kg which resulted in $M_1 = 200 + 75 = 275$ kg. Maximum speed of the vehicle was assumed 10 meters per seconds with the impact time of 100 milliseconds. Consequently, the force was derived from eq. (1-5); $F = 6875 \text{ N} \sim 7000\text{N}$.

Although the distortion energy in eq. (1-3) seems correct, there was no explanation for the term in eq. (1-4), which states that the transmitted force to the frame is equal to the energy divided by the impact time. It is understood that the conservation of momentum divided by impulse time could be assumed as the force acting on the matter ($\frac{\Delta P}{dt} = F$), but energy divided by time cannot be assumed as the acting force. This is not even dimensionally correct.

- Estimation of wheel bump forces. An assumption was made that when the vehicle goes over a bump, the entire weight of the vehicle is felt as two point loads transmitted to the chassis, through the suspension.

These two point loads were equated to the weight of the chassis. Hence,

$$2F = M_1 \times g \quad (1-6)$$

$$F = \frac{1}{2} M_1 \times g \quad (1-7)$$

$$F = \frac{1}{2} 275 \times 10 \rightarrow F = 1375 \quad (1-8)$$

$$F = 1.1 \times 1375 = 1500\text{N (approx)}. \quad (1-9)$$

where safety factor was chosen to be 1.1 in eq. (1-8).

- Estimation of loading forces while heaving. For this condition, all the upper points of the frame were fixed while the four bottom points of the frame where the suspension is attached were loaded vertically. It was assumed that the entire weight of the vehicle was transmitted into two points, hence $F = 1500\text{N}$ similar to wheel bump forces was chosen.
- Forces in case of rollover. In case of rollover, IS 11821 (BUREAU OF INDIAN STANDARDS) defines a set of tests and acceptance conditions for agricultural tractors. The same conditions were incorporated for the Mini-Baja finite element analysis to see if the vehicle fails to meet the acceptance conditions.

According to IS 11821, estimation of rollover force was as follows. The strain energy absorbed by the structure is equated to the required input energy in joules (E_s) based on the equation below:

$$E_s = 1.4 \times Mt \quad (1-10)$$

where M_t is the mass of the vehicle, which in this case is estimated to be 200 kg. Therefore

$$E_s = 1.4 \times 200 = 280 \text{ J} \quad (1-11)$$

For a loading at the front and rear of the structure, the force F_t was taken as

$$F_t = 20 \times M_t \quad (1-12)$$

$$\text{Thus, } F_t = 20 \times 200 = 4000 \text{ N} \quad (1-13)$$

Estimation of impact forces were based on the collision of the Mini-Baja with another vehicle rather than a stationary object. While simulating a vehicle crash into a rigid wall is a highly non-linear plastic problem, simulating a vehicle crash to another vehicle is even more complex, because of the unpredictability of deformation behaviour of different components with respect to one another. Certainly, the problem cannot be analyzed with point loads on an elastic frame.

The main focus of reference [15] was to carry out a design check of the Mini-Baja chassis under estimated loading conditions and to minimize the weight of the frame keeping a safety factor of 2. The factor of safety is defined as the ratio of yield strength to maximum von Mises stress.

Obviously, vehicle impacts are highly dynamic cases where members are under large deformations. Therefore, by obtaining a maximum stress outputted from a linear code without plasticity or strain rates considerations, one cannot be confident that the results would be reasonably accurate. In such situations, the safety factor is not a satisfactory parameter for minimizing the weight.

In [16], finite element analysis was conducted on the frame of the Mini-Baja to analyze stresses and deflections present in the frame during a front impact crash as well as rollover crash scenarios. The purpose of this project was to observe where critical stresses were present in the frame and whether yielding takes place. First, a replica of the vehicle frame was modeled in ProEngineer. Then, loading conditions of front impact and rollover were obtained by simulating both instances in Visual Nastran at 30 mph. Areas

of high stress concentrations, such as joints, were captured by using h-adaptivity¹ on the frame.

The front impact was simulated by positioning the frame on a frictionless surface and colliding it against a rigid wall (figure 1.12). The frame was given a constant velocity prior to impact and additional mass was added to compensate for the weight of the driver and the drive train.

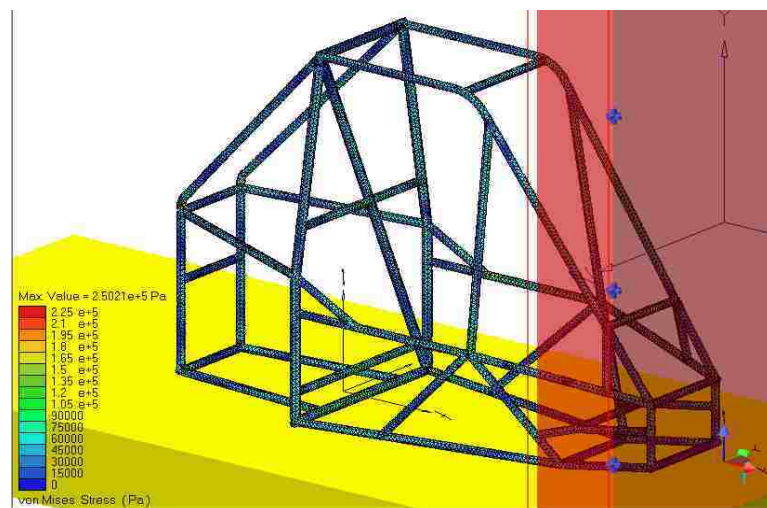


Figure 1.12 Front impact scenario in Visual Nastran [16]

Rollover was simulated by placing the vehicle on a frictionless curved path that would cause the car to rollover due to large centripetal forces and high centre of mass. The initial 30 mph velocity was slowed down slightly upon reaching the curve since this is likely to occur in practice (figure 1.13).

¹ h-adaptive and r-adaptive are two major mesh optimisation techniques used in today's FE commercial packages. In h-adaptive strategy, the connectivity of the elements as well as the total number of degrees of freedom may change while the polynomial degree of the shape functions remains the same. (i.e. one element can be divided into smaller elements in the deformation process)

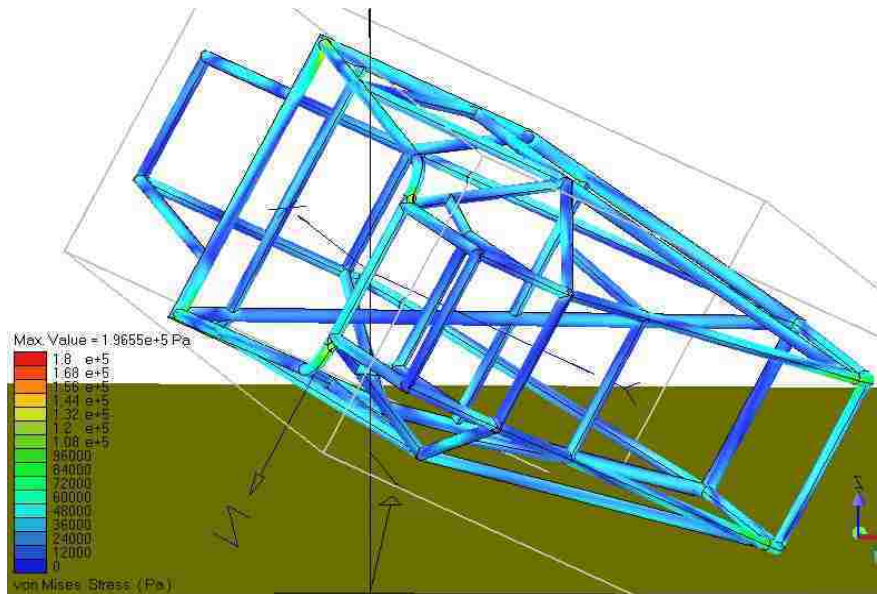


Figure 1.13 Rollover impact scenario in Visual Nastran [16]

From observing the location of the stresses in both the front impact and rollover, it was concluded that the main reason for such a high stress concentration in members was due to bending loads in long members. To avoid such loading, modifications such as moving supports closer to the centre of long members and even adding some supports, were made. Along with this, modifications were made between the base of the car and the front end, so that the front end could absorb more of the energy and not produce the bending loads throughout the cage [16].

In [17], the objective of the project was to perform a linear static analysis as well as a dynamic crash analysis. A frontal multi-body dynamic analysis using FE package LS-DYNA was created to determine acceleration response, energy dissipation and reaction forces of the frame structure.

A CAD model was created using Pro/Engineer Wildfire 4.0 and then the model was meshed with shell elements using Altair HyperMesh. After setting the parameters, the simulation was run using OptiStruct solver for static analysis.

According to the Motor Insurance Repair Research Centre, the maximum g-force that the Baja car will see is 7.9g. Therefore, this value was used as the impact force in the

static analysis that is roughly equivalent to the peak dynamic force observed during an impact. The corresponding force is calculated below:

$$F = M_1 \times 7.9g = 21092 \text{ N} \approx 4700 \text{ lbf} \quad (1-14)$$

Analytical calculation of the force was also done for assessing the values used. For a perfectly inelastic collision, the impact force was estimated using the equations:

$$W_{\text{net}} = \frac{1}{2} mv_{\text{final}}^2 - \frac{1}{2} mv_{\text{initial}}^2 \quad (1-15)$$

$$W_{\text{net}} = F \times d \quad (1-16)$$

Eq. (1-15) states that the change in kinetic energy is equal to the net work done, and the work needed to stop the car is equal to the force times distance. Therefore, for $v_{\text{final}} = 0$;

$$F \times d = -\frac{1}{2} mv_{\text{initial}}^2 \quad (1-17)$$

It is further assumed that the vehicle comes to rest at 0.1 sec after the impact and a vehicle speed of 17.88 m/s (40 mph) was used. Therefore, the distance traveled after the impact was 1.79 m. This leads to a force value of

$$F = \frac{-\frac{1}{2}mv_{\text{initial}}^2}{d} = 24,304 \text{ N} \quad (1-18)$$

Here, three different types of loads (i.e. 26,698 N (10g force), 21,092 N (7.9g force) & 24,304 N (analytical value)) were calculated and $26,698 \times 1.25 = 33,372 \text{ N}$ (7500 lbf) was chosen employing a safety factor of 1.25 with respect to the highest force estimated.

In this reference, a grid sensitivity study was performed to obtain an optimized mesh size. Both displacement and von Mises stress were used as criteria to perform mesh

convergence study for tubes which resulted in 4.24 mm optimum mesh size based on computational time and accuracy of the static results.

Results from static analysis were analyzed and consequently extra members were added to the frame. Optimal dimension and thicknesses of frame members were obtained which resulted in a new design as shown in figure 1.14.

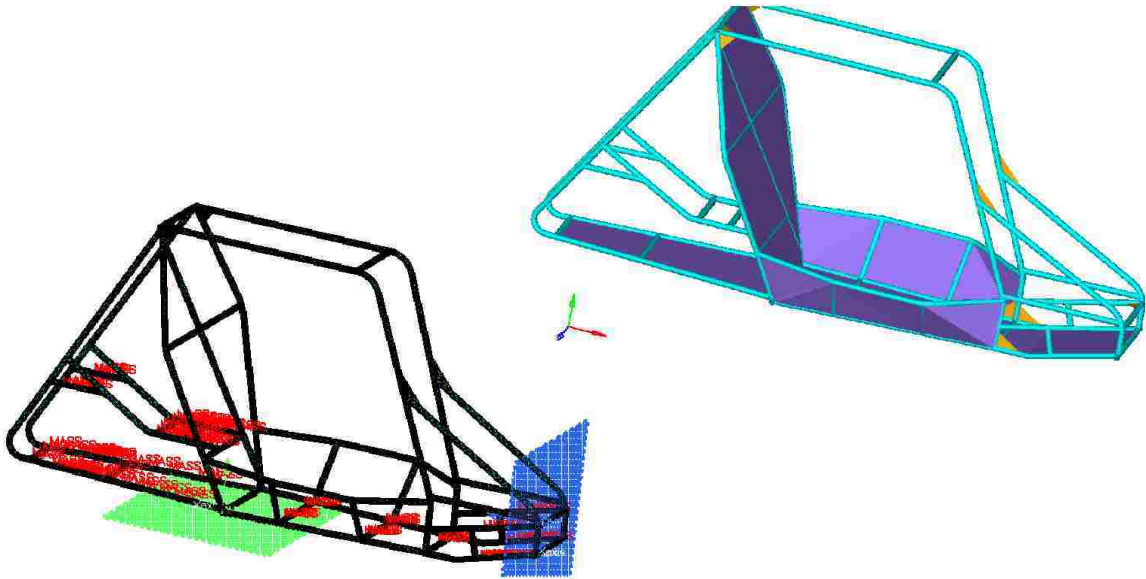


Figure 1.14 Left: finite element mesh with masses and rigid-walls; Right: optimized design of the chassis [17]

The finite element analysis software program employed for solving the dynamic impact problem was LS-DYNA. The weights of all the components were evaluated and equivalent weights were modeled in the form of solid rigid blocks. In order to reduce the computational time of the simulation, the mass of these rigid components were modeled as lumped mass elements assigned to nodal points using ELEMENT_MASS. These element masses are shown in red in figure 1.14. MAT_PLASTIC_KINEMATIC (MAT number 3 in LS-DYNA material library) card was used to model the plastic behaviour of the chassis's tubes.

To ensure proper interaction between components during a crash event, contacts between the components were specified using

CONTACT_TIED_SURFACE_TO_SURFACE. The analysis was carried out for the impact velocity of 15mph toward a rigid wall. RIGID_WALL_PLANAR was used as a simple way of treating contact between the frame's deformable members and the stationary wall. Rigid walls are shown with blue and green surfaces in figure 1.14. Since the project was limited to chassis crash analysis, the gravitational loads and frictional forces between the tire and road surface were neglected.

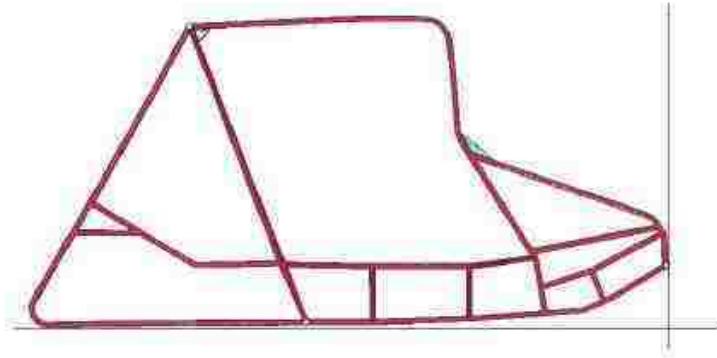


Figure 1.15 Deformation of the chassis at 0.030 sec [17]

Deformation of the roll cage is shown in figure 1.15 at 30 milliseconds toward the impact. The energy plot outputted for the frontal crash simulation is shown in figure 1.16. It is noted that the conservation of energy is well balanced and the hourglass energy is maintained at almost zero level throughout the simulation.

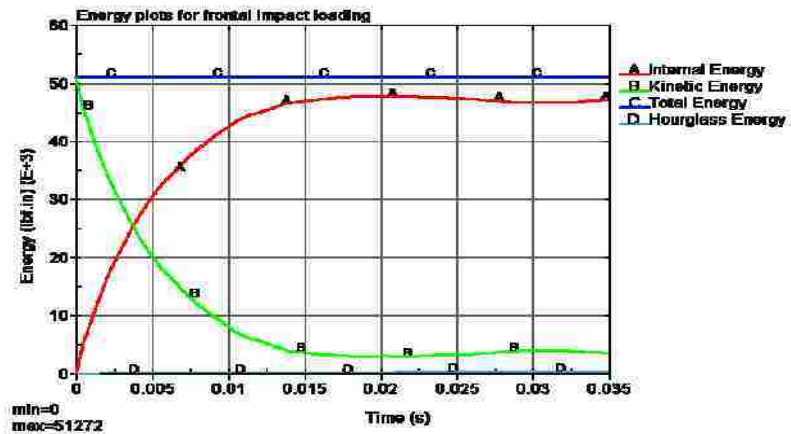


Figure 1.16 Energy plot for frontal impact [17]

1.5.2 Literature review of “Vehicle Crash Impact Analysis” papers

In this section, the literature related to analysis of generic frame structures is reviewed. Besides simple frame structures, some recent NCAC¹ publications regarding crash simulations in terms of modeling and validation are covered.

In reference [18], which is relatively old, it is pointed out that any structural analysis using finite element technique requires high speed computers. A generic automobile chassis frame structure, shown in figure 1.17, has been used as a model structure to be analysed dynamically using the finite element method. Natural resonances of the frame up to 100 Hz have been examined. The structure is taken as being made up entirely of beam elements with 58 and 22 nodes idealizations (figure 1.18). Every effort was made to ensure that the mass of the structure remained unaltered in these idealizations.

As a part of this study, it was concluded that this project would eventually lead to the development of computer programs capable of predicting the natural undamped frequencies and associated mode shapes of structures. Keep in mind that [18] dates back to 1972. To validate the computational results, the vibration characteristics of this structure were investigated using these programs and compared with results obtained from experimental work.

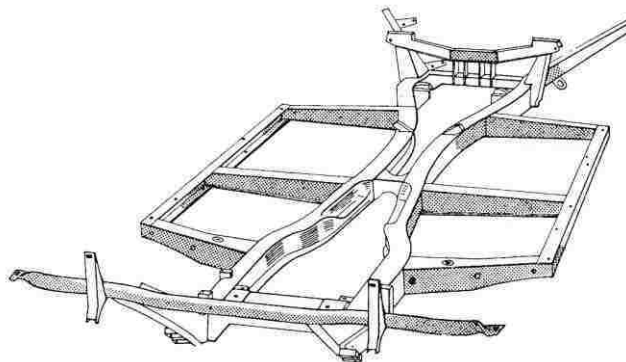


Figure 1.17 The chassis frame [18]

¹ The National Crash Analysis Centre

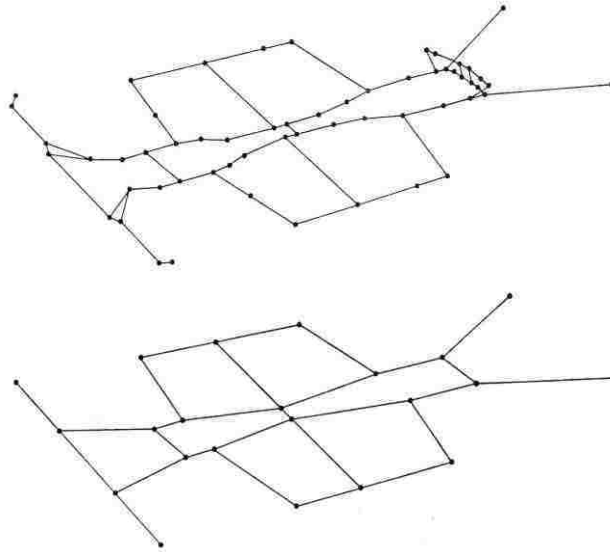


Figure 1.18 Idealization with 58 and 22 nodes [18]

Discussion on how a lumped mass idealization is used in place of a distributed mass idealization and how this choice affects the computer storage area as well as computer running time both at the assembly stage and in the subsequent eigenvalue analysis was presented. It is shown that the complications in programming of the distributed consistent mass approach would not economically justify the improved accuracy. By using the lumped mass idealization, the size of the structure which can be assembled within the core of the computer was almost doubled.

Furthermore, preparation of the structural matrices for the eigenvalue extraction was discussed in detail. In the study it was also assumed that all points on the structure were vibrating with simple harmonic motion and the effect of damping and non-linearity were ignored. Structural stiffness and mass matrices for eigenvalue extraction are related in the dynamic case by;

$$[[K] - \omega^2[M]]\{x\} = 0 \quad (1-16)$$

where the variables are defined below

K: Stiffness matrix

M: Mass matrix

ω : Natural frequency of harmonic motion

x: Degree of freedom

For beam structures of the type analysed in [18], the use of a lumped mass approach, with consequent release of much computer storage space, was fully justified. Two solution techniques of solving the classic eigenvalue problem of the form $[[A] - \omega^2[I]]\{q\} = 0$ were mentioned. The non-iterative program was faster for structures having few nodes, but for larger idealization having highly banded dynamic matrices, the iterative program was a more efficient one.

Although the reviewed paper [18] dates back to 1972, it is very important to note that from the very beginning of the development of finite element programming and analysis, researchers working in this field were always looking for different ways to reduce the computer run time and increasing the accuracy of the results.

References [19] and [20] deal with more recent experiences and difficulties that may arise during the development of an automobile finite element model. Due to the lack of blueprints and design data of the vehicles which were selected for crashworthiness simulations and tests [19], the process of reverse engineering had to be adopted to acquire geometric data needed for development of FE models.

Creating a fleet of FE “vehicles” is not a simple task of collecting existing models. While CAD programs and FE programs are standard tools for today’s manufacturers, they do not all use the same software nor do they reveal their proprietary models, even to government agencies. Therefore, the only option is to reverse engineer complete finite element models (FEMs) from actual vehicles and shop manual drawings. A new vehicle is disassembled until all relevant components have been measured. The measurements include mass, centre-of-gravity, and geometry. Coupon samples are also taken for destructive strength testing to obtain accurate material properties. Having been converted

into numerical data, the components of the car are then reassembled into a complete FE vehicle. The complete reverse engineering process consists of four steps [20]:

- Data collection
- Finite element model construction
- Model validation
- Model implementation

The digitization phase of data collection is the process by which a numerical representation of the vehicle's undeformed geometry is obtained for finite element analysis. The primary tool used for digitization in [20] was a segmented articulating measuring instrument. This device interfaces with the computer and is capable of accurately recording the position of a probe at the end of the arm. In [19], FaroArm digitizing equipment and accompanying software AnthroCAM were the major tools used to obtain the geometric data of the bus components. It allows for digitizing of points, scanning curves and construction of polylines for each structural component, (Figure 1.19). The flow chart of the project is shown in figure 1.20.

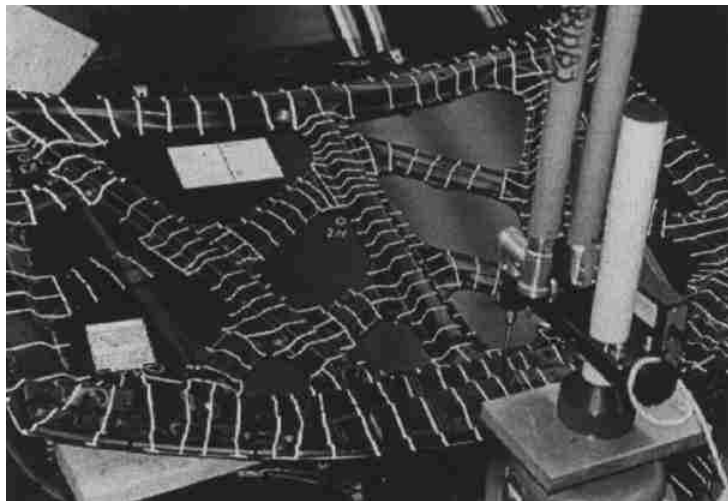


Figure 1.19 Digitization arm being used on underside of hood [20]

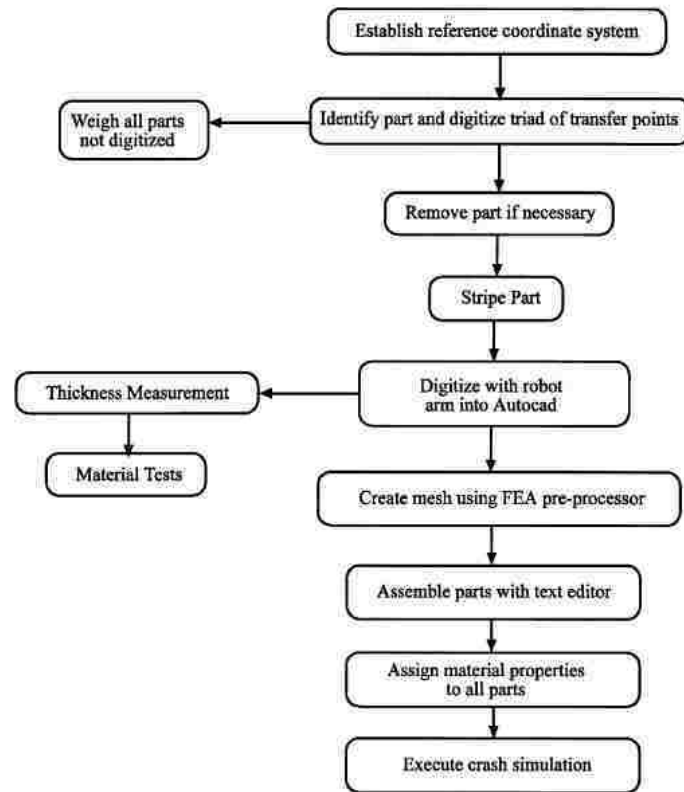


Figure 1.20 Flow chart of the project with digitization [20]

The first step toward the digitization process, followed by the determination of mass, centre of gravity, material properties as well as model validation for each component individual test and full vehicle tests and implementation of the model is available in detail in [20].

High cost of actual crash test experiments on one hand and difficulties with collecting accurate results from actual crash tests on the other hand lead to an increasing interest in finite element methods and computer simulations rather than actual tests [19]. It was justified in [20] that computer simulation also has its own drawbacks; in order to get reliable results from crash simulations; one should first find an efficient way to collect correct geometrical data of the actual model which is both complex and time consuming.

In [21], a finite element computer simulation of a New Car Assessment Program (NCAP)¹ and full scale crash test using LS-DYNA3D is described. The full scale test selected for this study is a 30mph frontal impact of a 1993 Ford Taurus vehicle into a rigid wall.



Figure 1.21 Consumer information label for a vehicle with at least one NCAP star rating [22]

The finite element models of the vehicle, a hybrid dummy and a driver side airbag were used to simulate this test, figure 1.23. The model validation focused on the comparison of the test and simulations in terms of crush depth in the front of the vehicle shown in figure 1.22, the acceleration at different locations of the vehicle as well as the head and chest accelerations and the femur loads of the dummy [21]. Validation of the individual models can be found in their corresponding references of this paper.

¹ In 1979, NHTSA (National Highway Traffic Safety Administration) created the New Car Assessment Program (NCAP), to encourage manufacturers to build safer vehicles and consumers to buy them. Since that time, the agency has improved the program by adding rating programs, facilitating access to test results, and revising the format of the information to make it easier for consumers to understand. The agency established a frontal impact test protocol based on Federal Motor Vehicle Safety Standard 208 (“Occupant Crash Protection”). According to FMVSS No. 208 the frontal impact for NCAP test is conducted at 56 km/h (35 mph) [22].

More recently, in an effort to improve the dissemination of NCAP ratings and as a result of the Safe, Efficient Transportation Act, the agency has issued a Final Rule requiring manufacturers to place NCAP star ratings on the automobile price sticker, Figure 1.21, [22].

	Full Scale Test Crush Depth (mm)	Simulation Crush Depth (mm)
C1	274	288
C2	320	340
C3	312	381
C4	305	389
C5	310	339
C6	280	308

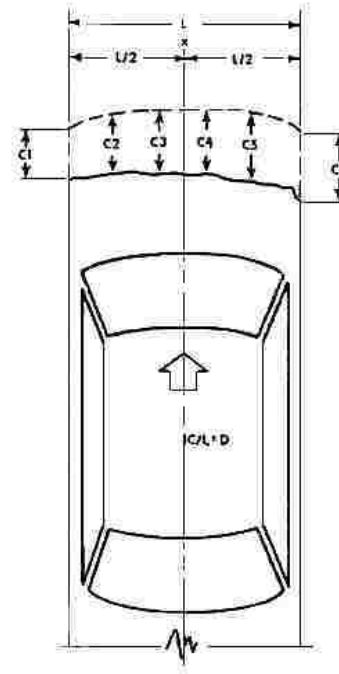


Figure 1.22 Crush depth location and comparison [21]

The model description like material models, element types, contact difficulties and summary of modifications in order to incorporate the dummy and the airbag models, application of injury assessment, experimental validation of the dummy, airbag model description and computer simulation are discussed in brief in report [21]. Different techniques and methods of comparison between crash tests and computer simulations as well as difficulties in recording accurate injury assessments like HIC (Head Injury Criterion) and CSI (Chest Injury Index) have been discussed. As the computer technology and code development become more advanced, the use of combined vehicle, dummy and airbag models that includes detailed mesh, sophisticated material models, contact algorithms, and parts connectivity for the prediction and assessment of occupant injury and the vehicle crash performance is within the reach of engineering community [21].

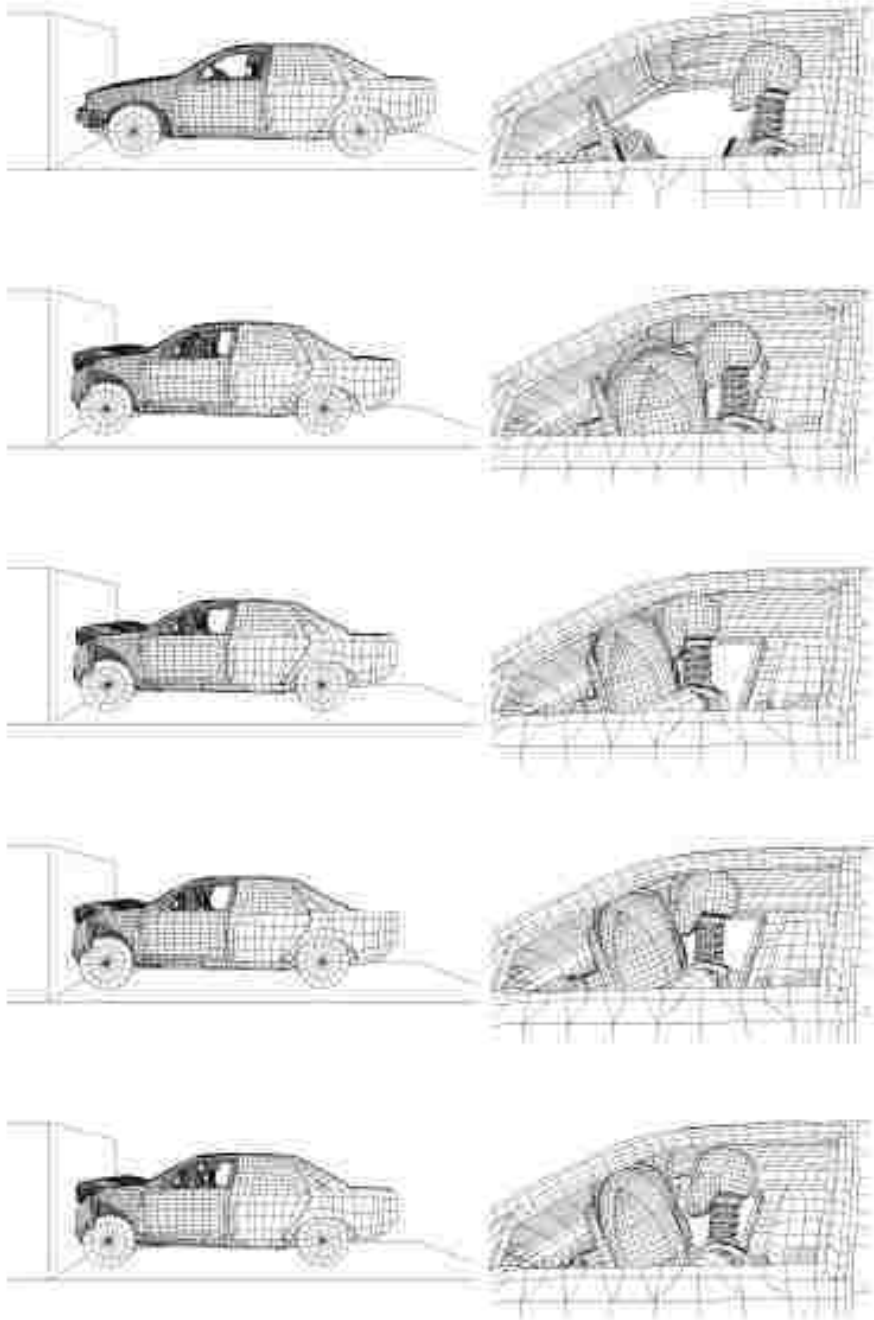


Figure 1.23 Crash output results at different stages of the simulation [21]

In [23], the development of a model for the 2006 Ford F250 pickup truck (figure 1.24) was discussed. Material data and properties for major structural components were

obtained through tensile coupon testing ¹ from samples taken from vehicle parts. Appropriate strain rate values were determined and included in the model for analysis of stress and strain behaviour in the crash simulation. It is worth mentioning that for accurate results one cannot simply include the stress-strain curves of the used material for the simulation. The material curves after manufacturing processes are different from that of the virgin materials.

Different validation graphs, such as acceleration of rear and front seats, acceleration of engine top and bottom locations, energy balances, total wall force as well as the vehicle stiffness were studied closely to come up with appropriate validation metrics which have already been suggested by the Society of Crash Engineering in order be adopted for the Mini-Baja vehicle. Comparison of the overall deformation of the vehicle in frontal crash with the conservation of energy toward the impact is shown in figure 1.25.



Figure 1.24 FE model of the 2006 Ford F250 [23]

¹ Stress-strain curves are derived from tests on samples of the material to be characterized (often called *coupons*) where a regular sinusoidal stress is applied by a testing machine which also counts the number of cycles to failure. This process is known as *coupon testing or tensile testing* [24].

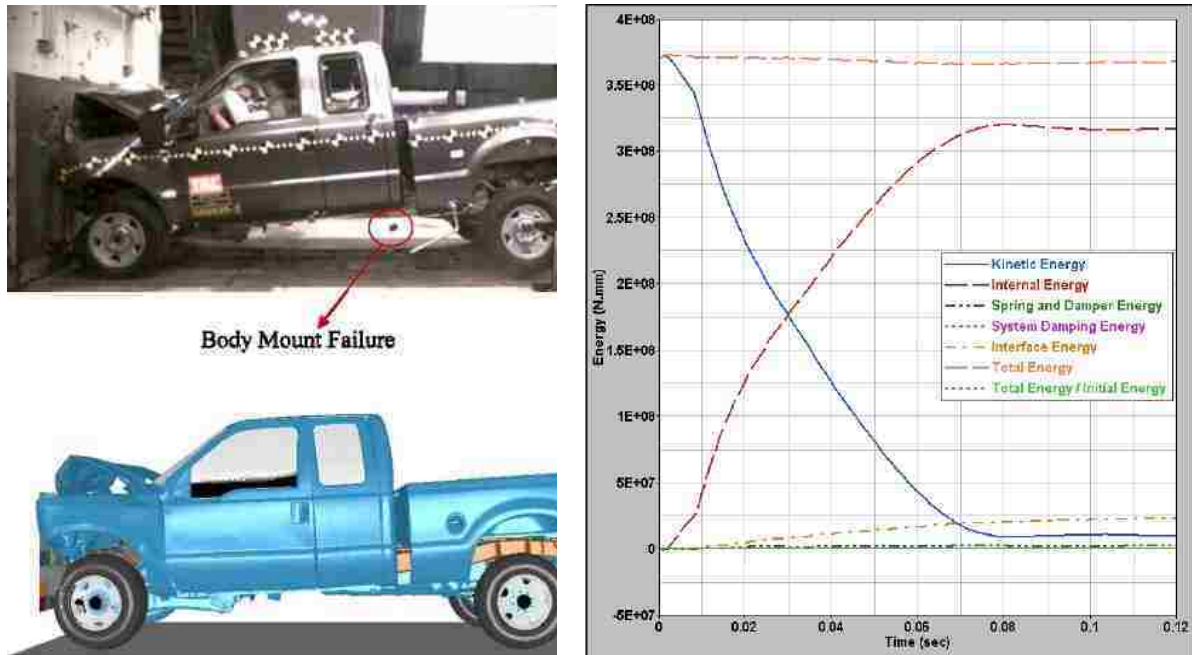


Figure 1.25 Left: comparison of the global deformation for NCAP test and simulation; Right: simulation data for energy balance [23]

In [25], the focus was mainly on a single unit truck impacting a roadside obstacle. It was noted that the response of any vehicle impacting a PCB (Portable Concrete Barrier) is primarily governed by the mass and suspension characteristics of the vehicle. When impacting roadside safety obstacles, the vehicle often experiences stability problems. The suspension response is particularly important for truck impacts. The severity of the crash as well as the characteristics of the truck with higher centre of gravity makes it less stable and more susceptible to rollover than other vehicles. Therefore, the suspension and the steering system was the major focus in [25].

An important aspect of a bullet-vehicle¹ is the ability to simulate its overall kinematics. For instance in case of a truck, existence of accurate models for mass distribution and response of wheels and suspension components are very important for capturing accurate kinematic responses. In the case of low impact angle of a single unit truck (SUT) into a portable concrete barrier (PCB), the spinning of wheels and

¹ Once a finite element vehicle model is validated successfully to represent full scale crash tests, the bullet-model can be applied to new crash scenarios with varied crash parameters, such as impact angle, vehicle speed, and even the new design of the roadside barrier.

suspension models should capture the truck riding up the barrier. If such capability is missing, the simulation results will not provide reliable information about the barrier's effect on the trucks kinematics. Using fixed tires in head-on crash is acceptable, but in the case of barrier impacts, especially when the tire is the first object that comes in contact with the obstacle, detailed wheel, suspension and steering models are needed. For a vehicle impacting a roadside hardware, the angular displacements (i.e. yaw, pitch and roll) of the impacting vehicle is greatly affected by its suspension and steering characteristics [25]. Hence, these metrics were compared and validated with actual test results as well as the overall rigid body motion of the truck which is shown in figure 1.26. In the case of a Mini-Baja vehicle, it can be seen that the response of the vehicle could be governed by the suspension as it is the first object that comes into contact with the wall.

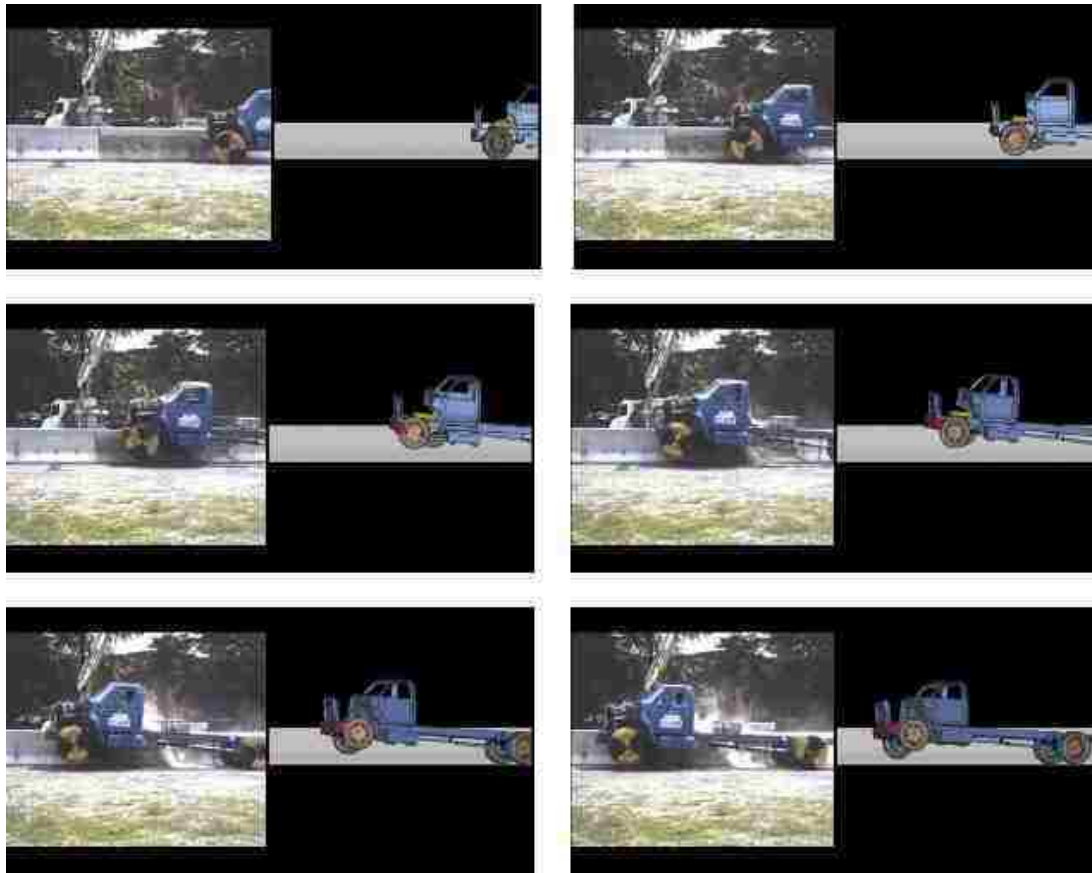


Figure 1.26 Simulation and impact test comparison [25]

In [26], a detailed discussion of the suspension of a pickup truck (figure 1.27) and its finite element model was described. Over the past years after the initial release of the model (Chevrolet C2500 pickup¹ truck), modifications and additional details have been incorporated into the finite element model to add capabilities, better represent dynamic response, and allow the use of the model in different scenarios.

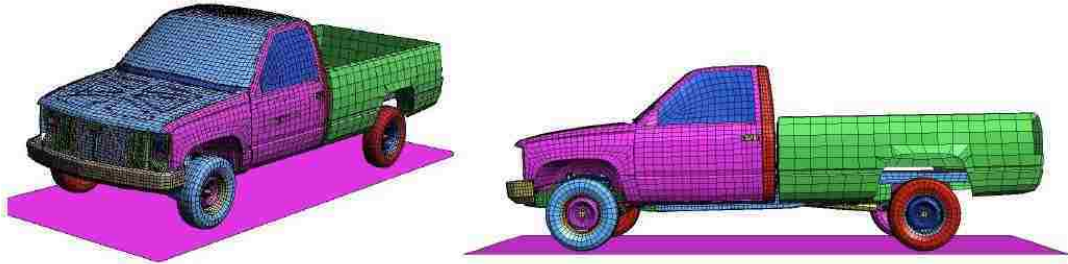


Figure 1.27 Finite element model of the C2500 pickup truck [26]

In this report, the modification made on the rear suspension finite element model were validated with actual pendulum tests² conducted at the Federal Highway Administration Federal Outdoor Impact Laboratory (FOIL) for the dynamic response of the model.

The characteristics of the pickup truck, including the higher centre of gravity, higher bumper and greater mass, tend to make it less stable and more susceptible to rollover, which can result in more severe crashes than for other vehicles. Therefore, the suspension and steering systems, which have great influence on roadside crashes, were the focus of several modifications to the finite element models [26].

¹ The importance of the pickup truck for roadside safety research was elevated by National Cooperative Highway Research Program (NCHRP) Report 350, published in 1993. The report contains the recommended procedures for testing and evaluating roadside safety features. The C2500 was chosen by the need to have a large test vehicle more representative of the fleet of vehicles operating on US highways, [26].

² Simulations for pendulum test 02025 (*figure 1.28*) and 02027 (*figure 1.29*) which are the two techniques in evaluating suspension systems, are discussed in reference [26].

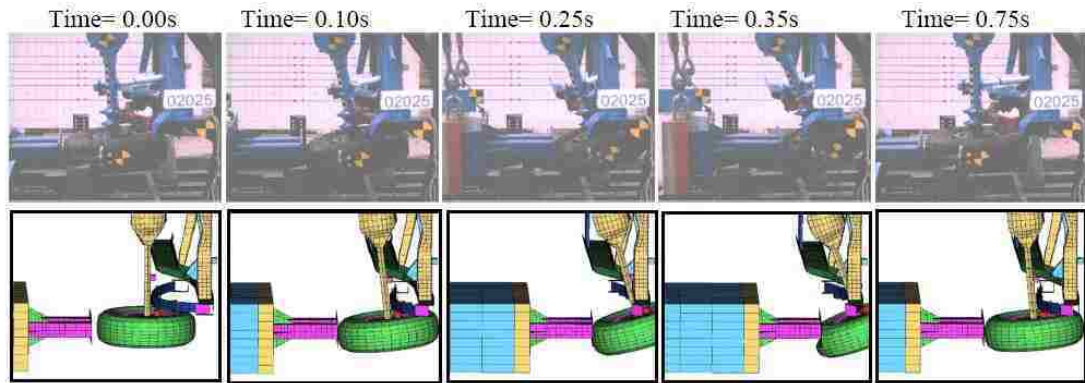


Figure 1.28 Comparison of pendulum test 02025 and simulation [26]

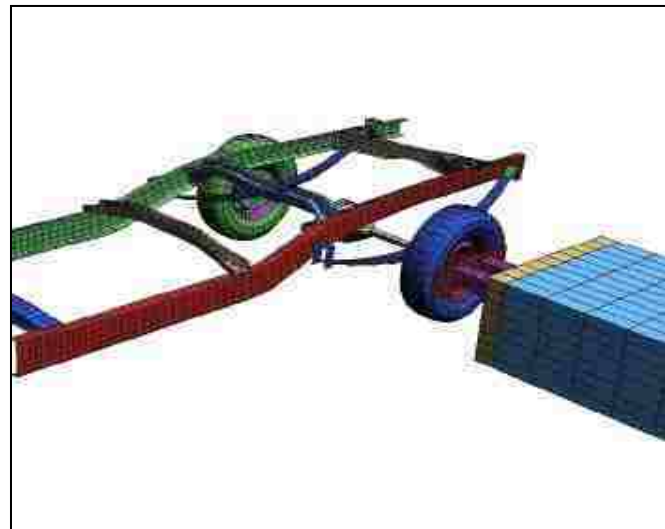


Figure 1.29 Comparison of pendulum test 02027 and simulation [26]

To validate these changes, pendulum tests that were performed on the pickup suspension were compared to simulation results. A summary of the validation results were based on the displacement of the rear axle, accelerations measured at different positions during test and the visual comparisons of the test film and initial simulation sequential. (Refer to [26] for more detailed graphs)

It is shown that modification on the suspension will change the overall reaction of the model to different impact scenarios. In this report, different modifications were made on the geometry, mesh, connections, constraints, joints and material to better capture the rigid body motion of the suspension in pendulum tests. It was concluded that in computer simulations, often is not very easy to model the actual geometry or physics within different components, so using different keyword commands in order to adequately resemble the actual model and realistic behaviour toward a crash scenario is very critical to overcome modeling difficulties.

Many different keyword commands (LS-DYNA) were implemented in these models for accuracy of the results; “Nodal rigid body constraint”, “Constrained extra nodes added to rigid body”, “Revolute joints”, “spherical joints”, “Spot-welds”, “Spring and dampers”, “Rigid-bodies” are some of many commands that have been studied closely for understanding the application and acceptable assumptions and hypothesis within vehicle modeling . These reports were very helpful in the process of the finite element modeling of the Mini-Baja vehicle which is discussed in detail in the following chapters.

CHAPTER II

FINITE ELEMENT THEORY WITH NUMERICAL EXAMPLE

2.1 Objectives and overview of Chapter II

In this chapter, a brief history of the finite element method and its practical application, often known as finite element analysis, is presented. An introduction of the fundamental concepts of the finite element method is discussed by focusing on classical beam theory and desired beam elements. Furthermore, a numerical example of a Z-frame structure is introduced which is solved by numerical implementation in Matlab and computer simulation in Catia. Results are compared in terms of accuracy and the example is modified for further discussion and analysis. This comparison validates the use of different elements employed in the full Mini-Baja model later in the thesis.

2.2 A brief history of finite element method

The rapid development of computing power has completely changed and revolutionized research and study in every branch of science and engineering. The dream that every engineering office would have a microcomputer has become a reality. According to Yang [9], personal computers in the 1980s were as popular as pocket calculators were in the 1970s and slide rules in the 1960s. Microcomputers have rapidly evolved to have exceptional memory, speed and correspondingly number crunching capabilities. Following this trend, analysis and design methods that provide computerized solutions to scientific and engineering problems have rapidly been used in increasingly routine fashion [9]. In this thesis the focus is on one such significantly developed method, the *Finite Element Analysis (FEA)*.

Finite Element Analysis (FEA) was first introduced in 1943 by R. Courant, who utilized the Ritz method of numerical analysis and minimization of variational calculus to obtain approximate solutions to vibration systems [27].

According to Fish and Belytschko [3], in the 1950s the finite element method was first developed in the aerospace industry. The major players were Boeing and Bell Aerospace in the United States and Rolls Royce in the United Kingdom at the time. Turner *et al.*, published one of the first papers that laid out the major ideas of the method in 1956; the paper discussed the "stiffness and deflection of complex structures". It established the procedures of element matrix assembly and element formulations, but did not use the term 'finite elements'. The second author of this paper, Clough, was a professor at Berkeley, and was at Boeing at the time. Subsequently, he wrote a paper that first used the term 'finite elements' and has been given much credit as one of the founders of the method. He worked on finite elements only for a few more years, and then turned to experimental methods, but his work ignited a tremendous effort at Berkeley, led by the younger professors, primarily Wilson and Taylor and graduate students such as Hughes, Felippa and Bathe, and Berkeley became the centre of finite element research for many years. This research coincided with the rapid growth of computer power, and the method quickly became widely used in the nuclear power, defence, aerospace and automotive industries [3].

Engineers and scientists worldwide use the FEA to predict the behaviour of structural, mechanical, thermal, electrical and chemical systems for both design and analyses. Its popularity can be shown by the fact that over \$1 billion is spent annually in the United States on FEA software and computer time [3]. A 1991 bibliography (Noor, 1991) lists nearly 400 finite element books in English and other languages. A web search (in 2006) for the phrase 'finite element' using the Google search engine yielded over 14 million pages of results. Mackerle (<http://ohio.ikp.liu.se/fe>) lists 578 finite element books published between 1967 and 2005 [3].

2.3 Finite element analysis fundamentals

The origin of finite element analysis can be traced back to the matrix analysis of structures where the concept of displacement or stiffness approach was introduced [28]. From a mathematical point of view, the finite element method is a form of the well-known Galerkin and Rayleigh-Ritz methods for finding approximate solution of differential equations.

In engineering analysis, physical problems can be converted into differential equations (e.g. equilibrium of forces acting on a loaded bar). Not only an equilibrium of forces on a bar, but also many other physical principles, such as mass balance and energy conservation lead to differential equations. In simple cases it is possible to integrate differential equations to obtain the exact solutions for problems. Over many years, different methods have been developed for solving various classes of differential equations. However, in many cases finding analytical solutions to complex problems become a very difficult and often impossible task. Writing differential equations for complex geometries with arbitrary 2-D and 3-D regions or satisfying complex boundary conditions makes it even more important for an alternative solver method.

Finite element method is one of the numerical methods for obtaining approximate solutions of ordinary or partial differential equations. Other numerical methods such as finite difference and boundary element methods may be competitive or even superior to the finite element method in some engineering problems [29], nevertheless the power of the FEM when dealing with complex geometry or complex boundary conditions has made it the preferred method of choice over the last few decades for solution of many practical problems.

There are two major methods used for finding of approximate assumed solution problems modeled as differential equations. In both methods the differential equation is first converted to an equivalent integral form and then solved for the assumed solution of linear or higher order form. In the Rayleigh-Ritz method the integral form is based on energy consideration, while the Galerkin method uses a residual weighted approach.

2.4 Finite element form of the assumed solution

Since the assumed solution should be defined over the entire solution domain, often a large number of terms should be included to accurately represent the solution [29]. In finite element method this problem is resolved by discretizing the solution domain into smaller subdomains called elements. Elements may have physical properties such as thickness, density, Young's modulus, shear modulus and Poisson's ratio. The assumed solution can easily be written for elements. Since they have simpler geometry,

usually a low-degree polynomial can be used. Locations where the assumed solution is defined are called nodal points, and unknown coefficients of the assumed solution are called nodal degrees of freedom which may include translations, rotations, and for special applications, higher order derivatives of displacements.

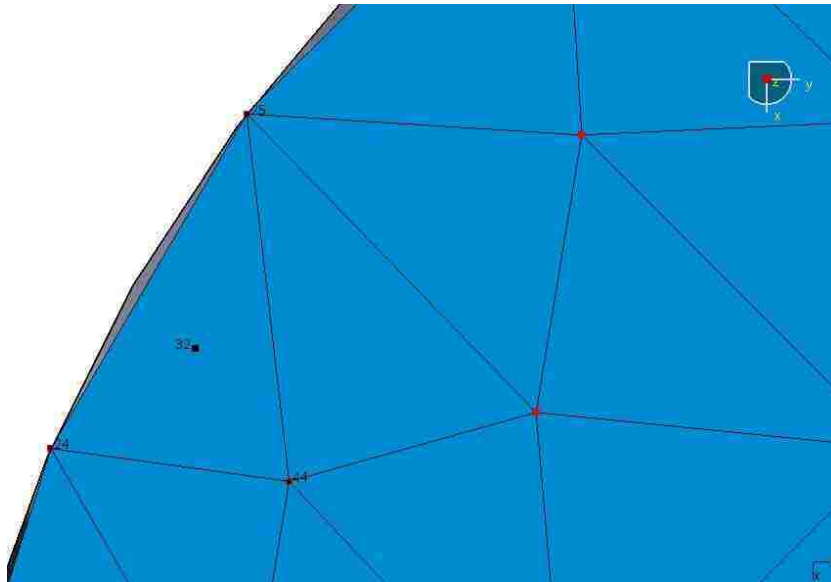


Figure 2.1 Element generation

In figure 2.1, a circular plate is discretized with triangular elements. Nodal points are shown with red dots and elements are in blue divided from each other with solid lines.

When the nodes displace, they will drag the elements along in a certain manner dictated by the element equation. In other words, displacements of any points in the element will be interpolated from the nodal displacements, and this is one of the reasons for the approximate nature of the solution. Using interpolation functions such as Lagrange or Hermite formulations, the solution can be written for each element based on nodal degrees of freedom. Finally, contributions of all elements are assembled together in a matrix format to solve for the entire solution domain.

For instance, consider a uniform straight beam shown in figure 2.2. The beam element is assumed to have two degrees of freedom at each nodal point. As shown in figure 2.2 these degrees of freedom are: a transverse deflection v and an angle of

rotation θ (or $\partial v / \partial x$). Corresponding to these two degrees of freedom, v and θ , a transverse shear force (F) and a bending moment (M) respectively act at each nodal point.

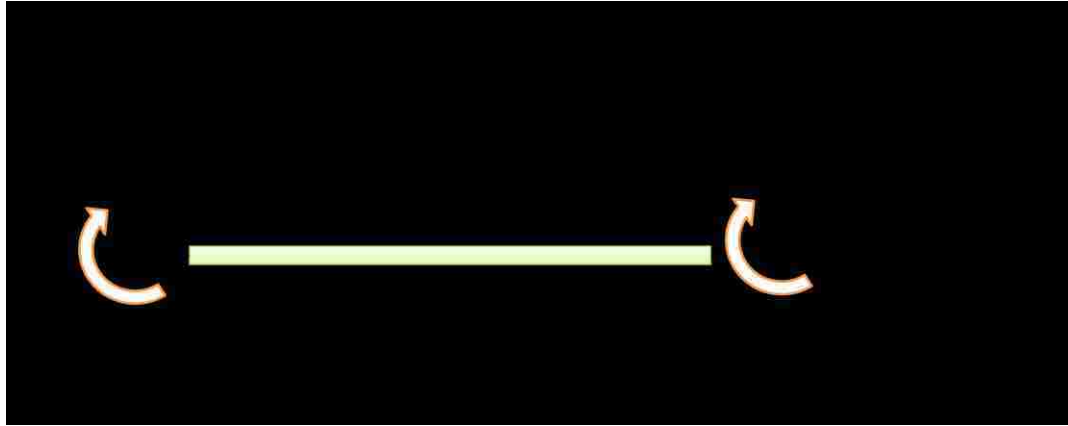


Figure 2.2 Beam element with uniform cross-section

In order to write an assumed solution over this beam element, four unknowns are involved, in other words, four degrees of freedom are needed to model the element.

$$v(x) = a_1 + a_2x + a_3x^2 + a_4x^3 \quad (2-1)$$

or,

$$v(x) = f_1(x)v_1 + f_2(x)\theta_1 + f_3(x)v_2 + f_4(x)\theta_2 \quad (2-2)$$

Here $v(x)$ is the transverse displacement function and describes the deflection behaviour of the beam element. $f_1(x)$, $f_2(x)$, $f_3(x)$, and $f_4(x)$ describe the distribution or shape of the displacement associated with the degrees of freedom over the element.

Note that the beam element considered above is just one simple example of many other types of elements that can be solved and discussed (i.e. truss, frame, rectangular, 2D triangular elements or 3D hexahedral elements). The same procedure can be adopted for other variety of elements with different degrees of freedom associated with the finite element equations.

2.5 Finite element library

One of the very first steps toward finite element analysis is to analyze the geometry of the problem, so as to come up with the best choice of element type suited to the geometry (beam, shell or solid). In figure 2.3, a complete library of elements available in most of today's FEA packages are shown.

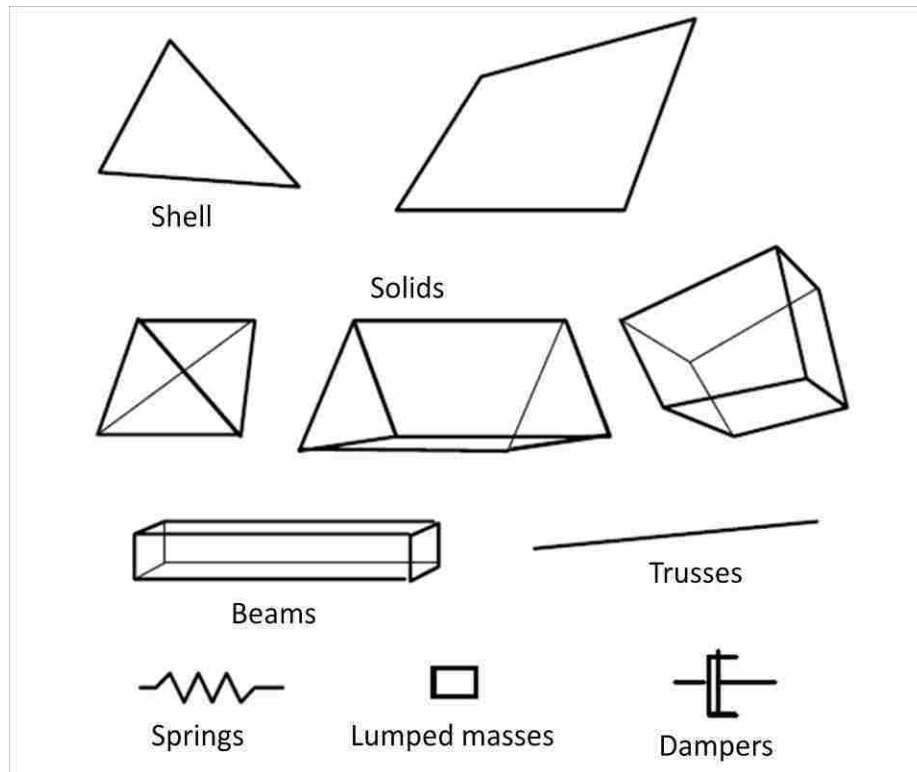


Figure 2.3 Element library of LS-DYNA [30]

The simplest category of elements is straight or curved one-dimensional elements also known as Beam elements with physical properties such as axial, bending, and tensional stiffness. This type of element is suitable for modeling cables, braces, trusses, beams, stiffeners, grids and frames. Straight elements usually have two nodes, one at each end, and an extra node to include the orientation of the cross-section. According to [8], for beam theory to produce acceptable results, the cross-section dimensions should be less than 1/10 of the structure's typical axial dimension. The axial dimension can be the distance between supports, the distance between gross changes in cross-section, or the wavelength of the highest vibration mode of interest. Furthermore, if the cross-section

dimensions was less than 1/15 of the typical axial dimension of the structure, it can be assumed that shear deformations are negligible and consequently “slender beams” can be used (refer to Euler-Bernoulli’s slender beam; section 1.4).

A two-dimensional element (Shell) is the combination of a membrane element (only axial, membrane forces) and a plate element (only bending stiffness). There are a variety of shell elements such as flat or curved triangles, rectangles and quadrilaterals. Nodes are usually placed at the element corners and, if needed for higher accuracy, additional nodes can be placed along the element edges or even inside the element. The elements are positioned at the mid-surface of the actual layer thickness. According to [8], a structure such as a pressure vessel, whose thickness is less than 1/10 of a typical global structural dimension, generally can be modeled with shell elements. Furthermore, if this ratio was less than 1/15, shear deformations are negligible and “thin shells” are used. The following are examples of typical global dimensions:

- The distance between supports
- The distance between stiffeners or large changes in section thickness
- The radius of curvature
- The wavelength of the highest vibration mode of interest.

Three-dimensional solid elements are used for modeling 3D shaped objects such as machine components. Common element shapes include Tetrahedral or regular and irregular Hexahedral. Nodes are placed at the vertices, interior, and possibly in the element faces. In principle, every object is 3-dimensional, and should be modeled with solid elements, but the required resources make it impractical even with today’s computing power [31]. In later chapters more discussion on element type and formulation on the Mini-Baja FE model is provided.

2.6 Z-frame example

In order to sum up the mathematical background of finite element theory mentioned above, a numerical example is chosen and modified as a case study. Mini-Baja vehicle consists of long slender members welded together at their joints making a

structure technically known as a space frame. For this reason a Z-frame example is taken as a benchmark from Bhatti's book [29], to investigate displacements and rotations at each node, and to compare the relative performance of different element types.

In figure 2.4 a 2D rigid-frame structure is shown (referred to as a Z-frame). Displacements and rotations for each nodal point are to be obtained by using the following numerical data:

A clockwise moment of $M = 20 \text{ kN.m}$ is applied over the right end of the frame. The middle member of the structure is loaded vertically by $P = 10 \text{ kN}$. Lengths of all the members are $L = 1 \text{ m}$, the area of cross-section is $A = 0.04 \text{ m}^2$, the second moment of inertia is $I = 0.0004 \text{ m}^4$, and the frame is made entirely of steel components with the elastic modulus $E = 210 \text{ GPa}$.

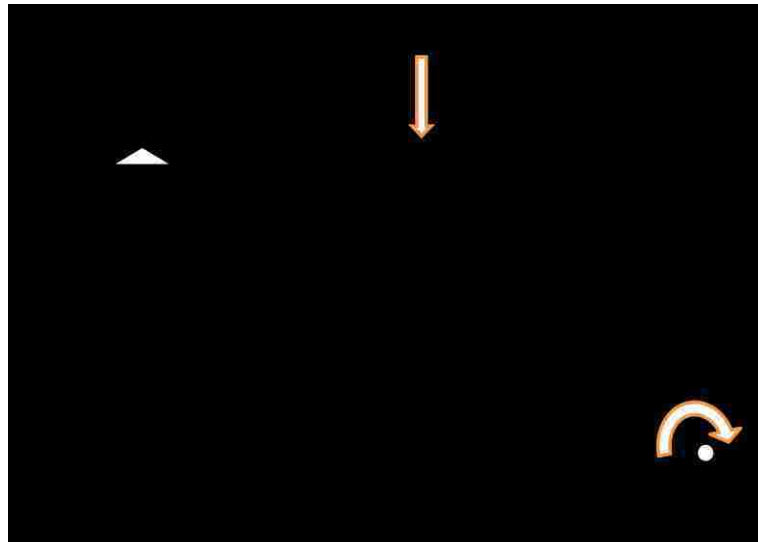


Figure 2.4 Z-frame setup

As a point of information, a rigid plane frame is a series of beam-type elements rigidly connected to each other. The term rigid implies that the original angles made between members at their joints remain unchanged after the deformation [32]. It is also assumed that the axial and flexural bending effects are uncoupled and transverse shear deformation is neglected according to small deflection theory.

Members in a rigid-jointed plane frame are designed to resist axial force, shear force and bending moments. The two node beam element has two degrees of freedom at each node, which are the transverse displacement and rotation as mentioned in section 2.4. In the case of an element having an arbitrary orientation with the horizon (figure 2.5), the theory is slightly more complicated.

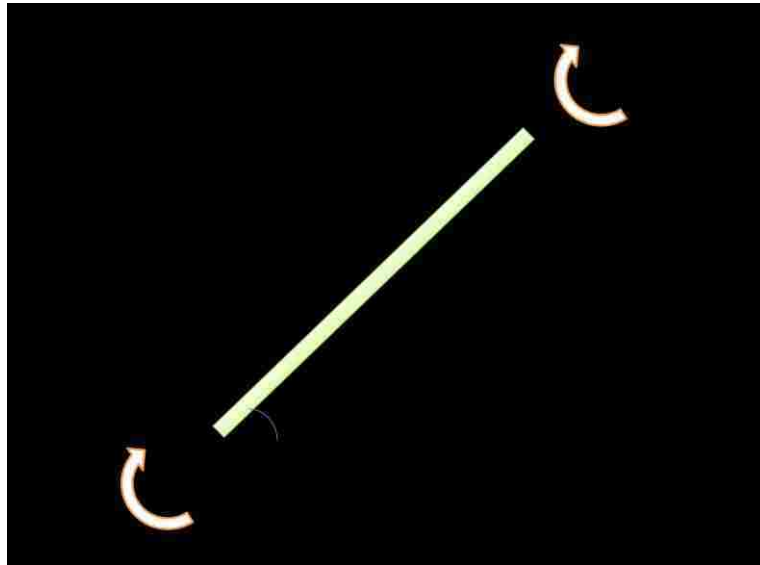


Figure 2.5 An arbitrary oriented frame element

Since axial and flexural behaviour of structural finite elements are unaffected by one another for small deformations, to assemble frame elements, the stiffness matrices of an axial deformation bar element is combined with a flexural stiffness matrix of a beam element, to form an element that can be used to analyze rigid-jointed planar frameworks. This matrix should undergo a coordinate transformation procedure to account for the arbitrary orientation α . In such a case $[K] = [T]^T[\bar{K}][T]$, where bar refers to the local coordinate, $[T]$ is the transformation matrix and $[K]$ is the axial-flexural stiffness matrix in global coordinates system.

In many applications, the coupling between the axial and bending forces can be very significant. Clearly the treatment presented in this chapter does not take into account such

scenarios. For further discussion on how this issue is resolved refer to [9] and [11], where the coupling effect is discussed in detail for variety of frame structures. Nevertheless the coupling effect does not have a significant effect on our specific Z-frame example. The magnitude of axial loading is not large enough for the coupling effect to exist.

The simplest possible model for the Z-frame is to use three beam elements connected to each other at their joints as shown in figure 2.6 below. Each node has three degrees of freedom; two displacement components of u and v in the x and y direction, and an angle of rotation θ .

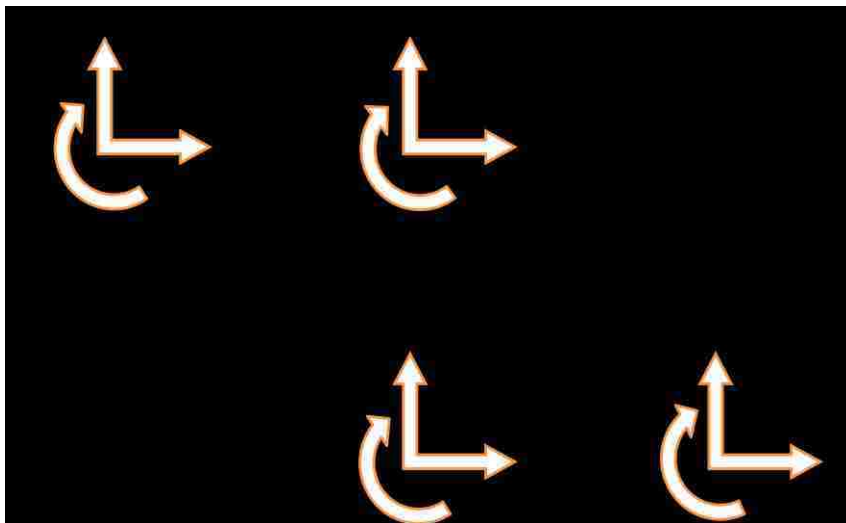


Figure 2.6 Three-element model for the Z-frame

2.6.1 Computer implementation (Matlab) for the Z-frame

The analysis of the planar frame shown in figure 2.4 can be performed by writing two Matlab functions, one for defining the element stiffness matrix and possible applied forces and moments, (Plane_Z_Frame.m) and the other, for computing nodal solutions, (Z_Frame_NodalDOF.m). When the two preliminary functions are inputted as (m files) into Matlab, a code defining the parameters of the Z-frame can be provided to solve for nodal unknowns. The two functions described here were implemented with the help of notes available in reference [29].

Plane_Z_Frame.m:

```
Function [ke, rq] = Plane_Z_Frame(modulus, inertia, A, qs, qt, coord)
```

This function generates equations for a plane frame element as a function of following numerical data:

modulus = modulus of elasticity

inertia = moment of inertia

A = area of cross-section

qs = distributed load along the element axis

qt = distributed load normal to the element axis

coord = coordinates at the element ends

It is known that the element stiffness can be related to nodal unknowns by

$$K_e d = r_q + R_{(\text{point loads and moments})} \quad (2-3)$$

In reference to eq. (2-3), K_e is the stiffness matrix of a frame element, d is the nodal unknowns or degrees of freedom associated with the element, and r_q is the matrix defining possible distributed loads in the axial or transverse direction. $R_{(\text{point loads and moments})}$ defines the point loads and moments applied on a specific node of the structure.

```

EI=modulus*inertia; EA = modulus*A;
x1=coord(1,1); y1=coord(1,2);
x2=coord(2,1); y2=coord(2,2);
L=sqrt((x2-x1)^2+(y2-y1)^2);
ls=(x2-x1)/L; ms=(y2-y1)/L;

```

ls and ms are cosine and sine of the angle between the element and the horizontal axis respectively (e.g. the angle α in figure 2.5). x1 and y1 defines the coordinates of the nodes and correspondingly the length of the element is obtained with the term L.

In order to write the stiffness equation for an element, first a differential governing equation is written with respect to equilibrium of forces acting on a differential element. Then this differential equation can be solved with either Galerkin or Rayleigh-Ritz finite element methods using an assumed solution and boundary conditions. Both methods result in stiffness matrices (k_e) and load vector (r_q) as follows:

```

ke = [(EA*L^2*ls^2 + 12*EI*ms^2)/L^3, ((-12*EI + EA*L^2)*ls*ms)/L^3,
      ...
      (-6*EI*ms)/L^2, -(EA*L^2*ls^2 + 12*EI*ms^2)/L^3, ...
      ((12*EI - EA*L^2)*ls*ms)/L^3, (-6*EI*ms)/L^2;
      ((-12*EI + EA*L^2)*ls*ms)/L^3, (12*EI*ls^2 + EA*L^2*ms^2)/L^3, ...
      (6*EI*ls)/L^2, ((12*EI - EA*L^2)*ls*ms)/L^3, ...
      -((12*EI*ls^2 + EA*L^2*ms^2)/L^3), (6*EI*ls)/L^2;
      (-6*EI*ms)/L^2, (6*EI*ls)/L^2, (4*EI)/L, ...
      (6*EI*ms)/L^2, (-6*EI*ls)/L^2, (2*EI)/L;
      -(EA*L^2*ls^2 + 12*EI*ms^2)/L^3, ((12*EI -EA*L^2)*ls*ms)/L^3, ...
      (6*EI*ms)/L^2, (EA*L^2*ls^2 + 12*EI*ms^2)/L^3, ...
      ((-12*EI + EA*L^2)*ls*ms)/L^3, (6*EI*ms)/L^2;
      ((12*EI - EA*L^2)*ls*ms)/L^3, -((12*EI*ls^2 + EA*L^2*ms^2)/L^3), ...
      (-6*EI*ls)/L^2, ((-12*EI + EA*L^2)*ls*ms)/L^3, ...
      (12*EI*ls^2 + EA*L^2*ms^2)/L^3, (-6*EI*ls)/L^2;
      (-6*EI*ms)/L^2, (6*EI*ls)/L^2, (2*EI)/L, (6*EI*ms)/L^2, ...
      (-6*EI*ls)/L^2, (4*EI)/L];

rq = [(L*(ls*qs - ms*qt))/2; (L*(ms*qs + ls*qt))/2; (L^2*qt)/12;
      (L*(ls*qs - ms*qt))/2; (L*(ms*qs + ls*qt))/2; -(L^2*qt)/12];

```

At this point, the stiffness equation and force matrix for one element can be obtained.

Z_Frame_NodalDOF.m:

```
Function [d, rf] = Z_Frame_NodalDOF (K, R, debc, ebcVals)
```

This function computes nodal solution and reactions with the following numerical data:

K = global stiffness matrix

R = global right hand side vector

debc = list of degrees of freedom with specified values

ebcVals = specified values

```
dof = length(R);  
df = setdiff(1:dof, debc);  
Kf = K(df, df);  
Rf = R(df) - K(df, debc)*ebcVals;  
dfVals = Kf\Rf;  
d = zeros(dof,1);  
d(debc) = ebcVals;  
d(df) = dfVals;  
rf = K(debc,:) * d - R(debc);
```

Using these functions, a code was written for the solution of the Z-frame example;

```
nodes = [0, 0; 1, 0; 1, -1; 2, -1];  
conn=[1,2; 2,3; 3,4];  
lmm=[1,2,3,4,5,6; 4,5,6,7,8,9; 7,8,9,10,11,12];  
R = zeros(12,1); R(5)=-10; R(12)=-20;  
K=zeros(12);
```

The term; `nodes`, defines the nodal coordinates of the frame. The term `conn`, defines the arrangement of each element between nodes. The term `lmm` and `lm=lmm(i, :)` dictate where the contribution of the element matrix is placed in the final global stiffness matrix. The integer 12 is the number of DOF in the Z-frame, and therefore, the stiffness matrix is written in the format of a 12 by 12 matrix.


```

for i=1
lm=lmm(i,:);
con=conn(i,:);
[ke,rq] = Plane_Z_Frame(210000000, 0.0004, 0.04, 0, 0, nodes ([1
2],:));
K(lm, lm) = K(lm, lm) + ke;
R(lm) = R(lm) + rq;
End

for i=2
lm=lmm(i,:);
con=conn(i,:);
[ke,rq] = Plane_Z_Frame(210000000, 0.0004, 0.04, 0, 0, nodes ([1
3],:));
K(lm, lm) = K(lm, lm) + ke;
R(lm) = R(lm) + rq;
End

for i=3
lm=lmm(i,:);
con=conn(i,:);
[ke,rq] = Plane_Z_Frame(210000000, 0.0004, 0.04, 0, 0, nodes ([1
4],:));
K(lm, lm) = K(lm, lm) + ke;
R(lm) = R(lm) + rq;
end;

K
R

debc=[1,2,11]; ebcVals=zeros(length(debc),1);
d = Z_Frame_NodalDOF(K, R, debc, ebcVals)

```

Each loop above will solve the stiffness matrix of each element. The contribution of the elements in terms of loading and stiffness are assembled in the global matrices with the use of $K(lm, lm) = K(lm, lm) + ke$ and $R(lm) = R(lm) + rq$. Once all the elements are solved for stiffness K and reaction R , the results can be obtained as shown in the matrix eq. (2-4). Note that matrix eq. (2-4) was derived intentionally with less decimal values for display purposes.

$$\left(10^6 \right) \begin{pmatrix} 8.4 & 0 & 0 & -8.4 & 0 & 0 & 0 & 0 & 0 & 0 & 0 & 0 \\ 0 & 1.008 & 0.504 & 0 & -1.008 & 0.504 & 0 & 0 & 0 & 0 & 0 & 0 \\ 0 & 0.504 & 0.336 & 0 & -0.504 & 0.168 & 0 & 0 & 0 & 0 & 0 & 0 \\ -8.4 & 0 & 0 & 9.408 & 0 & 0.504 & -1.008 & 0 & 0.504 & 0 & 0 & 0 \\ 0 & -1.008 & -0.504 & 0 & 9.408 & -0.504 & 0 & -8.4 & 0 & 0 & 0 & 0 \\ 0 & 0.504 & 0.168 & 0.504 & -0.504 & 0.672 & -0.504 & 0 & 0.168 & 0 & 0 & 0 \\ 0 & 0 & 0 & -1.008 & 0 & -0.504 & 9.408 & 0 & -0.504 & -8.4 & 0 & 0 \\ 0 & 0 & 0 & 0 & -8.4 & 0 & 0 & 9.408 & 0.504 & 0 & -1.008 & 0.504 \\ 0 & 0 & 0 & 0.504 & 0 & 0.168 & -0.504 & 0.504 & 0.672 & 0 & -0.504 & 0.168 \\ 0 & 0 & 0 & 0 & 0 & 0 & -8.4 & 0 & 0 & 8.4 & 0 & 0 \\ 0 & 0 & 0 & 0 & 0 & 0 & 0 & -1.008 & -0.504 & 0 & 1.008 & -0.504 \\ 0 & 0 & 0 & 0 & 0 & 0 & 0 & 0.504 & 0.168 & 0 & -0.504 & 0.336 \end{pmatrix} \begin{pmatrix} u1 = 0 \\ v1 = 0 \\ \theta1 \\ u2 \\ v2 \\ \theta2 \\ u3 \\ v3 \\ \theta3 \\ u4 \\ v4 = 0 \\ \theta4 \end{pmatrix} = \begin{pmatrix} 0 \\ 0 \\ 0 \\ 0 \\ -10 \\ 0 \\ 0 \\ 0 \\ 0 \\ 0 \\ 0 \\ -20 \end{pmatrix} \quad (2-4)$$

As shown in eq. (2-4), the degrees of freedom associated with the two ends of the Z-frame are restrained by the boundary conditions dictating $u1$ and $v1$ to be zero, as well as $v4$ at the roller support. A force $P = -10$ kN is applied at node number 2 which corresponds to the vertical degree of freedom $v2$. A moment $M = -20$ kN.m applying rotation on node number 4 corresponds to $\theta4$. Once the equation above is solved, nodal solutions are obtained as

$$\mathbf{d} = \begin{pmatrix} u1 = 0 \\ v1 = 0 \\ \theta1 = 7.84722222222224 \text{ e-05} \\ u2 = -1.69669139076119\text{e-21} \\ v2 = 6.85515873015875 \text{ e-05} \\ \theta2 = 4.87103174603175 \text{ e-05} \\ u3 = 1.89484126984126 \text{ e-05} \\ v3 = 7.03373015873018 \text{ e-05} \\ \theta3 = -1.08134920634922\text{e-05} \\ u4 = 1.89484126984126 \text{ e-05} \\ v4 = 0 \\ \theta4 = -0.000159623015873016 \end{pmatrix} \quad (2-5)$$

Note that displacements u and v are in meters and rotation θ is in radians.

2.6.2 Computer simulation (Catia) for the Z-frame

In this section, the determination of the nodal solutions which were obtained analytically in the previous section, are described and compared with the one obtained from Catia simulations. The major focus here is to validate the FE model created in Catia for further analysis and discussion.

The geometry of the frame was created in Catia as shown in figure 2.7, which was meshed with 3 beam elements each 1 meter with other numerical data given in the Matlab implementation. As shown in figure 2.7, the left end of the frame is free to rotate around the X-axis, meaning θ_1 is not zero while u_1 and v_1 are fixed. Nodes 2 and 3 are free to move and rotate and are not restrained. The right end is a roller support, denoting that only the vertical displacement v_4 is restrained. A 10 kN force is applied vertically at node 2 and a 20 kN.m counter-clockwise moment is applied at node 4.

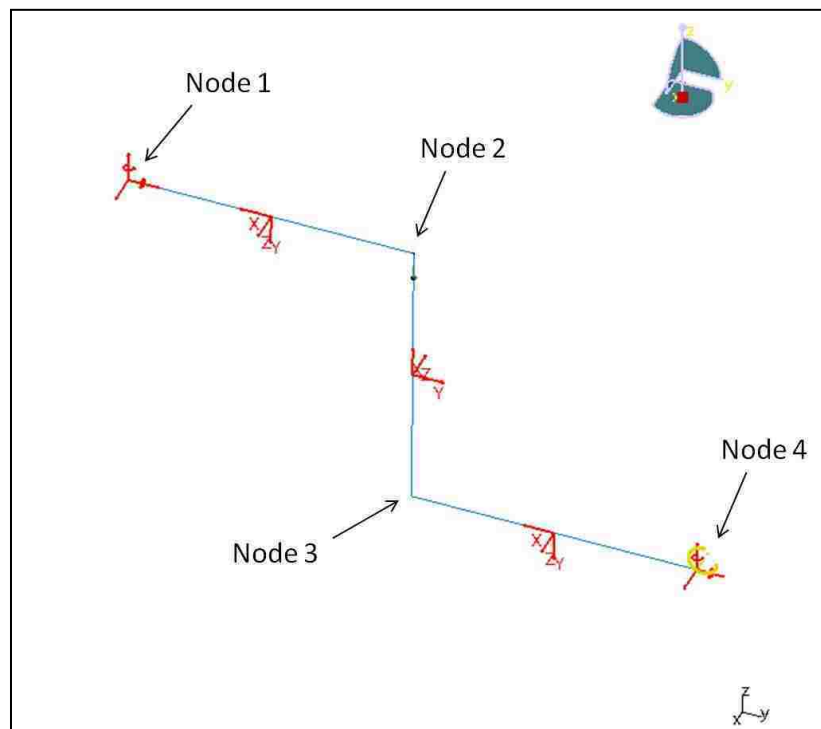


Figure 2.7 FE model of the Z-frame

The frame can be assembled with just one part and there is no need to define different parts corresponding to these 3 members. Furthermore, there is no need to define connections at the joints as it has identical sectional property.

Generative structural analysis toolbar in Catia was used for the analysis of the frame. The computed nodal displacements are shown in figure 2.8.

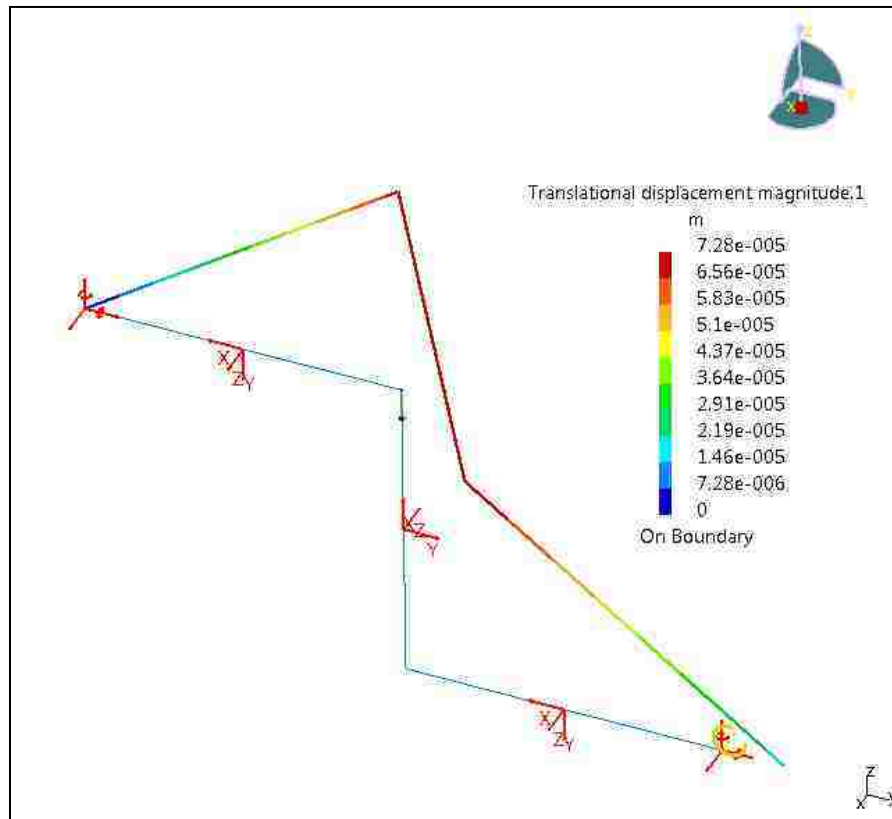


Figure 2.8 Nodal displacement of the Z-frame

By creating local displacement and rotation sensors for each nodal point, nodal solutions were obtained for the Z-frame. Table 2.1 reports nodal displacements in the frame. C2 and C3 are horizontal and vertical deflections corresponding to u and v respectively.

Table 2.1 Nodal displacement of the Z-frame

	x(m)	y(m)	z(m)	C2(m)=u	C3(m)=v
Node1	0	0	0	0	0
Node2	0	1	0	7.14049e-019	6.85516e-005
Node3	0	1	-1	1.89484e-005	7.03373e-005
Node4	0	2	-1	1.89484e-005	0

As you can see in figure 2.8, maximum displacements of the frame occur at node 3 which was confirmed by table 2.1. Table 2.2 corresponds to nodal rotations. Results reported in tables 2.1 and 2.2 are identical to those derived from Matlab in eq. 2-5.

Table 2.2 Nodal rotations of the Z-frame

	x(m)	y(m)	z(m)	C1(rad)=rotation about x axis	C2&C3(rad)
Node1	0	0	0	7.84722e-005	0
Node2	0	1	0	4.87103e-005	0
Node3	0	1	-1	-1.08135e-005	0
Node4	0	2	-1	-0.0001596230	0

2.6.3 Z-frame modified

In this section, the numerical values of the Z-frame structure are changed in a fashion that can be solved with different element types. It is intended to present a preliminary case study on the Z-frame and compare different element types in this particular structure. This section presents the modified version of the previous Z-frame modeled with beam, shell and solid elements.

In the earlier Z-frame model, the cross-sectional area and second moment of area were given as $A = 0.04 \text{ m}^2$ and $I = 0.0004 \text{ m}^4$, respectively.

Therefore, assuming a tubular section, the following two equations are valid;

$$A = \pi(R_{\text{out}}^2 - R_{\text{in}}^2) = 0.04 \text{ m}^2 \quad (2-6)$$

$$I = \frac{\pi}{4}(R_{\text{out}}^4 - R_{\text{in}}^4) = 0.0004 \text{ m}^4 \quad (2-7)$$

Solving for R_{out} and R_{in} gives $R_{\text{out}} = 0.1623 \text{ m}$ and $R_{\text{in}} = 0.1167 \text{ m}$. These values were rounded to $R_{\text{out}} = 0.15 \text{ m}$ and $R_{\text{in}} = 0.10 \text{ m}$.

All other numerical values are same as before; a clockwise moment of $M = 20 \text{ kN.m}$ with a vertical force of $P = 10 \text{ kN}$ is applied on nodes 1 and 4 respectively. Lengths of all the members are 1 meters each and the frame is made of steel with the elastic modulus of $E = 210 \text{ GPa}$ and poisson ratio $\nu = 0.3$.

A static analysis as well as a frequency analysis was employed on the modified Z-frame to compare the deformation shape of the structure as well as modes and their corresponding natural frequencies modeled with different element types. Figure 2.9 below shows a representation of the FE mesh for beam, shell and solid elements.

In the case of a solid mesh, it is known that the number of elements through the thickness plays a critical role in the accuracy of stress distribution. As the number of elements through the thickness direction is increased, a more accurate response can be produced. This, however, can be expensive since the smallest dimension of a solid element will control its run time or in case of dynamic events, its time step.

For the shell and solid FE mesh, a simple linear 0.03 m triangular and tetrahedron elements were used respectively. In case of beam elements, a 0.027 m mesh size was used to obtain the same element distribution between the 3 models.

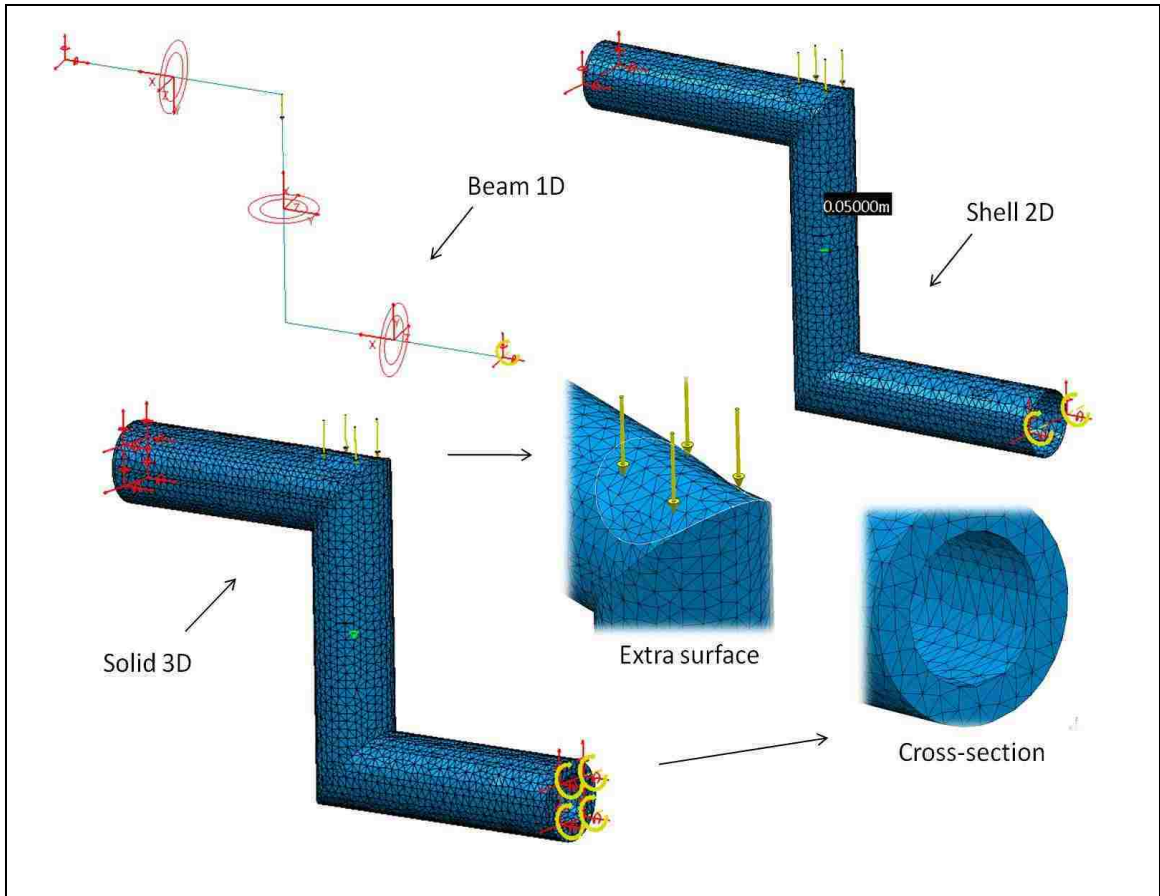


Figure 2.9 FE model of the Z-frame with beam, shell and solid elements

The tricky part when using shell and solid elements is how to apply the downward force P acting on node2. Normally, Catia applies the force on a surface or generally on a geometric entity such as a point or a line. Therefore, to create a more realistic loading condition in case of shell and solid models, an extra surface was needed. To do so, a sphere was created on the top of the frame, and a curved surface was created by intersecting the sphere and the structure. Then the surface was filled and sewed to the actual geometry to be able to mesh it as a part of the structure.

Figure 2.10 below, shows the deformation shape of the Z-frame. It is noted that the amount of deformation for solid and shell elements are almost equal while it is larger in the case of beam elements. Keep in mind that the intended purpose of this analysis was a

general comparison between different element types rather than proposing validation metrics.

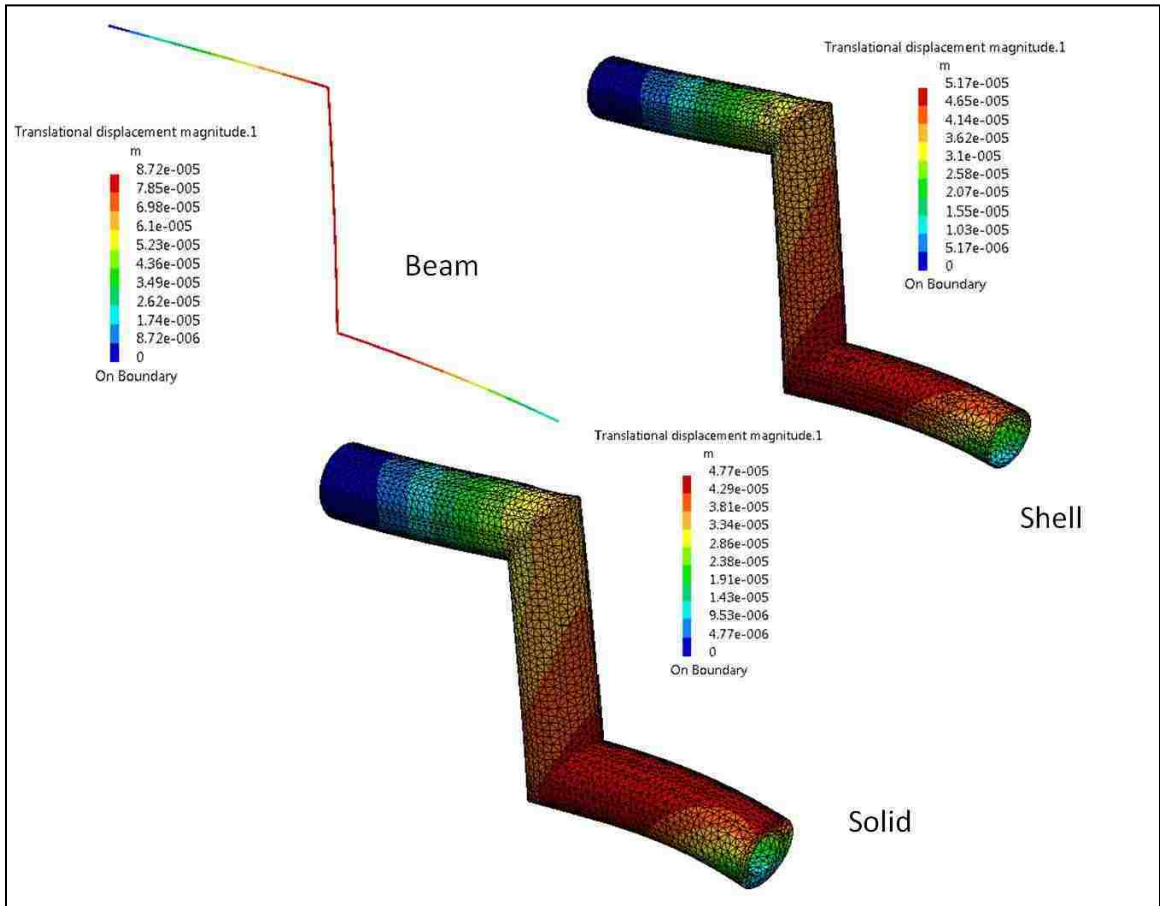


Figure 2.10 Displacement vector; beam, shell and solid

The results for the free vibration of the beam, shell and solid elements are described in table 2.3. In this table the values designated by “OP” refers to the out of plane modes of vibration, “V” refers to vertical behaviour modes of vibration and “H” refers to horizontal behaviour modes of vibration.

Table 2.3 Frequency analysis of the Z-frame ($R_{out} = 0.15 \text{ m}$, $R_{in} = 0.10 \text{ m}$)

mode	Frequency (Hz)		
	Beam	Shell	Solid
1	83.40 (V)	99.50 (H)	111.3 (OP)
2	111.9 (H)	107.3 (OP)	112.7 (H)
3	174.4 (OP)	135.2 (V)	149.1 (V)

For better visualization of the mode shapes, the figures below are presented regarding the frequency analysis of the Z-frame and corresponding mode shapes. A black solid Z-frame represents the model undeformed state, and the blue deformed mesh is the mode shape.

As shown in figure 2.11, deformed shapes of the structure which are shown with blue mesh, follow a vertical vibration behaviour. While this deformation is occurring at different direction for shell and solid elements, the corresponding natural frequencies are very close to one another.

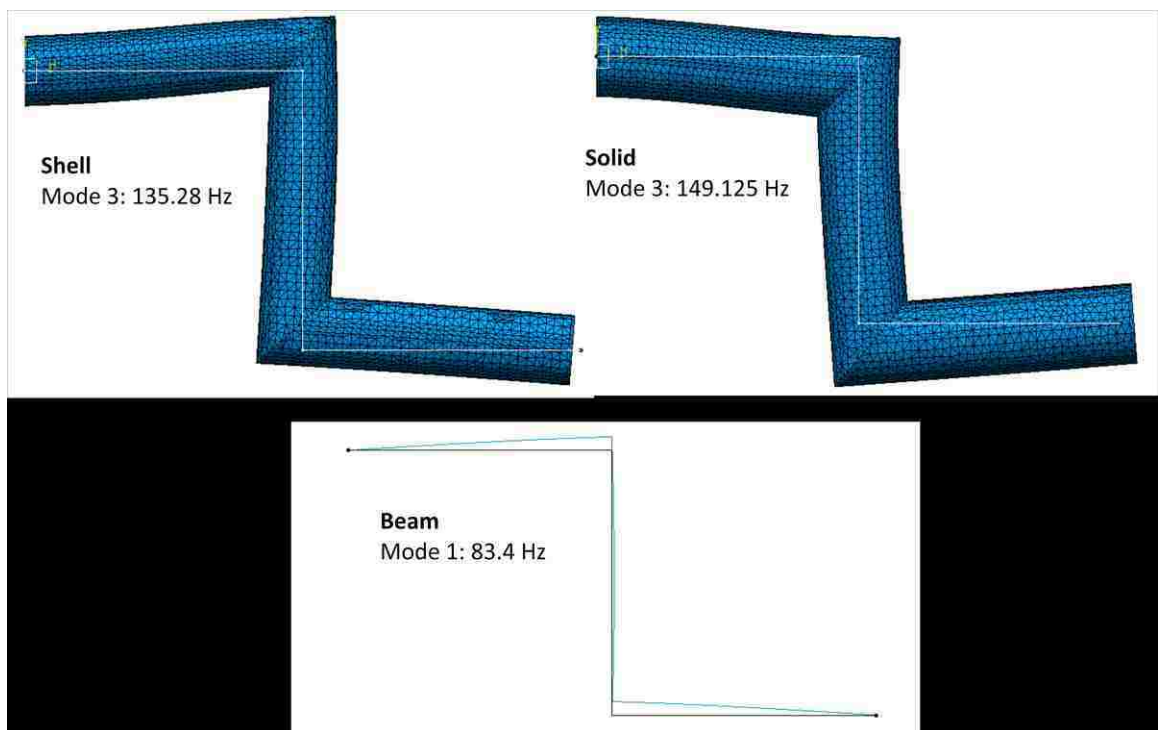


Figure 2.11 Vertical vibration behaviour of beam, shell and solid models

Figure 2.12 shows the horizontal vibration behaviour of the structure and figure 2.13 is the out of plane mode of vibration.

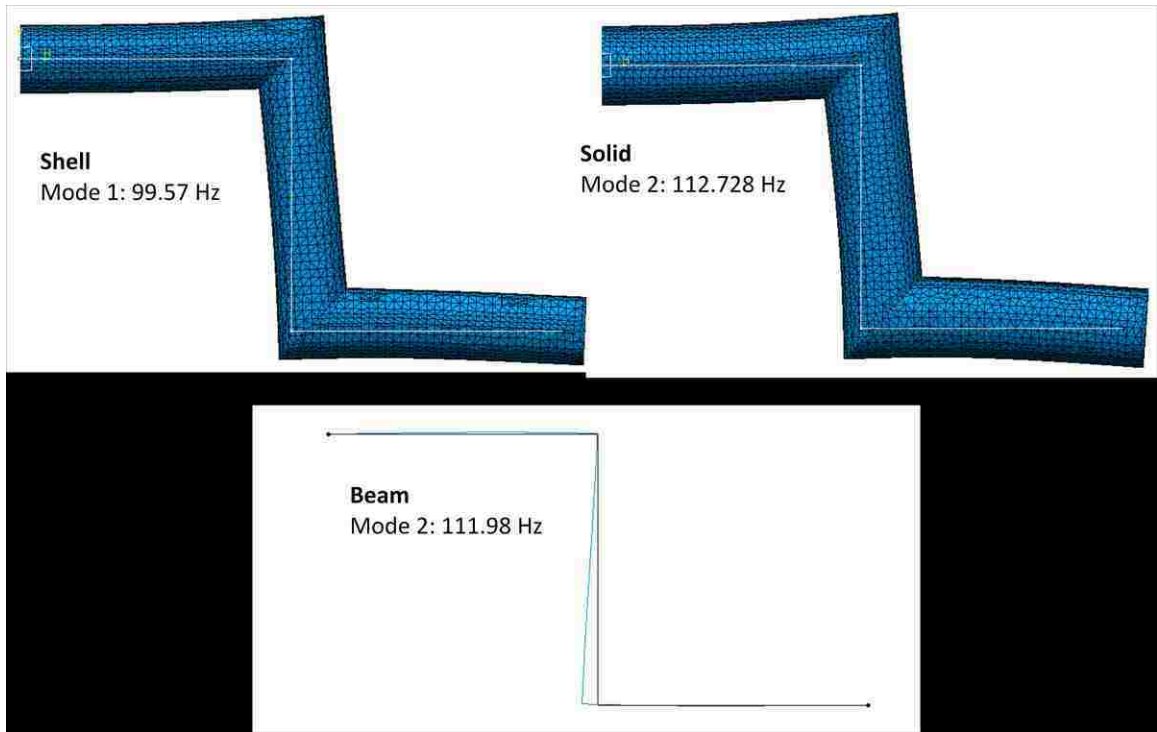


Figure 2.12 Horizontal vibration behaviour of beam, shell and solid models

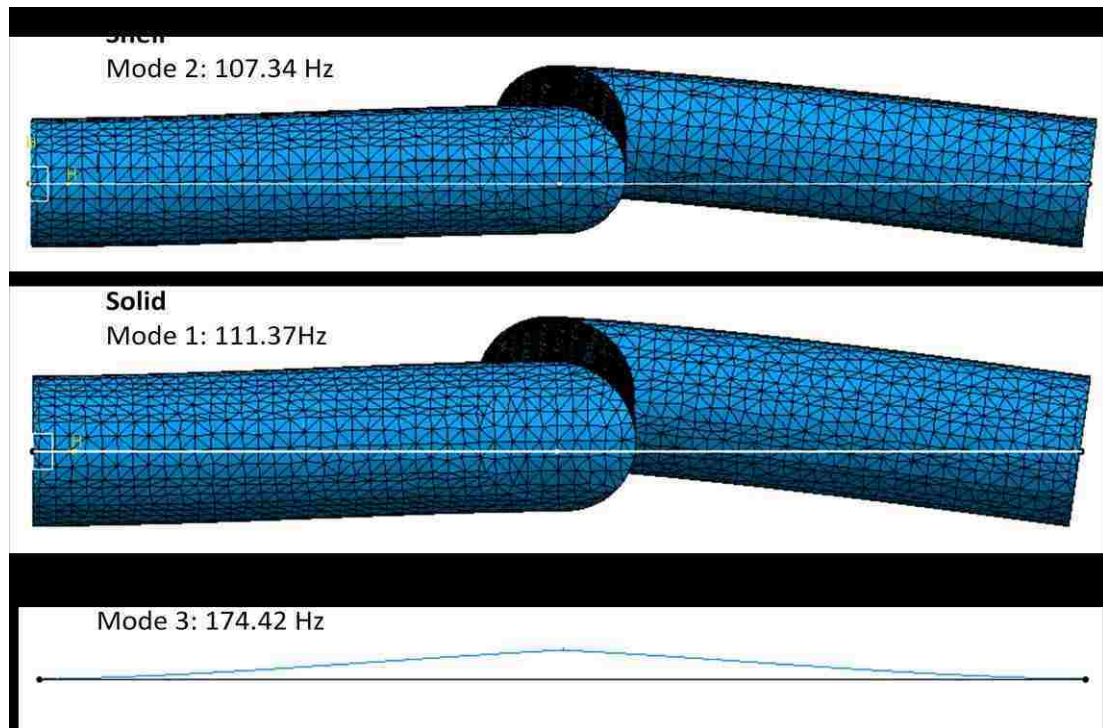


Figure 2.13 Out of plane mode of vibration of beam, shell and solid models

The von-Mises stress plots for the Z-frame are shown in figure 2.14. As shown in the figure, the locations of the maximum and minimum stresses are very close to one another in shell and solid models. Table 2.4 describes the stress values of the structure.

Table 2.4 von Mises stress for Z-frame ($R_{out} = 0.15 \text{ m}$, $R_{in} = 0.10 \text{ m}$)

	Range of von Mises stress	
	Shell	Solid
Max	8.18E+06	1.55E+07
Min	3.14E+04	3.19E+04

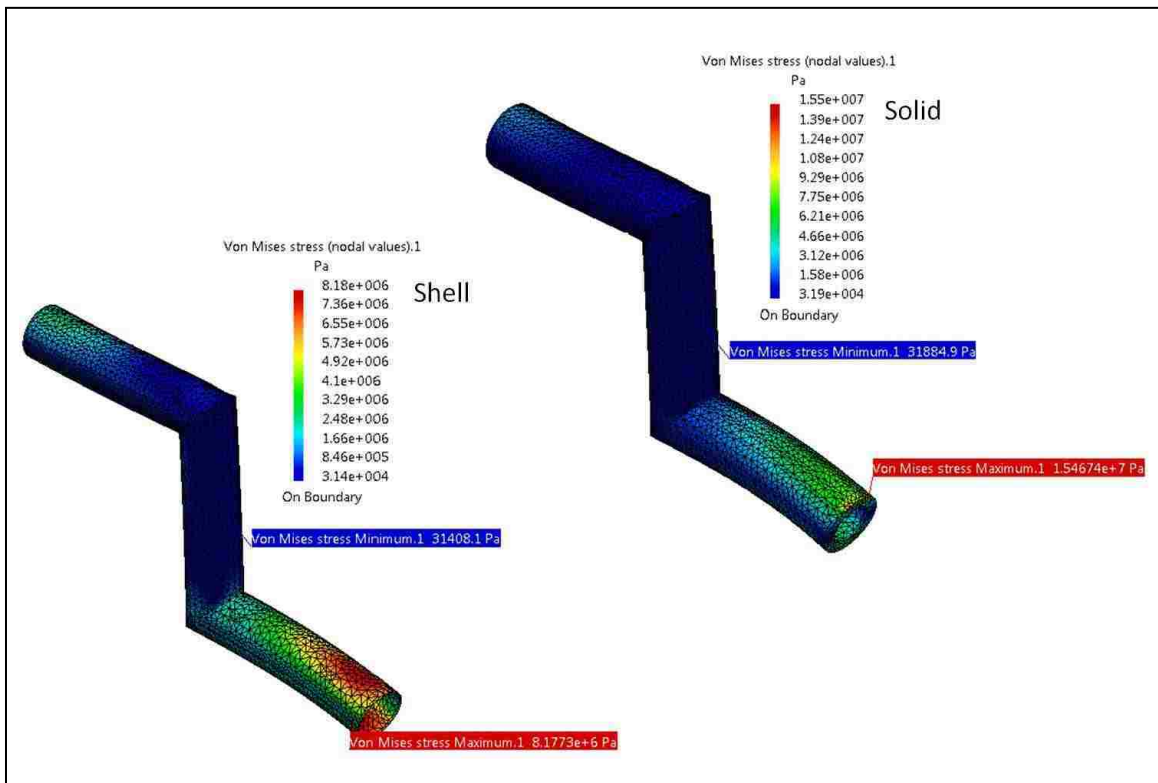


Figure 2.14 von-Mises stress contour; shell and solid

CHAPTER III

APPLICATION OF BEAM, SHELL, AND SOLID ELEMENTS FOR THE MINI-BAJA FRAME (LINEAR STATIC AND DYNAMIC ANALYSIS)

3.1 Objectives and overview of Chapter III

In this chapter, the modeling of the Mini-Baja frame with beam, shell and solid elements are implemented. Since this chapter covers a preliminary static analysis of the vehicle, the complete mock-up of the Mini-Baja frame was not modeled.

Knowing how the design reacts to different loading conditions would allow designers to make modifications in the FE model. A linear static analysis is a foundation for dynamic and non-linear finite element analysis. If a design cannot survive a linear static analysis, it has to be modified before moving on to more complex, time consuming and expensive dynamic or non-linear analysis. Therefore, a linear static analysis was first performed on the chassis frame. At the end of the chapter, a transient linear dynamic analysis is executed to determine the response of dynamic loads transmitted to the structure.

In [33], some key points on the analysis of frame structures are discussed. The main focus in [33] is how to design a cage structure rather than analyzing it. A simplified CAD model of the structure is introduced and discussed by describing two examples; Formula SAE and Baja SAE. This simplified model is very helpful for those who have interest in designing the chassis of such structures.

3.2 Mini-Baja modeling methodology

The purpose of this section is to present a fundamental knowledge of the methodology that was used to model the Mini-Baja structure for static analysis.

A CAD model of the preliminary design was available from the 2010 Baja team. Therefore, by using the existing CAD files as well as other actual measurements taken from the developed vehicle, an FE model has been created in Catia V5 for this thesis.

The finite element model was created using solid, shell and beam elements as shown in figures 3.2, 3.4 and 3.5. The solid idealization of the vehicle was meshed with 2.5 mm linear tetrahedron elements as shown in figure 3.1 (i.e. a total of 1,678,000 solid elements was used in the solid mesh). This element has three translational degrees of freedom at each node. Linear tetrahedron element has only one Gauss point¹, the gravity centre P1 of the tetrahedron.

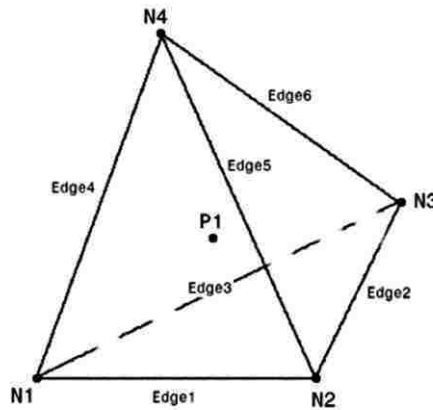


Figure 3.1 Linear tetrahedron solid element [34]

The reader should keep in mind that at the initial stage, there was no information available for the mesh convergence study of the model, and therefore, a relatively fine mesh was used in the static analysis to have some confidence in the accuracy of the results.

¹ The stresses are usually calculated at Gauss integration points, which is p1 in the case of figure 3.1. The element formulation and stiffness equations are written at these Gauss points, and correspondingly, stress and strain are evaluated at integration points. To find stresses at desired nodal point, the values from Gauss points are extrapolated to element edges and corners.

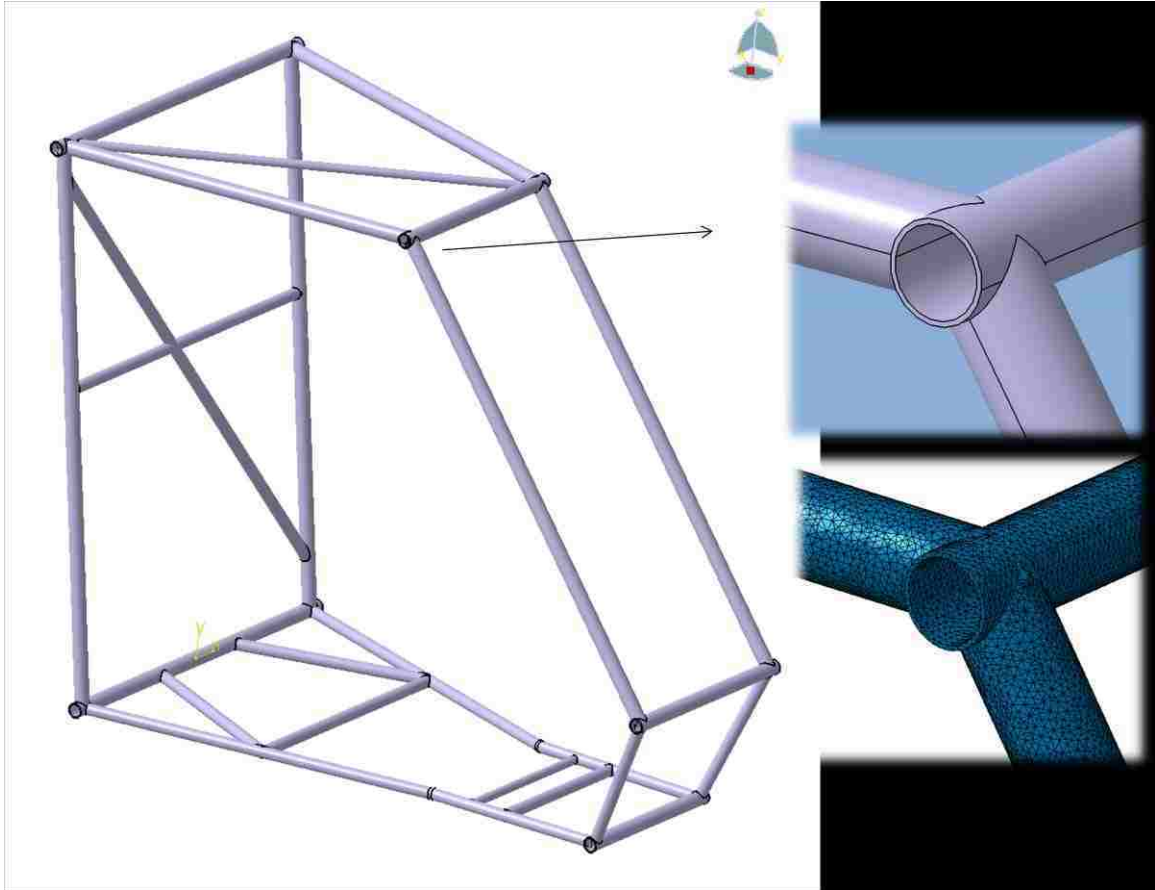


Figure 3.2 Solid idealization of the Mini-Baja structure

A fully parametric model of the structure was created to ensure that future changes could be made easily. It is worth noting that in modeling with different element types, a parametric model could be of much help due to major differences between shell, beam, and solid idealizations, (i.e. while a structure can be modeled with solid elements from the actual dimensions, shell model should be created with respect to the middle surface through the thickness. Note that Catia by default divides the shell thickness by two and applies it on both sides of the middle surface. In the case of a beam model, a totally different approach, the wireframe of the structure, is used to generate the model with appropriate sectional properties).

The shell model was meshed with 2.5 mm linear triangular elements as shown in figure 3.4, (i.e. a total of 555,300 shell elements was generated for the shell model). The

element used for shell model has 6 degrees of freedom at each node (3 translations and 3 rotations) with one Gauss point P1. As a point of comparison, note that the parabolic triangular element has 6 nodes and 3 Gauss points.

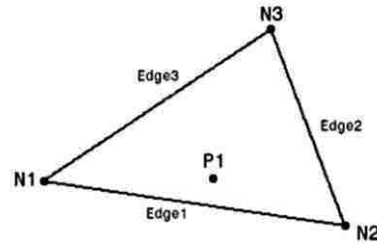


Figure 3.3 Linear triangular shell element [34]

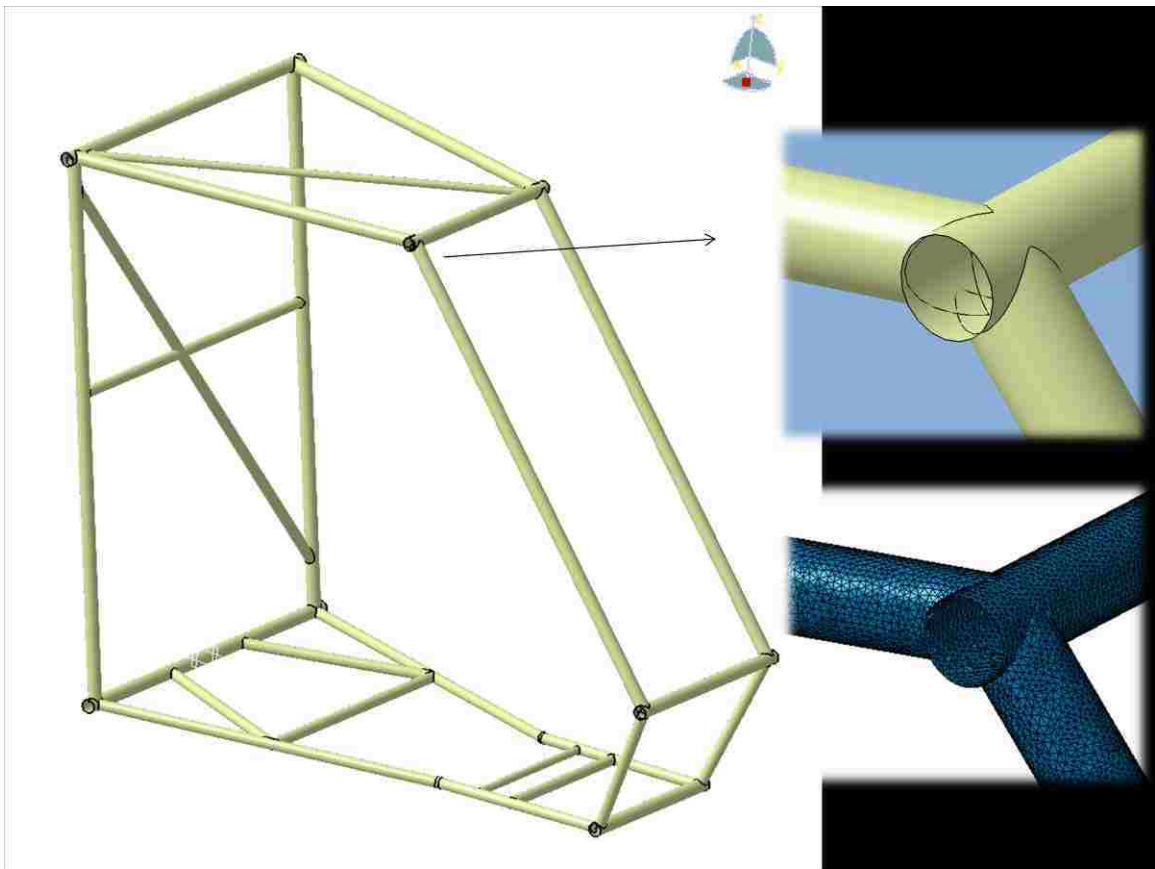


Figure 3.4 Shell idealization of the Mini-Baja structure

The beam model was meshed with 1.9 mm beam type elements as shown in figure 3.5, (i.e. a total of 9,300 beam elements was used in the model).

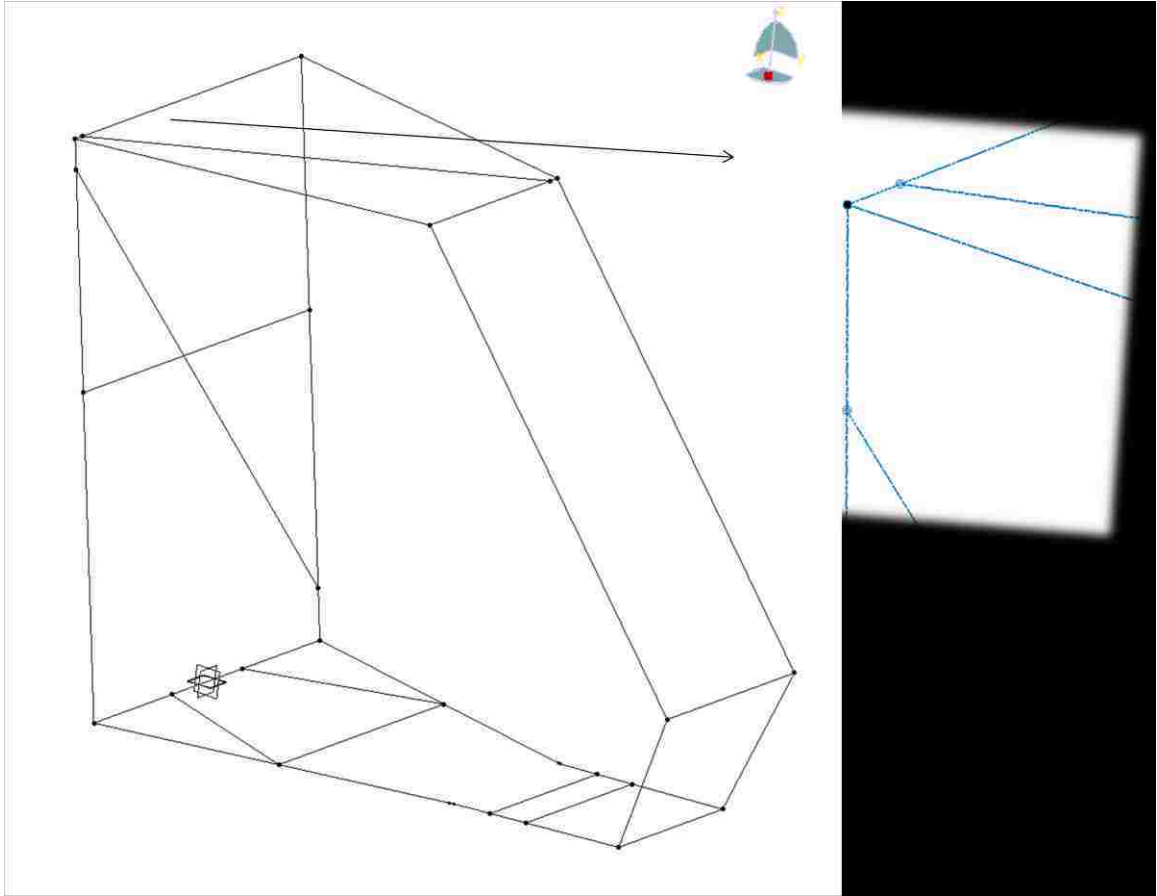


Figure 3.5 Beam idealization of the Mini-Baja structure

The next step in the analysis was the selection of different parameters for the static simulation. The parameters included material properties, section properties, loading conditions, weld joints and other simulation related considerations.

3.2.1 Material properties

All the tubes in construction of the Mini-Baja are made of 4130 Chromoly. Steel 41xx is considered a family of steel grades, as specified by the Society of Automotive Engineers (SAE). Alloying elements of 4130 are composed of chromium and molybdenum and, as a result, are often referred to as chromoly steel or CRMO. They have an excellent strength to weight ratio. It is easily welded and it is considerably stronger and harder than standard 1020 steel. Examples of applications for 4130 include structural tubing, bicycle frames and roll cages.

Alloy composition and mechanical property of this material are given in tables 3.1 and 3.2 below. Stress-strain curves given for a couple of steel grades are also displayed in figure 3.6 for comparison.

Table 3.1 Alloy composition of 4130 chromoly (by weight) [35]

SAE grade	% Cr	% Mo	% C	% Mn	% P (max)	% S (max)	% Si
4130	0.8–1.1	0.15–0.25	0.28–0.33	0.4–0.6	0.035	0.04	0.15–0.35

Table 3.2 Mechanical properties of 4130 steel [35]

Material	Condition	Tensile strength [psi (MPa)]	Yield strength [psi (MPa)]	Elongation in 2" [%]	Hardness (Rockwell ¹)
4130	Cold drawn ² -normalized	85,000–110,000 psi (590–760 MPa)	70,000–85,000 psi (480–590 MPa)	20–30	B 90–96

¹ The Rockwell scale is a hardness scale based on the hardness of a material. The Rockwell test determines the hardness by measuring the depth of penetration of an indenter under a large load compared to the penetration made by a preload.

² Cold working, also known as work hardening or strain hardening, is the strengthening of a metal by plastic deformation. This strengthening occurs because of dislocation movements within the crystal structure of the material. Any material with a reasonably high melting point such as metals and alloys can be strengthened in this fashion.

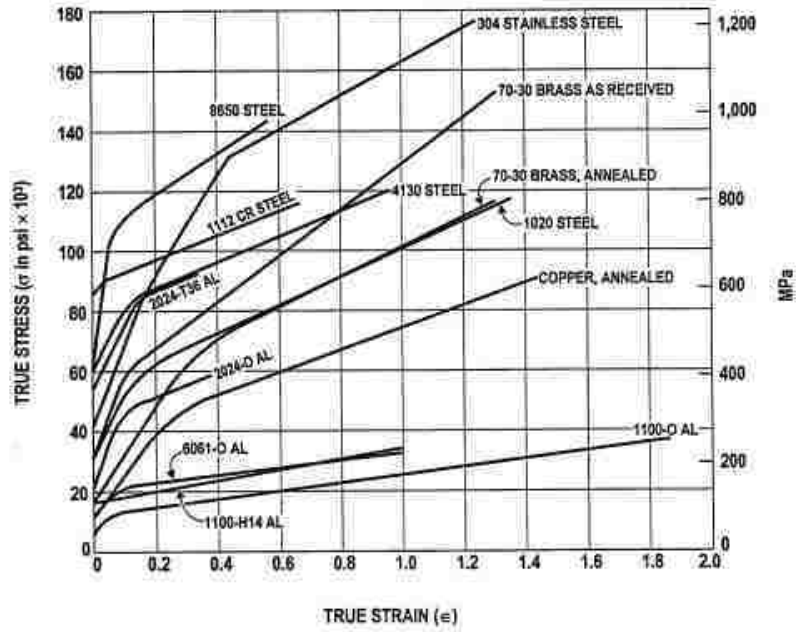


Figure 3.6 Stress-strain curves of different grades of steel [35]

Structural properties of the 4130 chromoly, inputted for the static simulation in Catia, are given in table 3.3 below.

Table 3.3 Structural property of 4130 chromoly used in static simulation

Material	4130 Chromoly
Young's modulus	2.050e+011Pa
Poisson's ratio	0.29
Density	7850.00kg_m3
Coefficient of thermal expansion	1.17e-005_Kdeg
Yield strength	4.351e+008Pa

3.2.2 Sectional property

Sectional properties for the solid model are automatically dealt with in Catia without user interface. The shell model was created using the middle surface of the tubes with corresponding thicknesses as shown in figure 3.7 (b). Beam model as shown in figure 3.7 (a) was created with respect to the wire idealization of the structure with tubular sectional property and corresponding radii. The tubes' thicknesses range from 0.049 inch for long members to 0.069 inch in cross members, as shown in figure 3.7.

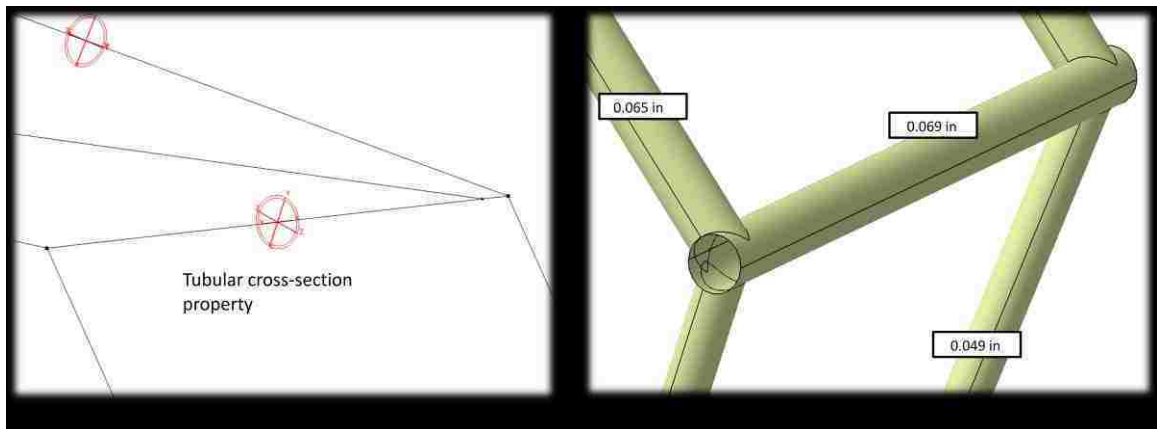


Figure 3.7 Sectional property of beam and shell models

3.2.3 Loading condition

Frontal impact is a non-linear dynamic event, but to do a preliminary linear elastic or quasi-static analysis on the frame, first the magnitude of the impact force should be estimated. Therefore, one needs to compute the force to be used in the static analysis that is roughly equivalent to the peak dynamic force or average dynamic force observed during an impact.

To find an appropriate value of impact force transmitted to the frame, the principle of linear impulse and momentum was applied to the system shown in figure 3.8. Impulse and momentum is conserved for any isolated collision (i.e. in the current case, inelastic collision). While conservation of impulse and momentum can be valid for any

collision, conservation of kinetic energy is usually not. Kinetic energy can be converted to thermal energy and internal strain energy due to deformations in collision, and therefore, kinetic energy is not preserved in an inelastic collision. The conservation of kinetic energy can be used in analyzing of elastic collisions where no deformation is happening, (e.g. striking of two billiard balls).

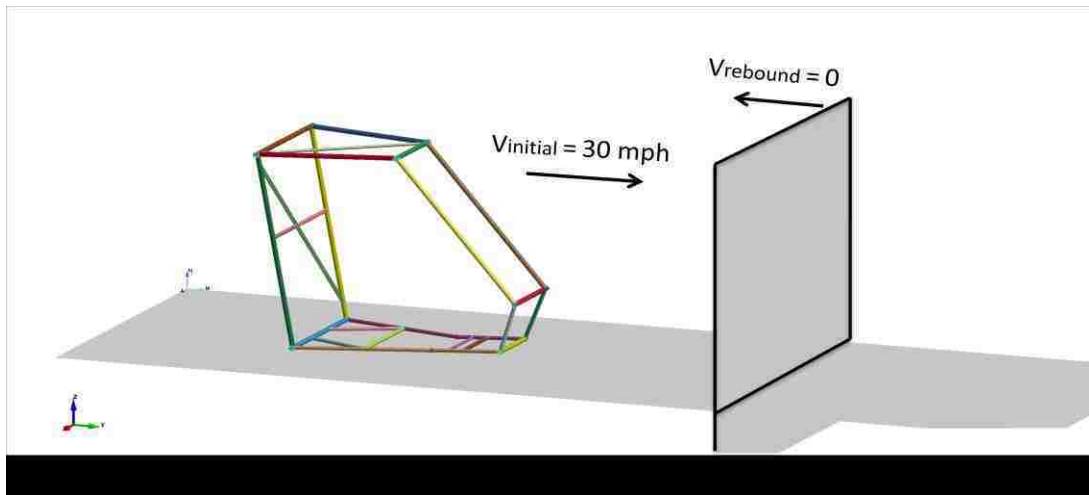


Figure 3.8 Linear impulse and momentum applied on Mini-Baja frontal collision

It was assumed that the initial velocity of the vehicle is 30 mph (or 13 m/s), as this is the maximum velocity that a Mini-Baja can achieve. Mass of the structure constructed of chromoly 4130 is 17 kg, and since the impact time of vehicle crash is of the order of milliseconds, impact time of 0.01 sec was assumed. Furthermore, it was assumed that the rebound velocity of the vehicle backward after the impact is negligible, i.e. $V_{\text{rebound}} = 0$.

Hence,

$$F = ma = m \frac{\Delta v}{\Delta t} = \frac{\Delta P}{\Delta t} \quad (3-1)$$

where, $P = mv$

$$F = \frac{\text{The change in momentum}}{\text{The time to make the change}} \quad (3-2)$$

By calculation of F in eq. (3-2), the impact force is estimated to be $F = 22,100 \text{ N}$.

3.2.4 Connections

Components of the Mini-Baja vehicle are welded together at their joints (also known as fish-joints). In regard of the wireframe model, two structural beam elements properly connected together behave like a fully welded connection (i.e. beam elements will transmit forces and moments). To make a perfect connection at the joints, all degrees of freedom should be coupled together, and therefore, all translational and rotational degrees of freedom can be transmitted through the welded connection.

For the solid and shell model, the connection was modeled using rigid seam weld in Catia V5. If the mesh is compatible, Catia uses a seam weld to connect a line of nodes on the first surface directly to a line of nodes on the second surface. If the mesh is incompatible, a spot weld distributes the connection between the surfaces among several nodes automatically. Catia uses a curved path at the joint to define the weld between two tubes as shown in figure 3.9. The mesh quality was ensured for the best possible idealization of the joints since it has a critical role in the deformation characteristic of the structure as well as stress distribution through the cage. For seam weld connections, a step-by-step tutorial is provided in Appendix “A”.

It is necessary to use a fine mesh in the vicinity of the weld since it uses very small rigid beam connectors between nodes. These connections consequently would result in coupling of all degrees of freedom between the two corresponding nodes at the joint.

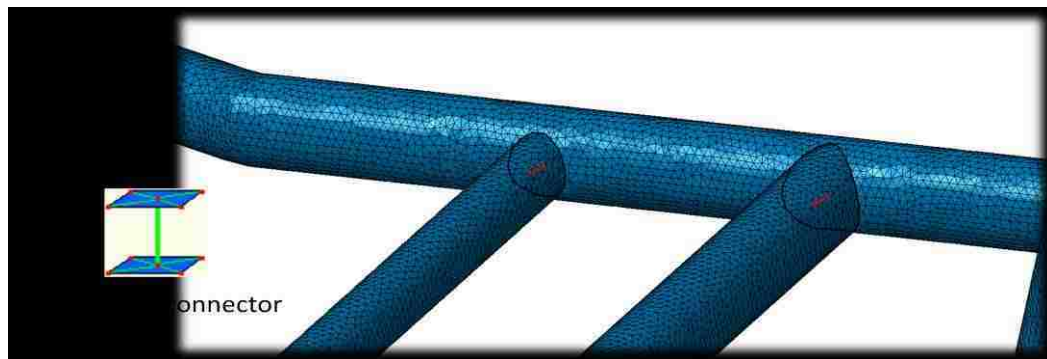


Figure 3.9 Seam welded connection CATIA V5

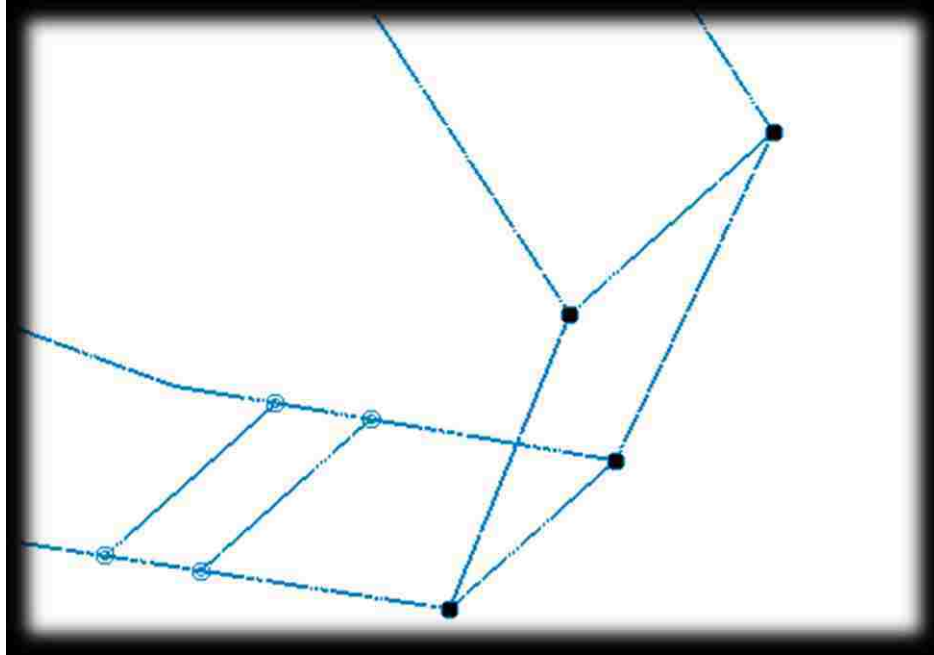


Figure 3.10 Weld-connection for the beam model CATIA V5

In the beam model, there are two types of connections used to create a fully welded frame. As shown in figure 3.10, the black dots are those connected rigidly at the joints with rigid connection property. For those connections where a line is intersecting another line in the middle, as shown in figure 3.10 by blue dots, first a node should be created on the mesh at the corresponding joint, and then the two corresponding points are connected together using a rigid node to node connection property. A step-by-step tutorial on this connection issue in wireframes is provided in Appendix “B”.

3.3 Static results

After setting the parameters, the simulation was run using Catia V5. To develop a sense of behaviour in a front crash scenario, the bottom back end of the frame was clamped to be fixed and the back frame was constrained not to deflect horizontally. Subsequently, a static analysis was run for the current problem to find out the deformation contours and von Mises stress distribution. Figures below show the deformation shape for the beam, shell and solid models.

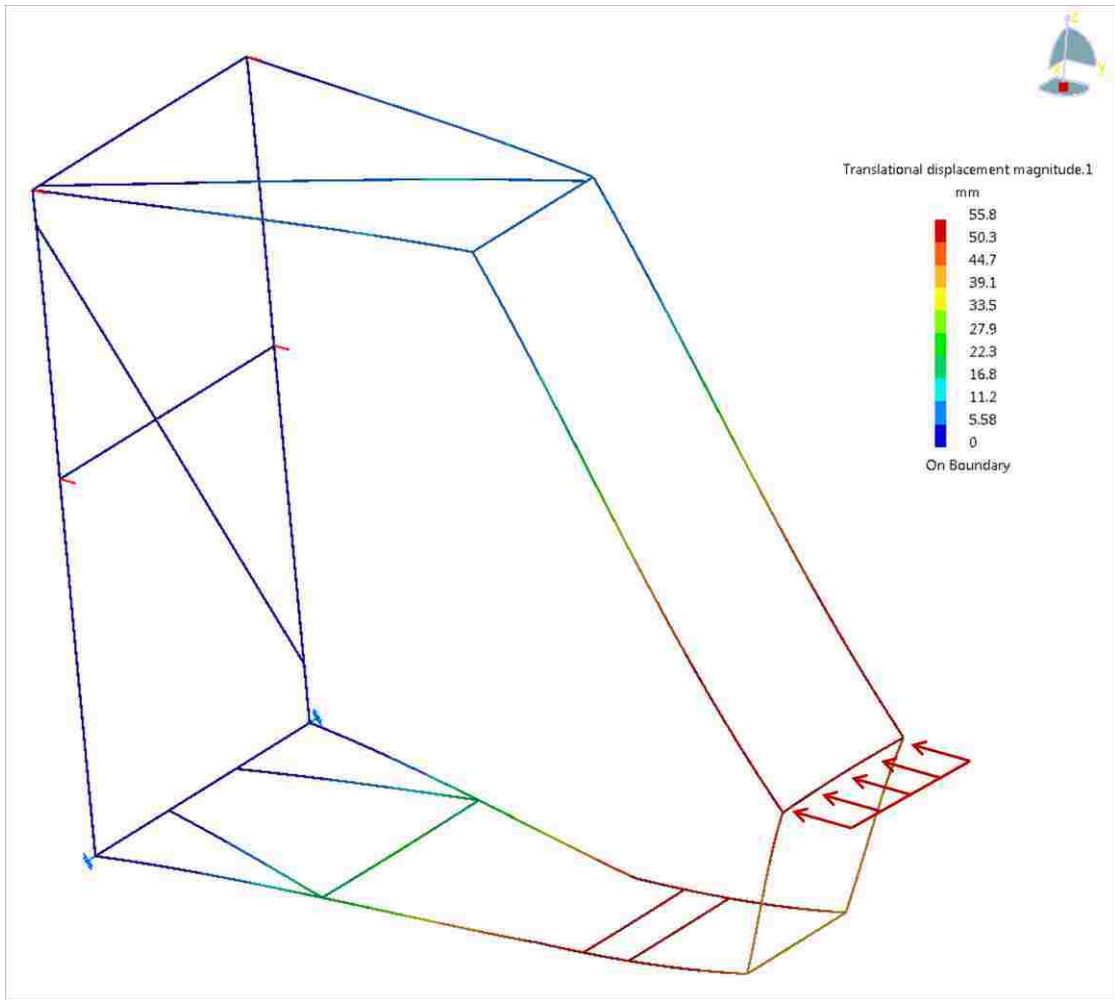


Figure 3.11 Deformation shape for the beam model

Although the deformation contour is almost the same for all three models, the value differs among them. The maximum deformation occurs in the shell model as shown in figure 3.12 while the beam model deflects the least.

There are many factors that can contribute to the accuracy of the final results. Mesh sizes and type of mesh is one of those factors that can be very important in the analysis. It is one of the key factors in characterizing a distribution of displacement or stress in elements. For the current static analysis, relatively stiff elements triangles and tetrahedral were chosen for the shell and solid models, respectively.

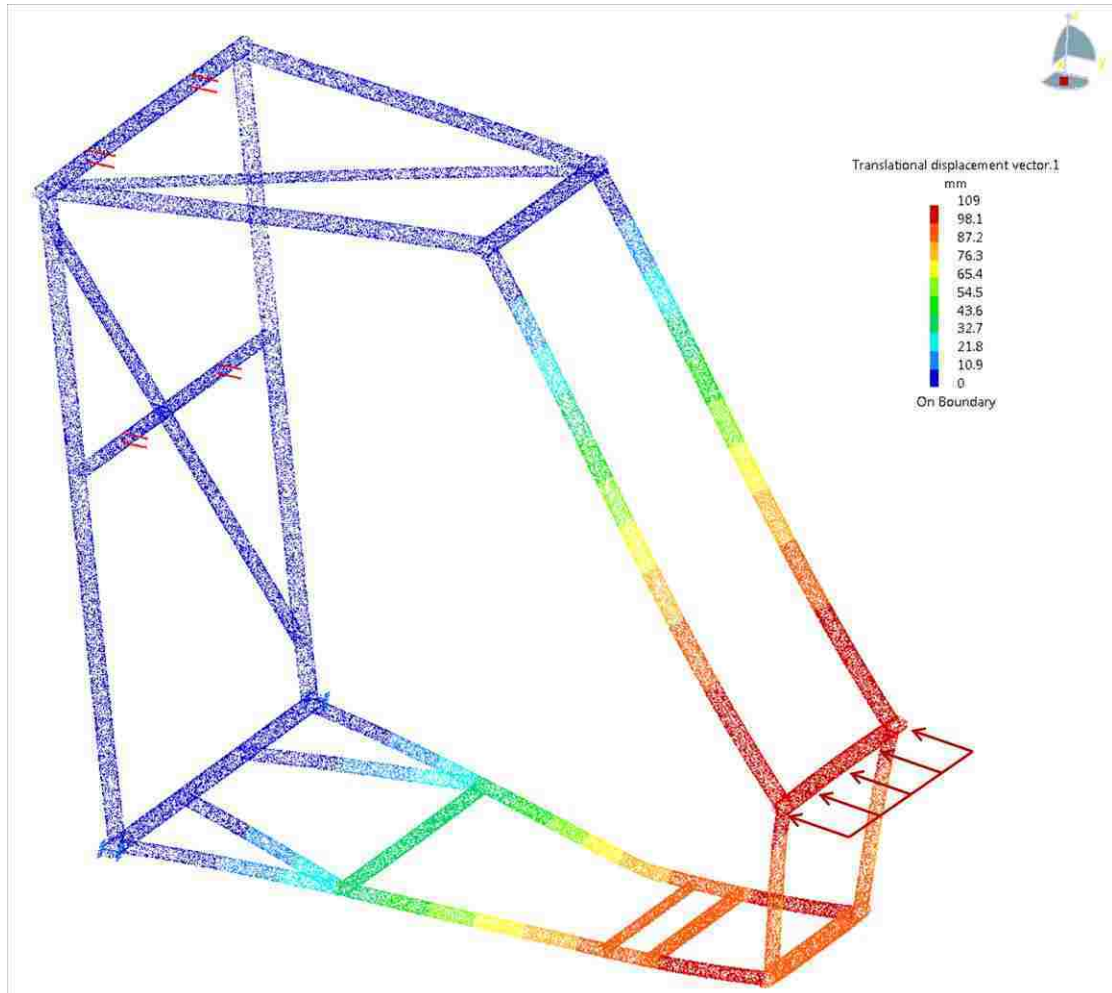


Figure 3.12 Deformation shape for the shell model

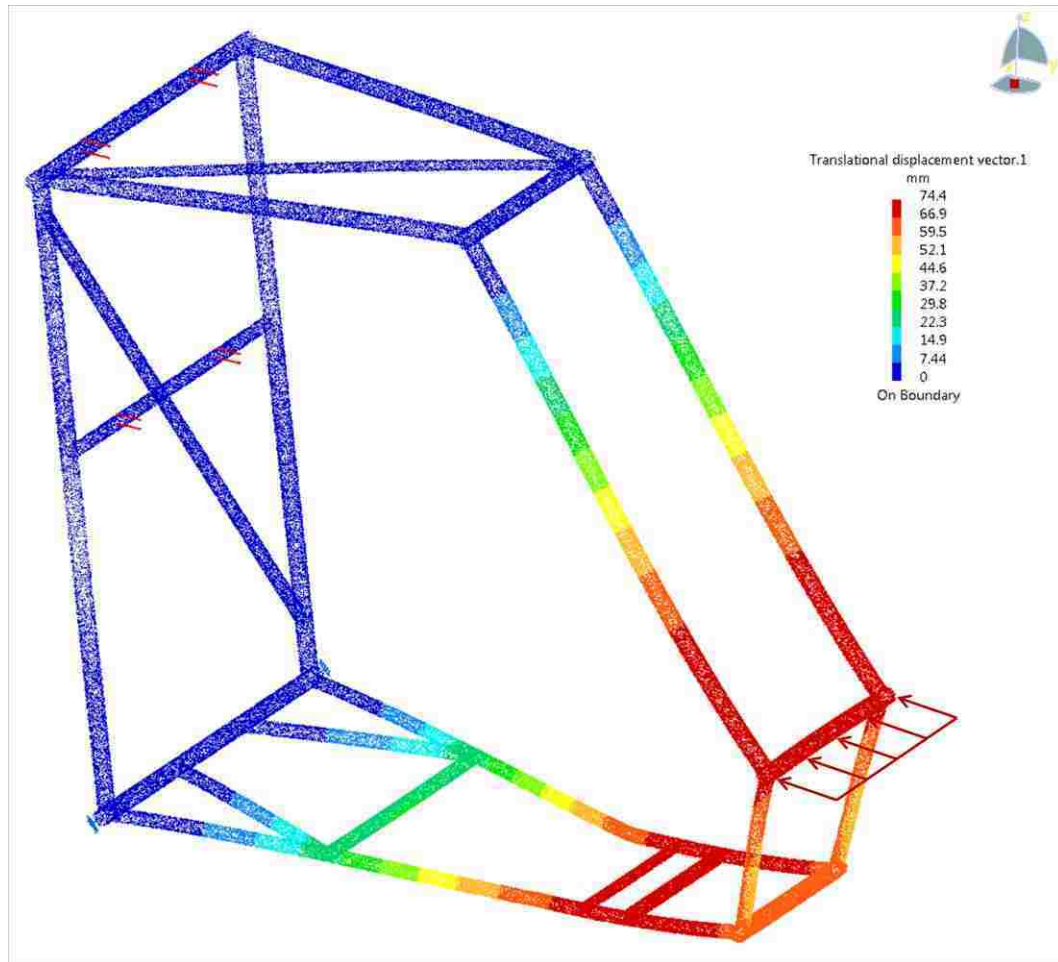


Figure 3.13 Deformation shape for the solid model

The von Mises stress distribution is shown for the shell and solid models in figures 3.14 and 3.15. The analysis determines the intensity and the areas of the highest von Mises stresses that the frame members are subjected to for the applied load. The location of the maximum stress is different between the two models. Nevertheless, the distribution of the stress is reasonably identical and the stress values are almost the same.

Based on the comparison made between the three models, it was concluded that the shell idealization is the more reasonable option for the finite element analysis of tubular frame structures. The beam model is very helpful in the preliminary analysis of the structure since the modeling is much easier and is the most computationally efficient choice. Furthermore, although the solid model can be characterized as the ideal FE model, in order to obtain accurate results, a greater number of elements are needed.

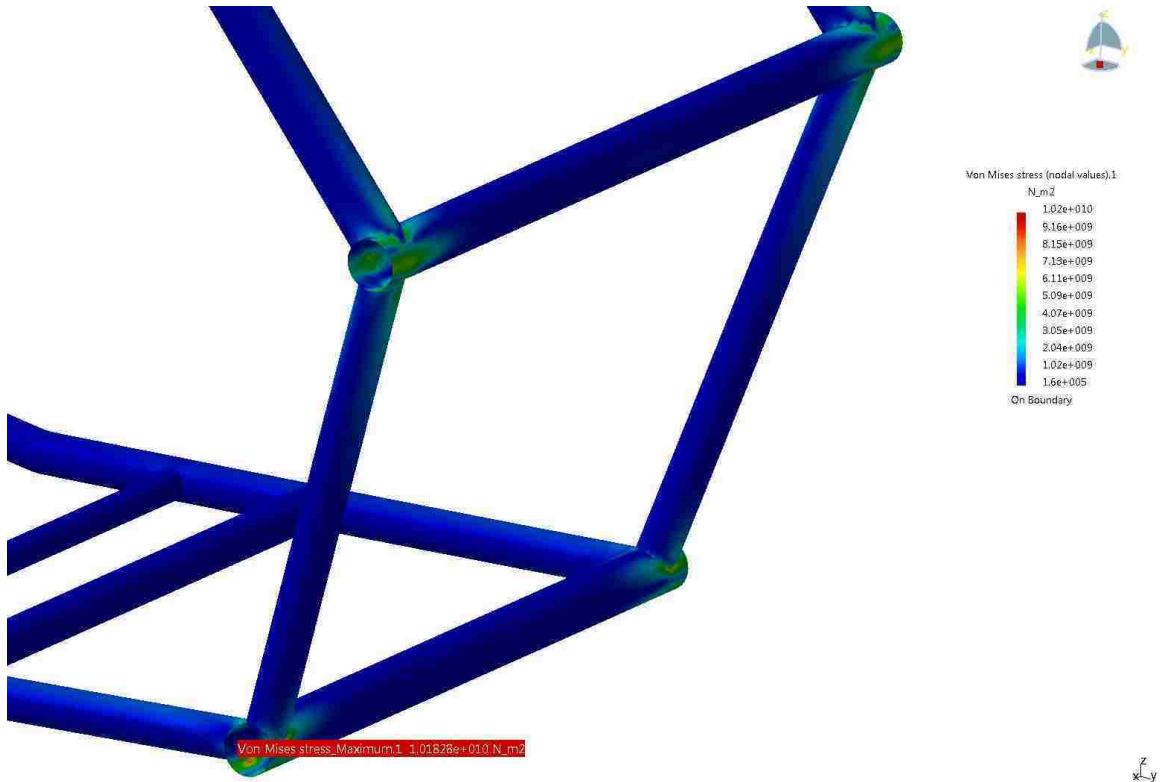


Figure 3.14 von Mises stress distribution for the shell model

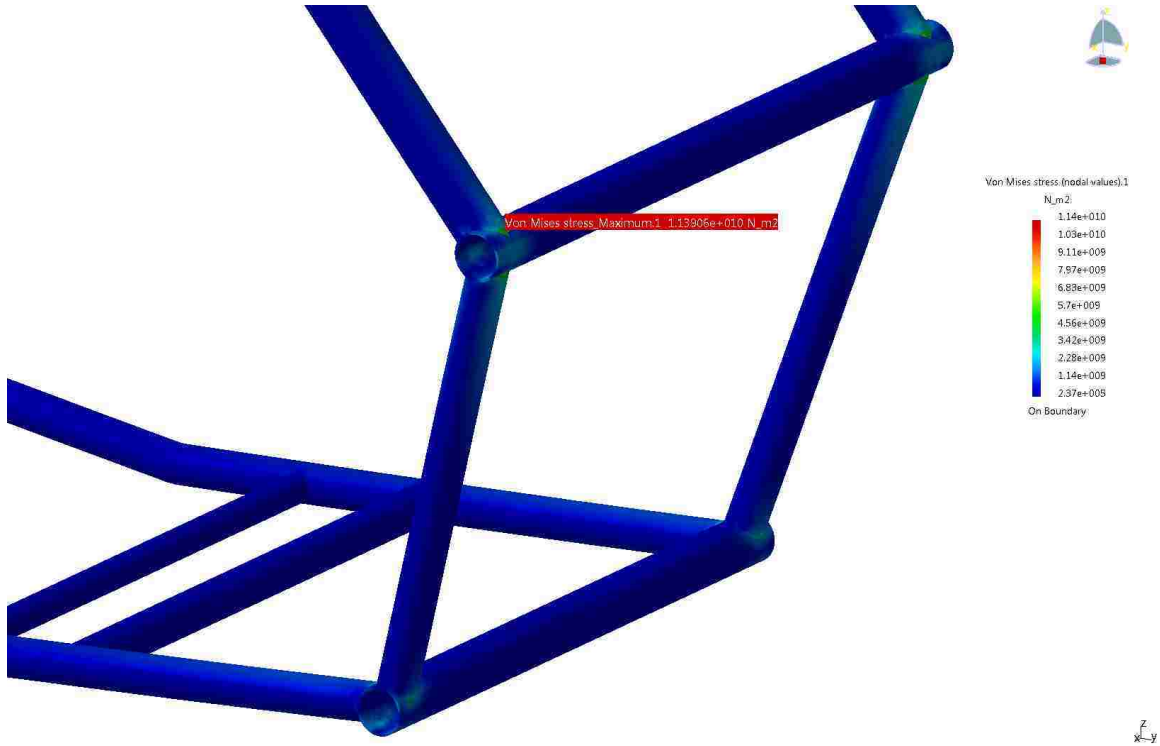


Figure 3.15 von Mises stress distribution for the solid model

3.4 Transient dynamic analysis

Since the response of the Mini-Baja vehicles is known to be dynamic, in this section vertical dynamic loads transmitted through the suspension of the frame are discussed by using the transient dynamic analysis case in Catia V5. It is assumed that the vehicle goes over a bump at relatively high speed resulting in a dynamic behaviour.

Transient dynamics analysis, often called “Time-History Analysis”, is a technique used to determine the dynamic response of a structure under the action of any general time-dependent loading. This type of analysis is used to determine the time-varying displacements and stresses as it responds to any combination of transient or harmonic loadings.

Generally speaking, all loads in nature are transient, (they vary as a function of time). However, this does not mean that the problem being studied responds dynamically. In dynamic analysis, the time-scale of loading is such that the inertia and damping effects are considered to be important. Therefore, the equation of motion from static events $[k]\{x\} = F$ turns into $[m]\{\ddot{x}\} + [c]\{\dot{x}\} + [k]\{x\} = f(t)$ in dynamic events. If the frequency of loading is much smaller than the natural frequencies of the structure, the analysis can be solved statically. This assumption is normally applied when the frequency of loading is less than one third of the lowest natural frequency of the structure [36]. But, if the input frequency of the loading is too high, a transient analysis taking into account the inertia effect must be performed. This effect is schematically shown in figure 3.16. The damping effect is discussed in section 3.4.1.

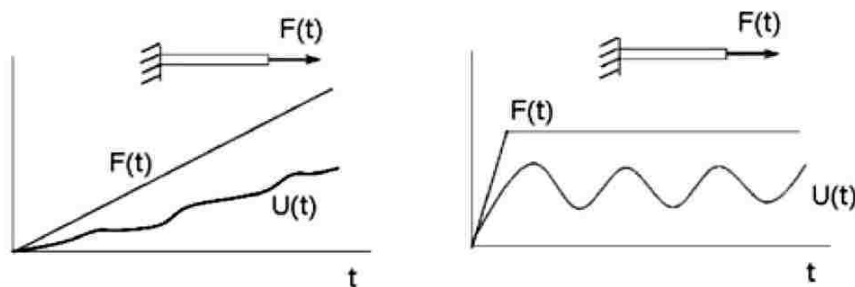


Figure 3.16 Left: static response for a slowly varying load; Right: dynamic response for a fast varying load [31]

Within Catia, the technique used to analyze transient dynamic problems is modal superposition. It can be performed only after the frequency extraction procedure since it is based on the structure's vibration modes of the system. After an eigenfrequency analysis has been used to find the eigenvalues of a model, the software automatically calculates the modal participation factor¹, the effective mass², and the composite modal damping³ for each mode so that these variables are available for use in subsequent linear dynamic analysis [8].

As mentioned before in Chapter I, the frequency extraction procedure used in all FEA packages, calculates the frequencies and the corresponding mode shapes of a system. This involves the equation for free vibration analysis:

$$[[K] - \omega^2[M]]\{x\} = 0 \quad (3-3)$$

where the variables are: K = Stiffness matrix, M = Mass matrix, ω = Natural frequency of harmonic motion, x = Degrees of freedom.

Once the classical structural eigenvalue problem in eq. (3-3) is solved for desired natural frequencies and corresponding mode shapes, eq. (3-4) corresponding to the dynamic load excitation in a transient dynamic response case is implemented [34]:

$$F(t) = \sum_k C_k F_k M_k(t) \quad (3-4)$$

where t is the time, F_k is the static load, $M_k(t)$ is the time modulation, and C_k is the scale factor.

The approximations in this analysis procedure are the linearization of the problem, meaning that the loadings are assumed to vary piecewise linearly with time, and a finite number of eigenmodes are used for the representation of the system. It is understood that

¹ Participation factor is a variable that indicates how strongly motion in the global x-, y- or z-direction or rotation about one of these axes is represented in the eigenvector of that mode [8].

² If the effective masses of the modes used in the analysis add up to a value that is significantly less than the model's total mass, this suggests that modes that have significant participation in excitation in that direction have not been extracted correctly [8].

³ Composite modal damping provides an option to define a composite damping factor for each material. These are assembled into fractions of critical damping values for each mode [8].

the number of modes extracted from the frequency analysis must be sufficient to model the dynamic response of the system adequately.

3.4.1 Damping effect

In dynamic analysis, in addition to the inertia effect, damping is also present in some form or other within structures. The damping present can be thought of as an “energy absorber”. The following diagram shows the response of a single degree of freedom system displaced from the equilibrium position with respect to amount of damping present.

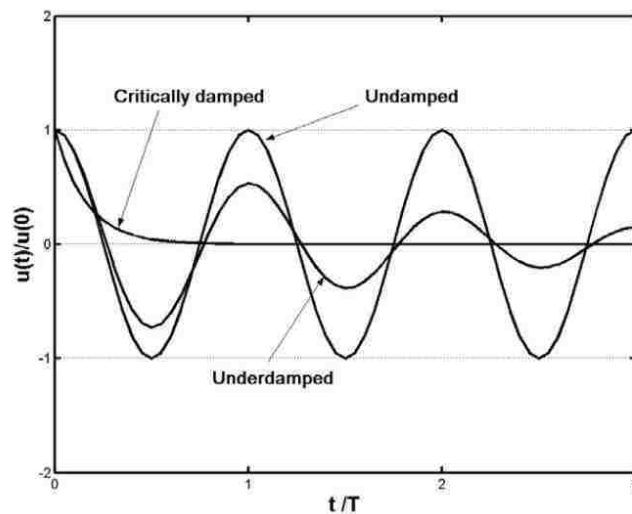


Figure 3.17 Structure response for different types of damping [37]

If the level of damping is high, then the structure is critically damped and the response curve shows a steeper variation as shown in figure 3.17.

If there is no damping present (undamped), then the energy is not dissipated in the structure and the amplitude of the response remains unchanged. Underdamping is the most frequent form of damping present in most structures [36].

3.4.2 Dynamic force

The force transmitted to the frame while the vehicle goes over a bump as shown schematically in figure 3.18 was modeled using the eq. (3-5). According to [38] the magnitude of the transmitted force at a critical speed is given by

$$F_{tr} = 2\pi v_0 \frac{y_0 km}{\lambda c} \quad (3-5)$$

where F_{tr} is the transmitted force. The data used to estimate the transmitted force is $v_0 = 13$ m/s, $y_0 = 0.088$ m (3.5 inch), $\lambda = 0.3$ m (12 inch), $k = 5e4$ kg/s², $c = 1200$ kg/s and $m = 17$ kg as displayed in figure 3.18. Note that this formula assumes that the vehicle travels at a constant speed. Furthermore, it was assumed that the deflection of the bump is sinusoidal and that the damping of the vehicle's suspension is light.

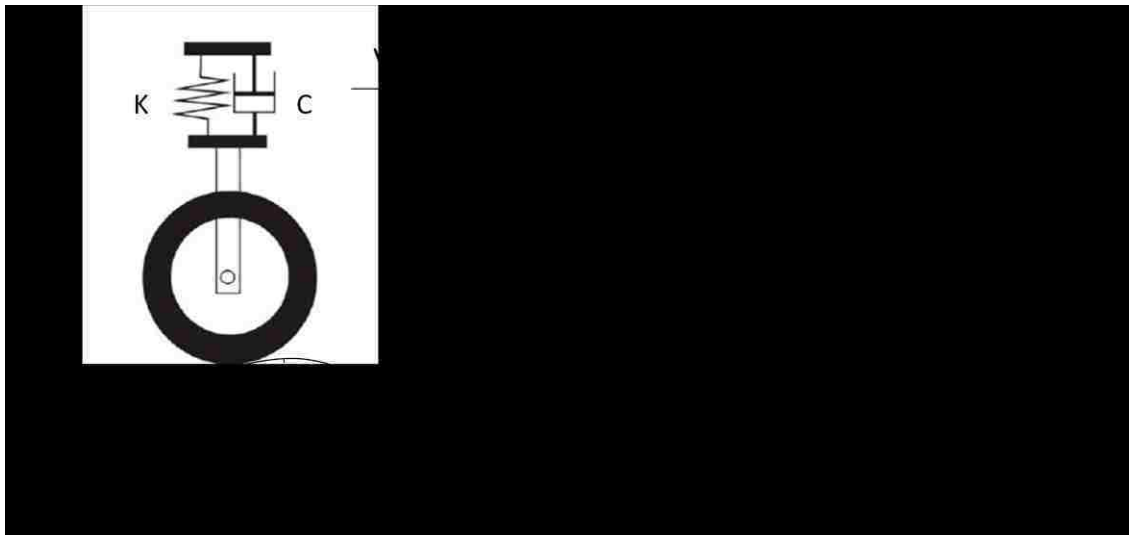


Figure 3.18 Schematic diagram of a vehicle model over a bump

By inputting the desired values to eq. (3-5) for the 17 kg model, the calculated transmitted force is $F_{tr} = 17000$ N. Keep in mind that the whole mass of the model was used intentionally instead of a quarter model. This introduces a safety factor of 4 in the force estimation.

3.4.3 Transient dynamic simulation

The procedure of transient dynamic analysis in Catia V5 consists of a combination of static, frequency and transient dynamic case. As noted in eq. (3-4) first a static analysis is run by applying the amplitude of the dynamic load at the desired location, then the frequency analysis is run to obtain the natural frequencies and corresponding mode shapes. Finally, the transient case is added by selecting the number of desired frequency extractions. A step-by-step tutorial is provided regarding the transient dynamic analysis in Appendix “C”.

The Mini-Baja frame was constrained at the top and at the left bottom as shown in figure 3.19 and 3.20. Pivot restraints in Catia were used at three different locations as shown to constrain the frame while the right corner goes over the bump. To simulate this situation, the dynamic load calculated in section 3.4.2 was applied upward at the right corner.



Figure 3.19 Constraint condition for dynamic analysis

Initially the simulation was run statically by the constant force of $F_{tr} = 17000$ N where translational results are shown in figures 3.21 and the von Mises stress is also displayed in figure 3.22.

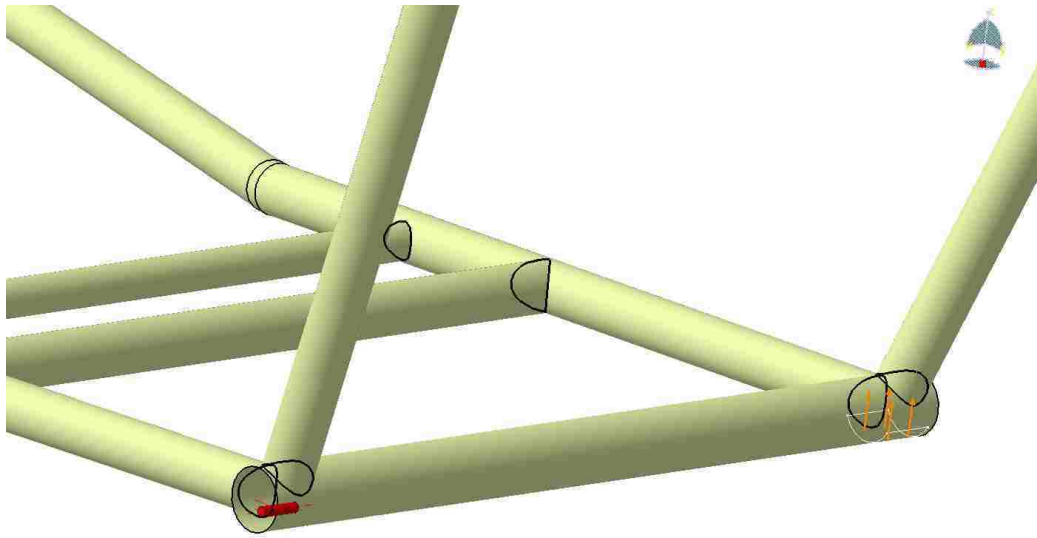


Figure 3.20 Constraint condition for dynamic analysis

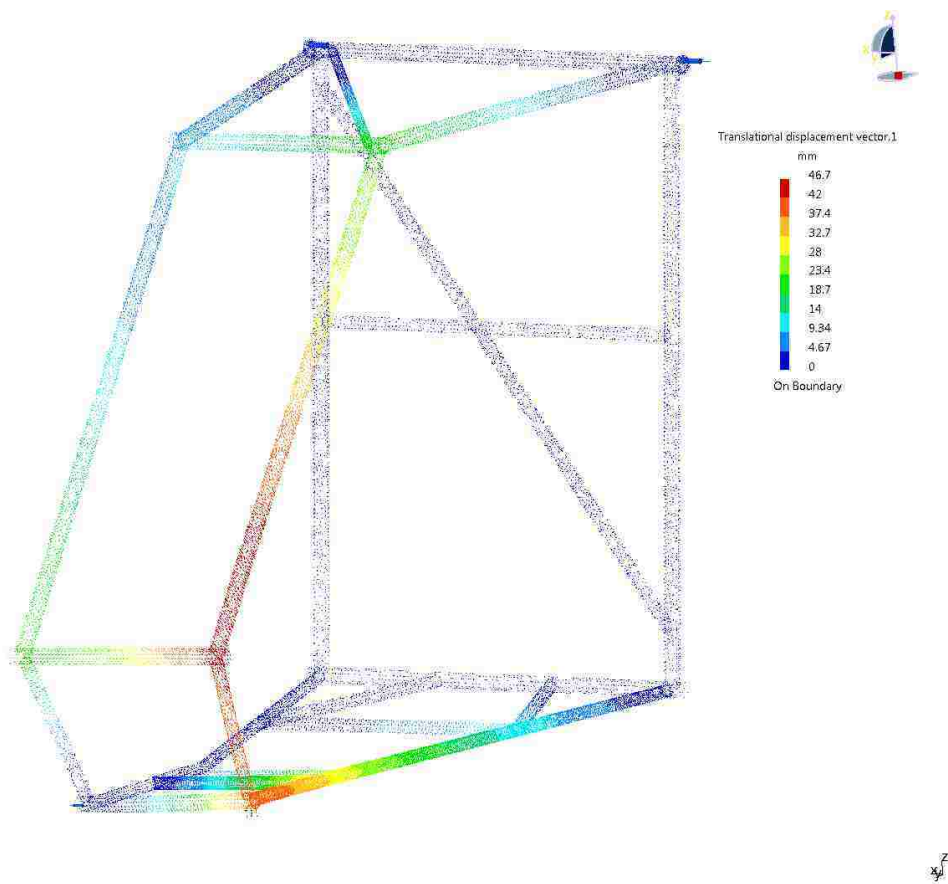


Figure 3.21 Deformation shape in static analysis

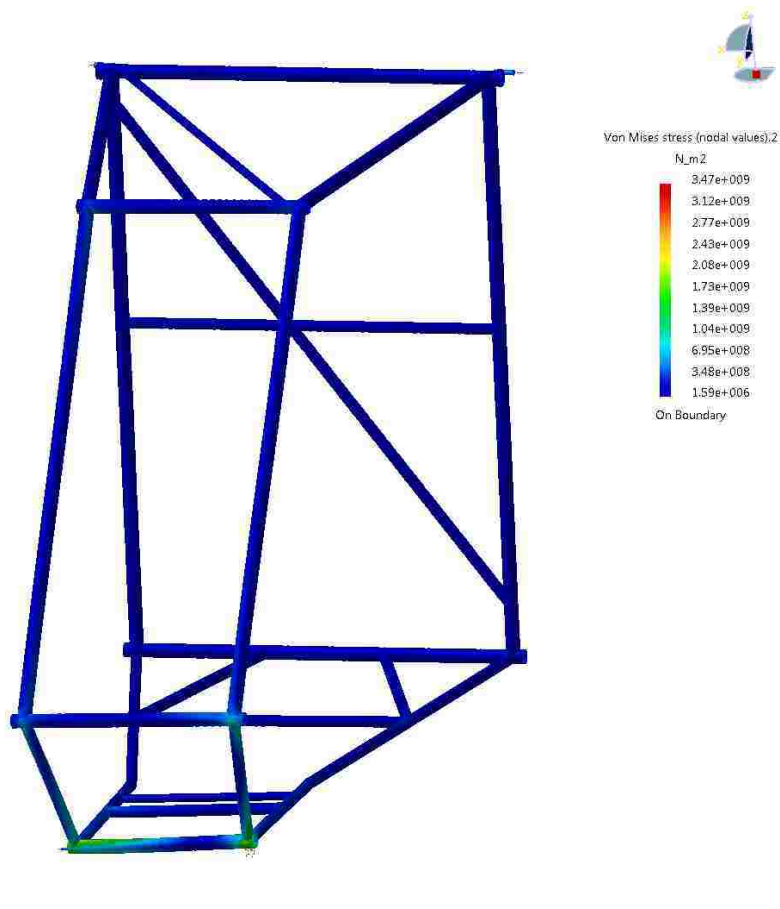


Figure 3.22 Stress contours in static analysis

It is worth mentioning that the frequency extraction was run using 100 mode shapes which resulted in the range of frequencies shown in table 3.4.

Table 3.4 Number of modes and corresponding natural frequencies

Number of modes	Frequency (Hz)
1	37.61
2	50.37
3	56.18
4	67.59
:	:
:	:
98	939.71
99	951.36
100	953.86

Finally, by selecting the frequency analysis as a base for the modal superposition cases, the transient dynamic analysis was run. Keep in mind for applying the dynamic load, a time modulation curve is needed to apply the magnitude of the static load with reference to time. It takes 0.022 seconds for the Mini-Baja frame to pass over the defined bump based on assumptions discussed in section 3.4.2. The time modulation of the applied load is shown in figure 3.23.

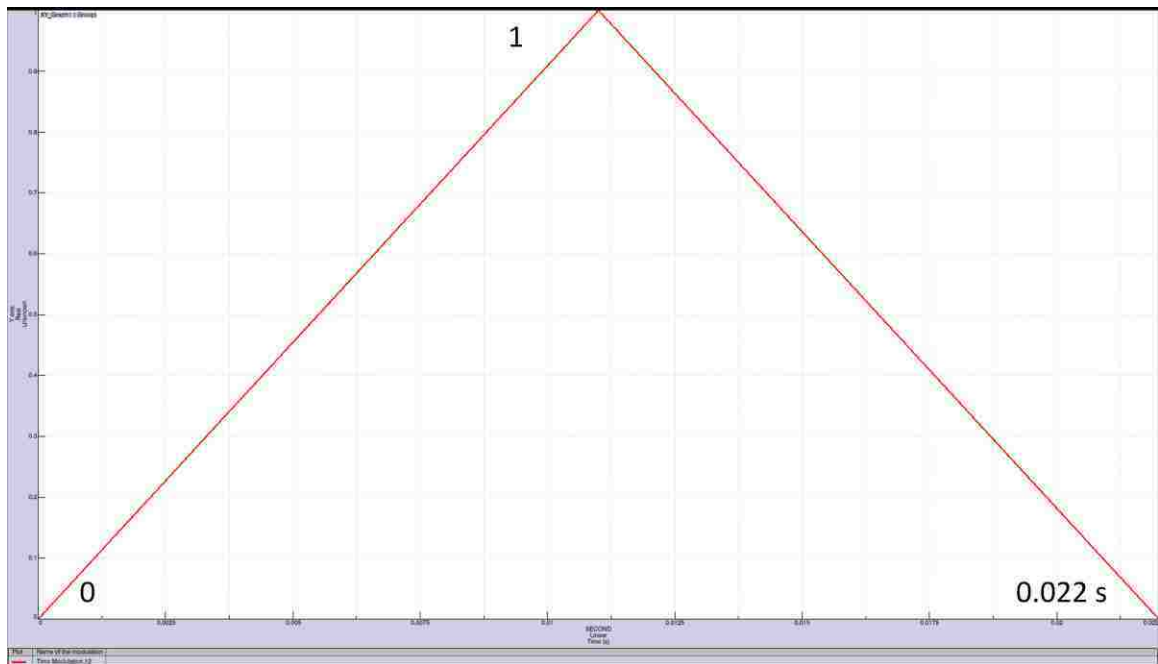


Figure 3.23 Time modulation of the dynamic applied load

The maximum displacement of the frame occurred at the time 0.0135 seconds as expected. This time corresponds to a location where the maximum amplitude of the dynamic load was transmitted to the frame. As shown in figure 3.24, the frame was displaced almost 60 millimetres in the global coordinate system.

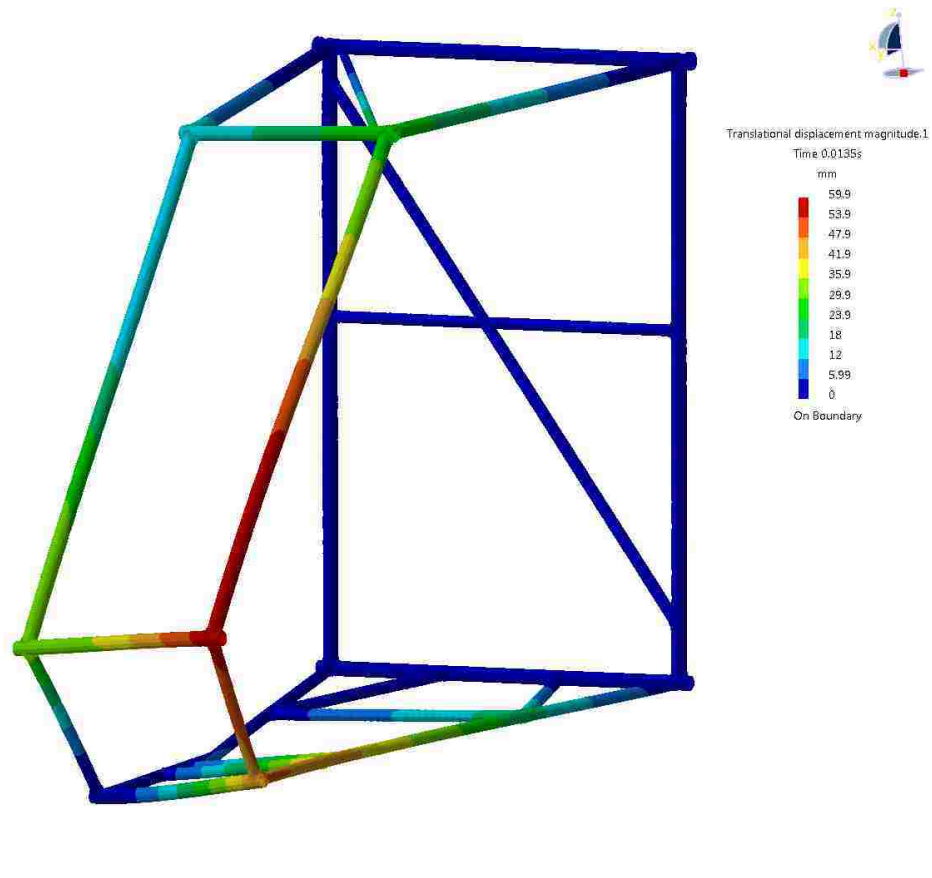


Figure 3.24 Maximum displacement of the frame at 0.0135 sec in dynamic analysis

A node exactly under the location of the applied load was chosen to plot the displacement graphs. The selected point is shown in figure 3.25 with a red dot.

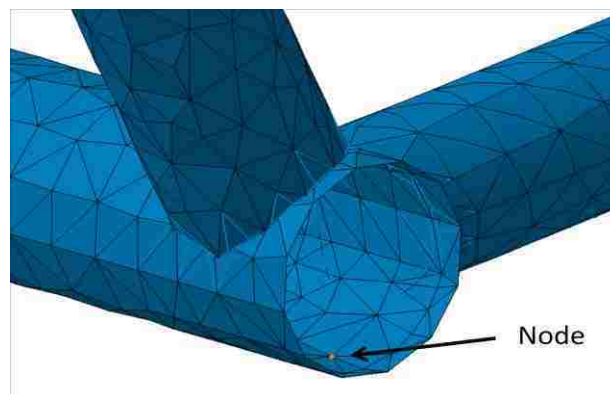


Figure 3.25 Node for displacement graphs

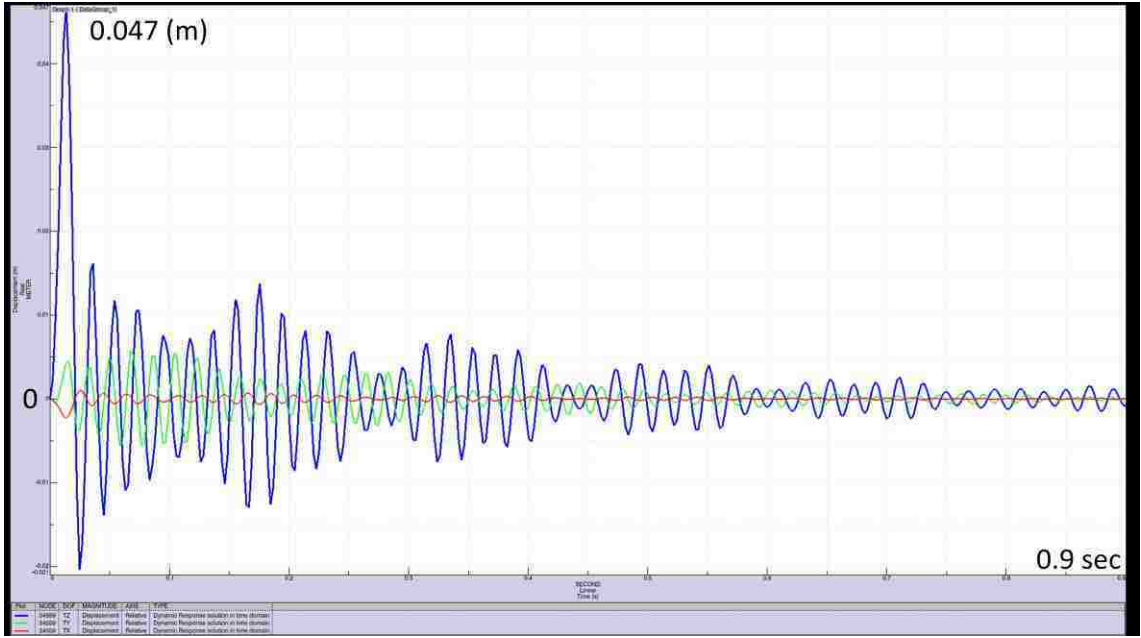


Figure 3.26 Three components of the displacement response of the selected point for the time duration of 0.9 sec

Although the duration of the applied load was 0.022 seconds, in order to get the full response of the frame, the simulation was run for 0.9 seconds.

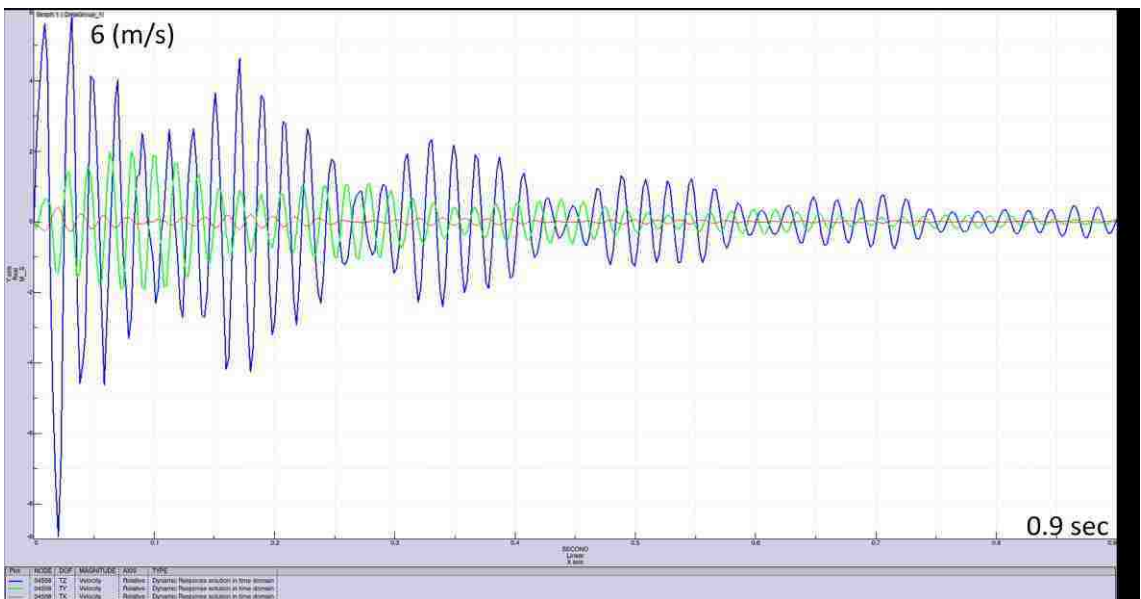


Figure 3.27 Three components of the velocity response of the selected point for the time duration of 0.9 sec

Figures 3.26 and 3.27 indicate that the response of the frame to dynamic loading is being damped due to 1% critical damping applied to all the modes of the system. As previously shown in figure 3.16, this type of response is very common in transient dynamic analyses since the inertia effects and damping effects are significant.

The distribution of the von Mises stress through the cage is shown in figure 3.28. It is noted that the maximum magnitude of the stress corresponds to the time 0.0135 seconds, exactly after the peak of the load was transmitted.

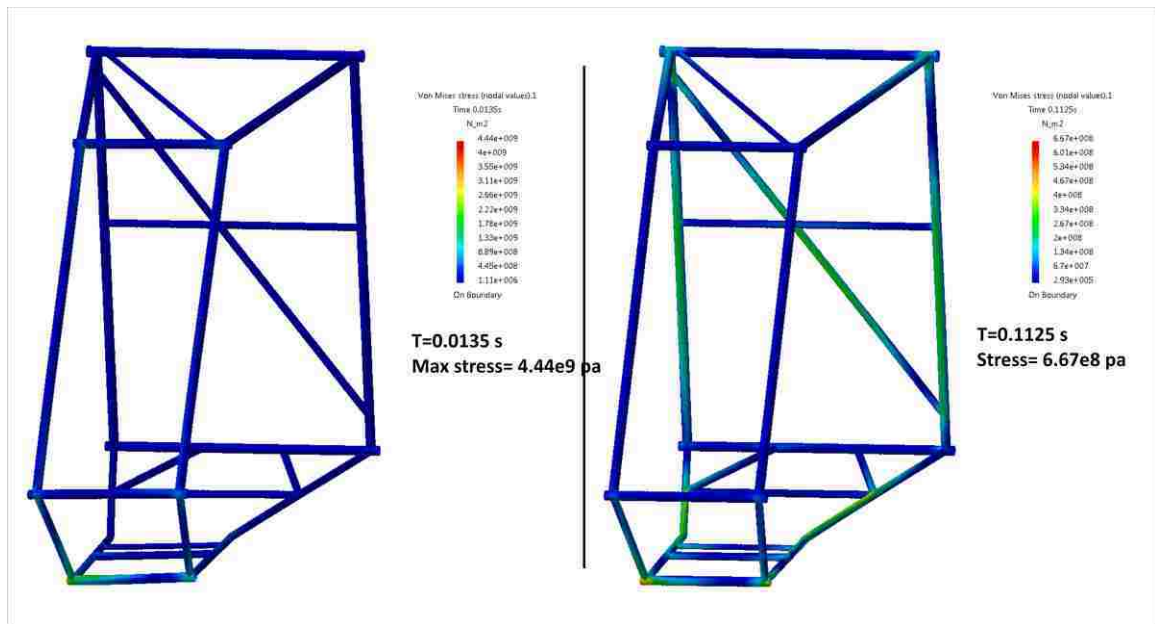


Figure 3.28 Distribution of von Mises stress through the cage in time

As mentioned earlier in section 3.4, the modal superposition procedure uses the frequency extraction to solve the dynamic response of structures. The computational effort involved in obtaining the response by modal superposition method is relatively small, especially when compared to the cost of direct integration of the governing equations used for general analyses. The term “direct” means that prior to numerical integration, there is no transformation of the equations into a different form. On the other hand in modal superposition, the equations of motion are transformed to the modal coordinates and the Duhamel integral is used for integration purposes.

The central difference method (explicit) and Newmark method (implicit) are two numerical methods used for direct integration of the equations of motion in time. In following chapters the application of the central difference method is employed for the non-linear response of the Mini-Baja vehicle.

3.5 Mesh convergence study

Mesh size has an important role in both convergence and accuracy of the numerical solution. Generally speaking, a finite element model with a finer mesh produces more accurate results, but can be computationally expensive. This means that the numerical simulation with a single run, regardless of the mesh size, provides no information on the accuracy and correspondingly element size of the model [31]. Hence, mesh convergence studies were performed to obtain a suitable mesh size.

Based on this method, a sequence of simulations was run for the static analysis of the shell Mini-Baja model for obtaining an acceptable mesh size. The convergence study was performed based on both maximum displacements and stresses variation in the cage. Initially a coarse mesh of 17 mm was used to study the effects of the frontal static loading on the frame. The mesh size was reduced further to 14 mm, 12 mm, 10 mm, 8 mm, 6 mm, 4 mm, 2.5 mm (the size used in the static analysis; section 3.2), 1.5 mm, and 1 mm. The results obtained from each mesh size are compared in table 3.5.

Table 3.5 Variation of maximum displacement and stress due to change in shell element size

Number	Mesh size (mm)	Number of elements	Max. stress (pa)	Max. disp. (mm)	Computation time
1	1	3,570,600	2.01E+10	112	1.5 hour
2	1.5	1,478,700	1.72E+10	109	50 min
3	2.5	603,200	1.32E+10	108	10 min
4	4	225,079	9.92E+09	105	7 min
5	6	155,000	8.98E+09	104	4 min
6	8	57,800	4.11E+09	78	2 min
7	10	39,631	2.32E+09	66	1 min
8	12	30,712	2.31E+09	62.9	1 min
9	14	26,101	1.72E+09	43.3	5 sec
10	17	17,757	9.47E+08	31.8	5 sec

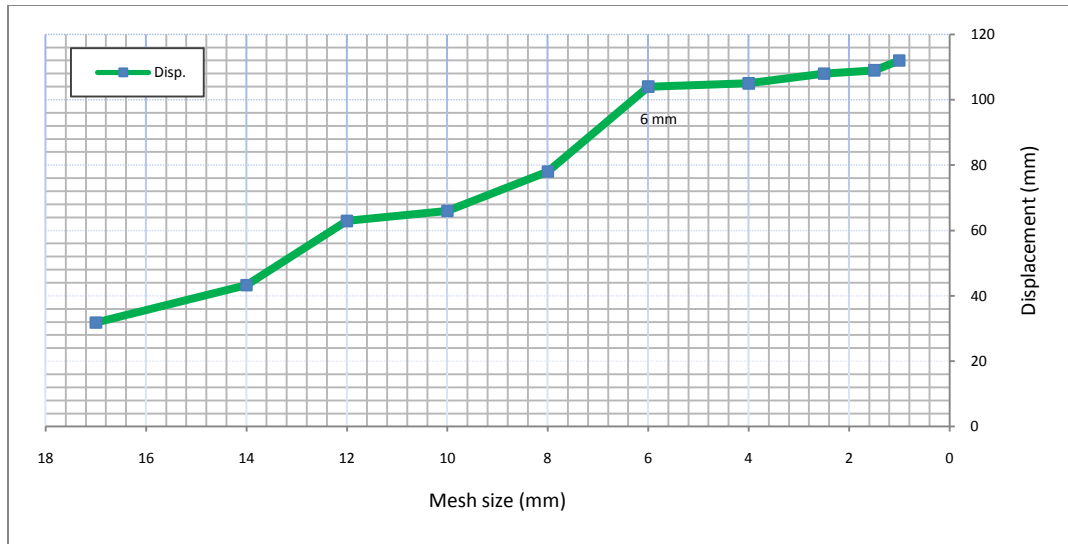


Figure 3.29 Mesh convergence study for maximum displacement

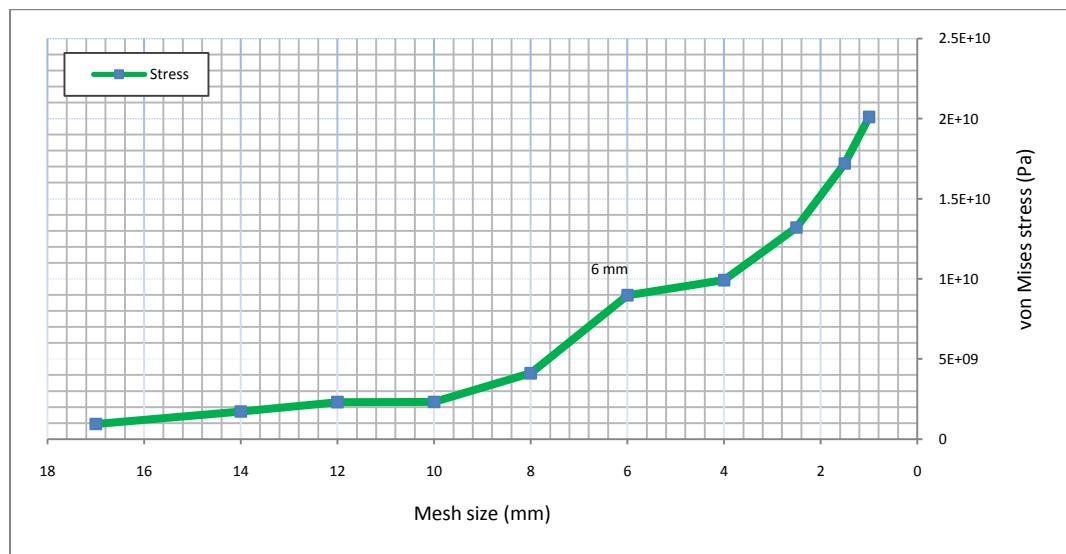


Figure 3.30 Mesh convergence study for maximum stress

Figure 3.30 plots the trend in maximum von Mises stress as the element size decreases to 1 mm. It is known that displacements converge faster than stresses, which can be observed by comparing figures 3.29 and 3.30. However the second entity is more important on this issue and obviously the curve in figure 3.30 has not converged to an acceptable value. Therefore, a number of selected critical points were chosen in the model for further mesh convergence study for a more reliable element size based on stress values.

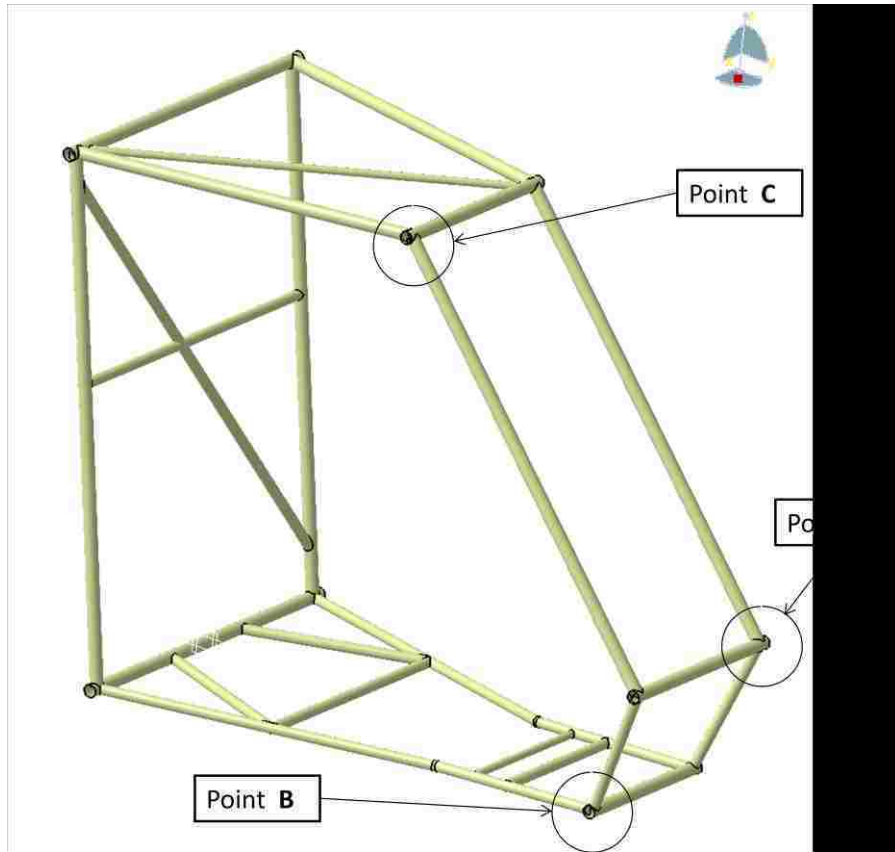


Figure 3.31 Selection of points for the mesh convergence study

By knowing that the maximum stress is acting on the front member, points A and B were selected at the front portion of the cage. It was understood that the correct application of the welds were significantly dependent on the mesh size at the joints. Therefore, point C was also selected to observe the variation of the stress and displacement at the upper joint. Keep in mind that if tubes are attached perfectly, joints should be able to transmit the displacement behaviour throughout the cage and the correspondingly stress is propagated in members attached by the joints. Upper long members are under considerable bending stress and therefore point C was selected in order to examine the function of the upper joint with respect to mesh size. This examination is presented in table 3.6.

Table 3.6 Displacement and stress at selected points in the frame

mesh size	Displacement(mm)			Stress(Pa)		
	A	B	C	A	B	C
1	106	101	2.51	6.04E+09	9.64E+09	2.59E+09
1.5	104	99	2.68	5.93E+09	8.95E+09	2.51E+09
2.5	102	97	2.72	5.47E+09	8.82E+09	2.33E+09
4	99	94.7	2.56	5.39E+09	6.84E+09	2.03E+09
6	98	93	2.19	5.40E+09	6.57E+09	1.66E+09
8	74	68	1.06	3.40E+09	1.00E+09	8.15E+08
10	55.9	50.9	2.2	1.28E+09	5.26E+08	4.98E+08
12	55.3	49	4	2.31E+09	4.67E+08	4.66E+08
14	39.6	27.4	16	1.41E+09	4.11E+08	3.38E+08
17	27.4	5.9	31.2	5.10E+07	8.77E+06	1.97E+08

Figure 3.32 indicates that the curve corresponding to the displacement at point C follows a different trend compared to the other points. This is due to the fact that joint C is not capable of simulating the weld connection at large element sizes (more than 12 mm). It is noted that as the elements get finer, the joint is capable of resisting the bending stress but at coarse elements the weld is not functioning accurately and therefore bending will consequently deflect the whole structure resulting in unrealistic amount of displacement at the joint.

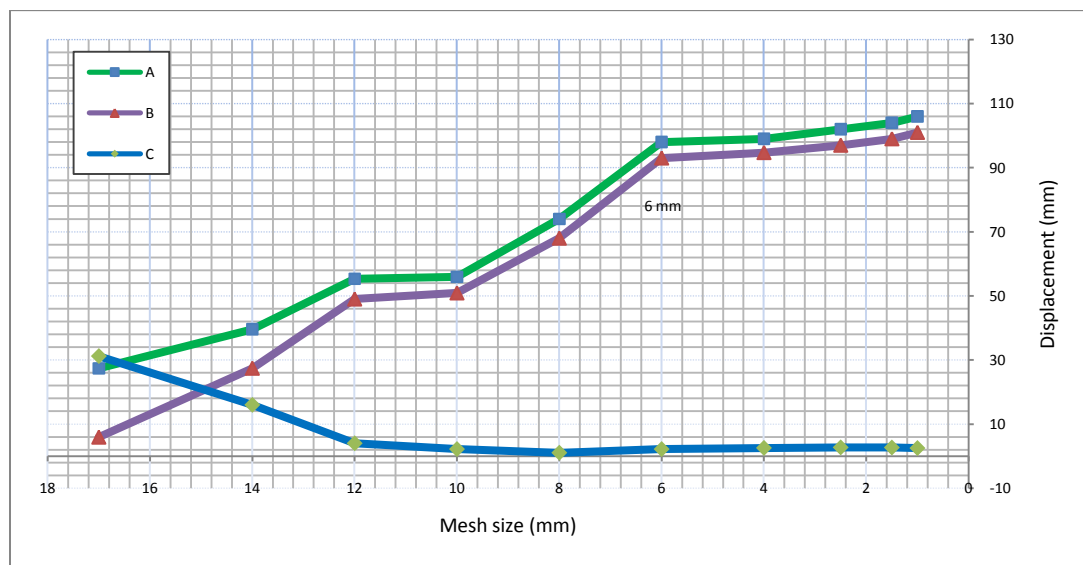


Figure 3.32 Mesh convergence study for displacement at selected points

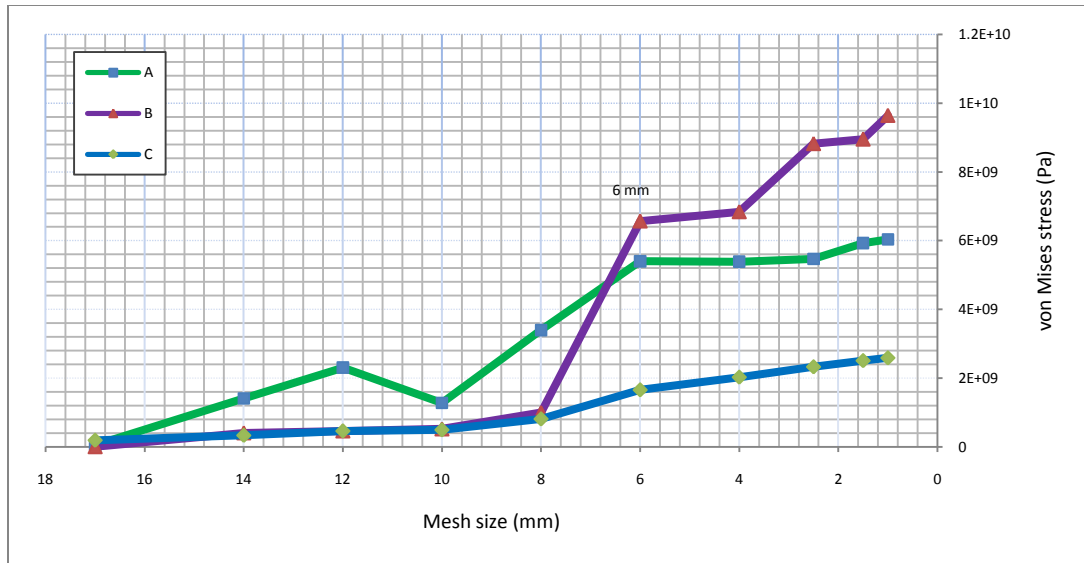


Figure 3.33 Mesh convergence study for stress at selected points

In numerical simulation one key criteria that helps selecting the acceptable mesh size is computational run time versus the mesh size. In figure 3.33 it is noted that when the element size was decreased to 6 mm, the stress curves started to converge and therefore, an element size of 6 mm was selected as a compromise between run time and accuracy. Please note that the computational time given in table 3.5 is only for a static simulation. Therefore, care should be taken since the mesh is being selected for the more computationally expensive explicit non-linear simulations.

CHAPTER IV

NON-LINEAR DYNAMIC ANALYSIS OF THE MINI-BAJA FRAME IN FRONTAL CRASH (LS-DYNA)

4.1 Objectives and overview of Chapter IV

In this chapter, first some key parameters that directly affect the non-linear dynamic analyses and correspondingly the behaviour of a structure to an impact scenario are discussed briefly. Furthermore, the mock-up of the Mini-Baja frame is completed with the addition of necessary structural members in the cage. Moreover, some important aspects and issues that arise in interpreting the results of non-linear explicit finite element simulations are discussed in detail. The finite element software LS-DYNA was used for the analysis of the Mini-Baja vehicle in a frontal impact scenario.

The LS-DYNA program was first developed at Lawrence Livermore National Laboratory by John Hallquist. In 1989, he founded the company Livermore Software and Technology, which markets the program.

Initially, the program had non-linear explicit dynamic capabilities only, which were used primarily for crashworthiness, sheet metal forming and prototype simulations such as drop tests. Hallquist quickly added a large range of capabilities, such as static analysis, heat transfer, and fluid solid interaction [3].

Some of the key factors in the success of the DYNA codes were the development of contact-impact interfaces, the degree of vectorization, and the use of one-point quadrature elements. The latter issue has become somewhat irrelevant with the new generation of computers, but this combination enabled the simulation with models of substantial size to make full scale simulation of problems, such as a full scale car crash, feasible [6].

The frame of any structure is the “skeleton” of the vehicle. In the case of Mini-Baja, the roll cage provides a framework to protect the driver from injuries. In the event

of accident and collisions, the roll cage is designed to absorb as much of the inertia as possible to decrease the impact of the collision to the driver.

It is understood that vehicle crashes are highly non-linear dynamic events and therefore a great amount of computational time is needed to simulate a real vehicle accident. Hence, before jumping into modeling the whole frame, first the front portion of the vehicle was assembled for a frontal crash. A consistent set of units were used for all the numerical models in this thesis. Calculations are based on mass in kg, time in sec, length in mm, and the rest of the units will derive from this base units. Therefore, stress will be in $\text{kg}/(\text{mm} \cdot \text{s}^2)$ or KPa, force will be in $(\text{kg} \cdot \text{mm}/\text{s}^2)$ or mN and work will be in $(\text{kg} \cdot \text{mm}^2/\text{s}^2)$ or μJ .

4.2 Key parameters of a non-linear explicit vehicle simulation

Progressively through this thesis, to account the non-linear behaviour of the Mini-Baja frame, more complexity is being incorporated to the model in terms of material, contact, and other simulated related parameters. The purpose of this gradual progression is to develop a more realistic response of the Mini-Baja vehicle in the frontal crash scenario.

As the starting point on this issue, various technical information and recent modeling complications were studied closely to better understand the difficulties both in modeling and simulating of non-linear vehicle's finite element models. Therefore, in this section some general information of important aspects of non-linear vehicle's finite element models are briefly discussed.

4.2.1 Implicit vs. explicit time integration methodologies

For many analyses it is clear whether implicit or explicit schemes should be used. Implicit is more efficient for solving smooth non-linear problems. On the other hand, explicit is the clear choice for complex non-linear analyses. There are, however, certain static or quasi-static problems that can be simulated well with either algorithm. Typically, these are problems that usually would be solved with implicit schemes but may have difficulty converging because of contact or material complexities.

The explicit integration method solves for the unknown values of displacement, velocity and acceleration at each new time ($t + \Delta t$) using the known values at time (t) as the initial condition. The implicit integration method on the other hand solves for the unknown values at each new time ($t + \Delta t$) using data at time (t) and time ($t + \Delta t$). For a multi-degree of freedom system, implicit scheme require more computational time at each time step compared to explicit scheme [5].

Whereas implicit scheme uses iteration to determine the solution to a non-linear problem, explicit scheme determines the solution without iterating by explicitly advancing the kinematic state from the previous increment [5]. Even though a given analysis may require a large number of time increments using the explicit method, the analysis can still be more efficient than the implicit scheme, because each iteration in implicit scheme requires the solution to a large set of linear equations.

Another advantage of explicit algorithm is that it requires much less disk space and memory than implicit scheme for the same simulation [8]. For problems in which the computational cost of the two programs may be comparable, the substantial disk space and memory savings of explicit method makes it the method of choice.

Using the explicit method, the computational cost is proportional to the number of elements and roughly inversely proportional to the smallest element dimension. The comparison between the computing cost of implicit and explicit method is given in figure 4.1 [8].

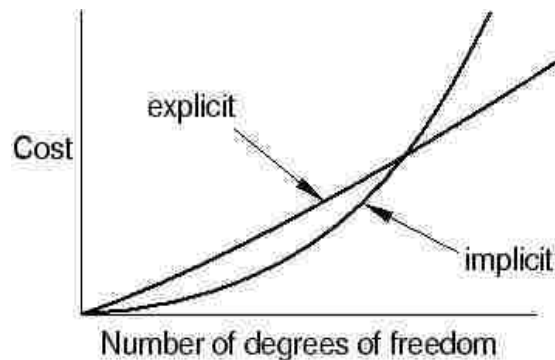


Figure 4.1 Cost versus model size in explicit and implicit methodologies [8]

4.2.2 Viscoplastic material model

Material properties of the 4130 chromoly tubes were described for an elastic condition in section 3.2.1. But, as a vehicle undergoes a plastic deformation process where structural steel deforms under different strain rates, an appropriate material model which takes both plasticity and rate effects into account has to be chosen for the numerical model. Material model 24 from the material library of LS-DYNA which is the most commonly used strain-rate dependent material model in automotive impact engineering (MAT_PIECEWISE_LINEAR_PLASTICITY; elasto-plastic material) was chosen for this numerical simulation.

The curve for plastic behaviour in LS-DYNA plasticity model should be the residual true strains after unloading elastically. This conversion is schematically shown in figure 4.2 and the expression is presented in eq. (4-1). It is shown in figure 4.2 that while the structure has been recovered elastically e^e , the plastic strain e^p remains as a permanent strain due to the plasticity of the material; $e = e^e + e^p$.

$$\text{Effective plastic strain (input value)} = \text{total true strain} - \text{true stress}/E \quad (4-1)$$

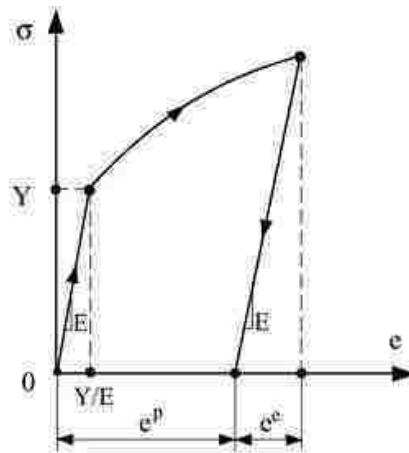


Figure 4.2 Determination of effective plastic strain

The curve shown in figure 4.3 describes the plastic behaviour of the 4130 chromoly that has been inputted to the software.

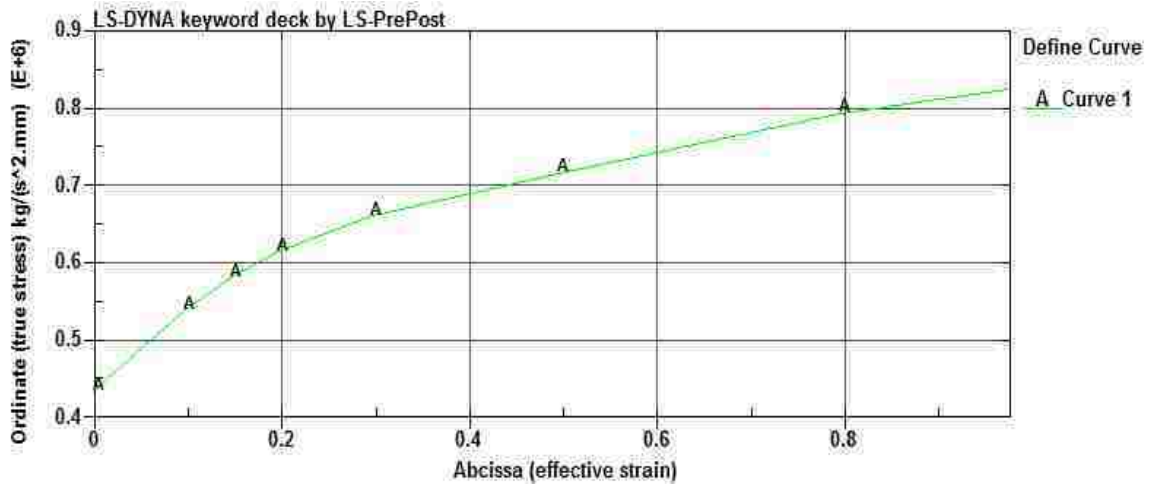


Figure 4.3 4130 chromoly plastic behaviour

When using MAT_24, one should input a smooth stress-strain curve utilizing a minimal number of points. Input of noisy non-linear data may cause unstable behaviour. Full iterative plasticity has been invoked for shells, by setting appropriate commands in CONTROL_SHELL keyword card.

Viscoplasticity is a theory in continuum mechanics that describes the rate-dependent inelastic behaviour of solids. In this context “rate-dependence” means that the deformation of the material depends on the rate at which loads are applied. To display what is happening in rate-dependant material models, figure 4.4 is provided. To explain the stress-strain behaviour shown in blue in figure 4.4, the material at first is loaded at a strain rate of 0.1/s. The strain rate is then instantaneously raised to 100/s and it remains constant at that value for some time. At the end of that time period the strain rate is dropped back to 0.1/s and the cycle is continued for fluctuating values of strain. This behaviour is displayed for the response of the material between just two corresponding strain rates. To fully define this behaviour, a model with plasticity that has a rate-dependent stress-strain curve should be incorporated. It is clear that without incorporation of appropriate strain rate dependency into the material model the stress distribution can be inaccurate.

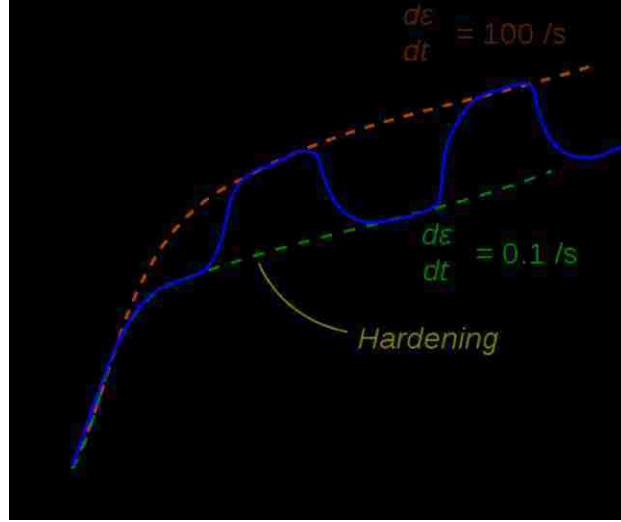


Figure 4.4 Stress-strain response of a viscoplastic material at different strain rates [39]

Strain rates are accounted by using the Cowper-Symonds strain rate term with parameters of C and P considered as 40.4 and 5 respectively (these constants can be functions of temperature and possibly other predefined state variables of a material). There are three options available to account for the strain rate dependency with material 24. The first option is when the viscoplastic formulation is off and the yield stress is scaled with term [30]

$$\sigma_y = \left[1 + \left(\frac{\dot{\epsilon}}{C} \right)^{1/p} \right] \cdot \text{SIGY} \quad (4-2)$$

Here σ_y is the yield stress, SIGY is the initial yield stress, $\dot{\epsilon}$ is the strain rate, c and p are Cowper-Symonds strain rate parameters. If the viscoplastic option is active then the yield stress is computed from [30]

$$\sigma_y(\epsilon^p_{\text{eff}}, \dot{\epsilon}^p_{\text{eff}}) = \sigma^s_y(\epsilon^p_{\text{eff}}) + \text{SIGY} \cdot \left(\frac{\dot{\epsilon}^p_{\text{eff}}}{C} \right)^{1/p} \quad (4-3)$$

where σ_y is the dynamic yield stress, σ^s_y is the static stress which is inputted as a curve, and SIGY is the initial yield stress which is multiplied by the Cowper-Symonds rate term.

The third option is a more general approach where the rate effects can be accounted for by defining a table of curves (LCSS) as shown in figure 4.5. Each curve is specified for a particular strain rate. In this thesis the first option (eq. (4-2)) were used to account for the strain rates.

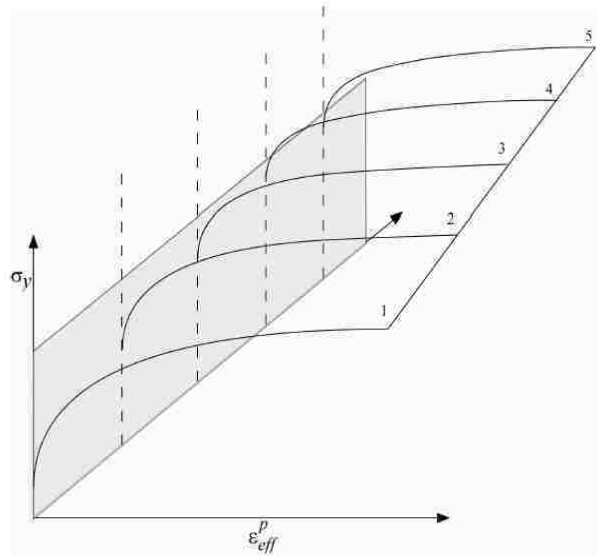


Figure 4.5 Yield stress vs. effective plastic strain at different strain rates [30]

4.2.3 Shell elements and B-L-T element

Shell elements can be regarded as plate bending elements combined with plane membrane elements. That is, a shell carries load both in the plane (membrane forces), and perpendicular to the surface. Shell problems generally fall into one of two categories: thin shell problems and thick shell problems. Thick shell counts the effects of transverse shear deformation whereas thin shell neglect it ($\gamma = 0$).

Membrane element by definition cannot have rotational degrees of freedom. It can only have translational degrees of freedom as needed. Therefore, only in-plane stiffness is formulated. Very small out-of-plane stiffness will be applied just to provide stability on the element. Consequently, only in-plane forces (membrane forces) are admissible, refer to figure 4.6.

Plate element does not account for the out-of-plane rotational degree of freedom. The other rotational degrees of freedom can be applied in the plane of the element. Nodal forces, nodal moments (except when about an axis normal to the element face) are supported.

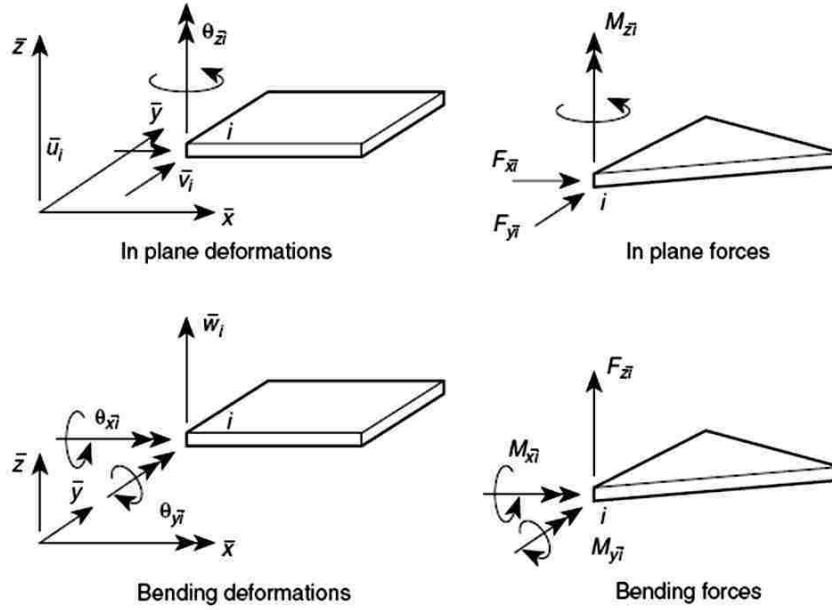


Figure 4.6 A representation of membrane forces on a membrane element and bending moments on a plate element [40]

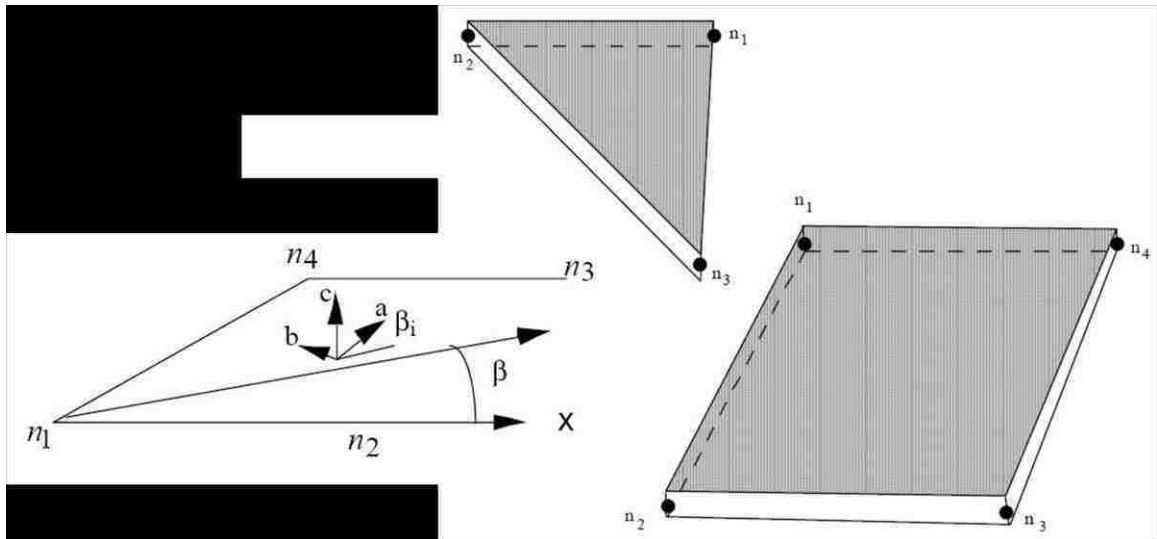


Figure 4.7 LS-DYNA shell elements, node numbering for normal direction [30]

The stresses are calculated as a superposition of membrane forces and bending moments. For a linear elastic thin shell the normal forces are independent of z and the bending stress varies linearly with z ; $\sigma_i = \frac{N_i}{t} + \frac{12M_i z}{t^3}$ [41].

Stresses are evaluated at so called integration points within the element. An element needs 4 integration points to be fully integrated. Elements with less integration points are called under-integrated. At every integration point a number of integration points through the thickness can be used to describe the non-linear behaviour of stress variation. Furthermore, as the number of integration points through the thickness increases, a more accurate stress can be determined through the thickness. Keep in mind that acceleration, velocity and displacements are evaluated at nodal points, but stress and strains are evaluated at integration points.

The most frequently used shell element in impact engineering is the so called Belytschko-Lin-Tsay (B-L-T) element. It was first implemented in LS-DYNA as a computationally more efficient element comparing to Hughes elements. It is considerably more efficient than the other types of shells and this advantage depends on several mathematical simplifications [42]. However, because of these simplifications, it has some disadvantages. It loses stiffness considerably when it is warped and it is therefore not appropriate for analysing warped structures. But yet, has proven to be fairly accurate in crash worthiness applications [42]. Element formulation 16 in LS-DYNA is the fully integrated option of it. For warped B-L-T shells, shown in figure 4.8, warping stiffness has been added to warped elements by setting appropriate command in CONTROL_SHELL keyword card.

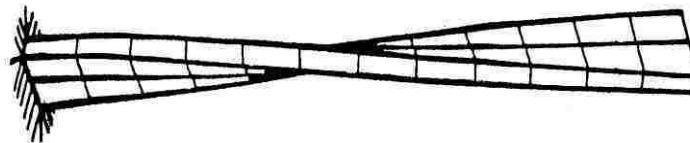


Figure 4.8 Representation of warped shell elements [42]

4.2.4 Hourglass energy modes

Since only one integration point in the plane of B-L-T is used, zero energy modes may occur. Zero energy modes are also known as “hourglass” modes because of their shapes. Two typical hourglass modes are shown in Figure 4.9 (b).

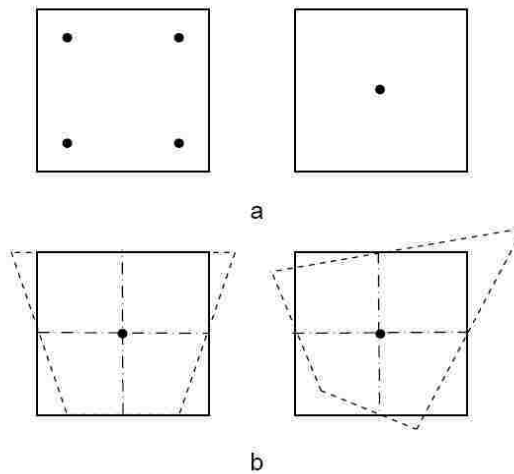


Figure 4.9 a) A fully integrated element to the left and a under integrated element to the right; b) Two hourglass modes for the under integrated element [41]

Since the strain is only evaluated in one point, it is possible that no strains occur in that point as shown in figure 4.9. Therefore, the strain energy of the element is zero even though the element is considerably deformed which is an unrealistic situation. For a fully integrated element, the hourglass effect will not be present since it has sufficient number of integration points in element formulation.

After any FE analysis, it is essential to check the hourglass energy. One way to see if the model is accurate is to compare the hourglass energy with the internal energy. It is known that the ratio should be less than 10%; otherwise, the hourglass energy is excessive.

An element formulation of higher degree can affect the critical time step of the analysis considerably, and therefore fully integrated element formulation is rarely used in an explicit finite element solver. Therefore, the hour glassing control must be addressed.

Next two common approaches to combat zero energy modes (hour glassing) are mentioned;

- An hourglass force can be added to the equation of motion in LS-DYNA to control the formation of zero energy modes. Forces are applied to nodes to eliminate hourglass deformation shapes. Depending on the physics of the problem hourglass forces can be the function of displacement (stiffness form) or velocity (viscous form).
- The other option is to carefully use the fully integrated element formulation in critical regions. Keep in mind that this approach is more complex since it needs localized sectional properties.

Application of different methods used to control zero energy modes are compared and discussed later in this chapter.

4.2.5 Time step and mass scaling

The time step of an explicit finite element analysis is determined as the minimum stable time step in any deformable element of the mesh. In general, the Courant-Friedrichs-Lewy (CFL) condition given in eq. (4-4) [20] is a necessary condition for stability. As a consequence, the time step must be less than a certain value in explicit computer simulations; otherwise the simulation will produce incorrect results.

$$\Delta t \leq \frac{L_c}{c} \quad (4-4)$$

Where L_c the characteristic length and c is the sound speed in the material. This equation roughly corresponds to the transient time it takes for an acoustic wave to propagate through an element using the shortest characteristic distance. Physically, this requires that the numerical time step be smaller than the time needed by the physical wave to cross the element. The CFL condition thus tells us that we cannot numerically calculate the effects of a stress wave in locations physically unreachable in the elapsed time [20].

During the solution one loops through the elements to determine a new time step size by taking the minimum value over all elements [30];

$$\Delta t^{n+1} = \text{TSSFAC} \times \min \{ \Delta t_1, \Delta t_2, \Delta t_3 \dots \Delta t_n \} \quad (4-5)$$

Where n is the number of elements, TSSFAC is a fudge factor for stability reasons (default in LS-DYNA =0.9)

For beam and truss elements, $c = \sqrt{\frac{E}{\rho}}$ and therefore, Time step in beams are evaluated by; $\Delta t_{\text{critical}} = L_c \cdot \sqrt{\frac{\rho}{E}}$ (4-6)

For other elements refer to [30] for more information on L_c in two and three dimensional elements.

It can be seen in eq. (4-6) for beam elements, and consequently for shell and solid elements that the time step of an explicit simulation is a function of density.

LS-DYNA allows increasing the minimum stable time step by adding virtual mass to those critical elements which decreased the time step. This is called mass scaling and is routinely used to control the time step and to reduce computational time in crash simulations. This additional mass may be up to 2-7% without introducing unfavourable mass effects and can be justified by looking at the energy balance of the system.

4.2.6 Contact and friction modeling

In dynamic finite elements, particularly when used for crash modeling, deformations are much larger than those typically seen in static analysis. Accurately modeling the contact within a structure needs describing the inter-part contact between different parts of the model as well as intra-part contact when a part buckles in upon itself.

For a complicated model with many parts, such as a full vehicle model, the automatic contact algorithms are preferred. As the structure collapses, the contact table is periodically updated at each time step. In the case of a penalty-based contact, when a

penetration is found a force proportional to the penetration depth is applied to resist, and ultimately eliminates the penetration as shown in figure 4.10.

The contact force is calculated as $F_N = k\delta$, where k is the stiffness of the spring placed between the slave and master and δ is the penetration distance. The stiffness of the spring for a shell element is given as [37];

$$K = f_s k \frac{A}{L} \quad (4-7)$$

Where $k = \frac{E}{3(1-2\nu)}$ is the bulk modulus, A is the face area of the segment being penetrated, and L is the maximum shell diagonal being penetrated. For shell elements f_s is the scale factor for the interface stiffness [37].

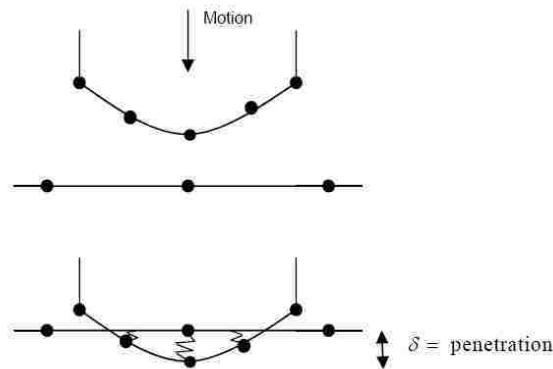


Figure 4.10 Penalty contact algorithm in LS-DYNA [37]

One consequence of assembling a model from many parts is that some initial penetrations can occur; this introduces some initial localized stress. The program can handle small initial penetrations by adjusting the locations of the nodes automatically. But, large initial penetrations, however, can cause the local stresses to exceed the materials yield stress. In these cases, the initial node positions have been readjusted manually.

An automatic `SINGLE_SURFACE` contact algorithm with an automatic `SURFACE_TO_SURFACE` contact which are both a penalty-base algorithms were used to prevent penetration of different parts into one another. To model the weld connection

between tubes a TIED_SHELL_EDGE_TO_SURFACE constraint-base contact definition was used to connect the tubes together.

In figure 4.11 the tied contact algorithm mentioned above is shown. It uses a node set to connect the slave nodes of the blue component to the master segment created on the red component. It will tie both translational and rotational degrees of freedom of the slave nodes to the segment surface, thus allows moments to be transferred.

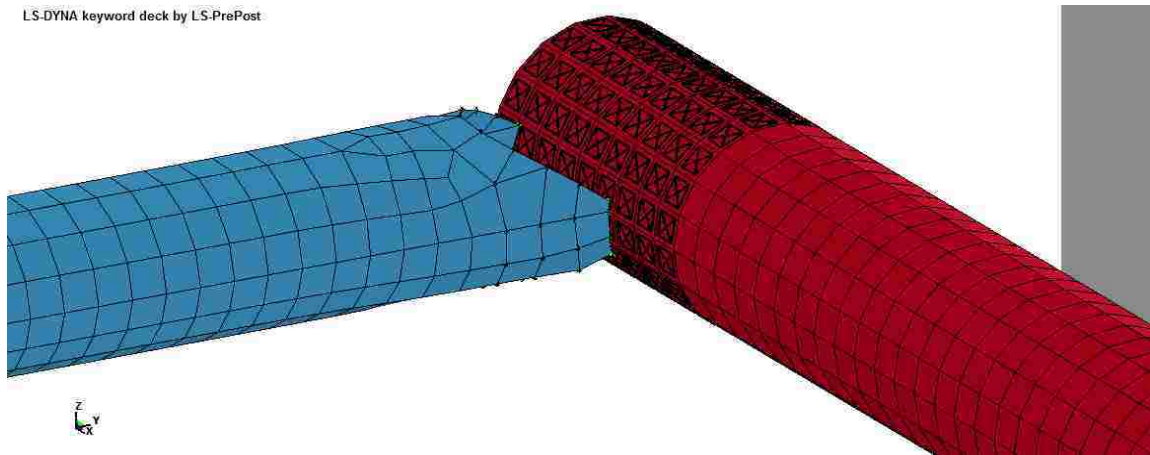


Figure 4.11 Tied contact between tubes

Besides the constrain connection defined to connect the tubes, other contact algorithms mentioned earlier were used to prevent any penetration of parts into each other. For that reason, frictions were an essential parameter to properly define the contact behaviour between parts.

In LS-DYNA the frictional force is given by the equation:

$$F_s = \mu F_N \quad (4-8)$$

Here F_N is the normal force acting on the slave node discussed earlier, and μ is the coefficient of friction, which is computed by the relation; [43];

$$\mu = \mu_d + (\mu_s - \mu_d)e^{-c|v|} \quad (4-9)$$

where, μ_s is the static friction coefficient, μ_d is the dynamic friction coefficient, c is the decay coefficient and v is the relative velocity between the slave node and the master

segment. The decay value determines the rate at which the friction coefficient transitions from μ_s to μ_d .

It is known that the static coefficient of friction should be larger than the dynamic coefficient, and experiences in LS-DYNA [43], suggests using a friction coefficient of about 0.1-0.15. It is also understood that in many crash simulations these values are inputted equally to avoid creation of additional noise in data. Based on the literature covered in crash engineering, as well as trials and errors implemented for this issue on the Mini-Baja crash simulations, values of static and dynamic coefficients were considered as 0.2 and 0.15 respectively. Furthermore, the decay coefficient was also considered as 0.001. For further discussion on friction modeling and friction graphs refer to [43].

The energy associated with the friction forces acting on surfaces in contact is the sliding energy. The sliding energy is the integral of the frictional forces times displacement and is commonly used as a validation metric in most impact type problems [43].

4.3 Simulation of the front portion of the frame (LS-DYNA)

First, the frontal portion of the vehicle as shown in figure 4.12 was subjected to a couple of tests to see the overall response of the structure toward impact. In these series of simulations the speed of the specimen was varied and different techniques were tested to control the accuracy of results regarding computational efficiency. The main objective of these tests was to run a preliminary analysis using explicit code.

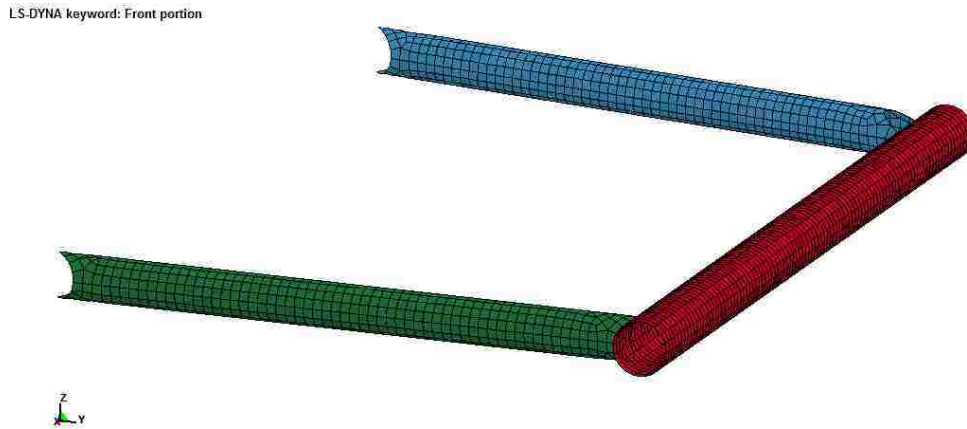


Figure 4.12 Front portion of the vehicle

In figure 4.13, specimens were subjected to impact a rigid wall at different speeds. The one traveling at 150 km/h hits the wall earlier and the amount of plastic strain is 0.7 comparing with the other one traveling at 60 km/h resulting in 0.3 plastic strains.

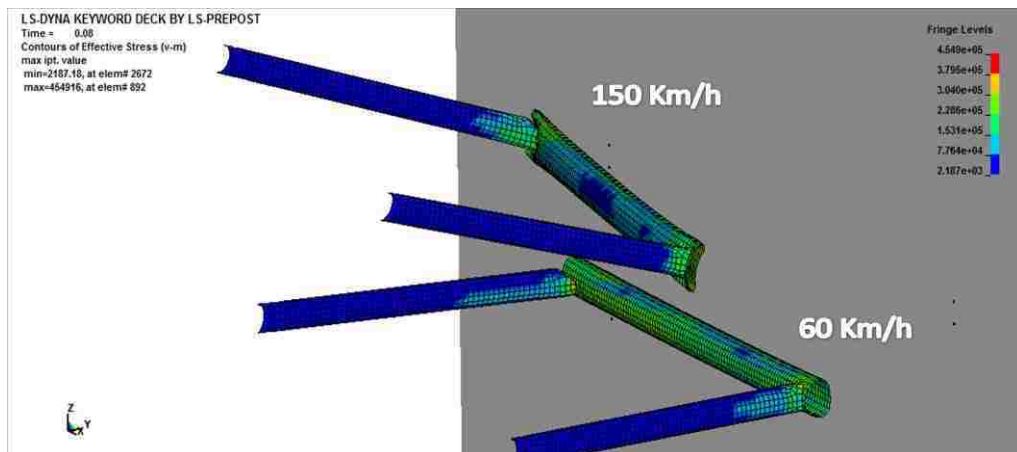


Figure 4.13 von Mises stress at different speeds for the front portion of the vehicle

In order to reduce the hourglass energy in the model, the different techniques which were discussed earlier were applied and the results are presented in table 4.1. The speed of 150 km/h was chosen for these examinations because a more destructive case was needed to be fully confident on the controlling techniques.

Table 4.1 Effect of different hourglass control techniques on accuracy and computational time

Type of model	Hourglass energy (μJ)	Elapsed time
1 Model (under integrated)	8.50E+06	1 min
2 Model (adaptive_2 deg + hourglass control)	1.60E+06	28 min
3 Model (fully integrated ELFORM 16)	0	14 min
4 Model (localized ELFORM 16)	1.85E+06	8 min

It is noted that the first model with under integrated element formulation has the highest amount of hourglass energy present. In order to explore the possibility of reducing this energy, the models 2 through 4 were looked at. First an adaptive mesh shown in figure 4.14 (i.e. based on an angle change relative to surrounding elements in each element to be refined), was implemented with the use of hourglass control (stiffness form) keyword card simultaneously which reduced the hourglass energy to 1.6E+6 μJ in model two. It was already expected that element formulation 16 results in zero hourglass energy since it has fully integrated element formulation. Nevertheless a localized approach of element formulation 16 was also implemented on the fourth model that resulted in much better computational time than in the third model.

LS-DYNA KEYWORD DECK BY LS-PREPOST
Time = 0.02, #nodes=23773, #elem=22438

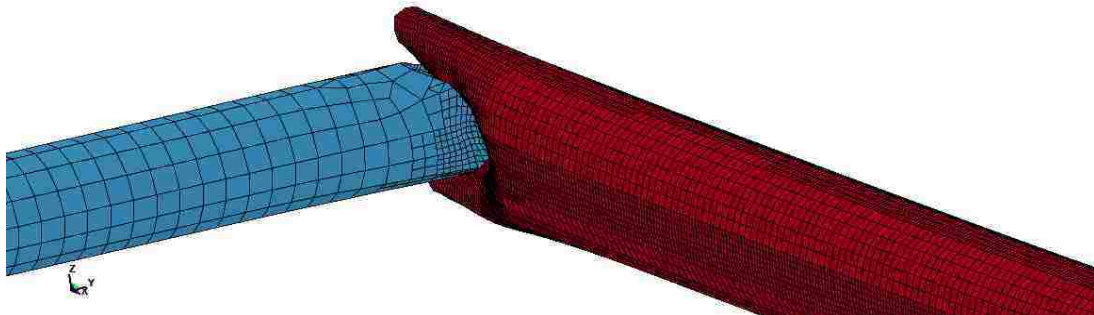


Figure 4.14 Adaptive method applied on the frame

The adaptive method implemented for the frame is a function of number of parameters such as angle change between surrounding elements. To see the effect of the threshold angle, table 4.2 below introduces 4 new models with different angle change varying from 2 to 16 degrees.

Table 4.2 Effect of adaptive method on zero energy modes

Type of model	Hourglass energy (μ)	Elapsed time
5 Model with adaptive mesh_2 deg	4.00E+06	28 min
6 Model with adaptive mesh_8 deg	4.30E+06	4 min
7 Model with adaptive mesh_12 deg	5.00E+06	2 min
8 Model with adaptive mesh_16 deg	5.55E+06	2 min

It is noted that as the number of elements generated due to adaptivity increases, the hourglass energy is decreased. The deformation shapes of the models in table 4.2 are shown in figure 4.16.

All eight models are schematically shown in a bar graph below with regard of hourglass energy.

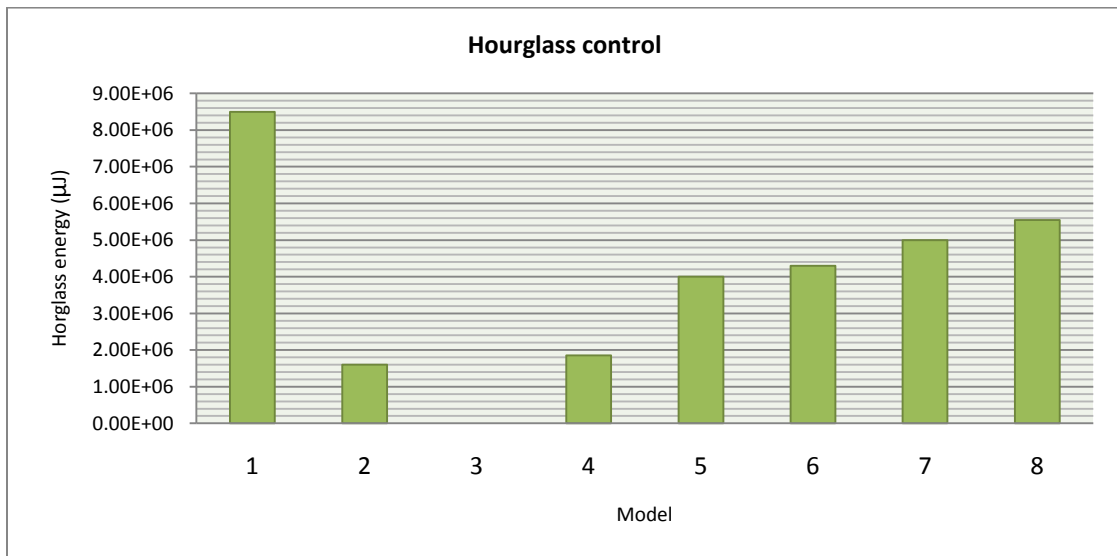


Figure 4.15 Hourglass energy vs. hourglass control models



Figure 4.16 Deformation shape of models with different adaptive refinements (in terms of the threshold angle)

Figure 4.16 shows the deformation shapes of adaptive refinement models; 5 to 8. It was noted that as the amount of elements are increased due to adaptive refinement, the amount of stress and correspondingly plastic strain decreases slightly. To address this change more accurately a new model was proposed and compared to other models in figure 4.17.

In figure 4.17, the deformation shape for model 1, 5, 3 and a new model with both fully integrated element formulation 16 and adaptive refinement method is presented. It is shown that the model with both methods has the lowest amount of deformation among other models. Model 1 is the under integrated model, model 5 is the 2 degree adaptive refinement method and 3 corresponds to fully integrated shell (ELORM 16). This model was proposed to show how these methods of controlling accuracy can misguide the user by producing more stiffness into the model.



Figure 4.17 Deformation vector of 4 different models

Throughout the simulations the total energy was $0.93E+9 \mu\text{J}$ and there was effectively no sliding energy or external work present in the system as shown in figure 4.18. Although the hourglass energy present was just 1% compared to the internal energy, these observations were helpful in both modeling and controlling of the full Mini-Baja chassis analysis. Figure 4.18 shows stable total energy throughout the simulation and reasonable correlation between the kinetic and internal energy.

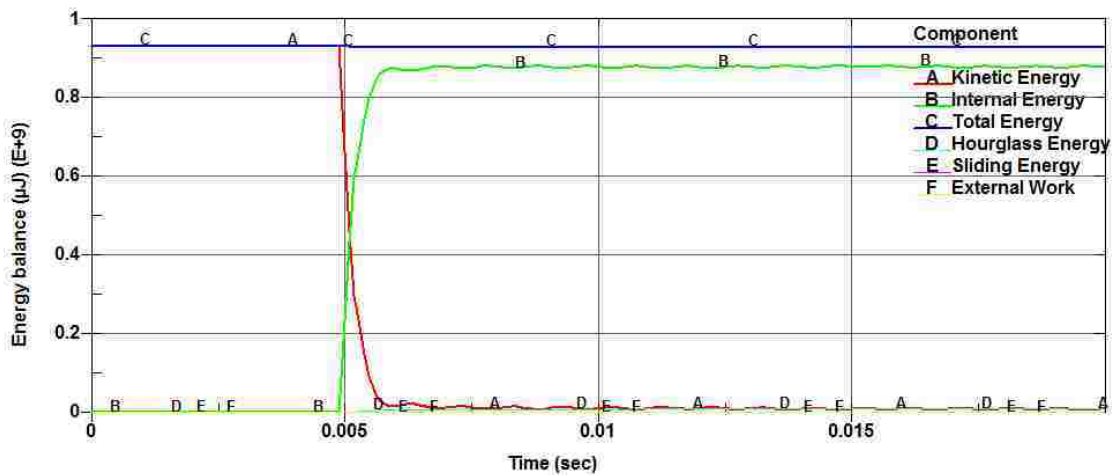


Figure 4.18 Energy balance for front portion at 150 km/h (model 1)

4.4 Frontal impact simulation of the Mini-Baja frame structure (LS-DYNA)

The complete mock-up of the frame was created in Catia. Then the frame was meshed with rectangular elements in LS-PrePost 3.1 with 6 mm element size. Figure 4.19 shows the frame with the added structural members.

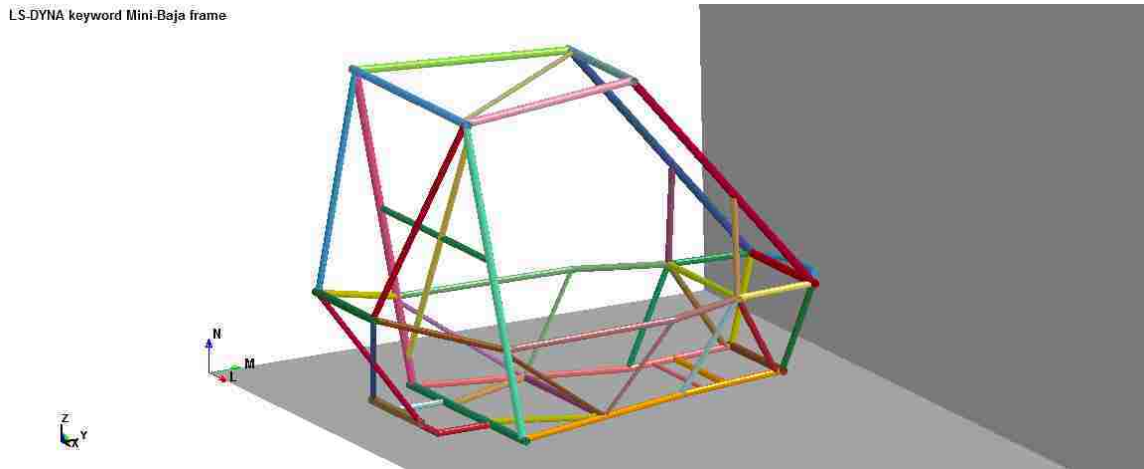


Figure 4.19 Mini-Baja frame structure

In the real Mini-Baja vehicle, there is a 28 kg engine located in the basket behind the frame. In order to account the mass of the engine, non-structural¹ mass has been defined over appropriate members. Current mass of the vehicle with the engine mass added to the structure is 53.6 kg.

Based on literature found from crash agencies, it was understood that the standard impact velocity for frontal rigid barrier crash is 48 km/h (based on NHTSA and NCAC publications and FMVSS NO. 208 standards [44]). Although the velocity was varied in several runs, but in this thesis results are only presented for 48 km/h. Therefore, the frame was subjected to a 48 km/h (13 m/s) initial velocity. Gravity has been incorporated into the model for a more realistic impact scenario.

¹ Non-structural mass distributes a defined mass over a selected part by an area weighted distribution method to all nodes of a given part

The analysis included an initial distance of 130 mm while the vehicle was coasting prior to impact. The purpose of this step was to let the structural members to settle down under the force of gravity.

The simulation was run for 0.045 seconds and the results for von Mises stress and plastic strain are presented in following figures. The frame hits the wall at $t = 0.0109$ sec, and loses contact with the wall and starts moving backward at $t = 0.033$ sec.

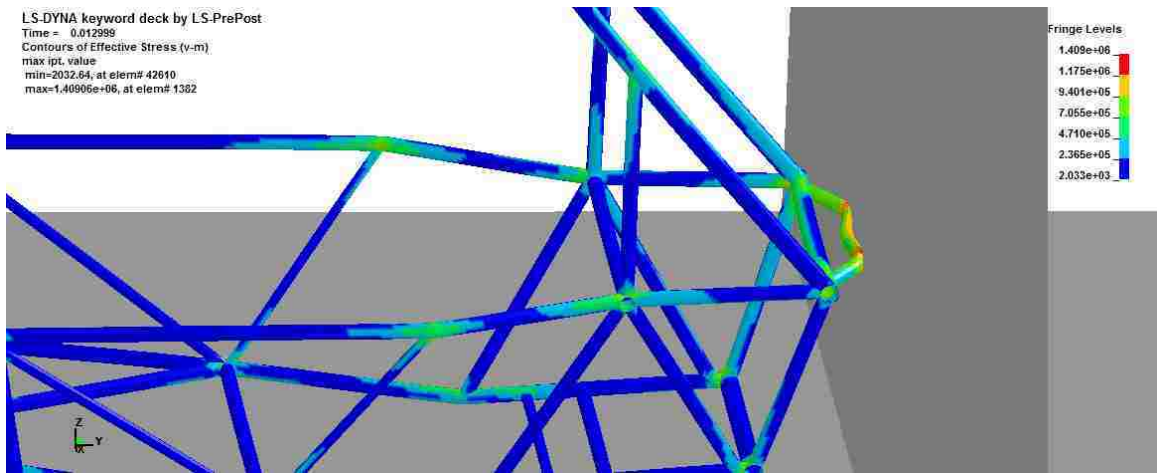


Figure 4.20 von Mises stress at 0.013 sec

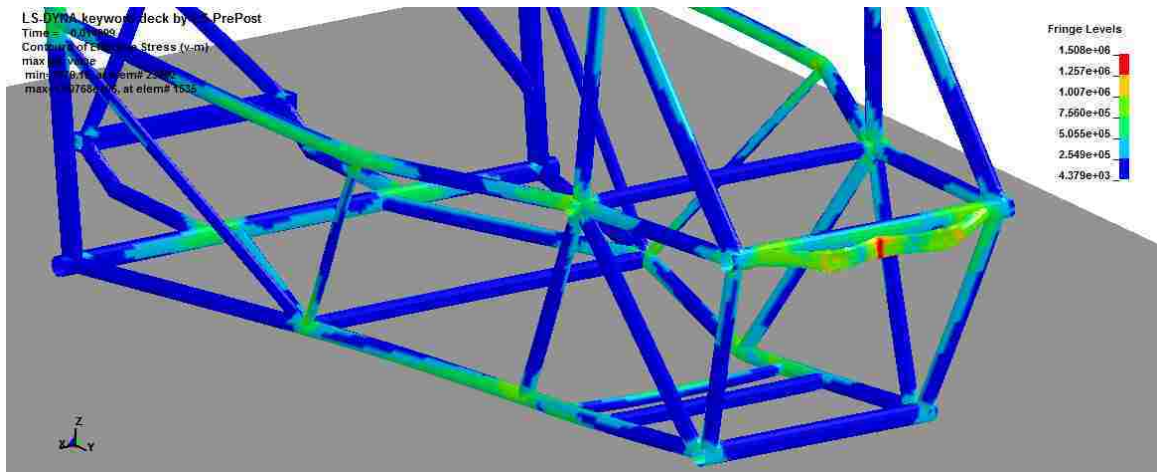


Figure 4.21 Maximum von Mises stress at 0.015 sec

The maximum plastic strain at the end of the simulation is shown in figure 4.22.

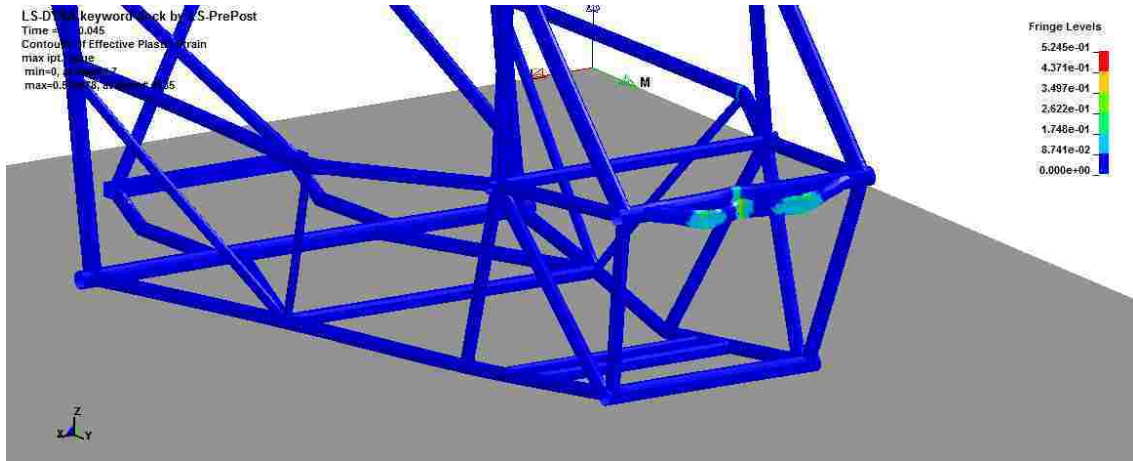


Figure 4.22 Maximum plastic strain at 0.045 sec

In order to show the importance of strain rate effect in a vehicle crash scenario, following figures 4.23 through 4.26 were captured at different instances of the simulation corresponding to different strain rates. It is shown that how this rate is changing rapidly with respect to time. It was observed that the strain rate kept fluctuating as the structure is under deformation where it reaches its highest value of 132/s at 0.014 seconds. After the frame loses contact with the wall the rate goes down from 30/s at 0.03 sec to 2/s at 0.045 seconds. Please note that these values are recorded by the software at the prescribed instances.

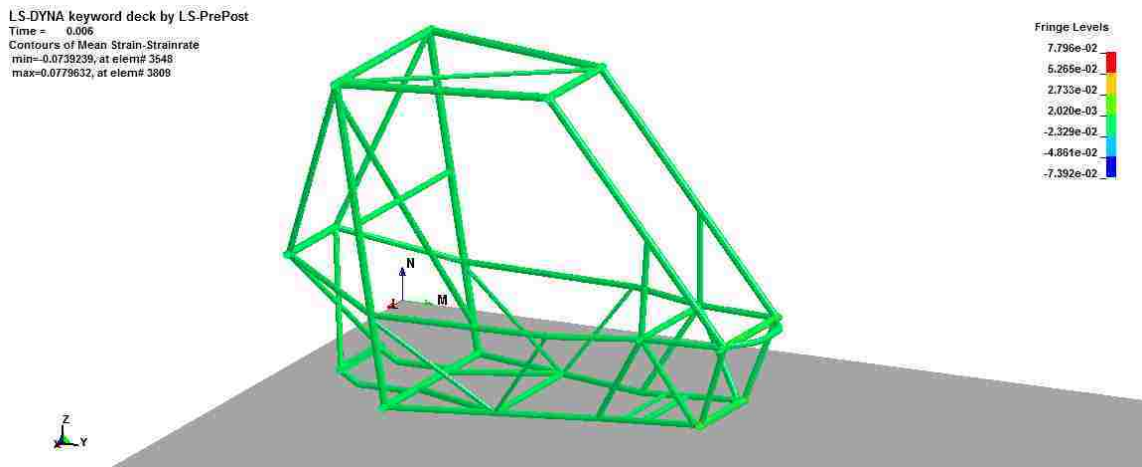


Figure 4.23 Strain rate of 0.08/s at 0.006 sec

LS-DYNA keyword deck by LS-PrePost
Time = 0.010998
Contours of Mean Strain-Strainrate
min=-90.6157, at elem# 1410
max=79.011, at elem# 60127

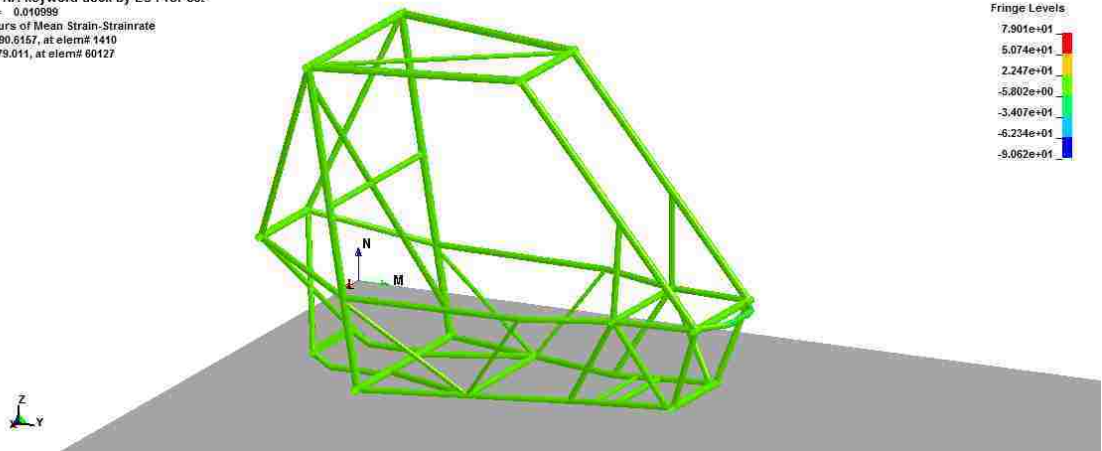


Figure 4.24 Strain rate of 80/s at 0.0109 sec

LS-DYNA keyword deck by LS-PrePost
Time = 0.014
Contours of Mean Strain-Strainrate
min=-142.77, at elem# 1329
max=131.708, at elem# 1722

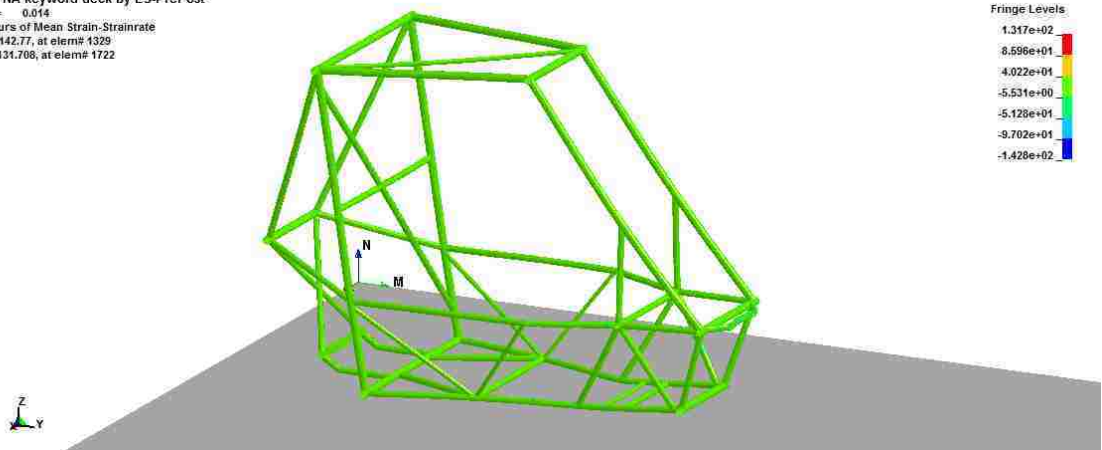


Figure 4.25 Highest Strain rate of 132/s at 0.014 sec

LS-DYNA keyword deck by LS-PrePost
Time = 0.038
Contours of Mean Strain-Strainrate
min=-4.11589, at elem# 29898
max=5.6088, at elem# 65161

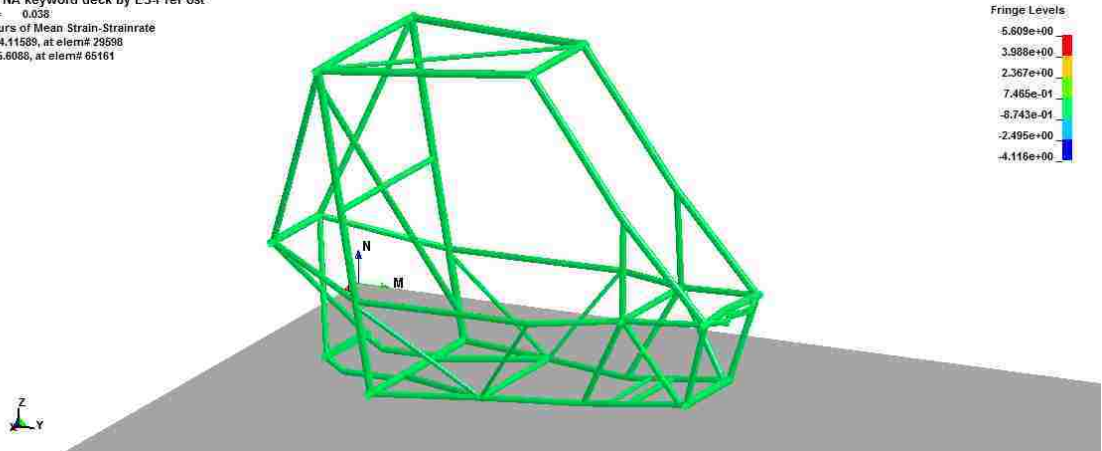


Figure 4.26 Strain rate of 5/s at 0.038 sec

Figure 4.27 shows the contours of nodal velocities in y-direction (direction of impact) at 0.0109 seconds, where the frame first touches the wall. At this instant of time, the nodes displaying with red have higher velocity than the nodes at the vicinity of the impact. This indicates that the rigid wall has slowed down the vehicle at the tip of the structure while the back of the frame is pushing the structure forward resulting in crushing of the bumper into the wall. The velocity is in mm/s, therefore, red points have the velocity of 13.7 m/s at this instant (initial velocity was 13 m/s).

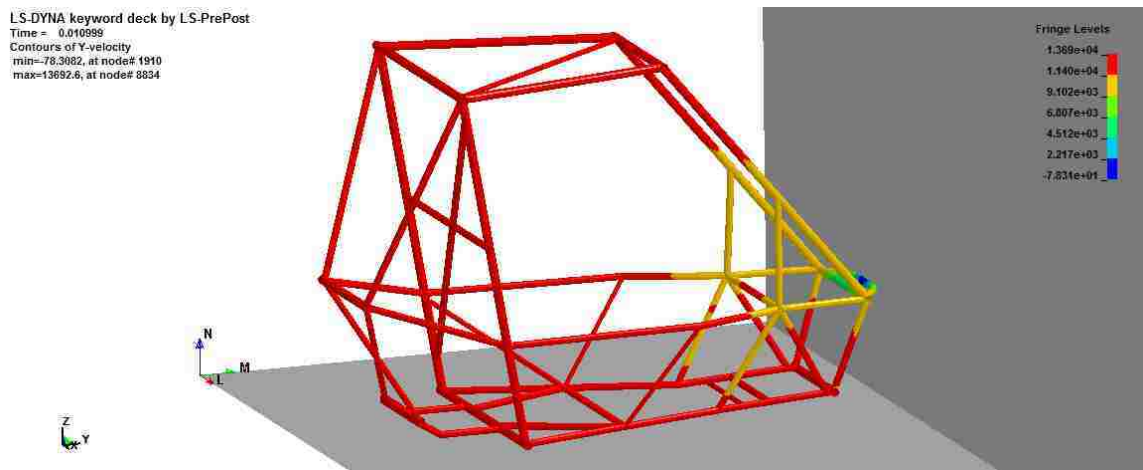


Figure 4.27 Velocity contour in y-direction at 0.0109 sec

In order to observe what exactly is happening at the joints, different values of contact forces were plotted at selected points A to H as shown in figure 4.28.

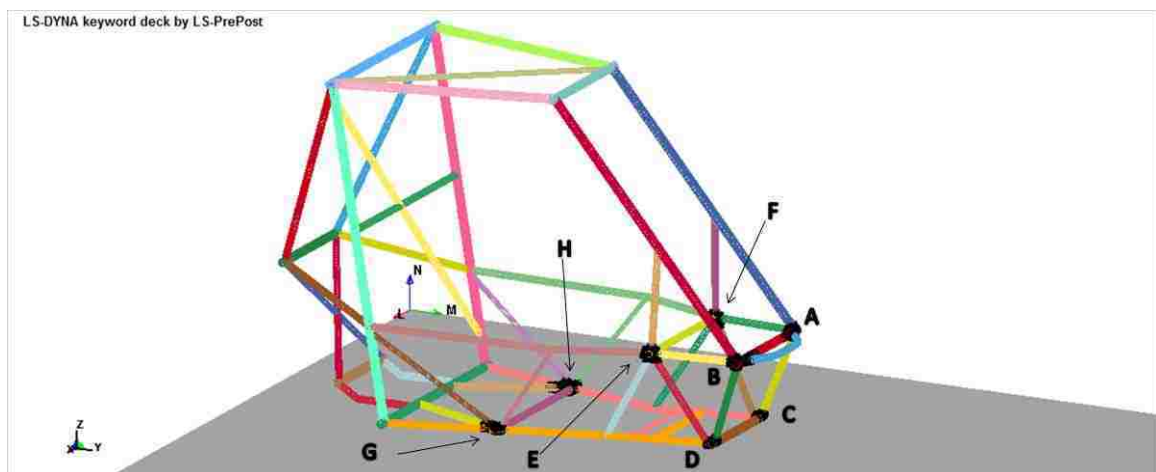


Figure 4.28 Selected joints for contact force

It is shown in figure 4.29 that the reaction force at the joints is fluctuating in time. The maximum amount of contact force was observed at regions A and B right in front of the structure as expected. Furthermore, it was observed that points G and H have the second highest values which are due to the large number of components meeting in the middle of the chassis. Moreover, interestingly it was noted that points E and F have one of the lowest reaction forces among all which can be interpreted because of the layout of the structural components around those joints. All the curves experience their maximum value exactly where the maximum wall force as shown in figure 4.30 is acting on the frame.

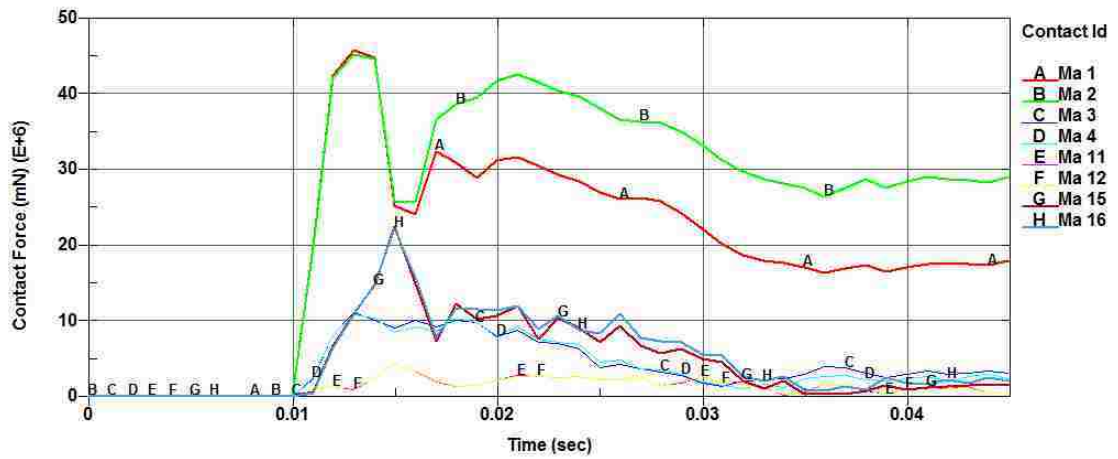


Figure 4.29 Highest contact forces at the joints

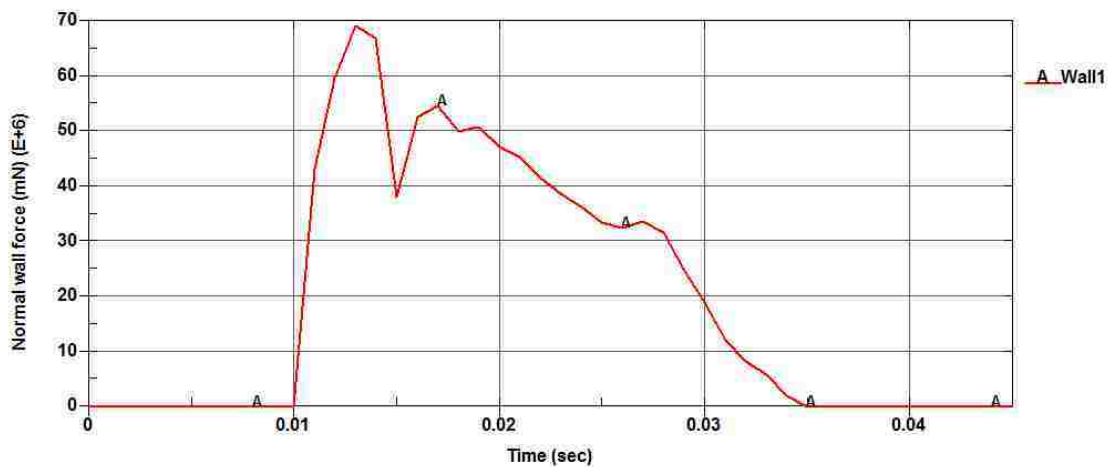


Figure 4.30 Rigid wall normal force

The computational time in this simulation was controlled by introducing mass scaling to the system. The amount of added mass was determined very carefully since the amount of kinetic energy present in the problem was high. The amount of mass increase during the simulation as it is shown in figure 4.31 has an increasing behaviour. This shows that as the frame undergoes deformation, elements get distorted and consequently more mass is being added to the system to balance the desired time step. With this amount of scaled mass, the computational time of about 25 hours was decreased to 30 minutes, and correspondingly the time step was increased from $5e-8$ to $9.8e-7$.

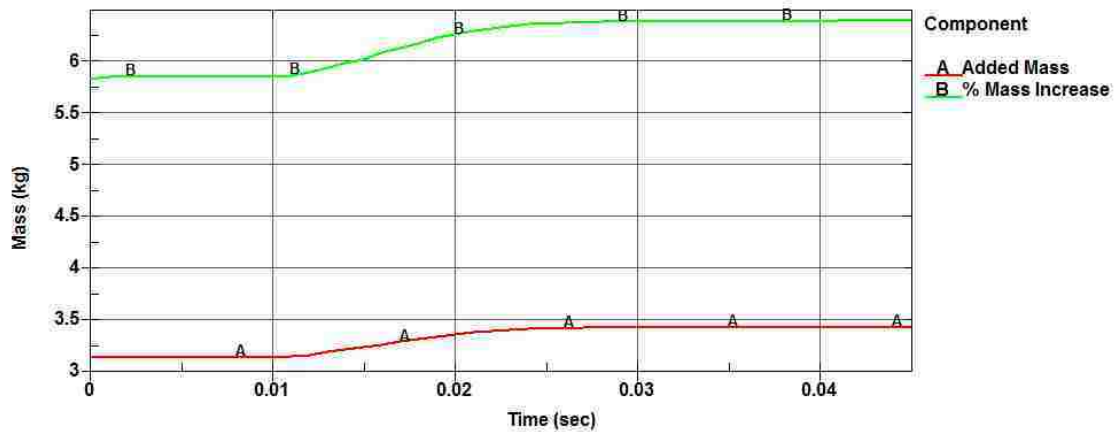


Figure 4.31 Percentage of mass increase

Figure 4.31 is a two phase diagram. It shows that at every instance, how much mass is being added to the system and correspondingly what is percentage of that added mass with regard of the total structural mass.

4.4.1 Energy balance

Examining the energy balance of a system can be thought as monitoring the balance of a system as to improve the reliability of the numerical simulation [45]. Investigation in energy components such as kinetic, potential, dissipated, and etc, during a simulation can be helpful in identifying the cause of the numerical instabilities of vehicle responses during an impact.

Interpreting energy balance information is based on the principle of the conservation of energy for a physical system. At any given instant in time, t , the total mechanical energy (E) of a system can be expressed as [45]:

$$E = W + T \quad (4-10)$$

where T is the kinetic energy and W is the potential energy. Furthermore, W can be split into internal strain energy and external work done;

$$E = T + E_{\text{internal}} - W_{\text{external}} \quad (4-11)$$

If all of the forces acting on a system are purely conservative, then eq. (4-11) states that the balance of kinetic energy, internal strain energy, and external work done is conserved at all points in time.

In real physical systems, however, non-conservative forces often play an important role and cannot be neglected. Irreversible processes such as plastic deformation of mechanical components and frictional sliding at contact interfaces dissipate energy in a non-conservative manner. In addition, in terms of writing an energy balance expression for a numerical model of a physical system, certain non-physical energy terms will need to be added to the energy term as well (e.g. hourglass energy). According to LS-DYNA this term is represented as follows;

$$E + W_{\text{external}} = E_{\text{kin}} + E_{\text{internal}} + E_{\text{si}} + E_{\text{hg}} + E_{\text{rw}} + E_{\text{damp}} = E_{\text{total}} \quad (4-12)$$

where, these parameters are as follows; E = total initial energy, W_{external} = external work done by the applied forces, E_{kin} = Kinetic energy, E_{internal} = internal energy, E_{si} = sliding energy, E_{hg} = hourglass energy, E_{rw} = rigid wall energy, E_{damp} = damping energy. The term in right hand side is known as the total energy of a system.

Summing all energies for a physical system at time t and normalizing with respect to the total mechanical energy gives the energy ratio during a numerical simulation as;

$$\text{Energy}_{\text{ratio}} = \frac{E_{\text{Total}}}{E + W_{\text{external}}} \quad (4-13)$$

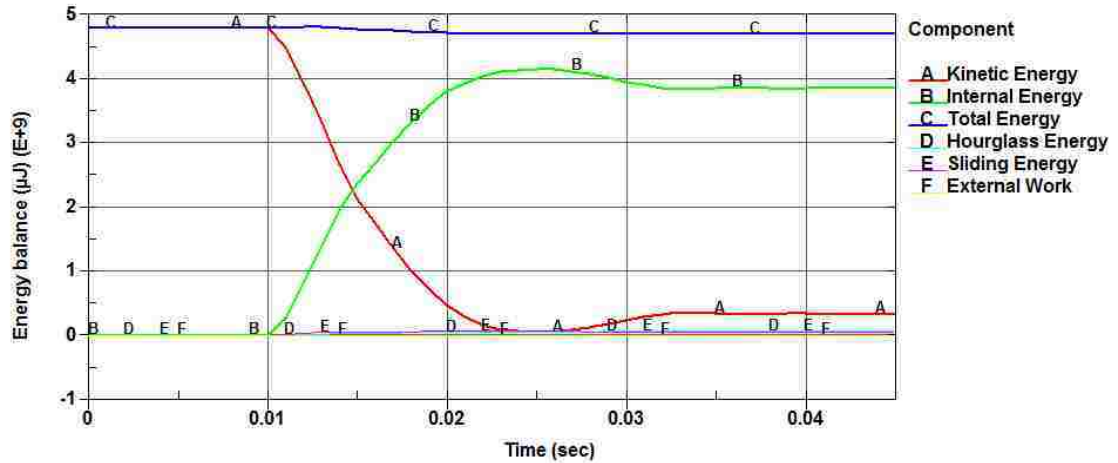


Figure 4.32 Energy balance for the complete mock-up at 48 km/h

Figure 4.32 refers to the energy balance of the Mini-Baja vehicle in the frontal impact scenario at 48 km/h which correlates with the law of conservation of mechanical energy. It shows that the total mechanical energy of the system E_{Total} is roughly constant with respect to time and changes in kinetic energy are balanced by changes in internal energy. The sliding and hourglass energy are well controlled below the acceptable level and no external work is done on the system.

Based on eq. 4-13, figure 4.33 is in regard of the energy ratio for the Mini-Baja frontal crash simulation, which shows a reasonable ratio toward the end. The ratio is kept between 1.063 and 1.038 during the impact.

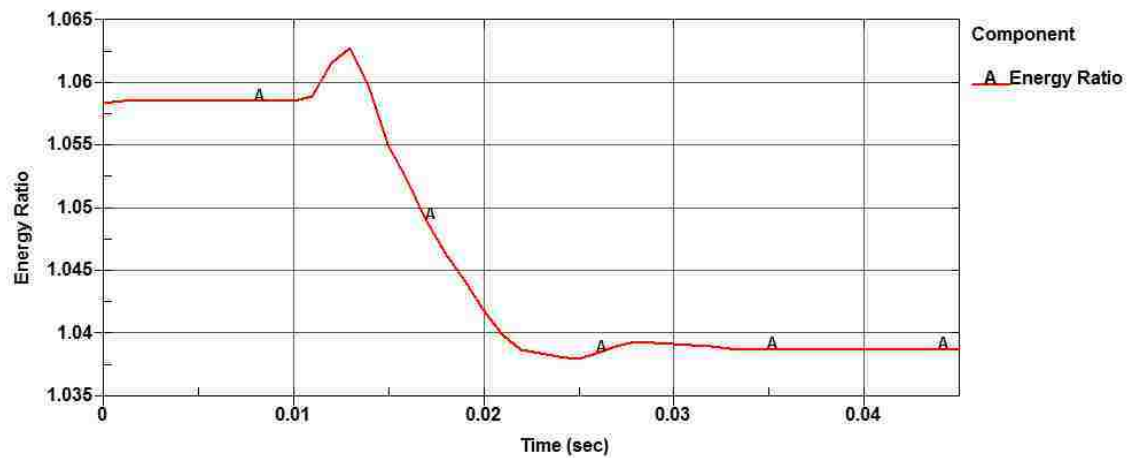


Figure 4.33 Energy ratio of the simulation at 48 km/h

CHAPTER V

EVALUATION OF THE FRONTAL CRASH OF THE MINI-BAJA VEHICLE BY (ABAQUS/CAE)

5.1 Objectives and overview of Chapter V

In order to create a sense of validation for the frontal impact simulation of the Mini-Baja vehicle that was discussed in previous chapter, in this chapter the Mini-Baja frame is modeled once again for validation purposes. The vehicle is implemented in the same crash scenario with incorporation of same assumptions as before. Furthermore, some important aspects and factors that can be critical and sometimes even decisive in finite element simulations are handled differently in this chapter to make sure that the vehicle response is reliable. The finite element software Abaqus/CAE was selected for the validation of the Mini-Baja vehicle in a frontal impact scenario in this chapter.

Abaqus is an engineering simulation program based on the finite element method, which can solve problems ranging from relatively simple linear analysis to challenging non-linear simulations. Abaqus was developed by a company called HKS, which was founded in 1978. The program was widely used by researchers because HKS introduced gateways to the program, so that users could add new material models and elements [3]. Material models include metals, rubber, polymers, composites, reinforced concrete, crushable and resilient foams, and geotechnical materials (soils and rock).

Abaqus is used in automotive, aerospace, and industrial products industries. The product is popular with academic and research institutions due to the program's ability to be customized. Abaqus also provides a good collection of multi-physics capabilities, such as coupled acoustic-structural, piezoelectric, and structural-thermal capabilities, making it attractive for production-level simulations where multiple fields need to be coupled.

In most simulations, including highly non-linear ones, the user need only provide the engineering data (structure geometry, material behaviour, boundary conditions, and applied loads) and Abaqus automatically chooses appropriate load increments and convergence tolerances and continually adjusts these parameters during the analysis to ensure accurate solutions.

5.2 Simulation of the front portion of the frame (Abaqus/CAE)

In order to model the frontal impact scenario in Abaqus/CAE, it was necessary to create the mesh in Abaqus/CAE environment with Abaqus meshing tools.

To be able to compare the results with LS-DYNA simulations, as in the previous chapter, first the frontal portion of the frame was modeled.

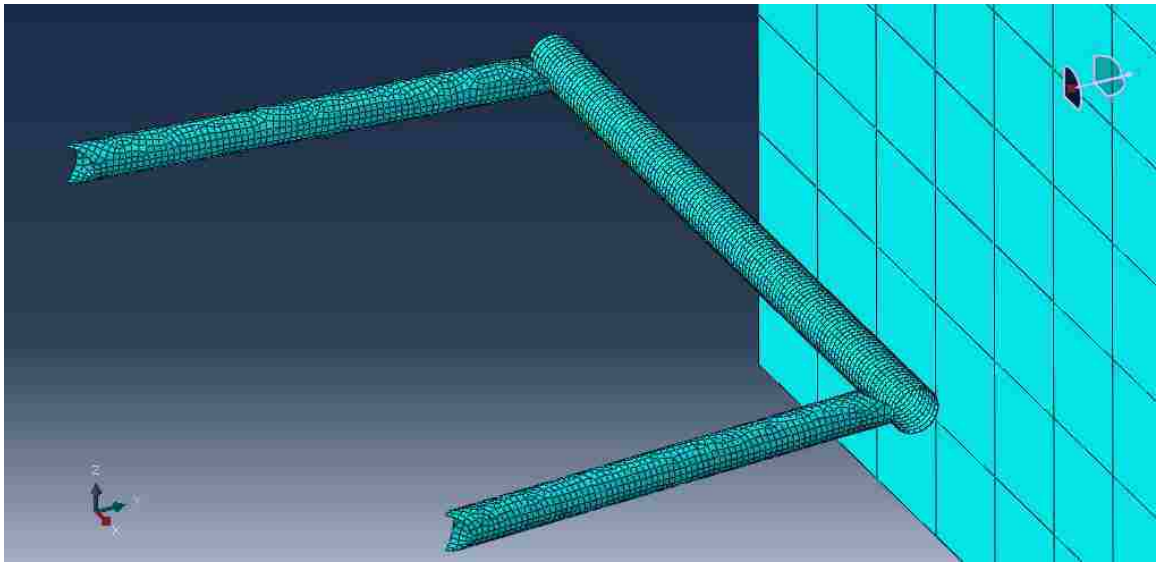


Figure 5.1 Front portion of the frame in frontal impact setup (Abaqus/CAE)

Abaqus/Explicit was used to solve this non-linear impact analysis. The reduced-integration, small membrane-strain¹ quadrilateral shell element (S4RSW) was used with incorporation of warping and hourglass control for the front portion. The element size was specified 6 mm as was the case in previous chapter.

¹ The small membrane strain elements are effective for explicit dynamics problems involving small membrane strains and arbitrarily large rotations [8].

The material model elastic-plastic was used with inclusion of strain rates dependency by power law hardening model.

Two types of rate-dependent models are offered for plasticity. The one that has been used here is based on the rate-dependent yield strength of the material model. This method is suggested by [8] for relatively high strain rate applications, such as dynamic events. This type of rate dependency can be introduced by overstress power law in following equation:

$$\dot{\epsilon}^{pl} = D(R - 1)^n \quad (5-1)$$

where $\dot{\epsilon}^{pl}$ is the plastic strain rate, D and n are material parameters, and R is the ratio of the yield stress at nonzero strain rate to the static yield stress ($R = \frac{\bar{\sigma}}{\sigma_0}$). Keep in mind that R at zero plastic strain rates is 1. Parameter of D = 40.4 and n = 5 are identical to C and P in Cowper-Symonds model discussed in section 4.2.2.

One of the crucial factors in large deformation analyses of vehicle crash is contact modeling. Within crash, it is a common scenario where contact non-linearity arises and therefore, structural response is highly dependent by the way those contacts are defined in the problem.

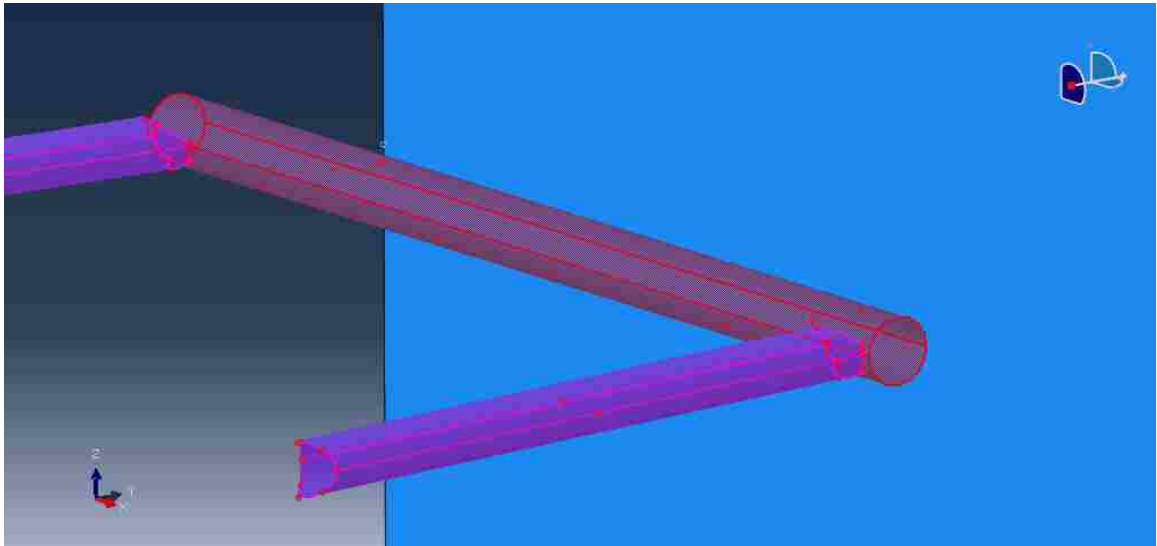


Figure 5.2 Tie contact (Abaqus/CAE)

The weld connections were defined by using constraints methods in Abaqus/CAE. As shown in figure 5.2 the nodes of the purple member are tied to the surface of the red member with a node to surface discretization method.

Furthermore, the contact between the structure and the wall as well as different components with each other were defined with a general explicit contact algorithm with coefficients of static and dynamic friction as 0.2 and 0.15 respectively and decay coefficient of 0.001.

The model was run first for 60 km/h and results in term of energy balance are shown in figure 5.3. Note that ALLAE is the amount of artificial strain energy, ALLWK is the external work, ALLFD is the frictional dissipation, ALLIE is the internal energy, ALLKE is the kinetic energy, and ETOTAL is the total energy of the system. In Abaqus/CAE, artificial strain energy is primarily the energy dissipated to control hourglass deformation. If the artificial strain energy is too excessive, it means that too much strain energy is dissipating to control hourglass deformations. A general rule is that it is desirable to keep the ratio of the ALLAE/ALLSE well below 10% (ALLSE is the elastic strain energy).

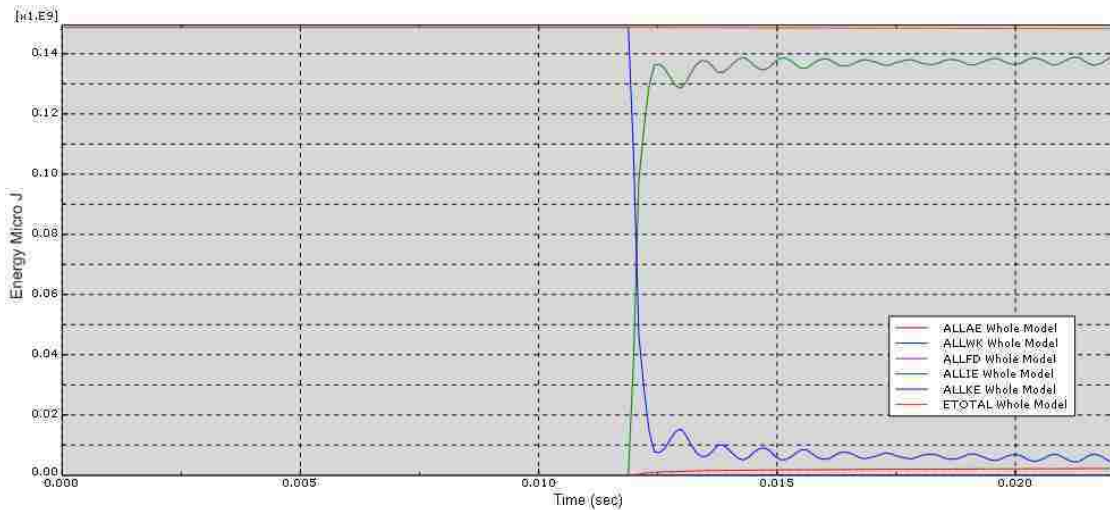


Figure 5.3 Energy balance for front portion at 60 km/h (Abaqus/CAE)

As it is observed in figure 5.3 the amount of artificial strain energy dissipated in the simulation is non-zero. In order to increase the accuracy of the solution the model was further studied. The linear, finite-membrane-strain, fully integrated, quadrilateral shell element (S4) was used for greater solution accuracy. For problems prone to membrane and bending-mode hourglassing, or for problems where in-plane bending is expected the element type S4 is suggested [8]. As shown in figure 5.4 the amount of artificial strain energy is well controlled by using fully integrated elements.

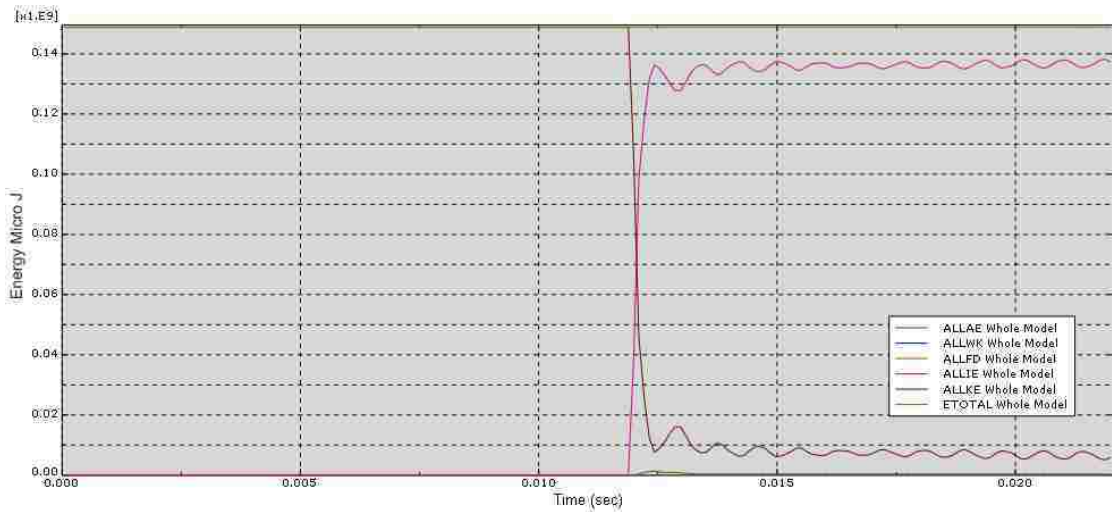


Figure 5.4 Energy balance for front portion at 60 km/h modified (Abaqus/CAE)

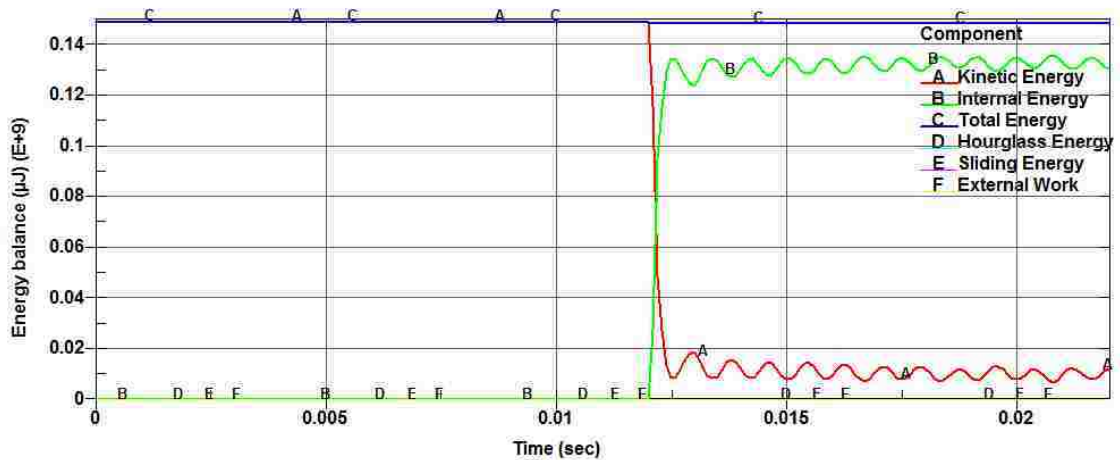


Figure 5.5 Energy balance for front portion at 60 km/h (LS-DYNA)

It is shown in figure 5.6 that the ratio of artificial strain energy to elastic strain energy resulted below 9% using S4 elements. Furthermore, it was observed that at the time 0.012 where the frame impacts into the wall is the instant where the maximum amount of artificial strain is being dissipated due to large number of distorted elements.

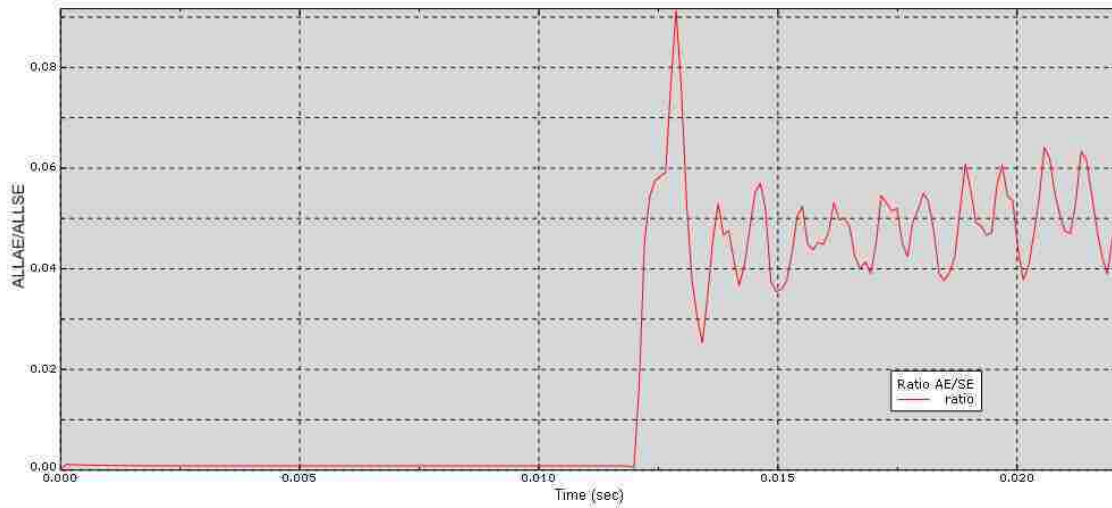


Figure 5.6 The ratio of artificial strain energy over elastic strain energy

In the following figures, the von Mises stress distribution over the front frame is compared between the LS-DYNA model and Abaqus/CAE model. The amount of plastic strain is 0.241 in LS-DYNA compared to 0.268 in Abaqus/CAE.

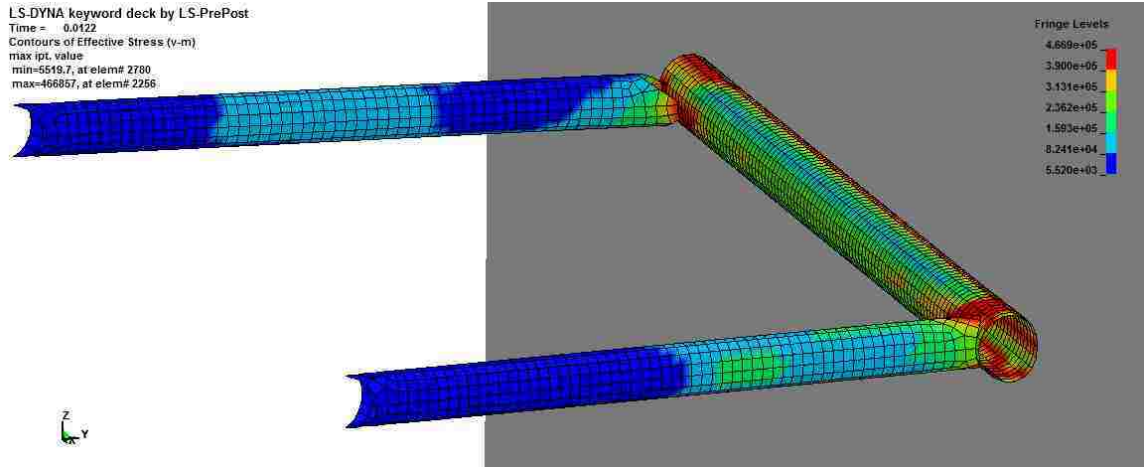


Figure 5.7 von Mises stress distribution of the front portion at 60 km/h (LS-DYNA)

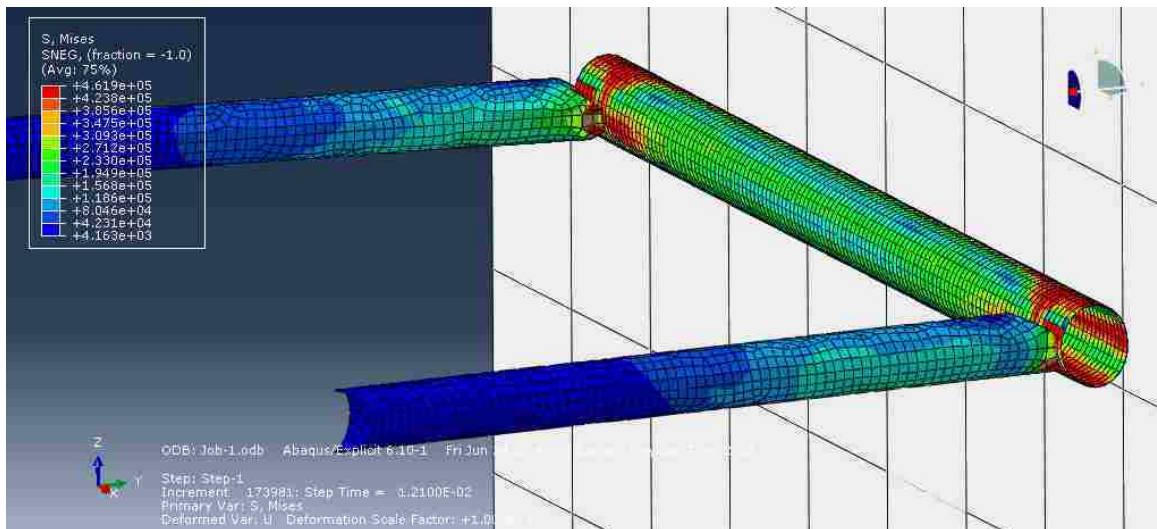


Figure 5.8 von Mises stress distribution of the front portion at 60 km/h (Abaqus/CAE)

The structure was also run for 150 km/h, and the results are compared with model 1 (LS-DYNA) proposed in section 4.3;

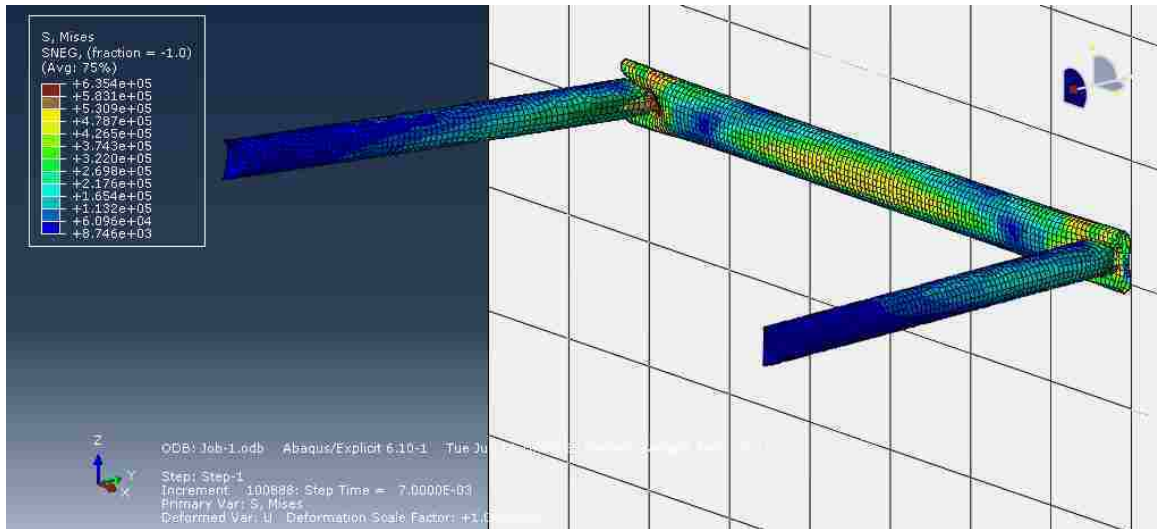


Figure 5.9 von Mises stress distribution of the front portion at 150 km/h (Abaqus/CAE)

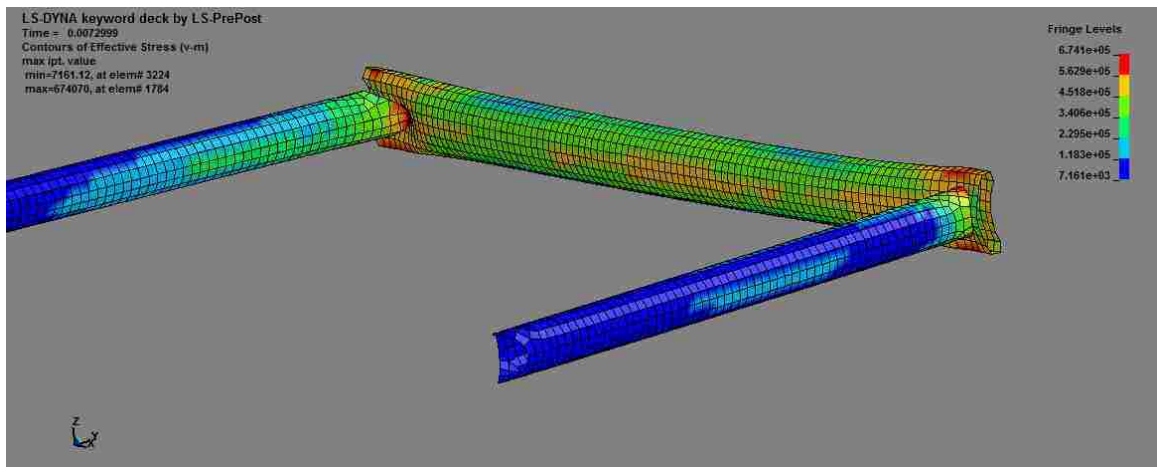


Figure 5.10 von Mises stress distribution of the front portion at 150 km/h (LS-DYNA)

The amount of plastic strain for the Abaqus/CAE model was 0.44 compared to the LS-DYNA model which was 0.43 at 150 km/h.

Results of the two models at 150 km/h are compared in terms of energy balance in figure 5.11. In this figure, I.E = Internal energy, E.W = External work done by applied forces, K.E = Kinetic energy, T.E = Total energy.

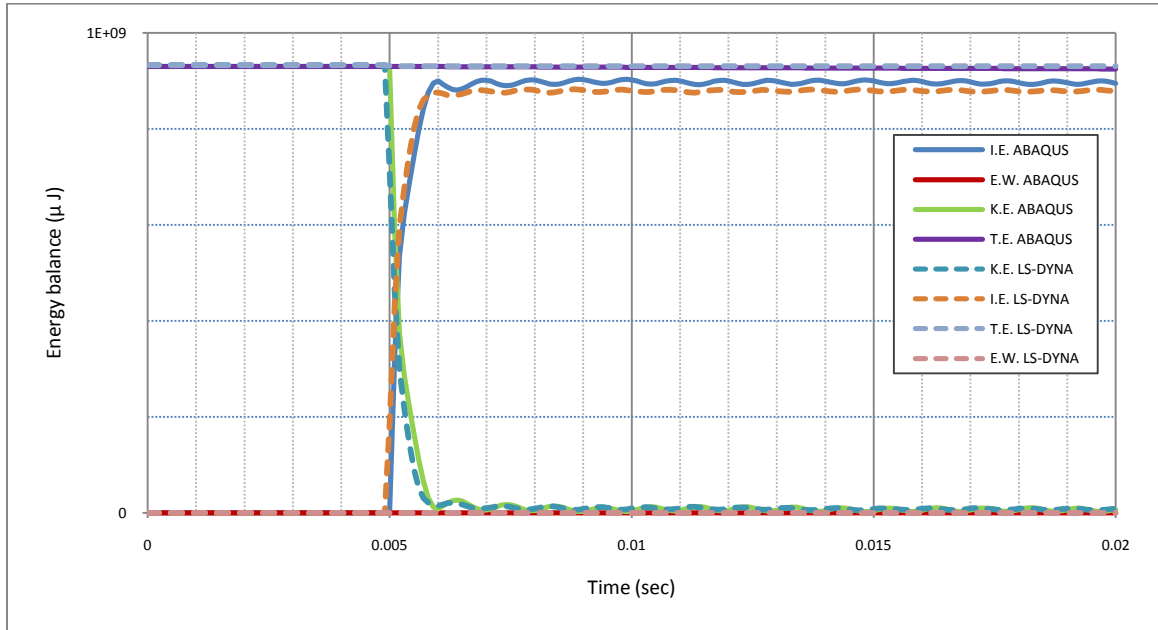


Figure 5.11 Comparison of energy balance of the front portion at 150 km/h

5.3 Frontal impact simulation of the Mini-Baja frame chassis (Abaqus/CAE)

The complete mock-up of the frame was modeled in Abaqus/CAE as shown in figure below. The computational time was controlled in a similar way, except that this time smaller time increments ($7E-7$) were used. Instead of using mass scaled solution based on elements, here a semi-automatic mass scaling on the whole model was used to obtain a target step time. It was intended to change the step time to see any possible effect of it on the model.

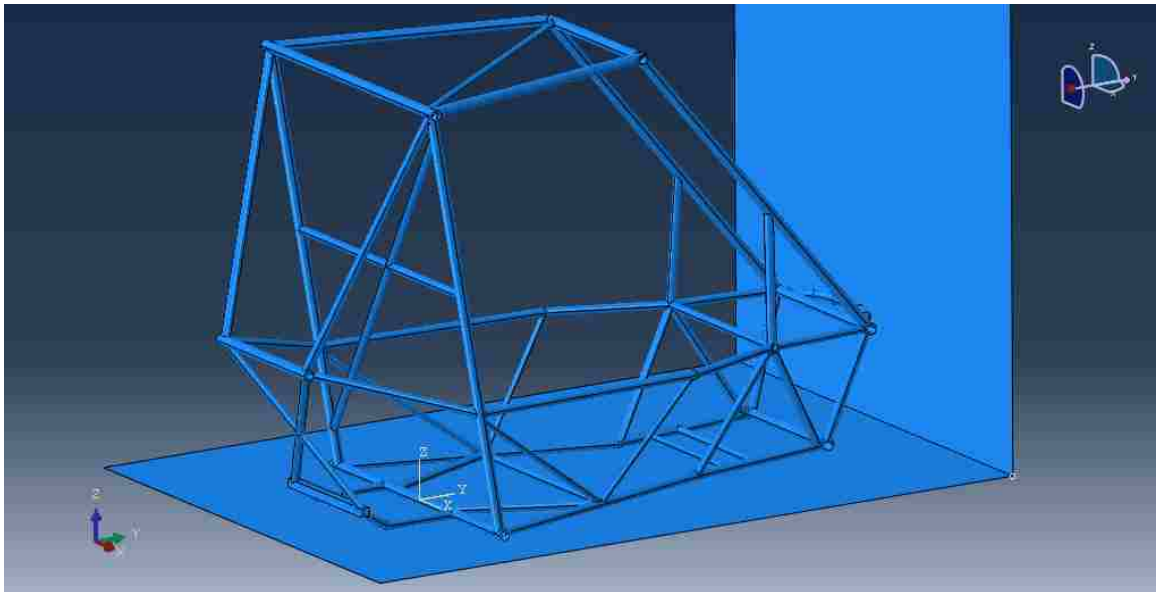


Figure 5.12 Frontal impact scenario of the Mini-Baja vehicle (Abaqus/CAE)

The linear, finite-membrane-strain, reduced-integration, quadrilateral shell element (S4R) was used to mesh the complete mock-up of the chassis. Plastic material model with inclusion of power law strain theory for effect of strain rates as discussed earlier was used.

Incorrect material orientation can be very costly in crash simulations where stress is typically very hard to obtain. Most finite element packages automatically resolve the issue of contact where material direction and normal direction are incorrect. However in order to get reliable stress distribution, one should be careful about material direction. Figure 5.13 is an example of an incorrect material direction that will consequently result in incorrect contact behaviour between the two tubes. Furthermore, the values of stress

outputted will be incorrect because the principle directions are mixed up. The inconsistency is due to the fact that for most elements the dominant stress is the circumferential stress, but for some elements it is the axial stress (shown in figure 5.13).

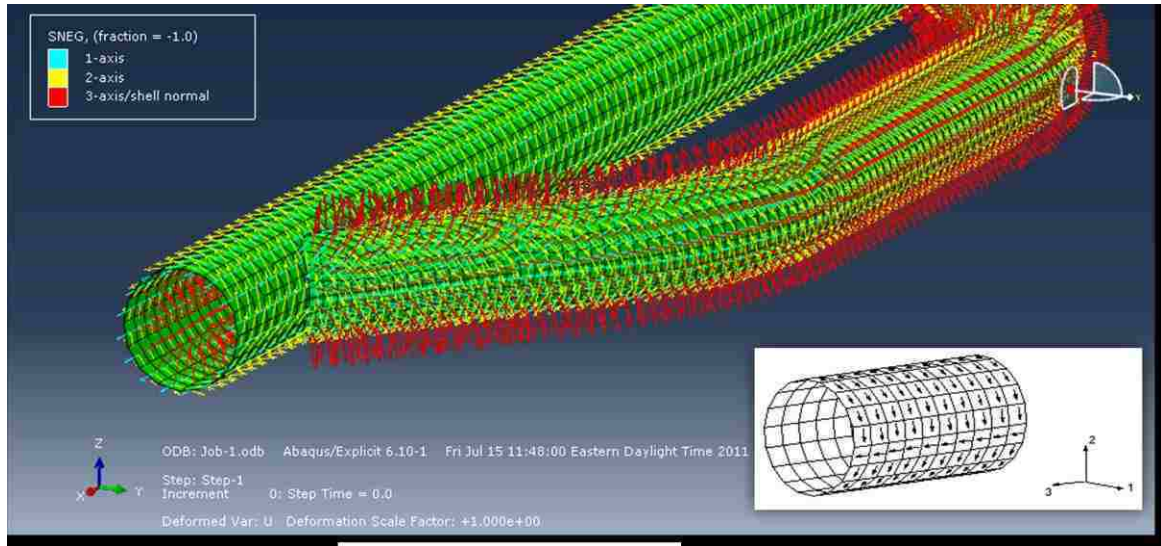


Figure 5.13 Example of a wrong material direction

The energy balance of the vehicle is shown in figure 5.14. As shown, the amount of artificial strain energy and frictional dissipation is rather excessive. Nonetheless the energy balance is well within the desired limit. Keep in mind that the intention of the Abaqus/CAE simulations was to develop an overall comparison between the two models to see if on the whole the response of the structure in frontal crash scenario makes sense. Therefore, no additional study was performed to decrease the excessive undesired energies, since there were fully discussed in previous chapter.

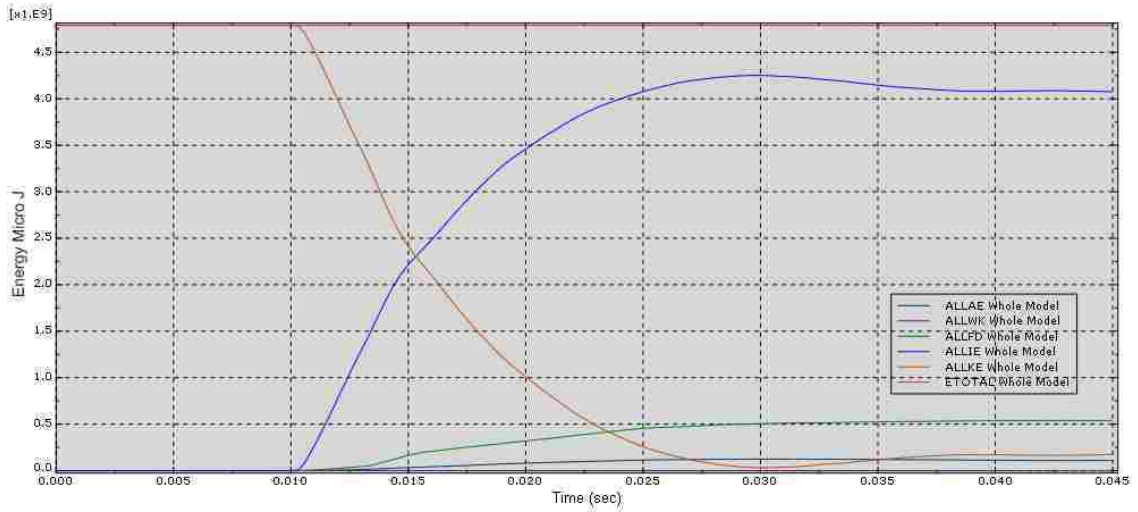


Figure 5.14 Energy balance of the frontal impact at 48 km/h (Abaqus/CAE)

In following figures, results regarding the stress distributions and plastic strain of the frame modeled in Abaqus/CAE are shown at instances similar to chapter 4. Results showed good coloration between the two models.

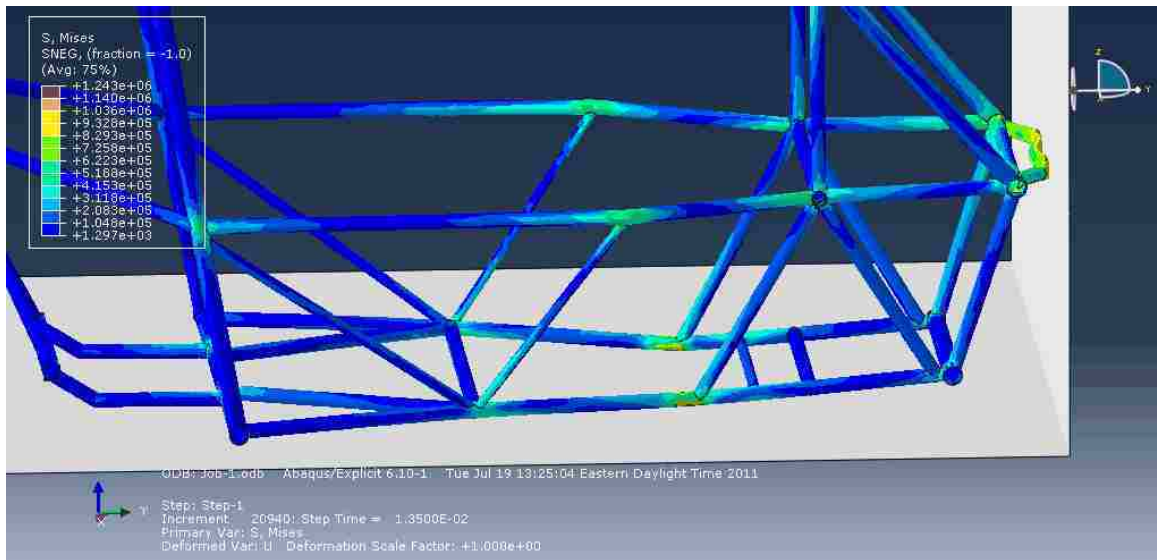


Figure 5.15 von Mises stress distribution at 0.013 sec (Abaqus/CAE)

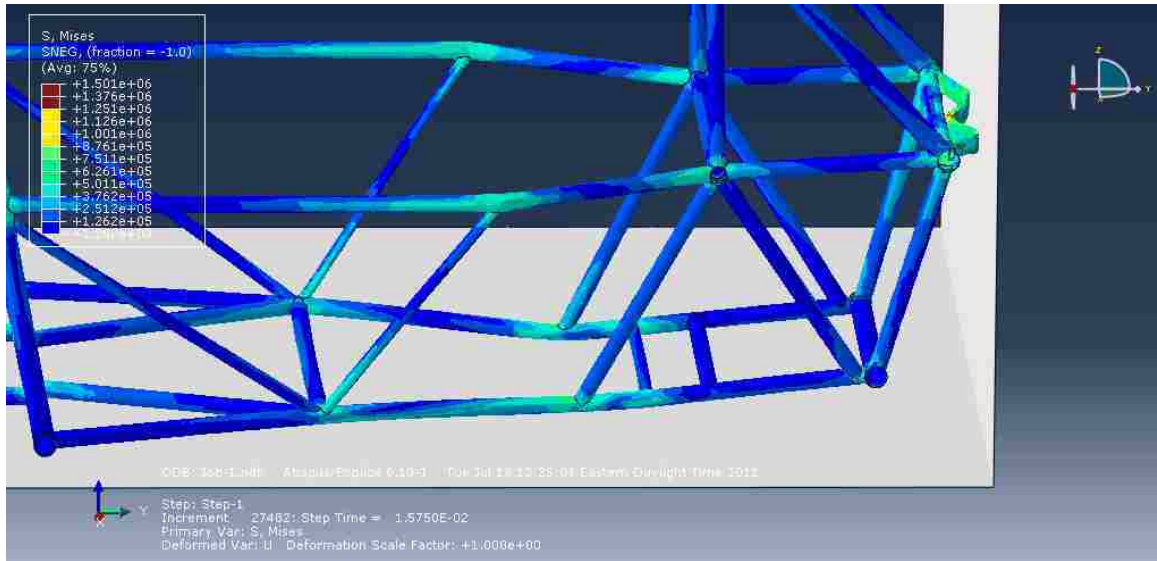


Figure 5.16 Maximum von Mises stress at 0.016 sec (Abaqus/CAE)

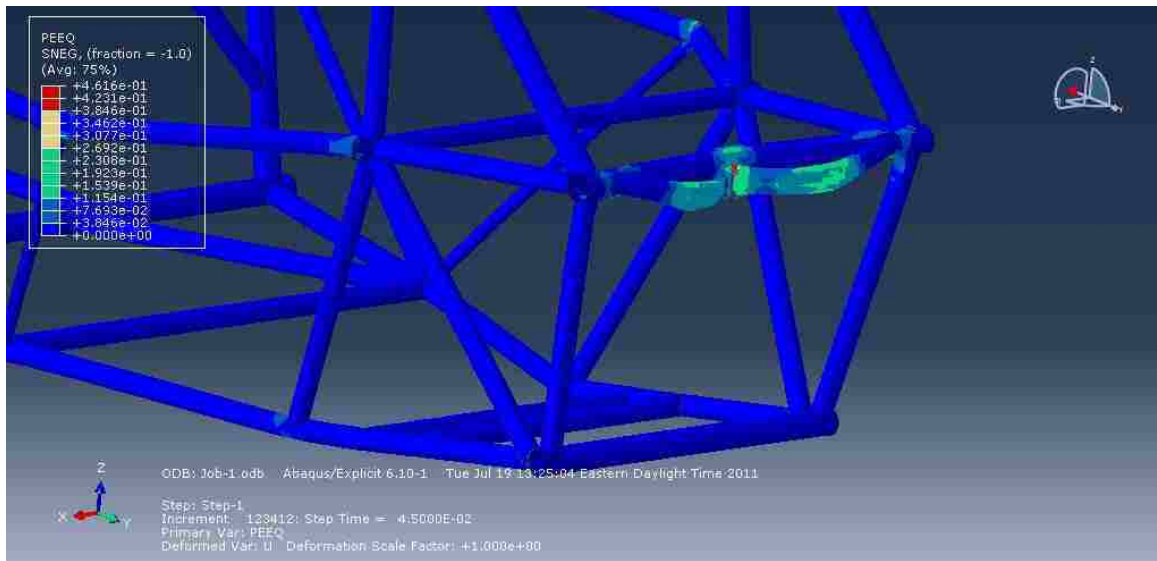


Figure 5.17 Maximum plastic strain at the end of the simulation 0.045 sec (Abaqus/CAE)

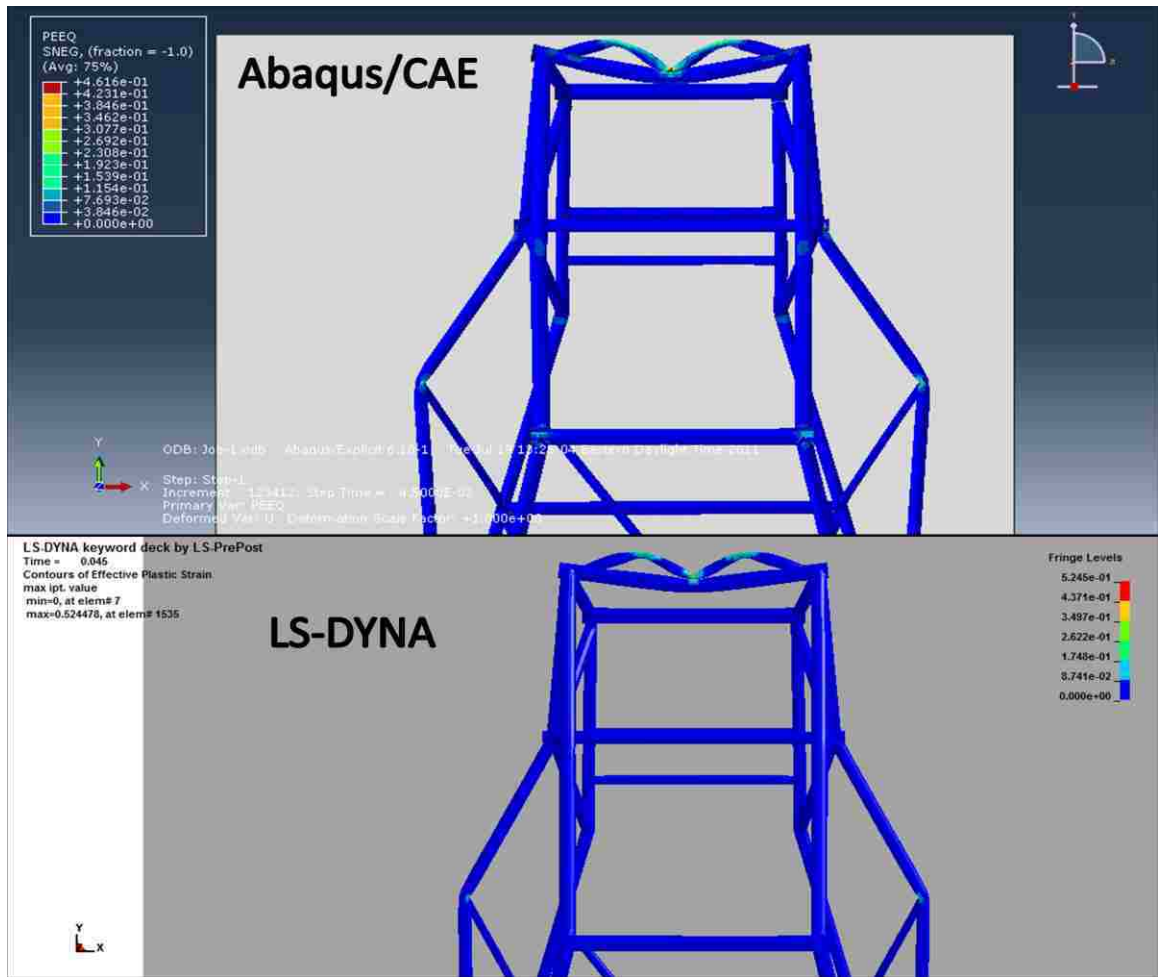


Figure 5.18 Maximum plastic strain at the end of the simulation 0.045 sec

5.4 Further comparison of LS-DYNA and Abaqus/CAE results

In this section different data curves outputted from each software are compared in one graph. In figure 5.19 the energy balance of the two models are compared. All the comparisons were made on the complete mock-up model at 48 km/h.

In these graphs; I.E = Internal energy, E.W = External work done by applied forces, K.E = Kinetic energy, T.E = Total energy, RF = Reaction wall force, and Disp. = Displacement.

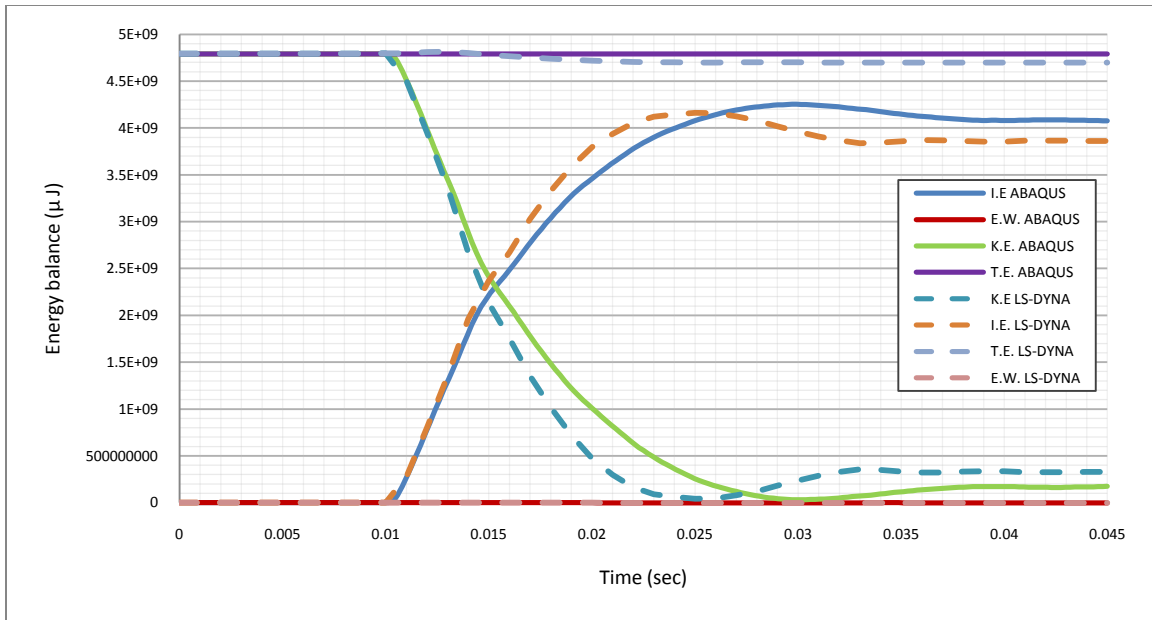


Figure 5.19 Energy balance of the full Mini-Baja mock-up at 48 km/h

In order to create a sense of comparison for the horizontal elongation of the frame from the sides, point “P” as shown below was selected to show the buckling behaviour of the frame outward. Results for x-displacement and the resultant displacement of the selected node are plotted in figure 5.21.

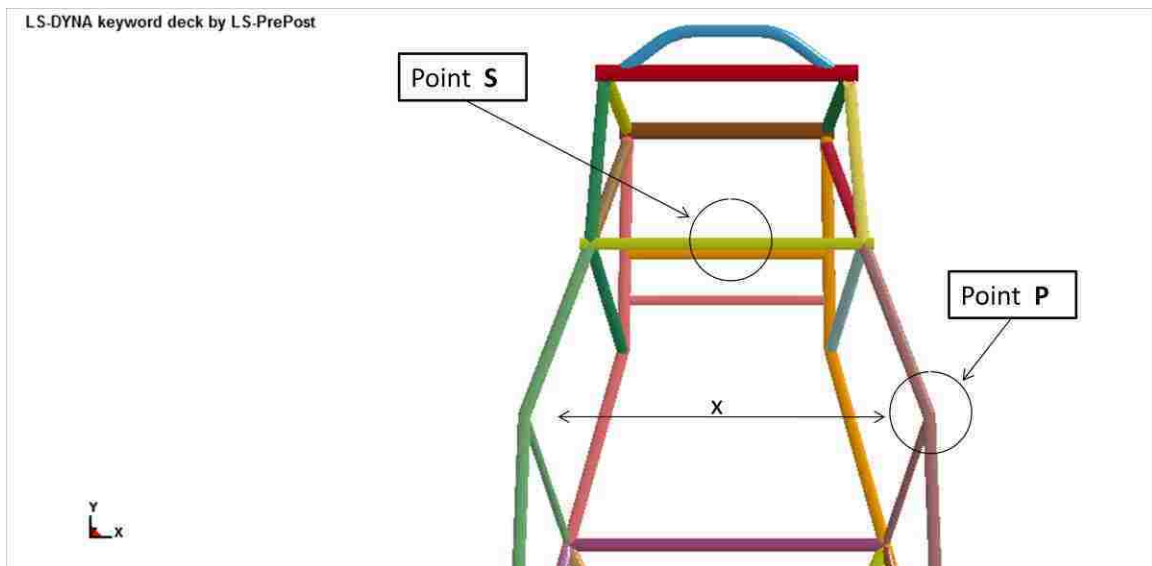


Figure 5.20 Selected point for side displacement

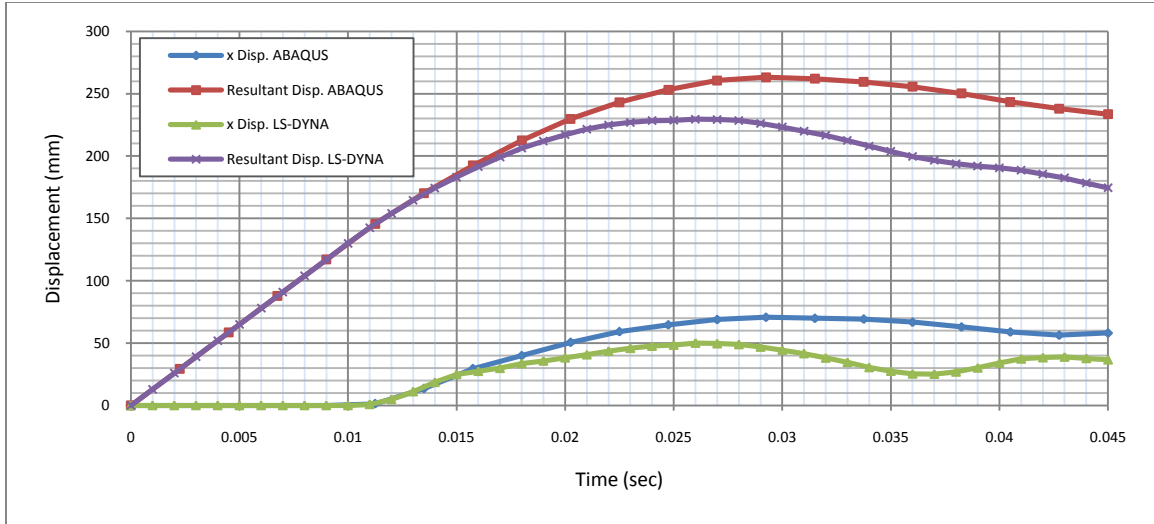


Figure 5.21 Side displacement of point (P)

It was observed as shown in figure 5.21 that the structure solved by LS-DYNA resembles a more dynamic behaviour. It can be seen in the x displacement behaviour of the point P that how the component oscillates back and forth after the impact (green curve). In LS-DYNA, vibration characteristic of the frame components has been captured perfectly whereas the curves corresponding to the model solved by Abaqus/CAE shows differently. To further study the vibration characteristic of components during the impact, another critical point “Q” was selected on the roof as shown in figure 5.22.

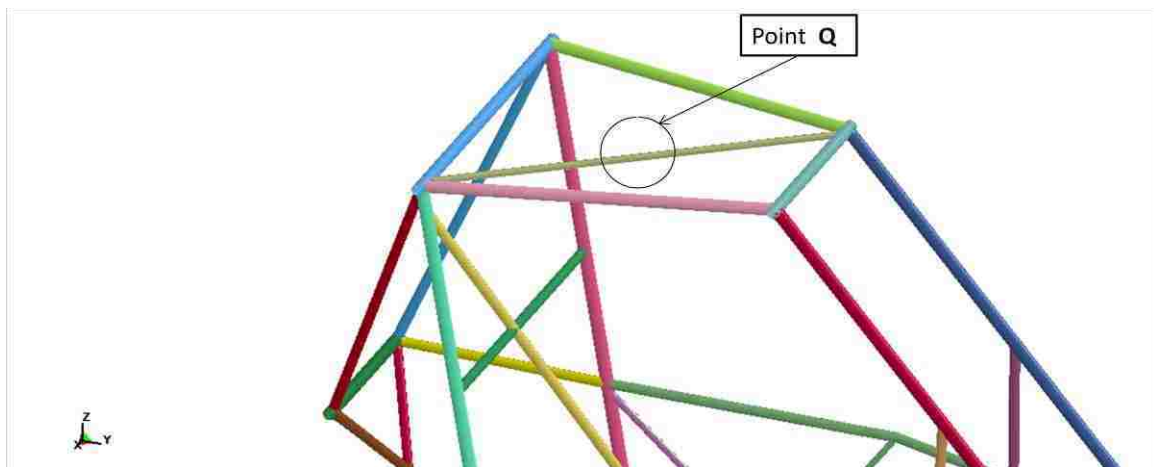


Figure 5.22 Selected roof point (Q)

Results based on z-displacement of point “Q” are plotted in figure 5.23. As it is shown, the magnitude of the vertical oscillation is much higher for the LS-DYNA model. Furthermore, it is noted that the corresponding direction of excitation are 180 degree out of phase between the two models.

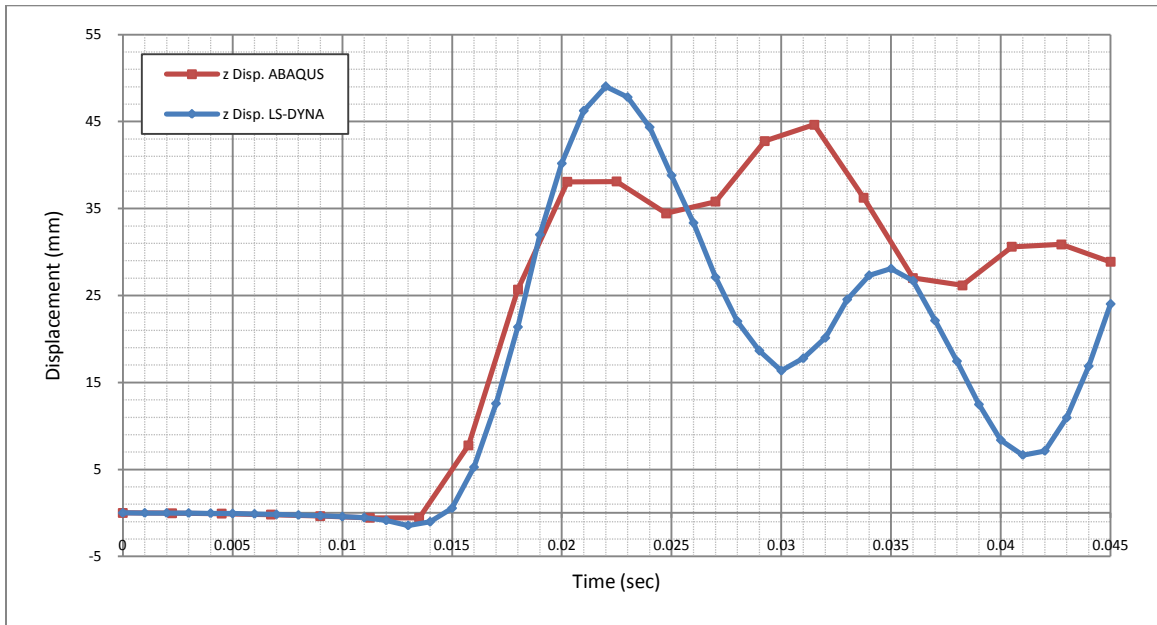


Figure 5.23 Vertical displacement of the roof point (Q)

In figure 5.24, the reaction of the wall is plotted for comparison. In order to provide a criterion for evaluation of the generalized stiffness in both models, in figure 5.25, the wall force is plotted versus the resultant displacement of a specific point “S” as shown in figure 5.20. The displacement of a middle member was selected that could be representing an overall displacement of the vehicle.

For a point of comparison, the generalized stiffness defined above for the LS-DYNA model is 437.5×10^3 N/m compared to 375×10^3 N/m (Abaqus/CAE) at 160 mm.

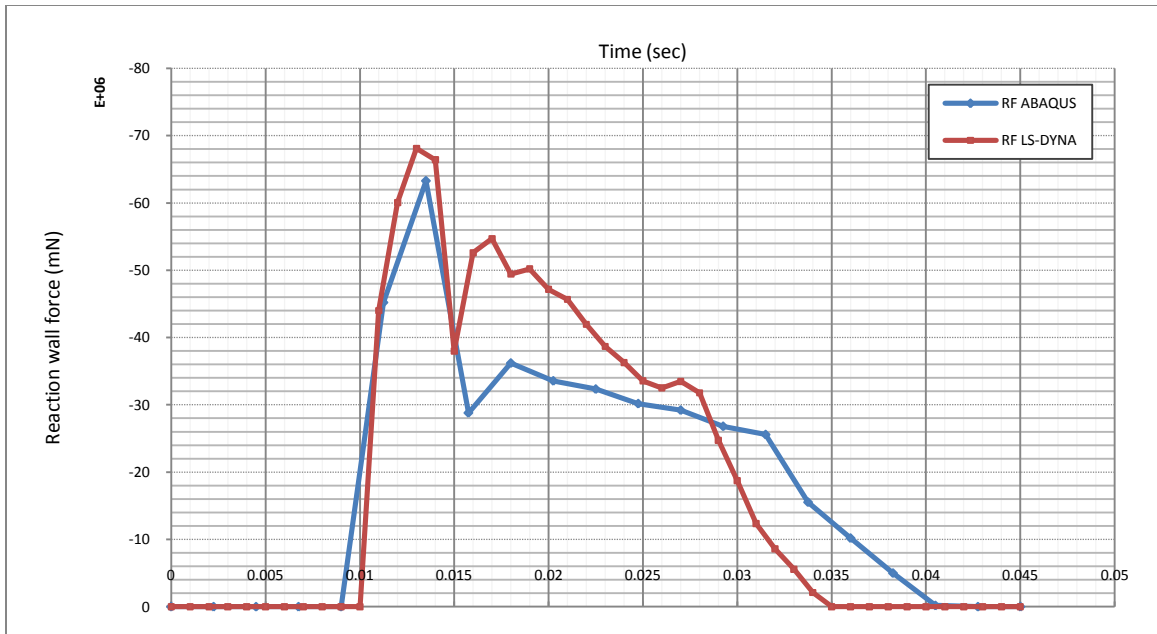


Figure 5.24 Wall reaction force

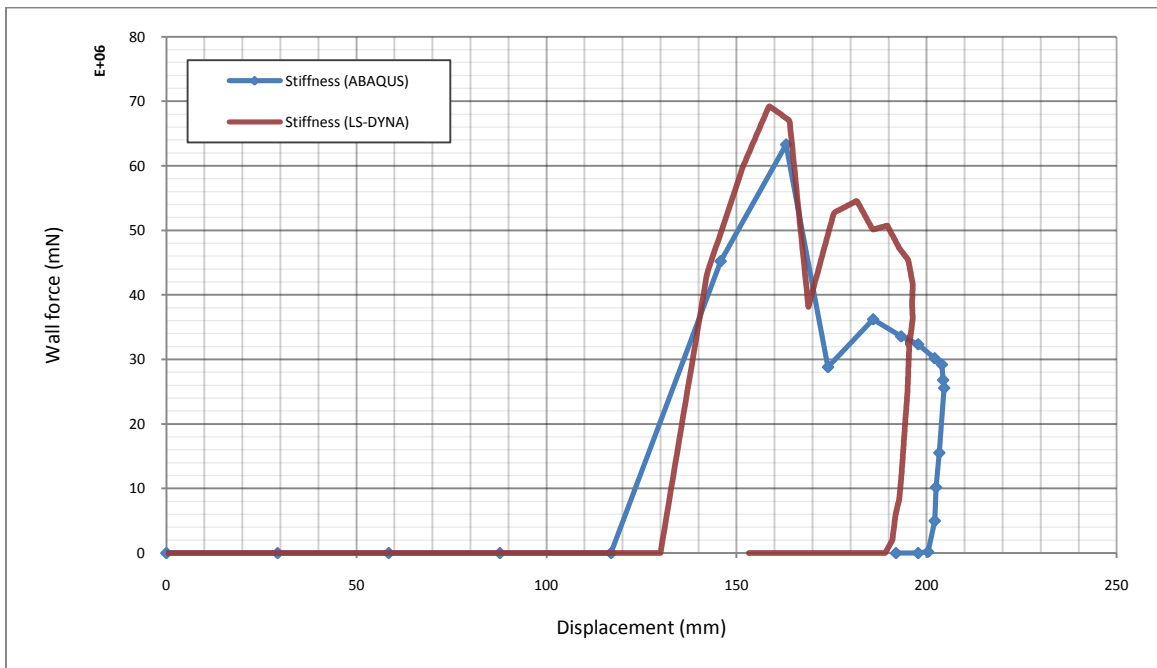


Figure 5.25 Reaction wall force versus resultant displacement (stiffness)

CHAPTER VI

A MORE COMPLETE MODEL OF THE MINI-BAJA VEHICLE FOR CRASH ANALYSIS (LS-DYNA)

6.1 Objectives and overview of Chapter VI

In this chapter, a number of extra components such as suspension arms, wheels, seat, and body parts were added to the Mini-Baja vehicle to create a more realistic model. The frame of the vehicle is the same one used in chapter 5.

As a first step, the tire assembly was developed and simulated as a sub model before incorporating it into the Mini-Baja finite element model. Subsequently, the body panels and suspension shocks are assembled into the previously discussed structure and simulated for an equilibrium test under the load of gravity. Although gravity is not an important loading condition in this problem, this step was used to ensure that desired contact and material models were properly functioning. In the final step, the entire finite element model of the Mini-Baja vehicle was simulated for crashworthiness assessment in front, side, and head-on crash scenarios.

6.2 Modeling of the tires

Tires were modeled based on the geometry and approximated shape of the actual tires used in the Mini-Baja vehicle. In figure 6.1, the front and rear tires used in the actual Mini-Baja vehicle are shown. The generated CAD representations of the tires are also shown in figure 6.2.

In this section, the tires undergo a severe deformation for verification and validation of the correct contact behaviour and checking any possible discontinuity in the deployment of the tires. The primary objective of this effort was to provide a general validation and to gain some insights on the performance of the tires. Keep in mind that just the tires were simulated here and the suspension arms and other additional components were assembled directly to the Mini-Baja FE model.



Figure 6.1 Actual tires and suspension assembly

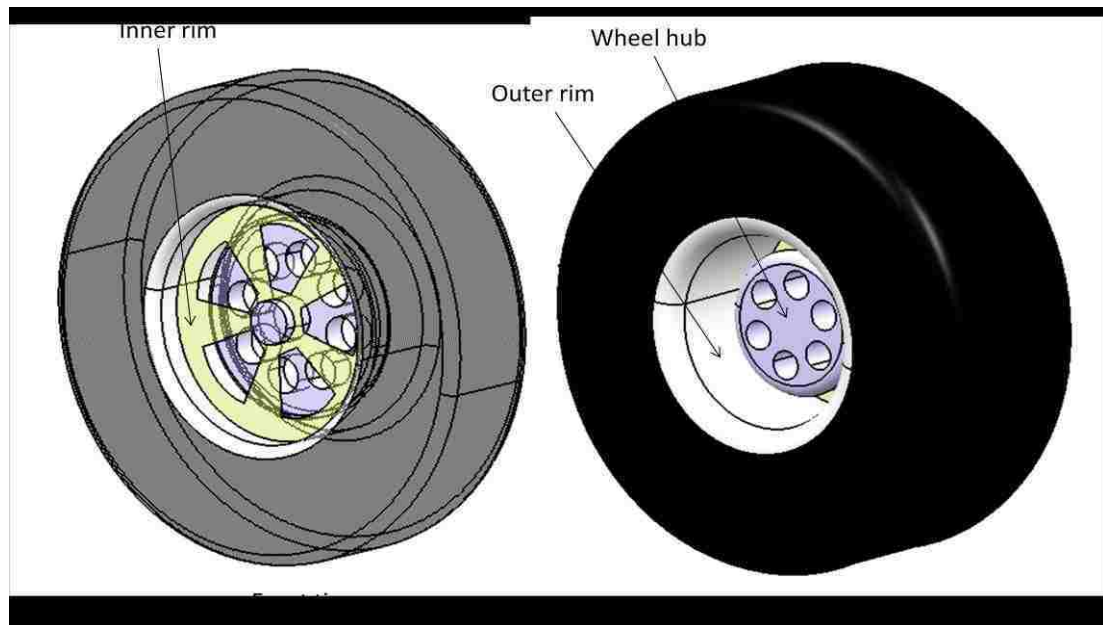


Figure 6.2 CAD model of the tire

To check the connection defined between different components of the wheel, a simulation was carried out where, the bottom end nodes of the tires were constrained in

all translational directions and a rigid wall were prescribed a downward motion crushing the tires harshly. It should be mentioned that the tires themselves were constructed from an appropriate elastic material and the outer rims were made of steel.

The inner rims and wheel hubs were made of rigid material and are connected to each other using rigid body constraints. All the components in the assembly of the wheels are modeled with shell elements with elements sizes ranging between 6 to 12 millimetres. The sectional properties are shown in figure 6.3.

These assumptions used in the modeling of the Mini-Baja's tire assembly were closely studied and taken from the actual FE vehicle models used by the society of crash engineers (NCAC).

LS-DYNA keyword deck by LS-PrePost

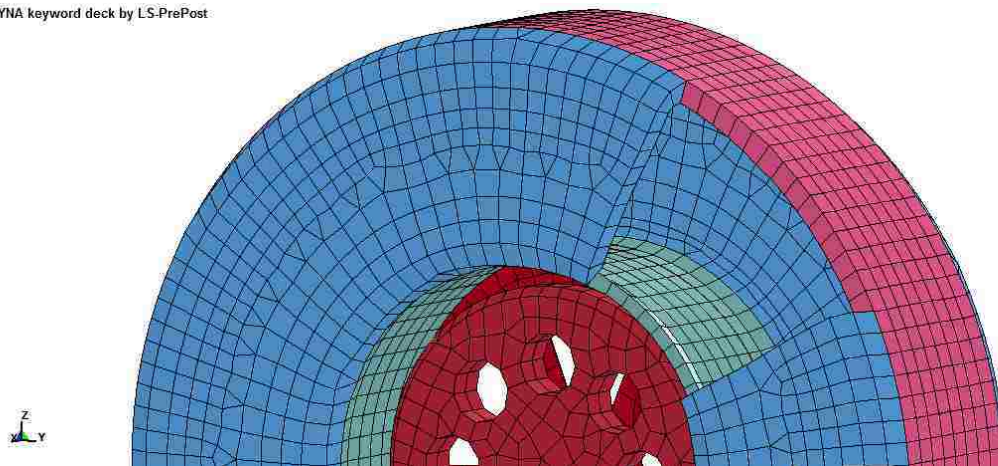


Figure 6.3 FE model of the tire assembly displaying the sectional thicknesses

As shown in figure 6.4 and 6.5 the tires are under a relatively large displacement of 90 mm due to the downward motion of the rigid wall. The intention was to produce a highly destructive scenario ensuring the correct functionality of the tires when used in the Mini-Baja crash simulations.

LS-DYNA keyword deck by LS-PrePost
Time = 0.04

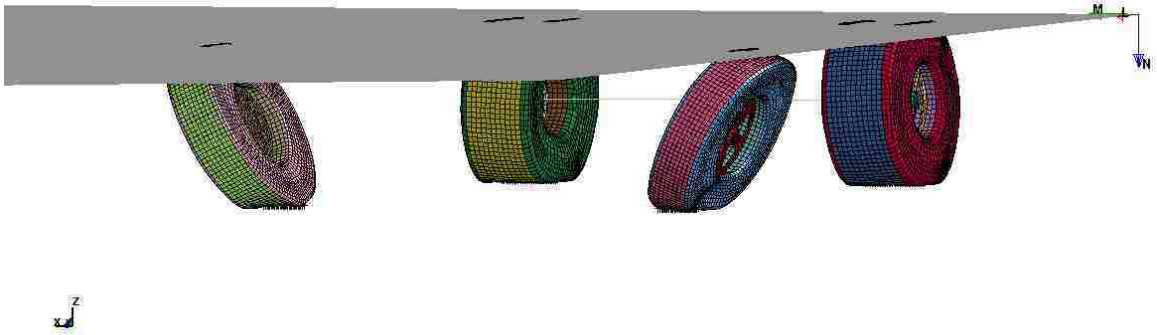


Figure 6.4 Deformation of the tires at 90mm displacement of the wall

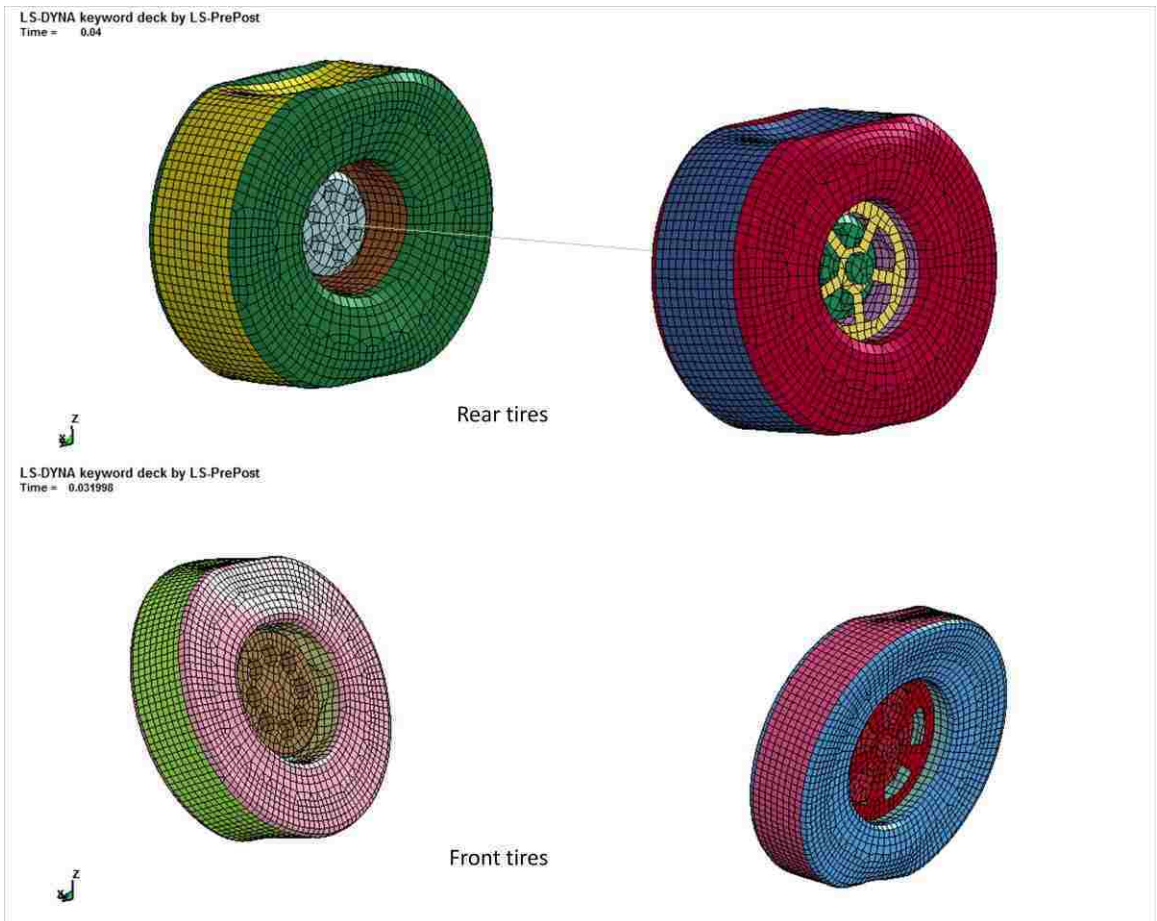


Figure 6.5 Deformation of the tires at 0.04 sec for the rear tires and at 0.032 sec for front tires

6.3 Simulation of the complete Mini-Baja vehicle

Ultimately a more complete mock-up of the Mini-Baja vehicle was constructed which includes; suspension arms, seat, and steering wheel. This mock-up is shown in figure 6.6. Many assumptions were made in order to prepare this FE model for the full frontal crash simulation. Some additional parts such as suspension arms and the rear axle were made of ordinary beam elements (Hughes-Liu with cross-section integration rule). Spring and dampers were constructed with simple discrete elements using spring elastic material and damper viscous material models respectively.

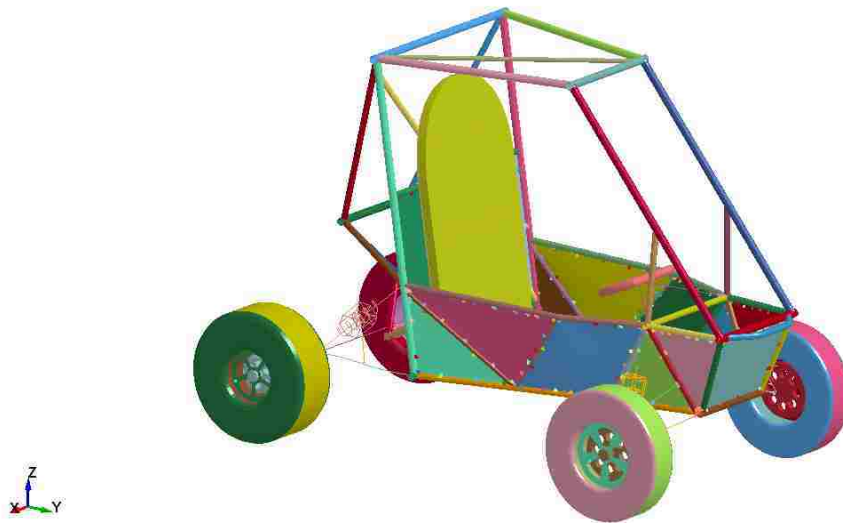


Figure 6.6 FE model of the completed Mini-Baja vehicle

The body panels are thin sheets of aluminum 6061 with 1 mm thickness. Material model 18 in the material library of LS-DYNA was chosen to define the body panels. This is an isotropic plasticity model with rate effects which uses a power law hardening rule. In this model, the yield stress σ_y is a function of plastic strain and obeys [30];

$$\sigma_y = k\varepsilon^n = k(\varepsilon_{yp} + \varepsilon^p)^n \quad (6-1)$$

where, ε_{yp} is the elastic strain to yield strain and ε^p is the effective plastic strain. K is the strength coefficient and n is the hardening exponent. The strain rate effect was accounted by using Cowper and Symonds constitutive model. The material properties of the aluminum 6061 are given in table (6.1) [46].

Table 6.1 Aluminum 6061 material properties

Material properties	AL-6061
Density kg/m ³	2.71E+03
Elastic modulus (Gpa)	6.89E+10
Poission's ratio	0.33
Yield stress (Mpa)	252
K (thin plate)	4.11E+08
n	6.30E-02
C	6500/25000
P	0.95

The body as it is shown in figures 6.7 and 6.8 is attached to the frame with nodal rigid bodies (NRB); this is a rigid body which consists of defined nodes each belonging to a deformable body. The nodal rigid body in the model prevents any motion between the corresponding constrained nodes.

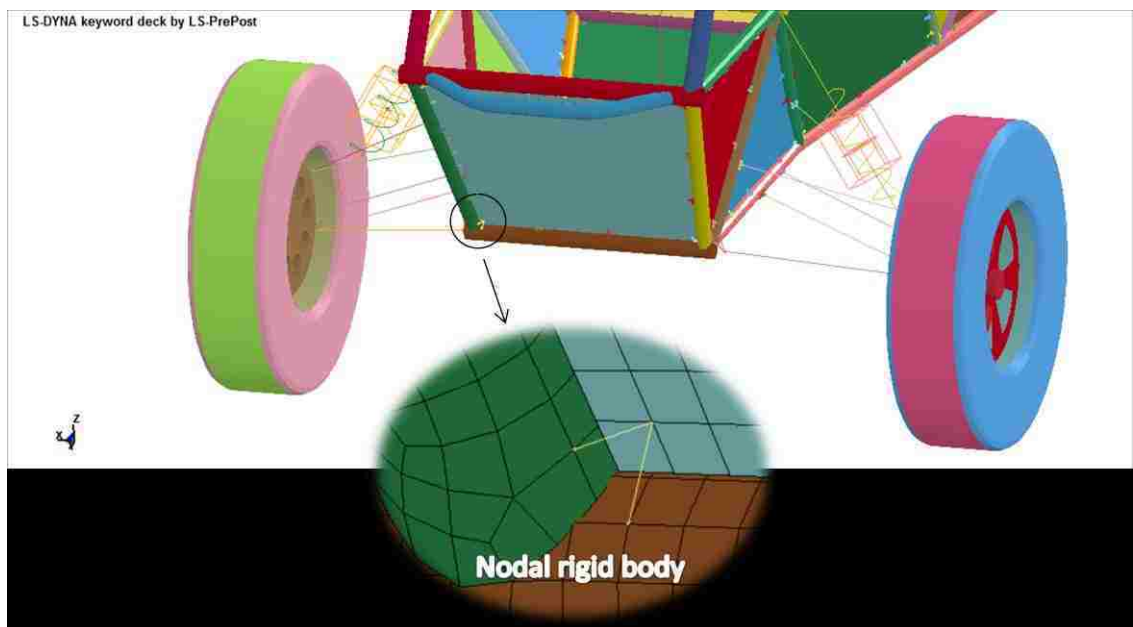


Figure 6.7 Body panels and nodal rigid body constrained

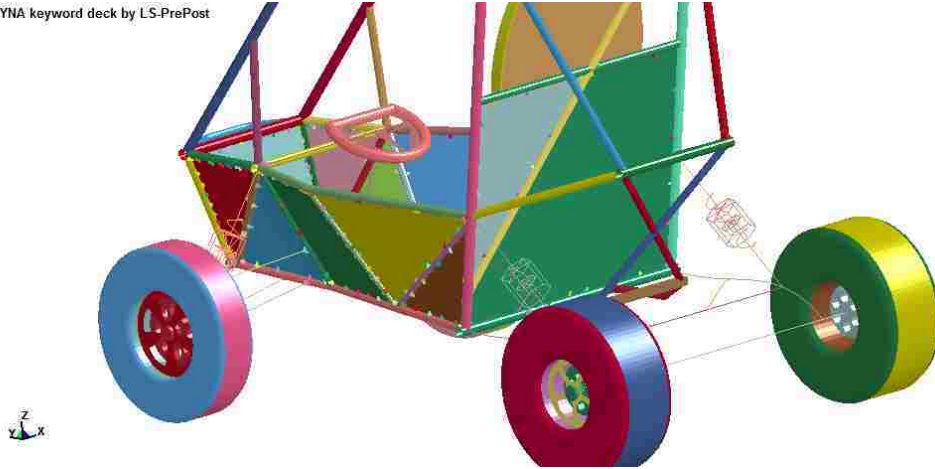


Figure 6.8 Body panels, rear suspension, and shocks

The material model 57 in LS-DYNA which is MAT_LOW_DENSITY_FOAM is a highly compressible low density foam and its main applications are for seat cushions and interior of the vehicle. This material model was used to define the Mini-Baja seat material. Typical loading and unloading stress-strain curves of foams are shown in figure 6.9. The loading curve for the Mini-Baja seat is shown in figure 6.10 and the unloading behaviour was defined with hysteresis and shape factors of 1 and 5 respectively.

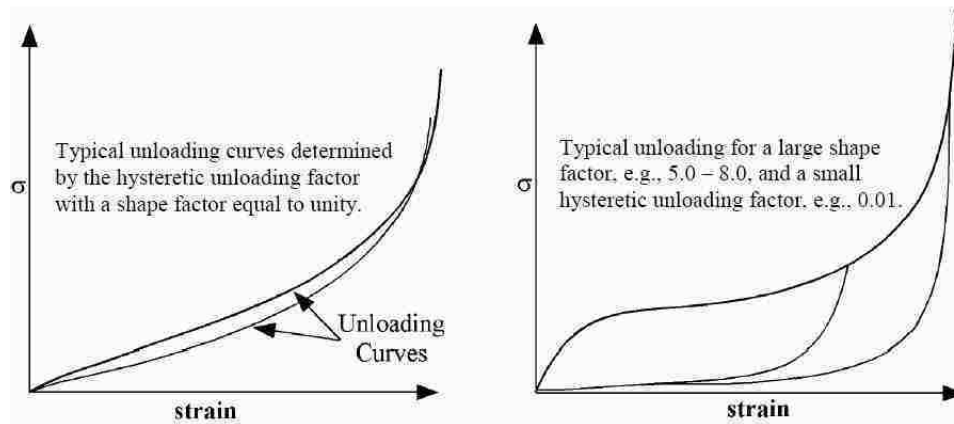


Figure 6.9 Behaviour of the low density foam [30]

In references [47] and [48], a detailed discussion on experimental tests and numerical modeling of the seats and cushions are available. The loading behaviour in the present model is based on experimental data given in [48].

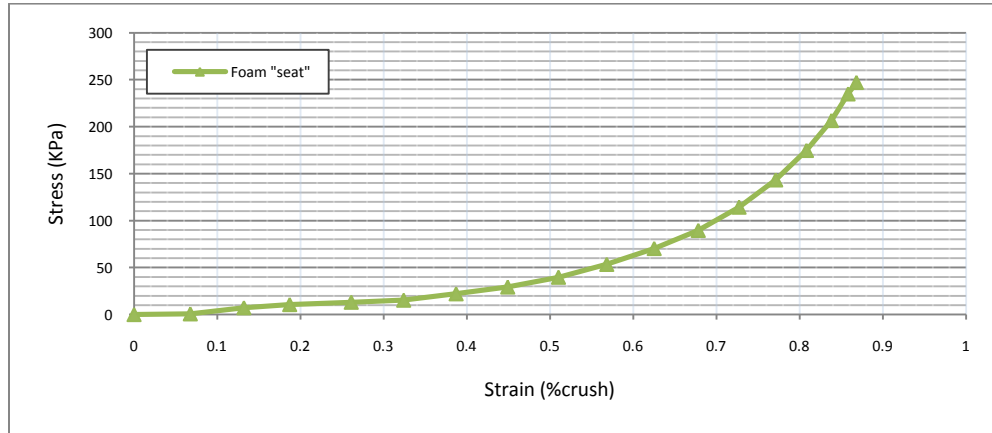


Figure 6.10 Stress-strain curve for the low density foam cushion

In order to account the rotation of the tiers, a revolute joint was created at each wheel assembly. The angular velocity of 51.181 rad/s was prescribed based on considerations shown in figure 6.11.

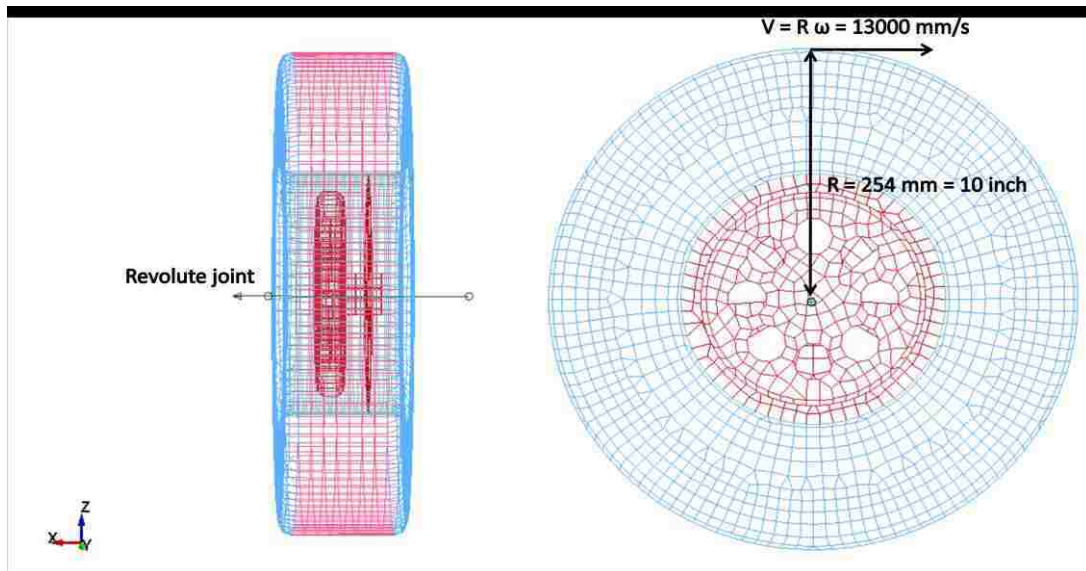


Figure 6.11 Revolute joint and angular velocity of the tires

6.3.1 The frontal crash of the Mini-Baja vehicle

The vehicle consists of 170,000 elements including; shell, solid, beam, discrete and lumped mass elements. The CAD files were generated in Catia V5 and then the components were meshed in Crash (HyperMesh) and LS-PrePost 3.1. These STEP files were then imported to LS-DYNA for implementation of the crash simulation.

Coefficients of static and dynamic friction were considered as 0.2 and 0.1 respectively. Furthermore the exponential decay coefficient of friction was assumed as 10. The undesirable excessive hourglass energy was controlled with the hourglass control and higher order element formulation in localized regions. The negative sliding energy was handled with additional contact modifications and manual master and slave adjustments.

A range of values for the corresponding constants of spring and damper discrete elements were available for the Mini-Baja vehicle. In order to verify the suspension assembly, an equilibrium test was performed on the Mini-Baja to check the functionality of the suspension as well as spring and damper constants. Consequently the constants of spring and damper were established as $5E+4$ N/m and 800 N.s/m respectively. In these series of tests, the force displacement response of the discrete springs was optimized so as the vehicle settles to equilibrium position under gravity loading. To check the equilibrium position, simulation were performed by dropping the vehicle onto a rigid ground under the action of gravity. Figure 6.12 shows the setup for this test.

Figure 6.13 shows the reaction force of the rigid ground when the vehicle is stabilizing. In approximately 0.4 sec the Mini-Baja vehicle reaches equilibrium, and the measured force is equal to the product of the mass of the Mini-Baja (212 kg for the complete model) and the acceleration due to gravity (the corresponding force at 0.6 sec is $2.146E+3$ N).

A “bw” 20 filter was used to reduce the numerical noise effects in the equilibrium simulation for the reaction force of the wall shown in figure 6.13.

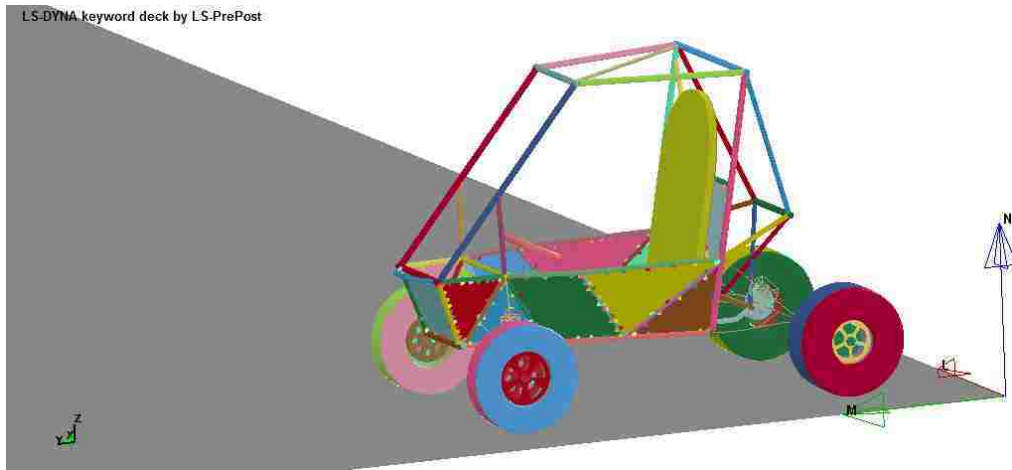


Figure 6.12 Test setup for equilibrium check

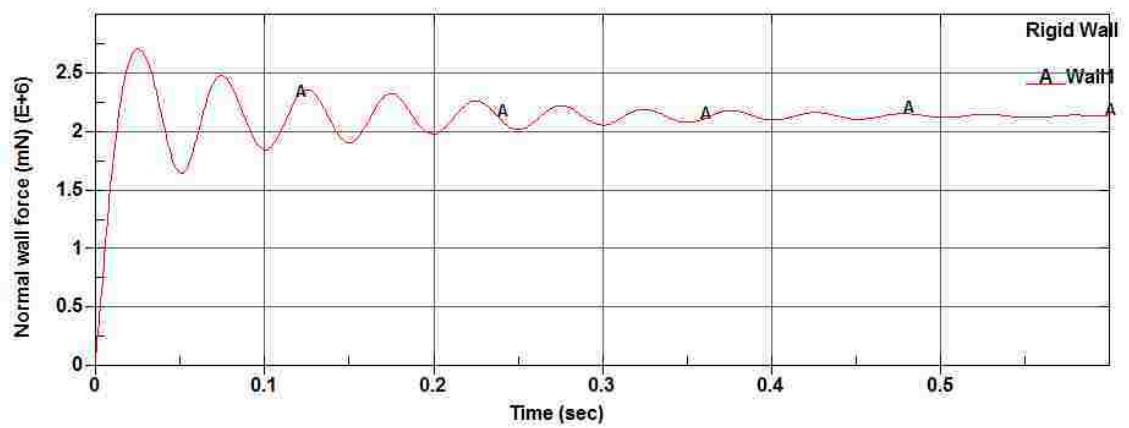


Figure 6.13 Reaction force of the rigid ground

Upon getting satisfactory results from the added components, the vehicle was given an initial velocity of 48 km/h (30 mph) approaching a rigid wall. Figures 6.14 were recorded at different instances of the simulation for the vehicle colliding into the rigid wall.

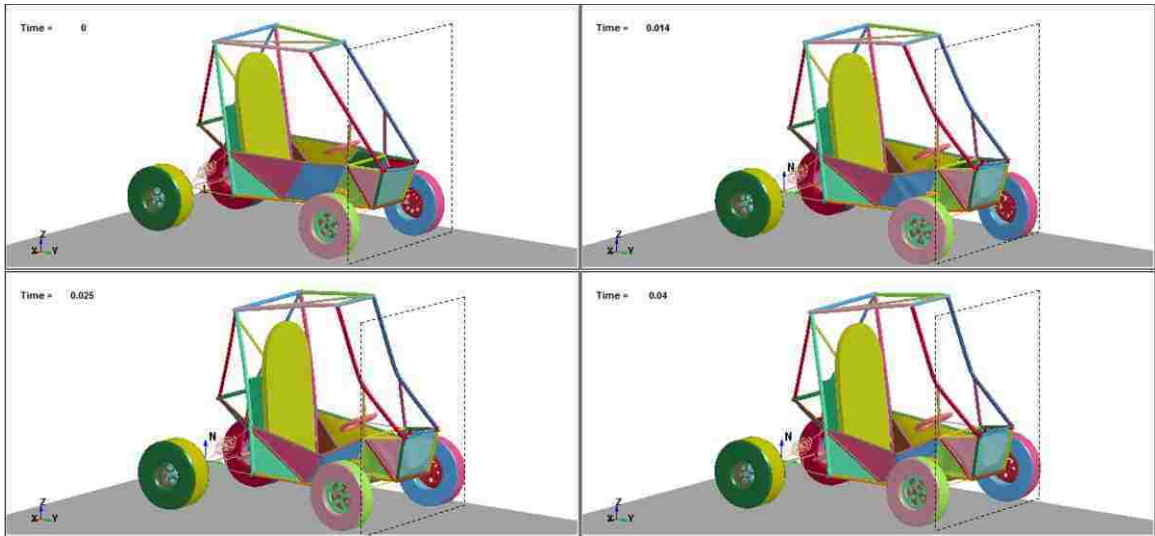


Figure 6.14 Isometric view of the detailed model simulation of the Mini-Baja vehicle into the rigid wall at 48 km/h

The maximum von Mises stress was $1.77E+6$ KPa at time $t = 0.011$ seconds in frontal crash simulation. The effective plastic strain at the end of the simulation was 0.83 mm/mm (shown in figure 6.15). Figure 6.16 through 6.18 shows the deformation of the Mini-Baja frame using the side, top, and front views.

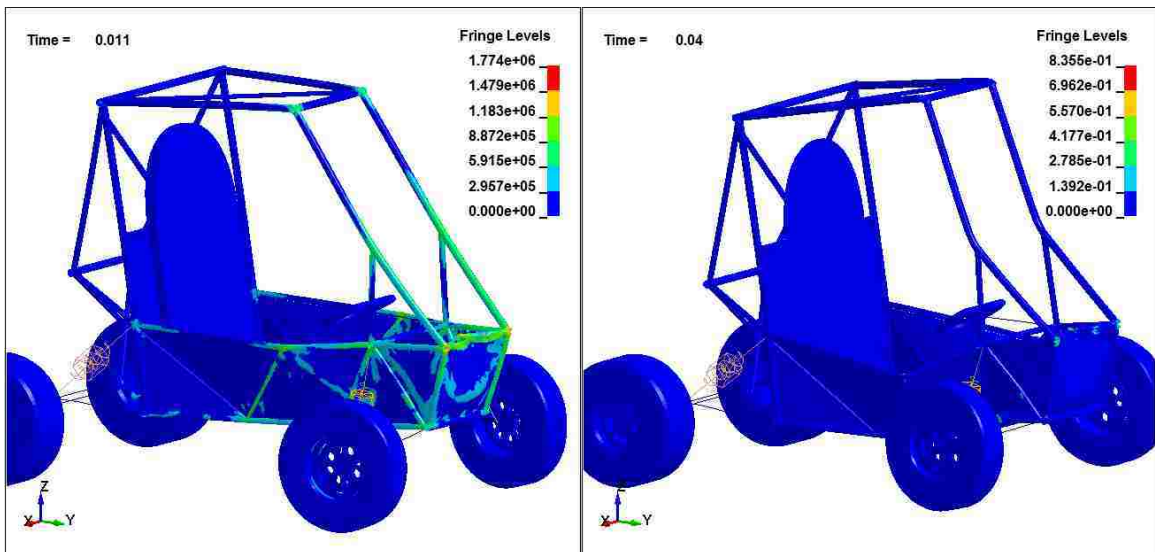


Figure 6.15 Left: the maximum von Mises stress at 0.011 sec; Right: effective plastic strain at the end of the simulation

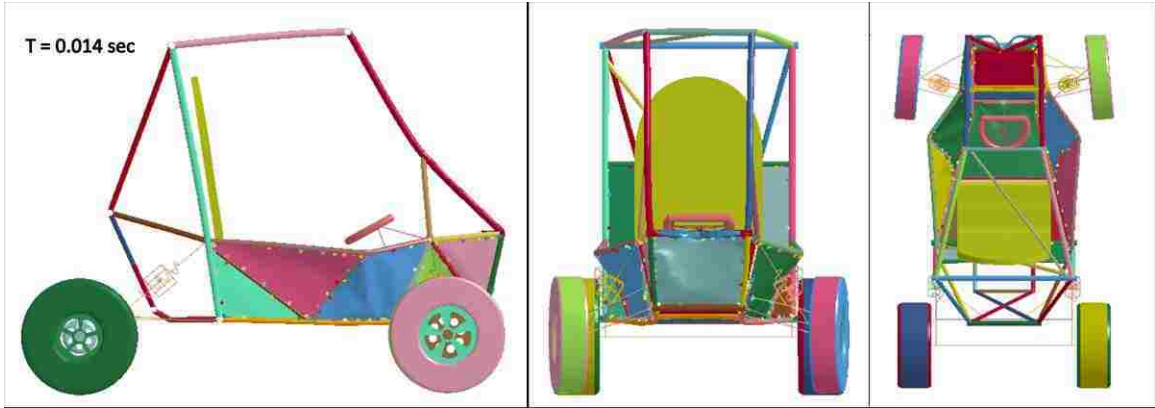


Figure 6.16 Side, top and front views of the deformation at $t = 0.014$ sec



Figure 6.17 Side, top and front views of the deformation at $t = 0.025$ sec



Figure 6.18 Side, top and front views of the deformation at $t = 0.036$ sec

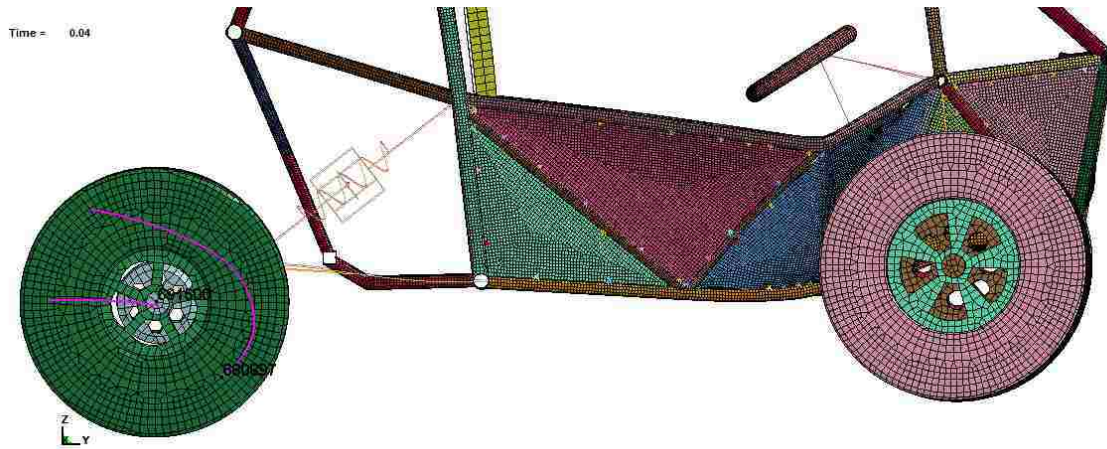


Figure 6.19 Traced nodes on the rear tire at $t = 0.04$ sec

Two corresponding nodes as shown in figure 6.19 on the rear tire were traced throughout the simulation to show the rotation of the rear tire affecting the deformation of the vehicle after the impact. It is shown that long after the crash of the vehicle into the rigid wall; the rear tire is still rotating which finally stops by the friction of the ground. In figure 6.20 the energy balance for the front impact scenario is given.

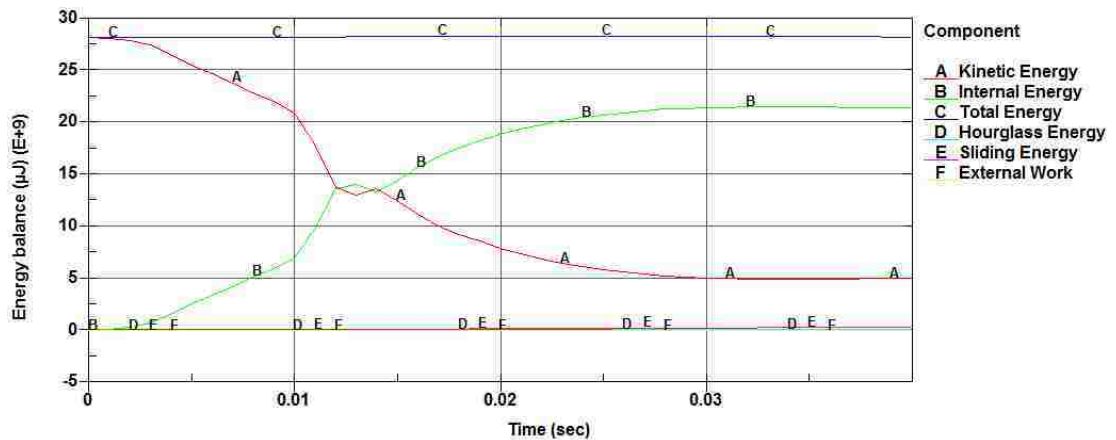


Figure 6.20 Energy balance for frontal crash at 48 km/h

It was observed that the front wheels are the first components that crash into the rigid wall, which tremendously can influence the behaviour of the vehicle in the crash. For this reason and also to explain the sudden change in the kinetic energy at 0.013 sec as shown in figure 6.20, the properties of the elastic tires were deliberately changed.

In figure 6.21 it is shown that as the tires were made lighter; the kinetic energy of the vehicle is decreased and therefore the rebound inertia of the tires in particular are less as well.

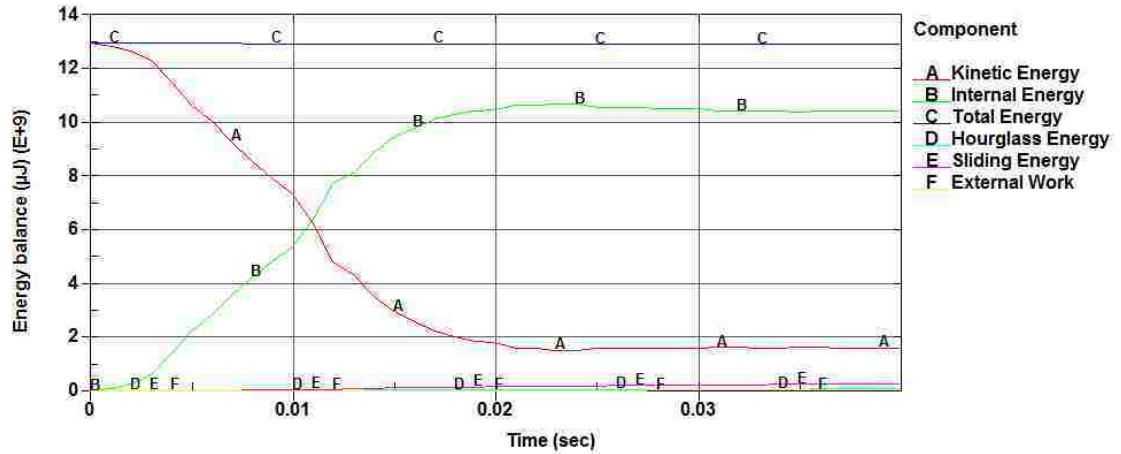


Figure 6.21 Energy balance for frontal crash at 48 km/h (low density tire)

In figure 6.22 the kinetic energy for 3 different tire densities is shown. It was observed that as the tires were lighter, the rotational inertia of front tires is less. In other words the tires would not tilt backward due to less momentum and are able to act as a shield in front the vehicle and damp much of the impact force and as a result, experience much smoother kinetic energy.

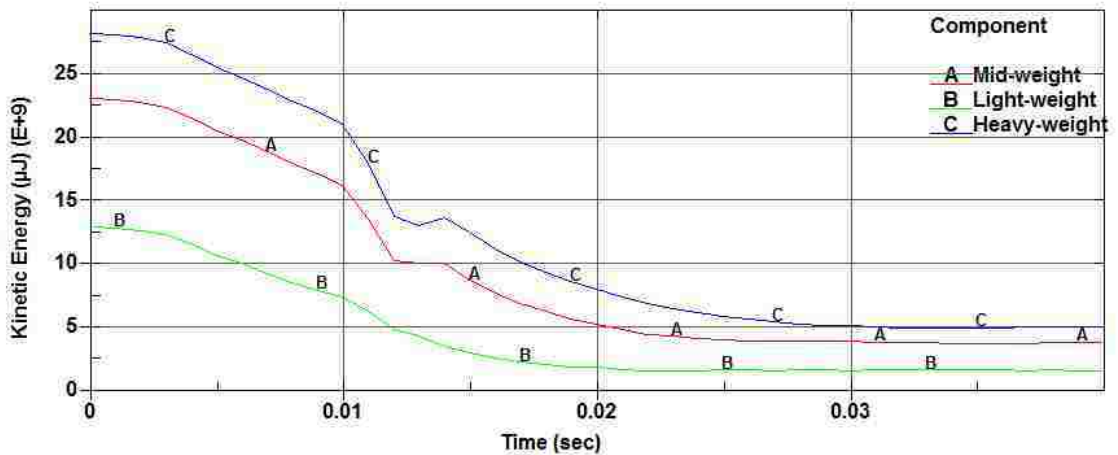


Figure 6.22 Kinetic energy based on density of tires at 48 km/h

Keep in mind that the discussion above was to clarify the sudden change in the kinetic energy in figure 6.20. Furthermore, one has to take into account that the correct material data that was implemented is the high density tires shown in figure 6.22, and the discussion presented was carried out intentionally for comparison purposes.

6.3.2 The side crash of the Mini-Baja vehicle

In this simulation, another sever scenario for the vehicle is proposed where the Mini-Baja impacts a rigid column from the side. The setup of the side crash is shown in figure 6.23.

Besides the severity of the damage to the structure, it can be thought as one of the worst case scenarios, which the driver inside the vehicle can experience. The base of the structure; the rectangular frame behind the seat is constructed from heavier and thicker tubes compared to the rest of the structure. Therefore, to fully observe the response of the vehicle in the side crash, two major locations of the rigid column are simulated.

In the first case, the column is next to the seat, while in the second case the column is distanced from the support frame in order to observe the maximum deformation of the frame at the centre.

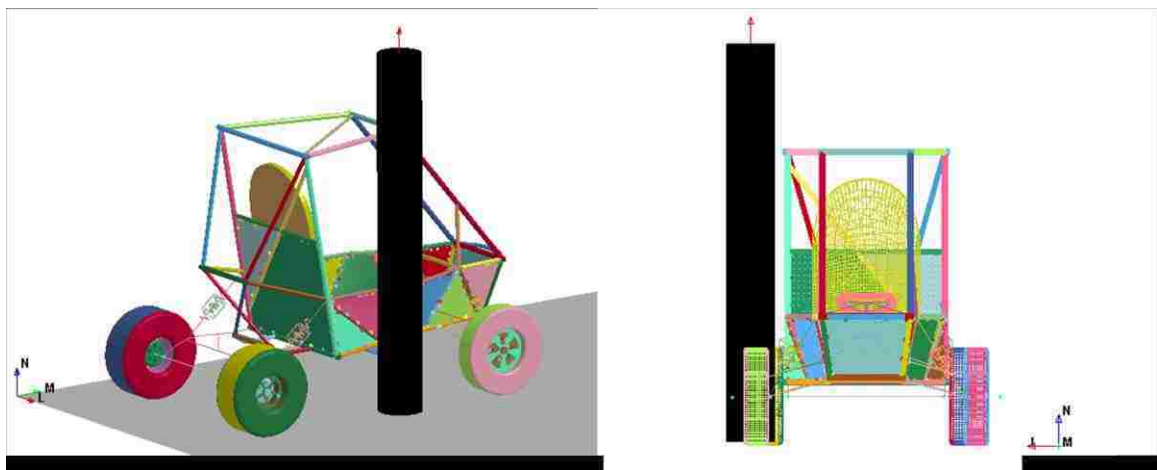


Figure 6.23 Side impact setup

The deformation sequence of the side impact simulation (first case where the column is next to the seat) is shown in figures 6.24 through 6.26 at selected instances in time.

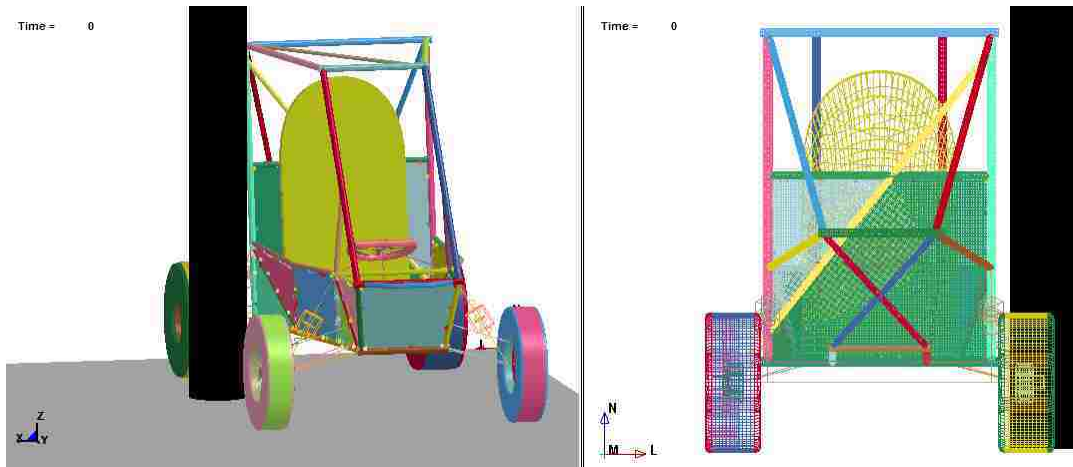


Figure 6.24 Sequential views of the side impact scenario 1 at initial position

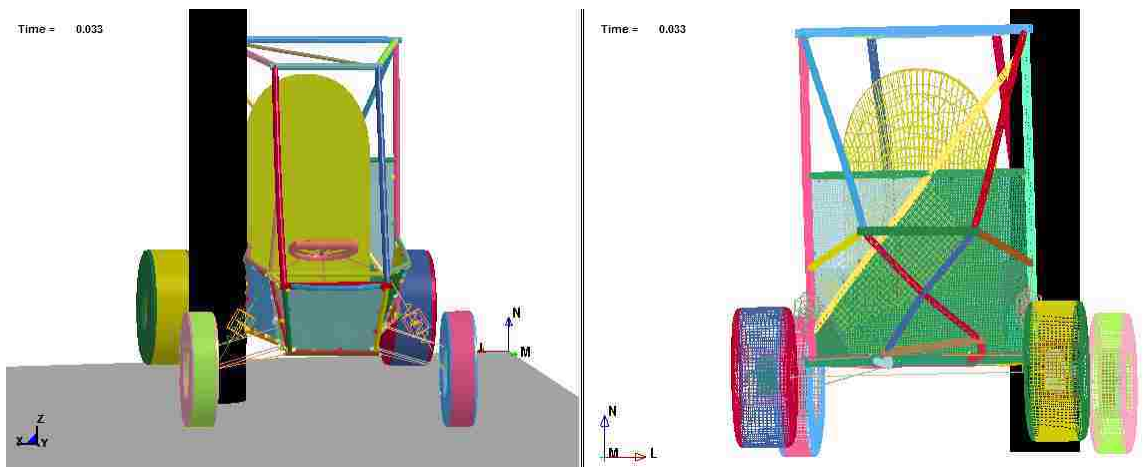


Figure 6.25 Sequential views of the side impact scenario 1 at $t = 0.033$ sec

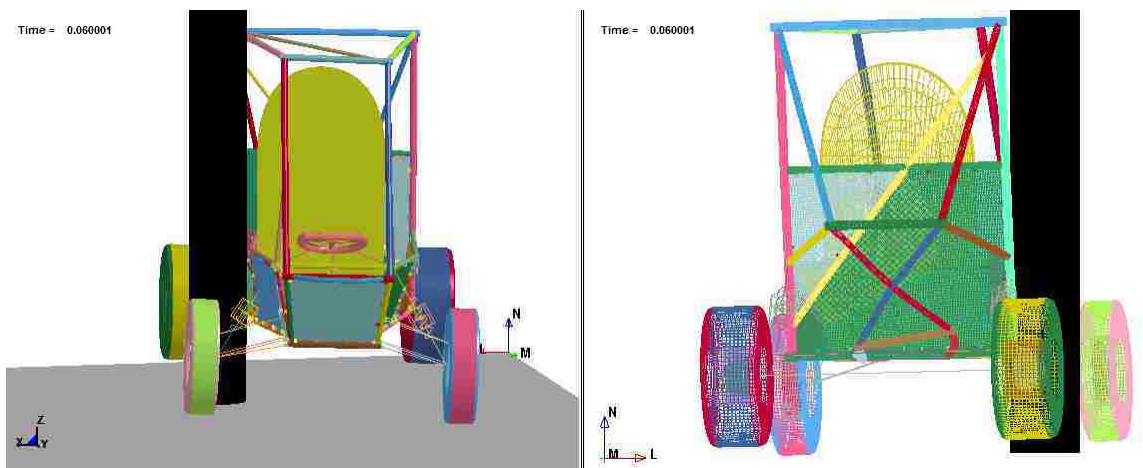


Figure 6.26 Sequential views of the side impact scenario 1 at the end of the simulation

The energy balance of the first case is shown in figure 6.27. The maximum von Mises stress of $2.88E+6$ KPa was distributed at time 0.007 seconds; just 3 ms after the frame impacted the rigid column. The effective plastic strain at the end of the simulation was 1.13 mm/mm.

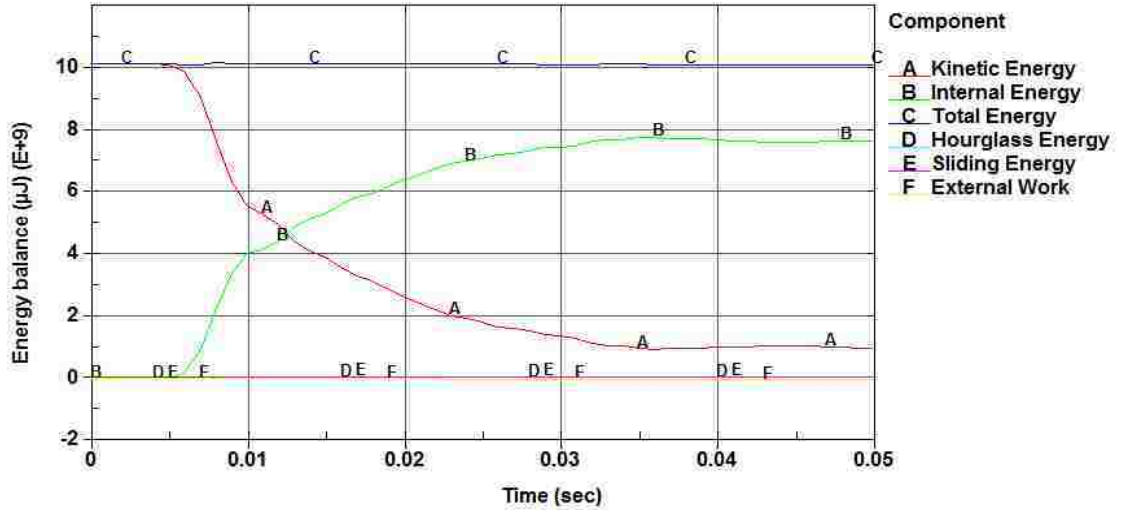


Figure 6.27 Energy balance of the side crash scenario 1 at 48 km/h

In the second simulation the rigid column was moved to the centre line of the vehicle to observe the maximum deformation contour throughout the frame. Figures 6.28 through 6.31 show the sequence of the side impact at selected instances.

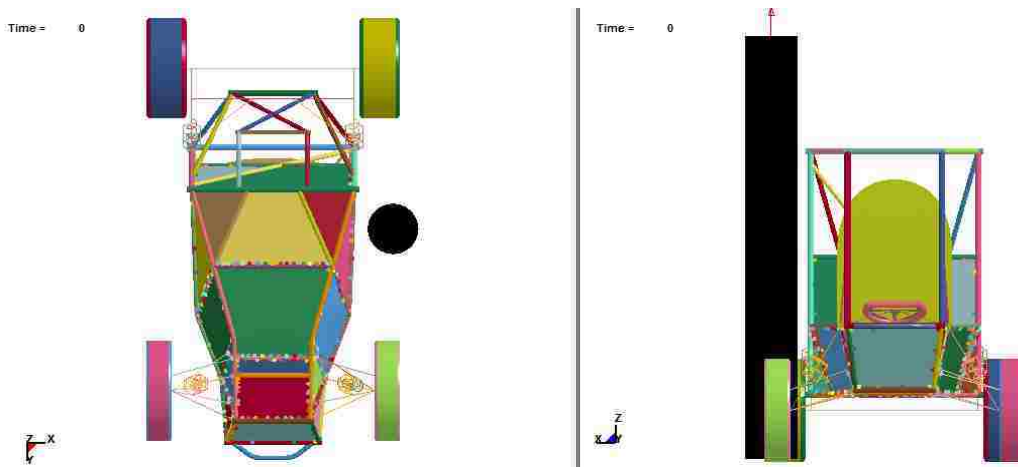


Figure 6.28 Sequential views of the side impact scenario 2 at initial position

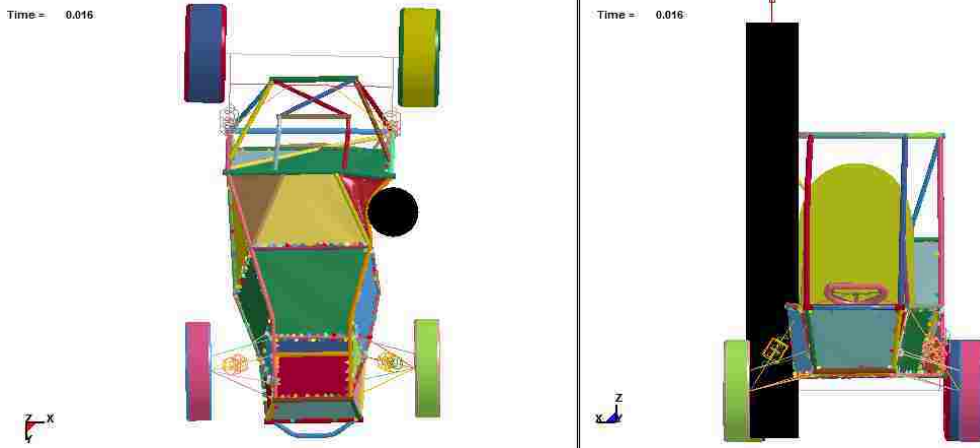


Figure 6.29 Sequential views of the side impact scenario 2 at $t = 0.016$ sec

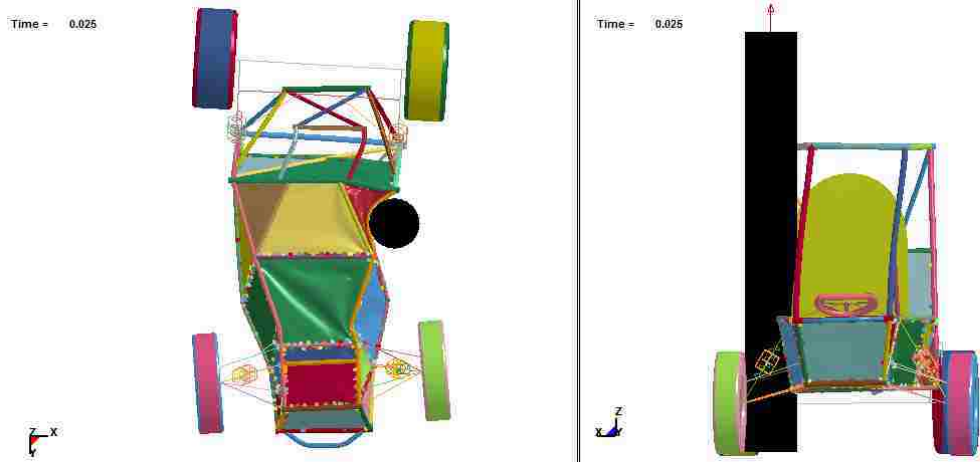


Figure 6.30 Sequential views of the side impact scenario 2 at $t = 0.025$ sec

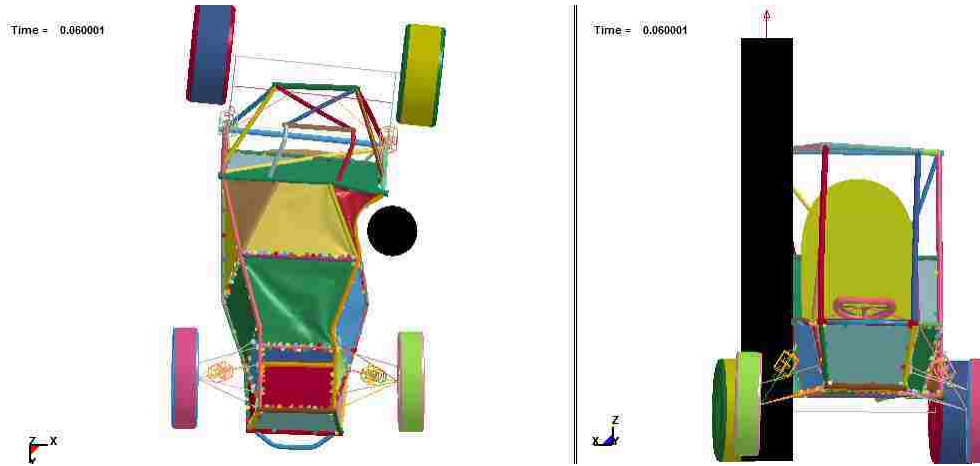


Figure 6.31 Sequential views of the side impact scenario 2 at the end of the simulation

The maximum von Mises stress in the second scenario was $1.43E+6$ at time 0.022 seconds. The effective plastic strain at the end of the simulation was 1.28 mm/mm. The balance of the energy for the side crash second case is shown in figure 6.32.

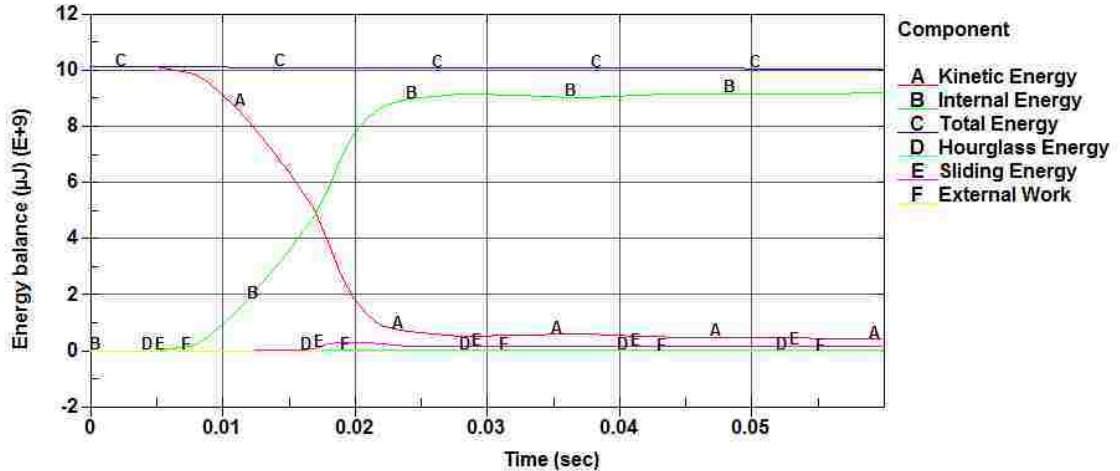


Figure 6.32 Energy balance of the side crash scenario 2 at 48 km/h

6.3.3 Head-on collision of two Mini-Baja vehicles at 30 degree impact angle

In references [44] and [49] some standard procedures and practices in conducting a vehicle-to-vehicle crash tests are discussed. It is mentioned that regarding the peak chest acceleration occurrences in comparison to frontal rigid barrier impacts, the 48 km/h velocity has been re-established for head-on collisions. Also, an impact angle of 30 degrees was chosen as a standard value for such a crash scenario. In [49] a complete flow chart representing different crash configuration for various crash modes regulated by NHTSA are given.

Based on the guidelines [44] and [49], a simulation is described where two Mini-Baja vehicles are subjected to collision as shown in figure 6.33. An initial velocity of 48 km/h has been set for the vehicles and the angle between the lines of travel of the two vehicles is 30 degrees.

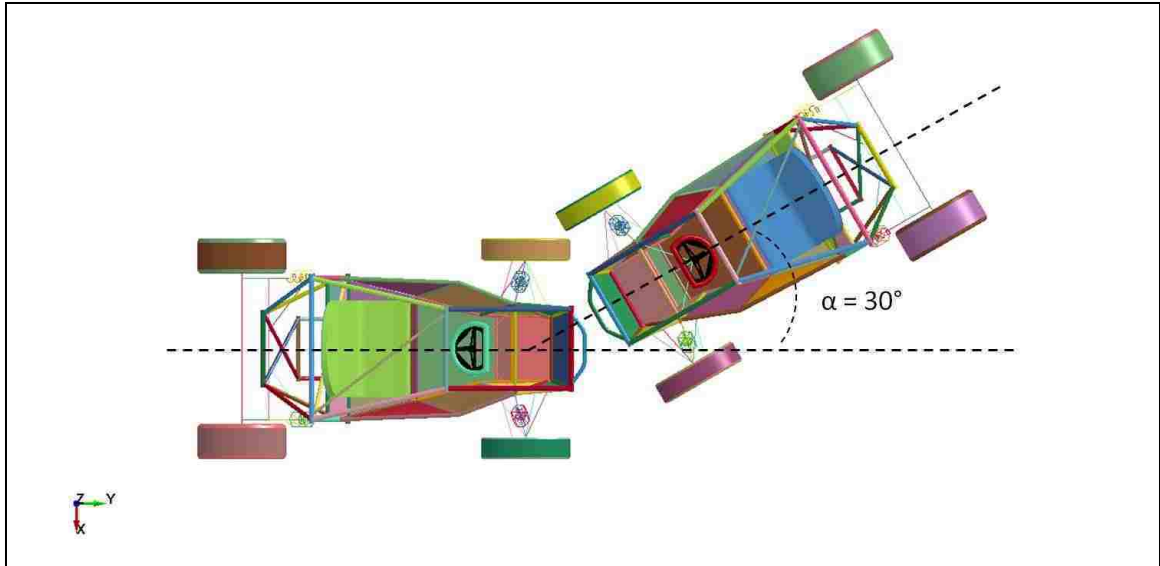


Figure 6.33 Configuration of the vehicle-to-vehicle crash at 30 degree impact angle

The distance between the two vehicles was prescribed in accordance with the orientation of the tires of the vehicles. The objective was to see the responses of the vehicles as they crash into each other; therefore, the model was setup in order to avoid the crash of tires against each other. Figures 6.34 through 6.37 show the sequence of the head-on collision at selected instances.

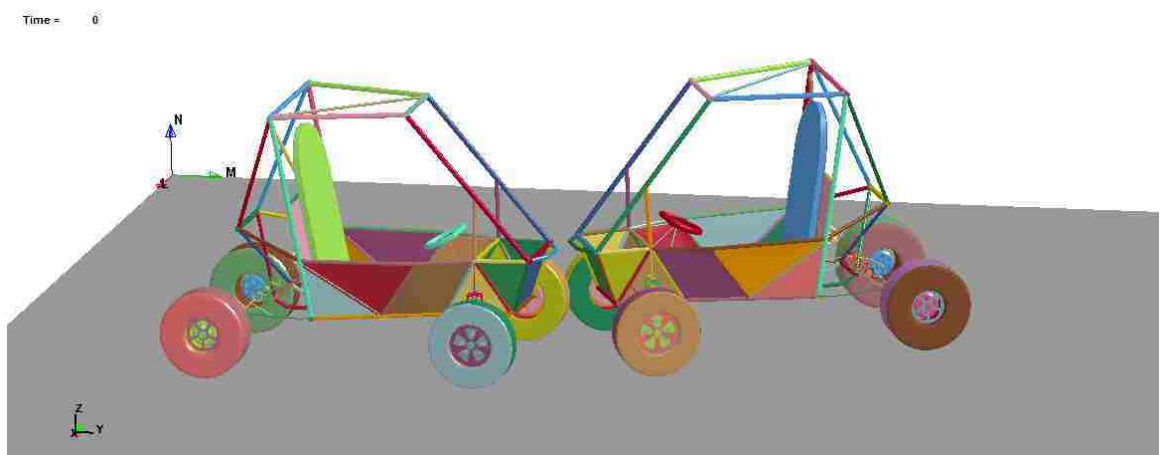


Figure 6.34 Sequential views of the vehicle-to-vehicle crash at initial position

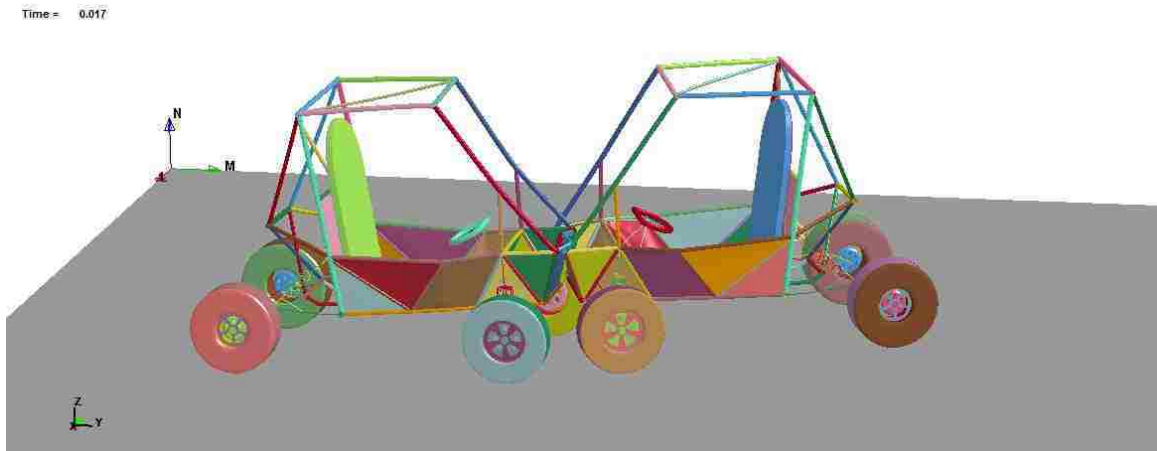


Figure 6.35 Sequential views of the vehicle-to-vehicle crash at $t = 0.017$ sec

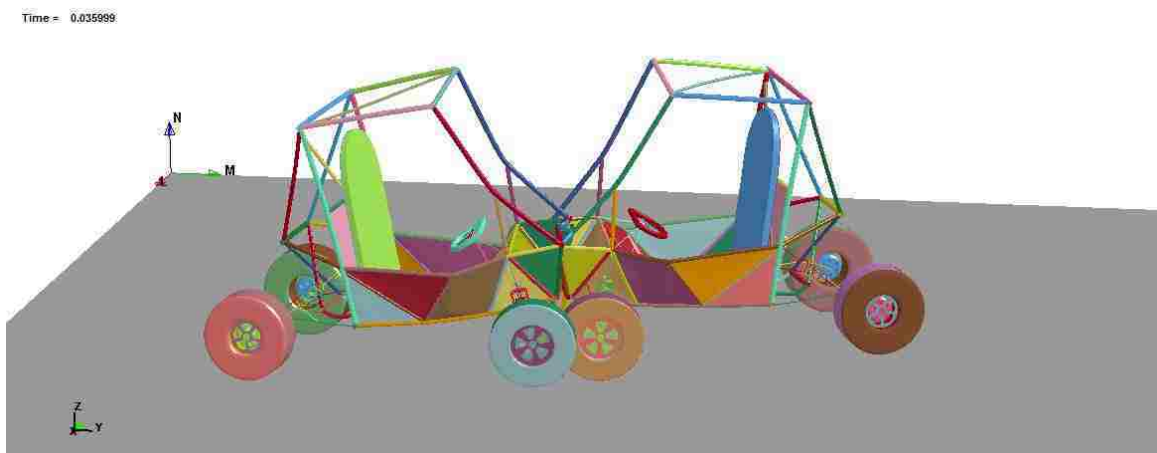


Figure 6.36 Sequential views of the vehicle-to-vehicle crash at $t = 0.036$ sec

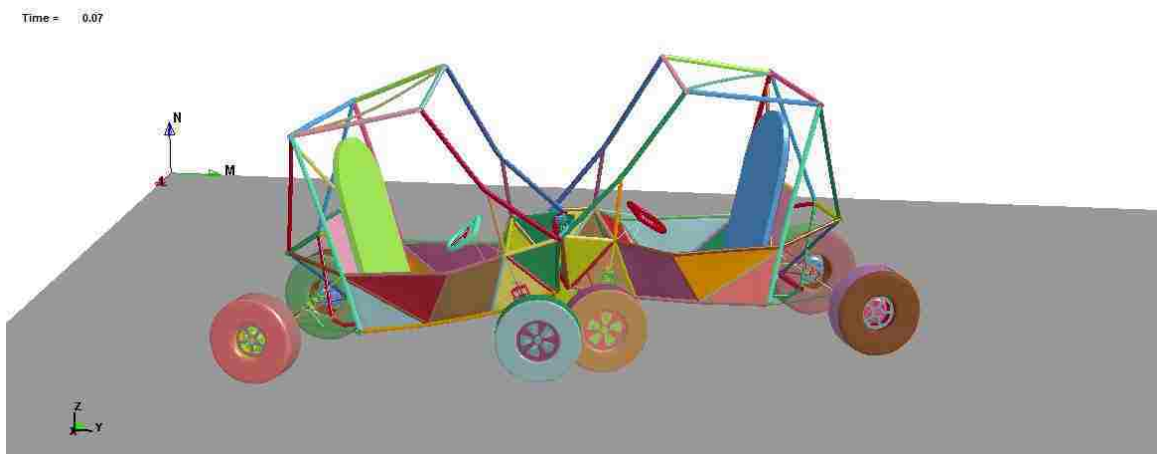


Figure 6.37 Sequential views of the vehicle-to-vehicle crash at $t = 0.07$ sec

The impact velocity of 60 km/h and 70 km/h was also simulated to ensure the stability of the model and the tendency to the increase of the plastic deformation and energies. Despite that, results are given for one particular speed (48 km/h).

The amount of hourglass energy as shown in figure 6.38 is 3.5 % compared to the internal energy, which is acceptable. Furthermore, it was also noted that the amount of sliding energy is increased as the vehicles are squashed into each other.

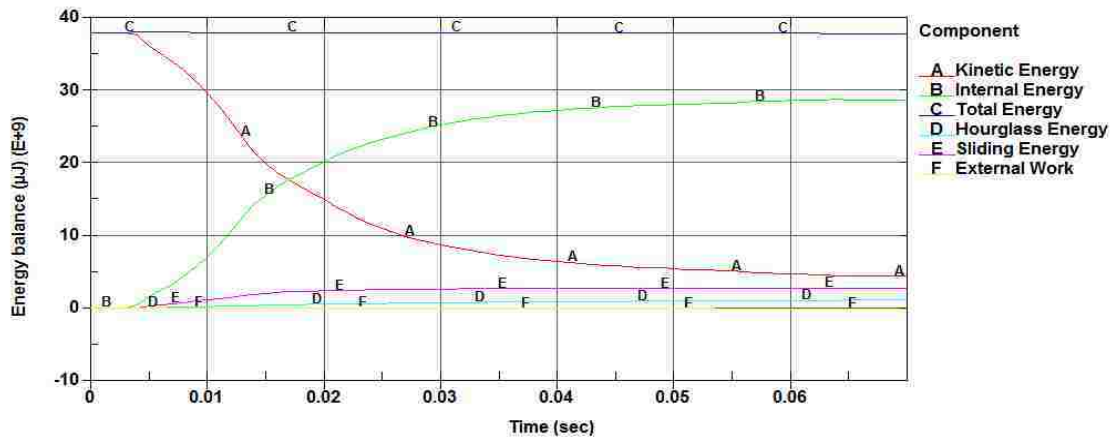


Figure 6.38 Energy balance of the vehicle-to-vehicle crash at 48 km/h

The distribution of von Mises stress is shown in figure 6.39. The amount of plastic strain for both vehicles is 0.87 mm/mm.

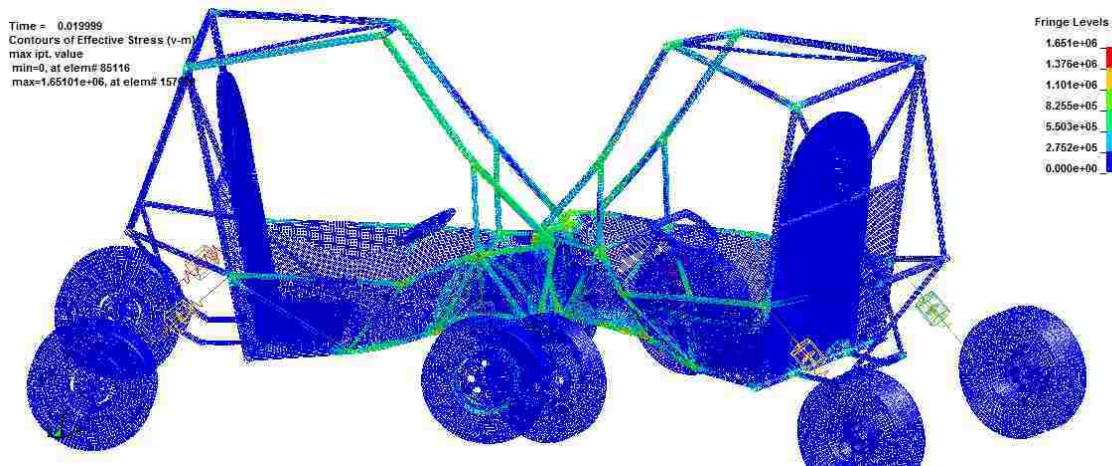


Figure 6.39 Maximum von Mises stress for vehicle-to-vehicle crash at t = 0.02 sec

CHAPTER VII

CONCLUSIONS AND RECOMMENDATIONS FOR FUTURE WORK

7.1 Conclusions

As stated in the introduction chapter, the objective of this thesis was to develop a general guideline and report the findings for the finite element analysis of tubular-type structures such as the Mini-Baja all terrain vehicle. In this context, two major approaches were considered. On one hand the finite element method could be utilized in the process of design optimization and fabrication of such structures, and on the other hand this tool can be employed in analyzing an existing structure. The objective of the present research was to perform a step-by-step study on the finite element analysis of the vehicle rather than for design purposes.

An attempt was made to distinguish between static, quasi-static, and dynamic analysis of Mini-Baja due to loading conditions. The research includes the implementation of finite element analysis for high deformation crash scenarios. In finite element analysis, the structure is broken up into small elements which are easier to analyze. It is the only approach that can be adopted for the solution of complicated structural problems.

In chapters 2 and 3, a comparison between beam, shell, and solid element idealizations was discussed. It was concluded that due to high computational cost of solid elements and disadvantages of wireframe idealizations, shell model is the ideal choice for analysing the Mini-Baja frame. Based on the simulations conducted, it was observed that in the static or the transient modal superposition analyses, it is important to constrain the frame as little as possible. Therefore, constraining and releasing the appropriate degrees of freedom are crucial in obtaining realistic results.

Based on the results presented in chapters 4 and 5; it was concluded that a localized higher order element formulation implemented simultaneously with hourglass stiffness-

form control is best suited for reducing the detrimental effects of the zero energy modes in deformation of the Mini-Baja structure.

It is clear that while the finite element method offers a powerful tool for analysis purposes, it requires a profound understanding of the finite element theory, the FEA software, and the structure being modeled. Generally speaking, the finite element method provides an approximate solution of a physical model; therefore, in creating a numerical model careful considerations should be employed to reasonably represent the exact physics of an event. In chapter 6, it was shown that many assumptions were necessary for incorporating the additional components into the Mini-Baja finite element model. It was also concluded that although assumptions were necessary in modeling a detailed vehicle, it is very important to carefully select appropriate keyword commands to define those desired assumptions.

Based on the findings in this thesis, some of the important parameters in analyzing Mini-Baja vehicle are listed below:

- Contact non-linearity is one of the most important factors in a crash scenario, and should be treated carefully to overcome inaccurate results. Automatic single contact algorithms are preferred in crash applications, but it was observed that local contact algorithms are more accurate in terms of a Mini-Baja vehicle.
- Higher order element formulations produce a more stiff response of the body and should be employed wisely.
- When meshing with shell elements, quadrilateral elements are preferred over triangular elements. Triangular elements do not have hourglass modes; however, they can lead to a stiff response. Furthermore, quadrilateral shells that are initially warped or that become warped due to deformation can lead to significant inaccuracies.
- Assigning meaningful friction coefficients on the rigid-walls are essential for correct impact characteristic of the vehicle crash.

- Nodal rigid bodies should be used very carefully since it is turning a deformable point to a rigid point in a deformable body, and therefore, should be created between nodes with small distances in assembly applications.
- In problems where mass scaling is employed, always the results should be checked. The kinetic energy for instance should be checked based on the mass and velocity of the vehicle ($E_{kin} = 0.5 m v^2$).
- Energy associated with different components should be plotted and interpreted in order to check if anything is unrealistic or any energy is excessive in one particular component.
- In finite element analysis a very minor error such as nodal numbering (normal shell directions) can result in erroneous results and therefore, manually checking the whole input code and keyword commands are essential.

To conclude this section it is worth reminding the reader that; the purpose of a vehicle chassis is to connect four wheels to a structure. While it should be designed to be as rigid as possible in bending and torsion it must be capable of absorbing as much of the inertia without excessive deflections. This is a key point for protecting the driver.

7.2 Recommendations for future work

In this thesis, the frontal impact problem was discussed for the Mini-Baja vehicle in detail. Furthermore, the side impact condition and a head-on collision was developed as well. It is highly recommended that future work on this project take the following bulleted items into considerations;

- In order to improve the accuracy in the crash problems, some additional components can be added to the frame. Among those; frame braces, accurate representation of the engine, protecting flocs about the vehicle, rivets and fasteners used in the assembly process are of major importance.
- It is suggested by the society of crash engineers to conduct a roll-over simulation which was intentionally left out of this thesis. Looking into this problem is highly recommended.

- To study the response of the frame when impacting roadside hardware, a barrier impact to be implemented. This barrier can be the standard terrain hardware in the Mini-Baja field competition.
- In order to conduct a roll-over and barrier impact simulation on the current Mini-Baja geometry, more accurate models of the steering wheels and suspension components are necessary. This is to capturing accurate kinematic response of the vehicle.
- To incorporate appropriate failure criterion for a more accurate response, a failure criterion has to be defined for welded joints as well as the body panels.
- To study the effect of a crash on human body, a Hybrid III¹ occupant dummy can be added to the system as shown in figure 7.1. Occupant dummy is necessary in design of restrain systems (seatbelt and airbags) for optimum occupant protection. A crash scenario where two Mini-Baja vehicles are colliding at 30 degree impact angle with inclusion of occupant dummies could be one of the next steps in analyzing Mini-Baja crashworthiness response. (Figure 7.2)

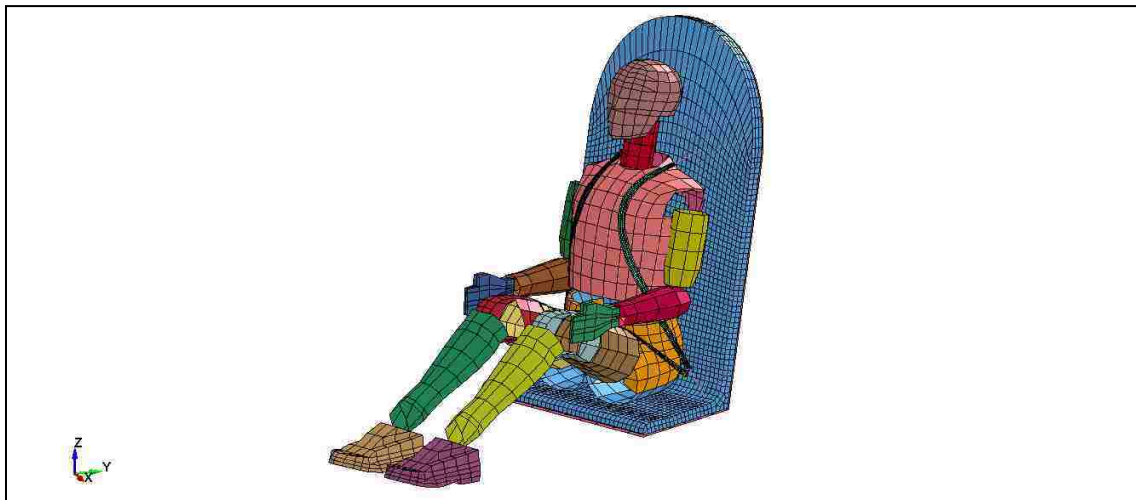


Figure 7.1 Hybrid III occupant dummy

¹ The Hybrid III dummy is an anthropomorphic test device (ATD) that represents the human body. By developing the geometry, weight, inertia, joint stiffness, and energy absorption characteristics of a human body, ATDs are expected to simulate human response when exposed to a crash scenario. Hybrid III dummies are frequently used for impact scenarios and safety assessments and prediction of established injury criteria such as HIC and Chest indexes [50].

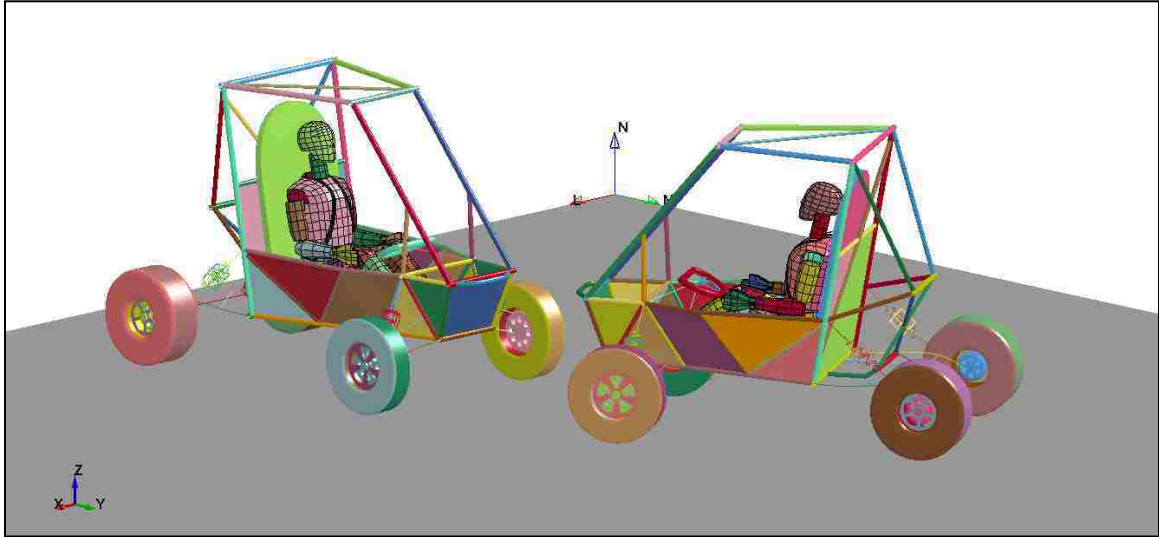


Figure 7.2 Two Mini-Baja's impact scenario at 30 degree impact angle

The following two recommendations are primarily addressed to the undergraduate students who are involved with Mini-Baja capstone-project for using finite elements in their work.

- Providing a criterion for analyzing the vehicle by students at the University of Windsor. Here, at the university, every year the students are teamed up to build a new vehicle to compete against each other and other universities. A consistent set of criteria can be introduced to compare the capstone-projects from year to year. Vehicle user defined over-all stiffness or pitch, yaw and roll rotations can be examples of such criterion.
- The Mini-Baja vehicle to be heavily instrumented to record the history of loads, accelerations, displacement, etc for comparison against the finite element simulations. In this area, certain tests such as speed bump test, gravity equilibrium check, and slopped terrain tests can be introduced as non-destructive crashworthiness tests.

REFERENCES

- [1] 2012 Baja SAE Rules; <http://students.sae.org/competitions/bajasae/rules/>
- [2] Safety Net (2009) Vehicle Safety–web text, The European Commission Directorate-General Transport and Energy, 2009.
- [3] J. Fish and T. Belytschko, “A First Course in Finite Elements”, Chichester, JohnWiley & Sons Inc., 2007.
- [4] R.D. Cook, D.S. Malkus, M.E. Plesha and R.J. Witt, “Concepts and Applications of Finite Element Analysis”, New York, JohnWiley & Sons Inc., 2002.
- [5] J. Bonet and R.D. Wood, “Nonlinear Continuum Mechanics for Finite Element Analysis”, Cambridge, Cambridge University Press, 1997.
- [6] T. Belytschko, W.K. Liu and B. Moran, “Nonlinear Finite Elements for Continua and Structures”, Chichester, JohnWiley & Sons Inc., 2001.
- [7] T.Y. Yang and G. Lianis, “Large displacement analysis of viscoelastic beams and frames by the finite-element method”, Journal of Applied Mechanics 1974, 74, pp. 635-640.
- [8] Abaqus/CAE 6.9 Documentation;
<file:///C:/SIMULIA/Documentation/docs/v6.9/index.html>
- [9] T.Y. Yang, “Finite Element Structural Analysis”, New Jersey, Prentice-Hall Inc., 1986.
- [10] T.Y. Yang, “Matrix displacement solution to elastic problems of beams and frames”, International Journal of Solids and Structure 1973, 9, pp. 829-842.
- [11] T.Y. Yang and C.T. Sun, “Axial-flexural vibration of frameworks using finite-element approach”, Journal of Acoustical Society of America 1973, 53(1), pp. 137-146.

- [12] T.Y. Yang and C.T. Sun, “Finite elements for the vibration of framed shear walls”, *Journal of Sound and Vibration* 1973, 27(3), pp. 297-311.
- [13] Solidworks Web Help, 1995-2011 Dassault Systèmes, <http://help.solidworks.com>
- [14] J. Hastie, “Mini-Baja Vehicle Design Optimization Technical Report”, College of Engineering, North-Eastern University 2005.
- [15] V. Jain and M. Singh, “Design of a Mini-Baja Chassis for Crashworthiness through Finite Element Analysis”, Indian Institute of Technology 2005.
- [16] C. Martinez Jr., “A finite element analysis of ‘steel horse’ frame”, The University of Texas-Pan American (UTPA), 2003.
- [17] N. Noorbhasha, “Computational analysis for improved design of a SAE BAJA frame structure”, Graduate College, University of Nevada Las Vegas (UNLV), 2010.
- [18] D.T. Anderson and B. Mills, “Dynamic analysis of a car chassis frame using the finite element method”, *International Journal of Mechanical Sciences* 1972, 14, pp. 799-808.
- [19] L. Kwasniewski, H. Li, R. Nimbalkar and J. Wekezer, “Crashworthiness assessment of a paratransit bus”, *International Journal of Impact Engineering* 2006, 32, pp. 883–888.
- [20] J.G. Thacker, S.W. Reagan, J.A. Pellettiere, W.D. Pilkey, J.R. Crandall and E.M. Sieveka, “Experience during development of a dynamic crash response automobile model”, *Journal of Finite Element in Analysis and Design* 1998, 30, pp. 279-295.
- [21] D. Marzougui, C.D. Kan and N.E. Bedewi, “Development and validation of an NCAP simulation using LS-DYNA3D”, Fourth International LS-DYNA3D Conference 1996, Minneapolis, September 5-6, pp. 319-332.
- [22] National Highway Traffic Safety Administration (NHTSA), <http://www.nhtsa.gov/>
- [23] “Development & Validation of a Finite Element Model for the 2006 Ford F250 Pickup Truck”, Technical Summary, December 2008, NCAC 2008-T-003.

- [24] H.E. Boyer, "Atlas of Stress-Strain Curves", ASM International, 2002.
- [25] "Validation of a Single Unit Truck Model for Roadside Hardware Impacts", Working paper, November 2003, NCAC 2003-W-001.
- [26] "Development and Validation of a Pick-Up Truck Suspension Finite Element Model for Use in Crash Simulation", Working paper, November 2003, NCAC 2003-W-003.
- [27] N.M. Baran, "Finite Element Analysis on Microcomputers", Oxford, McGraw-Hill Book Company, 1988.
- [28] W. Weaver Jr. and J.M. Gere, "Matrix Analysis of Framed Structures", 3rd Edition, Springer-Verlag, 1966.
- [29] M.A. Bhatti, "Fundamental Finite Element Analysis and Application", New Jersey, John Wiley & Sons Inc., 2005.
- [30] J.O. Hallquist, "LS-DYNA Keyword User's Manual" Livermore Software Technology Corporation, 2001.
- [31] N.G. Zamani, "Finite element analysis in solid mechanics; issues and trends", Physics in Canada 2008, 64(2), pp. 55-58.
- [32] D.L. Logan, "A First Course in the Finite Element Method", California, Brooks/Cole Thomson Learning Inc., 2002.
- [33] W. Riley, "Design and Analysis of Vehicular Structures", Master of Engineering Report, University of Windsor, 2000.
- [34] Catia V5 Documentation; "ELFINI finite element reference guide".
- [35] ASM Aerospace Specification Metals Inc., AISI 4130 Steel, <http://www.aerospacemetals.com/contact-aerospace-metals.html>
- [36] Ansys 13.0 Documentation.

- [37] J.O. Hallquist, "LS-DYNA Theoretical Manual", Livermore Software Technology Corporation, 1998.
- [38] W. J. Bottega, "Engineering Vibrations", Florida, Taylor & Francis Group, 2006.
- [39] <http://en.wikipedia.org/wiki/Viscoplasticity>
- [40] O.C. Zienkiewicz and R.L. Taylor, "Finite Element Method - Solid Mechanics", Oxford, McGraw-Hill Book Company, 2000.
- [41] I. Oskarsson, "A new h-adaptive method for shell elements in LS-DYNA", Division of Structural Mechanics, Lund University, 2006.
- [42] S. Bala and J. Day, "General Guidelines for Crash Analysis in LS-DYNA", Livermore Software Technology Corporation.
- [43] J.D. Reid and N.R. Hiser, "Friction modeling between solid elements", International Journal of Crashworthiness 2004, 9(1), pp. 65-72.
- [44] W.T. Hollowell, H.C. Gabler, S.L. Stucki, S. Summers, and J.R. Hackney, "Updated Review of Potential Test Procedures for FMVSS NO. 208", October 1999, NHTSA.
- [45] G.R. Consolazio, J.H. Chung and K.R. Gurley, "Impact simulation and full scale crash testing of a low profile concrete work zone barrier", The Journal of Computers and Structures 2003, 81, pp. 1359-1374.
- [46] S. Abotula and V. B. Chalivendra, "An experimental and numerical investigation of the static and dynamic constitutive behaviour of aluminum alloys", The Journal of Strain Analysis for Engineering Design 2010, 45(8), pp.555-565.
- [47] "Finite element analyses with IMPAXX energy absorbing foams in headliner applications (Modeling instructions and material models for use in FMVSS201U head impact simulations)", Trademark of the Dow Chemical Company.

[48] “Methodology for Seat Design and Certification by Analysis”, Report Number; Agate-WP3.4-034012-079, August 2001, prepared for National Aeronautics and Space Administration.

[49] S.L. Stucki, W.T. Hollowell and O. Fessahaie, “Determination of frontal offset test conditions based on crash data”, NASS/USA 1998, Paper Number 98-S1-O-02

[50] A. Nouredine, A. Eskandarian and K. Digges, “Computer modeling and validation of a Hybrid III dummy for crashworthiness simulation”, Journal of Mathematical and Computer Modelling 2002, 35, pp. 885-893.

APPENDICES

APPENDIX A

A. SEAM WELD CONNECTION

In order to provide a comprehensive tutorial for a seam weld connection in “Catia V5” a video tutorial was created and is attached by a DVD to this thesis.

The description of the seam weld tutorial is as follows; two circular tubes with diameters of 20 mm and 30mm with arbitrarily lengths are orientated as shown in figure A.1. The thicknesses of the tubes are 1 mm each. In this tutorial a seam weld connection is to be created at the joint.



Figure A.1 Seam weld connection tutorial

APPENDIX B

B. WIREFRAME LINE CONNECTION ISSUE

In order to provide a comprehensive tutorial for the line connection issue in wireframe structures, a video tutorial was created and is attached by a DVD to this thesis.

The description of the wireframe line connection tutorial is as follows; two lines as shown in figure B.1 with tubular cross-sectional properties are connected to each other at 90 degree angle. The dimensions of the lines are not important and can be assumed as desired. In this tutorial a rigid connection is to be created at the intersection for a perfectly rigid joint.

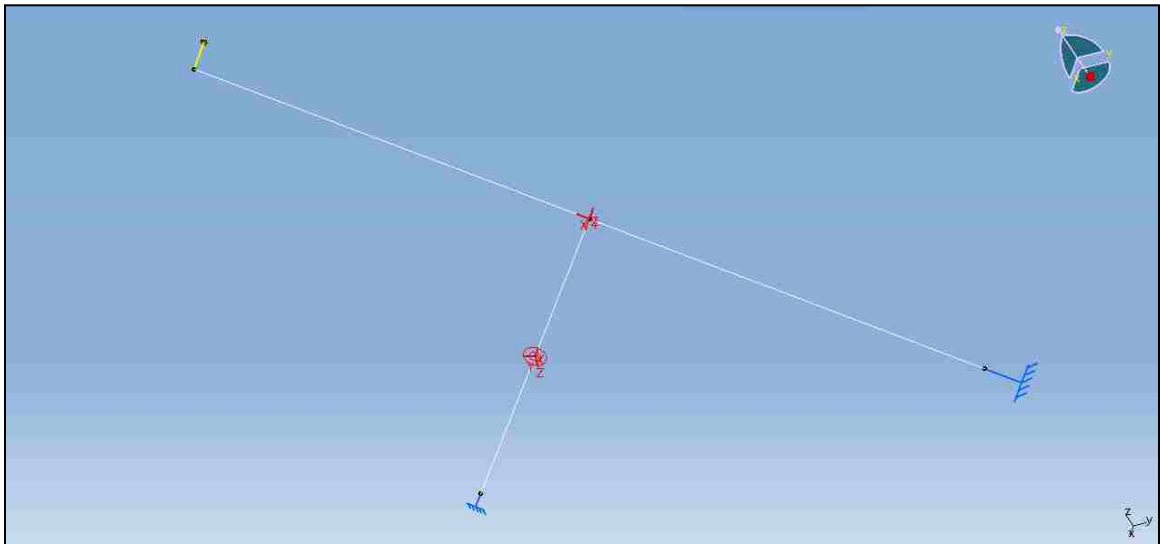


Figure B.1 Line connection issue tutorial

APPENDIX C

C. TRANSIENT DYNAMIC ANALYSIS

In order to provide a comprehensive tutorial for the dynamic analysis simulation in “Catia V5” a video tutorial was created and is attached by a DVD to this thesis.

The description of the transient analysis tutorial is as follows; a beam element as shown in figure C.1 with tubular cross-sectional property is orientated in y-direction. In this tutorial transient dynamic loads transmitted to the tip of the beam are analyzed with transient dynamic response case in Catia. The length of the beam can be arbitrarily assumed.

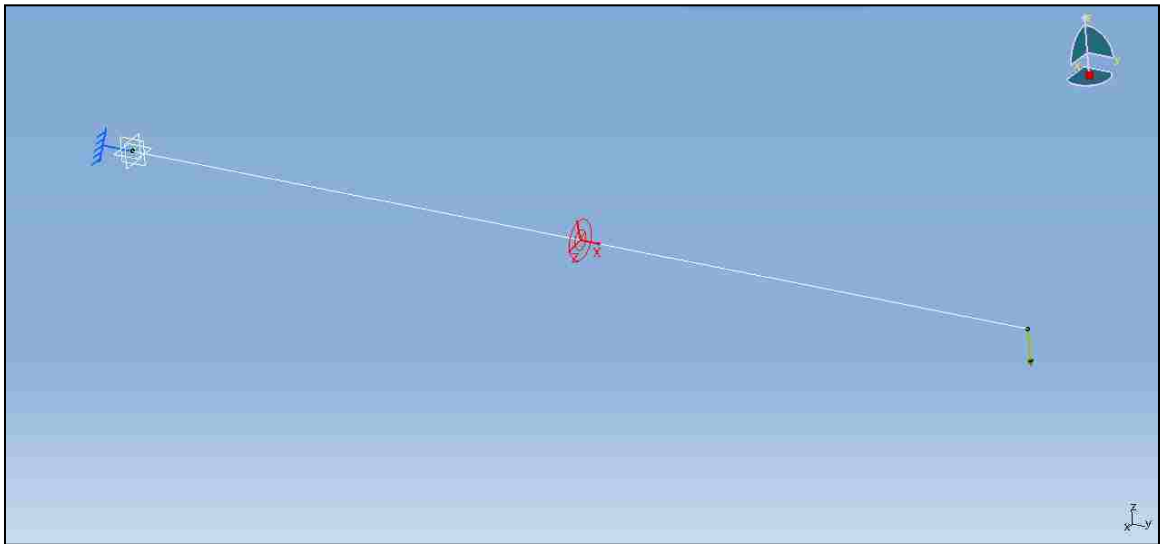


Figure C.1 Transient dynamic analysis tutorial

VITA AUCTORIS

NAME:	Babak Shahabi
PLACE OF BIRTH	Tehran, Iran
YEAR OF BIRTH	1986
EDUCATION	Saeed High School, Tehran 2000-2004 University of Science & Research Tehran, Iran 2004-2009 B.Sc. University of Windsor, Windsor, Ontario 2009-2011 M.Sc.